Improved Lifetimes and Synchronization Behavior in Multi-grid Inertial Electrostatic Confinement Fusion Devices

by

Thomas J. McGuire

Bachelor of Science, Aerospace Engineering
The Pennsylvania State University, May 1999

Master of Science, Aeronautics and Astronautics
Massachusetts Institute of Technology, June 2001

SUBMITTED TO THE DEPARTMENT OF AERONAUTICS AND ASTRONAUTICS
IN PARTIAL FULFILLMENT OF THE DEGREE OF

DOCTOR OF PHILOSOPHY IN AERONAUTICS AND ASTRONAUTICS
at the
MASSACHUSETTS INSTITUTE OF TECHNOLOGY

February 2007

Signature of Author_____
Department of Aeronautics and Astronautics
February 1, 2007

Certified by_____
Principal Research Scientist Raymond J. Sedwick
Department of Aeronautics and Astronautics, Thesis Supervisor

Certified by_____
Professor Manuel Martínez-Sánchez
Department of Aeronautics and Astronautics, Ph.D. Committee Chair

Certified by_____
Principal Research Scientist Oleg Batishchev
Department of Aeronautics and Astronautics

Accepted by_____
Jaime Peraire, Professor of Aeronautics and Astronautics
Chair, Committee on Graduate Students

Page intentionally left blank

Abstract

A high output power source is required for fast, manned exploration of the solar system, especially the outer planets. Travel times measured in months, not years, will require high power, lightweight nuclear systems. The mature nuclear concepts of solid-core fission and fusion Tokamaks do not satisfy the lightweight criteria due to massive radiators and magnets respectively. An attractive alternative is Inertial Electrostatic Confinement fusion. This extremely lightweight option has been studied extensively and to date has produced significant fusion rates of order 10^{10} reactions per second, but at low power gains, no higher than $Q = 10^{-4}$. The major loss mechanisms for the state-of-the-art IEC are identified via a detailed reaction rate scaling analysis. The use of a single cathode grid causes short ion lifetimes and operation at high device pressure for simple ion generation both fundamentally limit the efficiency of these devices. Several improvements, including operation at much lower pressure with ion guns and the use of multiple cathode grids, are verified with particle-in-cell modeling to greatly improve the efficiency of IECs. These simulations show that the greatly increased confinement allows for the development of significant collective behavior in the recirculating ions. The plasma self-organizes from an initially uniform state into a synchronized, pulsing collection of ion bunches. In simulations, these bunches are observed to be long-lived with lifetimes on the order of at least a tenth of a second, exceeding 20,000 passes. This represents a 3 order of magnitude improvement in confinement time and device efficiency. The synchronization of a bunch is due to the ion-ion interaction and kinematics of the well-confined IEC. The synchronization between beams is understood to arise from macroscale 'collisions' of bunches coupled with the kinematics of the device. Further, the collective effects limit the space charge buildup and higher densities result in violent ejection from the system.

An IEC device which exploits the synchronization effect can achieve high efficiencies and gain, with fusion as the fastest collision timescale. Despite the potential of operation at break-even, the total power output is limited by the relatively low achievable core densities. The immediate application for this work is inexpensive neutron generators useful for medical, security, research, and industrial applications, but use much less power than a state-of-the-art IEC. The results of this thesis suggest two future research directions. First, neutralization of portions of the ion flow could allow greater densities and increase power output to levels required for space travel. Second, the idea of using kinematics coupled with ion-ion collisions to control thermalization may be applied to other plasma confinement concepts.

Acknowledgements

I'd like to thank my advisor Ray Sedwick for supporting me through the years (7.5, but I'm not counting). This thesis wouldn't have been even close to possible without him. My girlfriend Jessica Marquez has kept me sane through the years and I want to say she is awesome. Also I have to apologize, because she now knows way more than I think she might like about fusion. My research partner, Carl Dietrich, has been working on fusion for almost as long as I have and it has made all the difference to have a compatriot to fire ideas at. Also, I am glad his experimental effort backs up a few of these predictions so that he can graduate and build me a roadable aircraft! (he decided to start a flying car company which just happens to be taking off….) I'd like to thank my committee members, Manuel Martínez-Sánchez, Oleg Batishchev, and John Hansman for helping to guide me through this adventure. I'd like to thank all my friends here at MIT over the years, I am so happy to finally join the ranks of the graduated! My family has been immensely supportive of their perpetual student-for-a-son, and I am glad they will soon be able to tell friends that their son finally has a job. Not to be forgotten is the Department of Defense NDSEG Fellowship, without which I would not have had the freedom to tackle this topic. I am glad that our country still supports academic freedom and education. Lastly, I'd like to thank the team at Berkley and Tech-X that developed the OOPIC program, and Suman Chakrabarti for pointing me to the program. Without it, I would have had to write my own PIC code, and I would still be coding….

Table of Contents

List of Figures

List of Tables

Nomenclature

(all units in mks unless otherwise noted)

A_c	=	acceptance, ratio of beam radius to beam opening radius
A_g	=	acceptance at a particular grid location
e	=	electron charge, $1.602 \cdot 10^{-19}$ Coulombs
E_{cat}	=	energy gained in moving a singly charged ion to the cathode grid
E_{fusion}	=	energy released by a fusion reaction
E_i	=	energy of incident particles
E_r	=	space-charge electric field radial to a beam
F	=	focusing factor, ratio of core radius to beam radius at cathode
$i_{in\text{-}beam}$	=	input current per beam
$i_{in\text{-}tot}$	=	total input current
i_{fusion}	=	portion of input current that fuses
KE_o	=	kinetic energy of a singly charged ion at the center of the device
#p	=	average number of passes (diameters) an ion makes through the device
p_{torr}	=	device background pressure [torr]
n	=	number density
n_{core}	=	core number density
n_{beam}	=	beam number density
N	=	number of beams, one beam corresponds to a diameter of the sphere
η	=	electrical conversion efficiency
R_a	=	outermost anode radius
R_{cat}	=	cathode radius
r	=	local radius of ion beam
r_c	=	core radius
r_g	=	beam radius at a particular grid
$r_{g\text{-}max}$	=	opening radius at a particular grid
r_{cat}	=	beam radius at the cathode grid
$r_{cat\text{-}max}$	=	opening radius in the cathode grid
v	=	velocity
v_i	=	velocity of incident particles
v_g	=	velocity at a particular grid location
v_{core}	=	velocity of ions in the core
v_{rel}	=	relative velocity of two fusing particles
V_{go}	=	central potential increase of a beam due to space charge
x	=	path length
x_{cat}	=	radial distance from core center to first grid along beam axis

y_{cat} = first grid radius measured orthogonally to beam axis
σ_{fus} = fusion cross-section
σ_a = atomic processes cross-section, combination of ionization and charge exchange
Φ = transparency of grids, fraction of area that is open
$\langle\rangle_c$ = average over core particle distribution
$\langle\rangle_p$ = average over an ion path from anode to core
%f = percentage of input ions that fuse
λ = wavelength of an instability
ω_p = plasma frequency
μ = ratio of incident to target particle mass in calculation of core averages

Chapter 1 Introduction

1.1 Motivation

The exploration and colonization of bodies outside the Earth-moon system will require large power sources for both propulsion and electricity. In order to enable moderately sized, fast missions to Mars and the asteroids, the high specific impulse of electrical propulsion will be necessary, but existing power sources limit the thrust levels. For manned missions and eventual colonization, massive spacecraft will require even more power. Solid-core nuclear fission reactors will surely power the first wave of these power-hungry missions, but they are quite massive and large improvements are necessary in the mass specific output of power systems. There are a number of candidate technologies, including gas-core fission reactors, Orion-derivative impulsive schemes, and magnetically confined fusion reactors.

Inertial Electrostatic Confinement Fusion, IEC, operates by electrostatically trapping fusion fuel ions in a spherical system of overlapping ion beams. As a spacecraft power and propulsion system, the low mass of electrostatic grids is vastly superior to massive magnetic coils required for Tokamaks or magnetic mirror confinement systems. By utilizing aneutronic fuel cycles, the massive shielding required of neutron-producing fission or fusion reactors is not necessary. IEC reactors with specific powers in the range of 1 to 10 kW per kg would reduce the Earth-Mars transit time from 6-8 months with chemical propulsion to 3 months [1]. A far-term system could reduce this to as little

as 8 days [2]. The trip times to the outer planets would be reduced to months instead of years. For slow-moving Earth-Mars cargo, the payload fraction of spacecraft would be enhanced from 0.3 for chemical to 0.6-0.9 for fusion. The increase for a 3 year Earth-Jupiter cargo mission is more impressive, increasing from less than 0.1 for chemical to over 0.8 for fusion.

While the initial motivation of this thesis was space propulsion, unfortunately it is still far from a viable concept. The sustaining motivation of this work is the interesting physics that was discovered as the confinement in IECs was improved. Further, the concept has near-term potential as an improved neutron source, even at the low power limitations shown later in the work.

1.2 Thesis outline and overview

This thesis is divided into 5 major sections:

1. Introduction and IEC background
2. Reaction rate scaling analysis
3. Multiple grid IEC concept
4. Synchronization phenomenon
5. Conclusions

The thesis is written in the same manner in which the research was conducted. First, the IEC concept was identified as a promising space fusion reactor technology. The problems with the concept are identified and analyzed in depth. Solutions to these problems are devised and then tested. Examination of the tests verified most of the proposed solutions and uncovered a new phenomenon, namely the synchronization process. This new phenomenon is analyzed and its impact on the IEC determined. This new knowledge points the way to several new research directions, namely the application of this phenomenon in other plasma devices.

1.3 What is an IEC and how does it work?

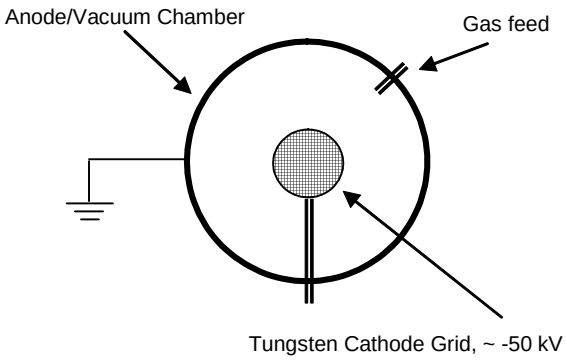

Figure 1.1, General IEC device configuration.

The general set-up of an IEC is shown in Figure 1.1. The ions are confined by electric fields supported by low mass, spherical grids. Laboratory systems have grids welded from stainless steel and refractory metal wire and the system is enclosed in a vacuum chamber. A space reactor would most likely have grids constructed of metal tubes which could support coolant and the system would be open to space vacuum. Ions are created at the anode via a glow discharge, electron impact ionization, or ion guns. The ions then fall into the center of the device. As they converge, fusion occurs between ions colliding with each other and with the background gas. Most of the ions that do not fuse on the first pass move towards the anode and are reflected. Ions then return to the core for another pass and this process repeats, yielding many opportunities to fuse. Fusion products stream away from the device core and are either collected by a solid wall thermal-based energy conversion system or a gridded electrostatic energy conversion system [3][4]. In general, the IEC is promising for the simplicity of the concept, its inherent low mass, the controllability of reactions, and the suitability to aneutronic fuels and direct energetic conversion [16].

1.4 History of IEC research

The IEC concept was invented by Philo T. Farnsworth, the inventor of television. His first patent was filed in January 11, 1962, followed by several others [5][6][7]. Supported by the ITT Corporation, Farnsworth and Hirsch constructed a device which used 6 inwardly directed ion guns mounted on a sphere, all injecting into a central cavity to produce 10^{10} neutrons per second in steady state operation using Deuterium gas. Despite this early success (their fusion output has yet to be exceeded), the gain of the device was quite low, a Q of $\sim 3 \cdot 10^{-4}$ [8][9].

On the theoretical side, the central region was predicted to form multiple potential wells, space-charge structures called 'poissors', basically a series of virtual cathodes and anodes which had the ability to trap particles. The poissors were solutions to the spherical Poisson's equation in absence of angular momentum, or non-radial motion. With increasingly more realistic models including varying degrees of angular momentum spread, the poissor solutions began to disappear. The poissor issue is still somewhat open as some experiments have detected the presence of at least a double well structure [18]. Overall, though, the key features of Hirsch's and other group's results agree well with a beam-background model for IEC fusion by Baxter and Stuart [10]. The neutron rate for almost all IEC experiments is observed to be proportional to the current and inversely proportional with background gas pressure.

Beyond the theoretical endeavors, experiments languished until the late 80's when George H. Miley at the Fusion Studies Laboratory at the University of Illinois at Urbana-Champaign tested a variation of the device based on a glow discharge ion creation mechanism. His group at Illinois developed simplified table-top devices that are

generally capable of producing 10^6 neutrons per second. The Illinois group has performed a large amount of experimental and theoretical work, including conceptualization of spacecraft systems relying on favorable power scalings arising from the poissor phenomenon. For near term prospects, they have tried to commercialize the devices as neutron generators through the European conglomerate EADS under the name 'FusionStar', but the operating cost of the device is too high due a high electrical demand. Recent work includes the development of a Fokker-Planck code to explore core convergence and the development of radio-frequency ion sources to facilitate low pressure operation [13][18][25].

Figure 1.2 IEC Nuetron Generator, 'Fusion Star', EADS.

The Illinois work was picked up by NASA Marshall Space Flight Center for a time and higher power pulse experiments were conducted in order to investigate the scaling laws at higher input powers. The conceptual studies of eventual spacecraft reactors rely on a highly favorable non-linear power scaling with input current. The effort is currently mothballed but was successful in showing operation at input current of 17 Amps at 50 kV with 100 microsecond pulses at 10 Hertz, giving a peak input power of

850 kW [25]. Despite this success, not enough work was done to verify the non-linear power scaling.

At the University of Wisconsin Fusion Technology Institute, a vibrant experimental program is investigating the ability of IECs to burn advanced fuels such as D-He^3 and He^3-He^3 in steady-state operation. Their device is quite large and can run at very high voltages (>150 kV). A key focus of the Wisconsin work is the demonstration of medical isotope production for positron emission tomography (PET) scans. Studies on advanced ion sources including radio frequency and helicon sources are trying to explore the low-pressure operating regime [11][14][15][22].

Related work has been conducted at the Los Alamos National Laboratory. There, an externally driven plasma mode, the periodically oscillating plasma sphere (POPS), is being investigated as a way to increase the core density. Other experiments include investigations into electron-based IEC systems and observations of instabilities in those systems [12].

Several universities outside of the United States including Kyoto University, Kansai University, Tokyo Institute of Technology, Kyushu University in Japan and The University of Sydney in Australia are working on the IEC as a neutron source[11]. In addition, numerous amateur hobbyists have built and tested devices that produce fusion, but at lower power and voltage levels then the laboratory efforts. Several gridless IEC concepts have been proposed, including a Penning-trap experiment at Los Alamos National Laboratory [12] and a polyhedral magnetic cusp concept by Robert Bussard. Bussard's concept is the subject of several papers and an experiment was funded by the Navy, but the results of those experiments have not yet been made public [16][17].

For all this effort, progress has stalled in terms of Q, the ratio of fusion power generated to electrical power input. While most experiments have been in the range of $Q=10^{-7}$, no one has yet to exceed Hirsch's Q of $3\cdot10^{-4}$. In addition, the neutron production rate of Hirsch has only recently been matched by other research groups. This lack of improvement hinders the ability of the device to be used as a long-life, steady-state (although inefficient) neutron source for radiological experiments. Furthermore, commercialization of small IEC neutron generators has been unsuccessful largely due to the high operating cost of the devices, which require kWs of power in comparison to small accelerator-based neutron generator tubes which use less than a kW for higher neutron output rate.

If the Q, and thus the electrical efficiency of these devices can be raised by a factor of 10-100 as I propose, the IEC will become superior in device lifetime and cost to small neutron tubes and superior in safety and output when compared with radiological neutron sources such as Californium-252. Ultimately, if the device can be improved up to and surpassing breakeven, it should prove to be an attractive option for space propulsion and power.

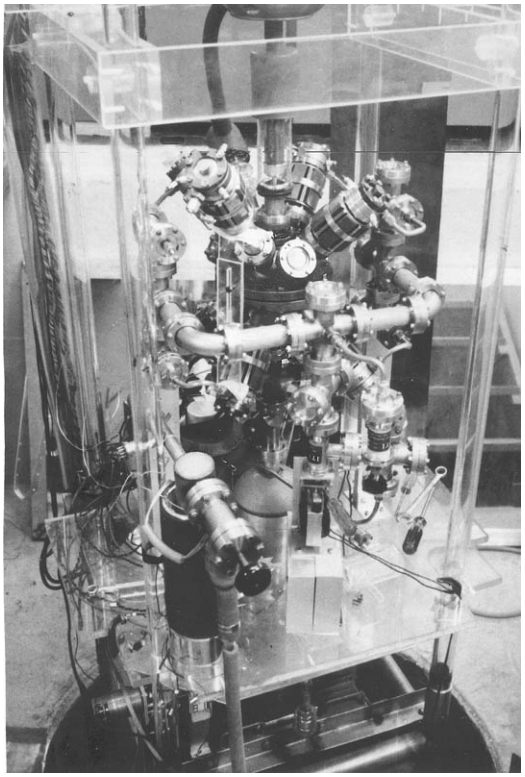

Figure 1.3 Hirsch ITT experiment set-up, cutaway view

1.5 Problems with the IEC concept

Much of the excitement surrounding this idea has been related to the very favorable power productions scaling with input current predicted by early theoretical efforts. Additionally, some early experiments showed rate scaling as strong as current to the third power, although this was at overall rates much lower than required by eventual operational reactors [25]. These scalings are based theoretically on the ability of multiple potential wells to trap plasma either so that it can fuse thermally or so that it can serve as a target for the recirculating ion beams. As the density of these trapped ions increases, the system output likewise improves. Unfortunately, these analyses were oversimplified and do not account for the main loss mechanisms in the system. The extrapolation of the scaling law from a Q-range of 10^{-7} all the way up to break-even is incorrect when one considers the lifecycle and associated energy losses of ions in the system. An initial

research task was to analyze the ion lifecycle in detail. Numerous problems with the current systems were found to severely limit the fusion gain.

All of the experiments to date have operated at relatively high pressures, in the range of 0.1-50 milliTorr. The high background gas pressure was required to produce the ion beams in significant density. Not only was the density required for electron bombardment to produce enough ions, the background density serves as a plasma target for the accelerated ions. In prior experiments, as the pressure was reduced to sub-milliTorr ranges, the fusion reactions would decrease below the measurement sensitivity. The problem with running at high pressure is that the probability of undergoing a charge exchange or ionization reaction is much greater than the probability to fuse. So while increasing the current will increase the neutron production, ultimately it will also increase the power losses since ions don't stick around long enough to fuse.

The key to achieving a breakeven device is to increase the fraction of ions that fuse, to the point where they overwhelm those ions that hit the cathode, which cause an energy loss. Proposed solutions such as high powered pulse operation do nothing to address the real issue of increasing the relative fusion probability. Let us examine briefly the other limiting effects on ion lifetime (directly related to its fusion probability).

All devices to date have used a single cathode grid which accelerates the ions. While poissor formation is very dependent on the radial symmetry of the electric fields, the cathode grids create large field asphericity near the grid. This effectively gives the radially flowing ions a transverse 'kick' every time they pass a cathode grid wire. Eventually this non-radial motion builds and causes the ion to go off its radial path and be lost to a cathode grid. This trajectory-effect limits the ion to no more than a few passes

for ions that aren't born very close to the center of a beam path where the transverse acceleration is small. Even ions born exactly on the center of the beam channel between grid wires will go 'off-radial' in less than 10 passes and strike a grid wire.

Furthermore, in existing systems, a high voltage stalk carries electricity to the inner cathode. The stalk greatly disturbs the spherical electric fields and this work will show that it causes all the trajectories in single grid devices to be limited to only one pass.

Another loss mechanism for the single grid devices is the unmitigated flow of electrons from the device core and cathode grid outwards to the anode or chamber wall. These electrons cause an electrical loss as great as the ions. The electrons are created via ionization events in the device core and through emission of secondary electrons when ions impact the cathode grids.

1.6 Proposed Solutions

The first step towards creating an efficient IEC is to lower the operating pressure so that ion lifetimes are no longer limited from atomic collisions. Now as the ions are given the chance to survive for many oscillations in the system, the ion trajectories must be confined to beams instead of allowing them to hit the cathodes.

The trajectories are to be made well-confined by introducing multiple acceleration grids, which behave similarly to an immersion lens in accelerators. The electric fields near the cathode now have the effect of focusing the ions instead of defocusing them as with a single grid. Perhaps more importantly for near term improvement, the multiple grids effectively shield the asymmetry in the electric field produced by the high voltage stalk which supplied the cathode, restoring a quasi-spherical field to the ion beam paths.

As the ions are confined for longer times (thousands to millions of passes) and the efficiency of the device increases, the space charge of the recirculation ion beam will become a significant source of ion beam thermalization. The space charge causes the beams to gradually expand with time. It may be possible to compensate some of this expansion by adjusting the multiple grid voltages, as is done in accelerators.

If the innermost grid actually decelerates the ions before they reach the core, the grid exerts a focusing force on the ions and more importantly creates a barrier against streaming electrons created in the device core. Instead of streaming to the anode and causing a sizable loss, the electrons are attracted to the much lower potential, causing much less losses. If this internal grid is constructed out a good emitter material such as a Tungsten-Tantalum alloy, then it may be possible to create enough secondaries to neutralize the incoming beams (much like an ion engine) thereby reducing space charge defocusing in the core region where ions are drifting at high density. This would also provide a way to inject electrons into the core region without relying on a high background pressure for ionization.

A very promising method of increasing the device efficiency is to decrease the ion losses by using a diverter setup. Instead of an ion eventually making its way to the cathode grid, the other grids are sized so that if a normally streaming ion would be on its way to impact the cathode, it would run into an intermediate grid at higher potential, causing less electrical loss. This would be accomplished by changing the relative size of grid wires and voltages between them. Simulations presented in Chapter 3 show that ions can be made to impact the innermost grid of a multiple grid system, where this grid is much higher potential than the main cathode grid, thereby reducing the ion power losses.

The difficulty of producting ions at lower background pressures will be somewhat countered by the increased confinement properties, since less ion input flux will be required. If pressure is reduced greatly in the pursuit of near break-even operation, it may be necessary to transition to ion beams which are created by ion guns outside the chamber, where the ion beams are pumped down and injected into the system at low kinetic energies.

The ultimate limiting factor in the IEC system is the ion space charge. For the ions to survive for the millions of passes required for breakeven operation, the recirculating ion beam current will become very large and cause the ion beam to be very defocusing. This can be alleviated by reducing the input current and allowing the beams to build in strength via recirculation. Chapter 4 discusses in detail the collective behavior that emerges due to the long-lived ion beams and the increased level of space charge. The ion beams are observed to self-organize into a system of pulsing bunches that show good long-term confinement properties. The space charge that drives these processes also appears to limit the density in the system. This will have to be eliminated or exploited in order for the IEC to produce significant fusion power.

We begin our quest to improve the IEC by analyzing the reaction rate scaling in detail in Chapter 2.

Chapter 2 Scaling Analysis

2.1 Introduction

Inertial Electrostatic Confinement Fusion (IEC) devices have produced fusion reactions in D-D, D-T, and D-He^3 plasma at rates of up to 10^{10} reactions per second [1][9][13][14]. These devices are relatively small, with chamber diameters less than a meter, and the research expenses to date have been on a much smaller scale than magnetic or target fusion. The electrical efficiency of IEC systems is still very low however, with only milliwatts of fusion power produced for tens of kilowatts input electrical power.

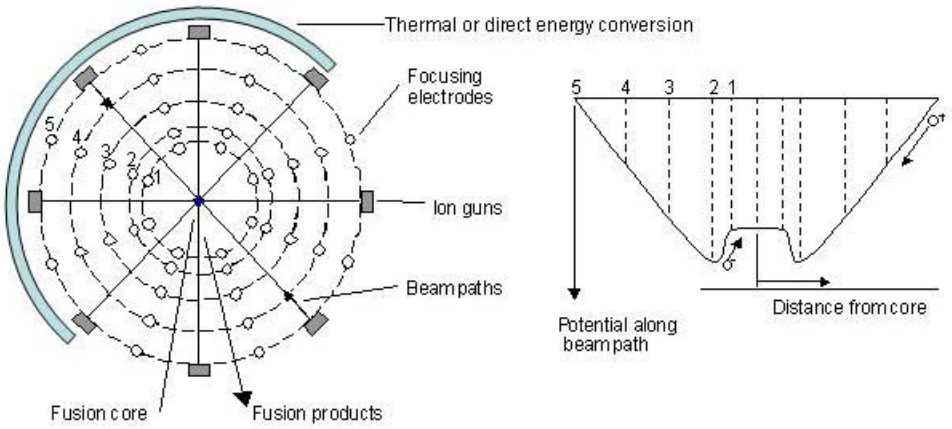

Figure 2.1, Multiple grid layout and potential structure along a radial beam path.

Theory and experiments have suggested that virtual cathodes and anodes can be created at the center of these systems, allowing plasma to be electrostatically trapped in these regions [9][18]. Proponents of this concept are hopeful that these potential

structures will allow favorable, highly non-linear reaction rate dependencies on input current and input power. However, these structures can be defocusing to the ions, causing build-up of unwanted non-radial velocity. By deriving the reaction rate scaling, this chapter will show the consequences of operating the device without the benefit or hindrance of these structures. Further, theoretical predictions of virtual cathodes and anodes have invoked an idealized spherical symmetry in the device which does not exist in gridded devices. The collection of grids and high voltage stalks create asymmetries which do not allow ions to oscillate in the device. These asymmetries can be exploited, however, by using multiple grids to create electrostatic lenses that actually focus the ions instead of causing them to deflect away from radial trajectories. Proposed improvements to the IEC are shown in Figure 2.1. Grids (#4 and #3) are introduced between the anode (#5) and cathode (#2) grids to provide electrostatic focusing of the ion beams [19]. In addition, a decelerating grid is placed inside the cathode in order to create an electron trap (#1), preventing electrons from freely streaming from the core to the anode. The ion density build-up at the device center is no longer an unrealistic, idealized collection of shell structures, but it is now the region of overlap from numerous recirculating ion beams. These improvements act to increase the ion lifetime, which from the following derivations of reaction rates, is the key to making the device more efficient so as to produce net power.

2.2 Reaction rates

Using a gridded IEC, one can estimate the fusion reaction rate by looking at contributions of beam-background and beam-beam interactions. Contributions due to

energetic neutrals produced from charge exchange (CX) collisions will be neglected here since they are lost immediately to grids and walls. The ions created by CX collisions are of too low energy to significantly contribute to the reaction rate and will be quickly kicked out by the non-radial fields.. The remaining two reaction sources must be integrated over the entire vacuum vessel and are given by:

$$\dot{r} = \int_V n_{back} n_{beam} \left(\sigma_{fus} v\right)_{beam/back} + \frac{n_{beam}^2}{4} \left(\sigma_{fus} v\right)_{beam/beam} dV \tag{2.1}$$

The problem is then to define the densities throughout the device volume. The background density is a linear function of pressure at a given gas temperature. The bulk gas in an IEC can be assumed to be at room temperature given a low power input and effective cooling of the vacuum vessel to the room temperature. From the ideal gas law and the pressure given in Torr, the background density can be expressed as:

$$n_{back} = 3.218 \cdot 10^{22} \cdot p_{torr} \tag{2.2}$$

The background density is assumed to be uniform throughout the chamber, which neglects the possibility of 'Star' mode microchannels selectively reducing the pressure along the channels. This is shown by calculation of the characteristic mean free path for ionization of the background gas by the accelerated ions. A peak ionization cross-section of $2 \cdot 10^{-20}$ m^2 and a high estimate of plasma density of 10^{20} m^{-3} gives a mean free path of 0.5 meters, which is much larger than characteristic beam and core dimensions in IEC devices [20]. Advanced systems with very high densities and trapped particle populations may however, modify the uniform background gas distribution, but are not considered in detail here.

The beam density is given by evaluating the ion beam particle flux:

$$n_{beam} = \frac{i_{in-beam}(\#p)}{evA} = \frac{i_{in-beam}(\#p)}{e\sqrt{\frac{2eE_{eV}(x)}{m_i}}\pi r^2(x)} \tag{2.3}$$

where the ion thermal energy is assumed to be negligible compared to the kinetic energy (acquired from the potential field) everywhere except the ion turnaround point at the anode. Also, '*#p*' is the number of passes an ion makes across the device, a non-dimensional measure of the ion lifetime. Thus, at any radial location, the ion distribution looks like a spike at the velocity corresponding to the local potential. This model is made to apply to a system in which ions are not yet confined to the point where thermalization of the ion energy is important. Thermalization here means the transfer of the ion radial kinetic energy into the transverse direction. Additionally, thermalization includes the upscattering and downscattering of energy in the radial direction. A break-even system would have ion beam thermalization, but current experiments do not yet confine ions long enough for this to occur. The ions are assumed to oscillate an average number of times through the system, and the beams are then populated by the recirculating ions such that the average number of passes multiplies the beam density.

This treatment also assumes that only ions that are traveling along the beam paths and have not undergone a collision are still 'confined'. Ions that are not traveling on these quasi-radial trajectories due to collisions have a greatly reduced probability for fusion and are considered to be lost. Treating the average number of passes as a metric for ion confinement is acceptable provided that ion confinement limits the ion lifetime. The ion lifetime can also be limited by other processes such as charge exchange,

ionization, and fusion. This will be shown later to be essential in understanding the performance of experiments to date.

The core density can similarly be written as the general beam density evaluated at the core position, but now multiplied by the number of beams that overlap in the core region.

$$n_{core} = \frac{Ni_{in-beam}(\#p)}{e\sqrt{\frac{2eE_{eV-core}}{m_i}}\pi r_c^{\,2}} \tag{2.4}$$

2.3 Beam-background reactions

The beam-background interactions are assumed to involve stationary neutrals, which is valid given that the wall temperature limits the temperature of the neutrals. With low input power, the wall can easily be kept cool. Even at elevated wall and grid temperatures (1000's of K) present in break-even reactors the neutral velocities are negligible compared to the charged particle velocities (keV's) and can be taken as stationary. Therefore, the relative velocity is given by the ion energy, which is a function of the position in the potential. The space charge of the ions is neglected and the potential is that of the background fields. The same relative velocity also defines the fusion cross-section. The beam-background contribution is evaluated over the volume of one beam and multiplied by the number of beams, as shown below in Equation (2.5).

$$\dot{r}_{beam-back} = 2\pi N \int_0^{R_a} n_{beam} n_{back} \sigma_{fus}(x) v(x) r^2(x)\, dx \tag{2.5}$$

The expressions for density can be substituted, yielding an expression where the dependence on the radius of the beams is eliminated and the spatial dependence is reduced to an integral of the cross-section over the path length. The total input current is

given by multiplying the input current per beam by the number of beams. Making these substitutions, the result is a linear dependence on input current and background pressure, for a given confinement time (number of passes).

$$\dot{r}_{beam-back} = \frac{i_{in-tot}(\#p)\cdot 6.436\cdot 10^{22}\cdot p_{torr}}{e}\int_0^{R_a}\sigma_{fus}(x)dx \tag{2.6}$$

The spatial dependence can be further simplified by assuming that the cross-section for fusion is negligible outside the cathode grid due to the $\sim\frac{1}{r}$ potential rise and quickly reduced energy of the ions. If the incoming ion beams are neutralized as they enter the cathode, they will drift through the center region with constant velocity, assuming that the core electrons are cool enough as to not create a potential well. Thus, the velocity and fusion cross-section will be constant within the cathode of the device. Under these assumptions, the beam-background reaction rate is given by:

$$\dot{r}_{beam-back} = \frac{i_{in-tot}(\#p)\cdot 6.436\cdot 10^{22}\cdot p_{torr}}{e}\sigma_{fus}(KE_o)R_{cat} \tag{2.7}$$

Below in Figure 2.2, the fusion cross-sections for a few of the reactions of interest are given [21]. Equation (2.7) is strictly valid for only a single species reaction such as D-D. Corrections for multiple species can be found by summing the interactions of each species with all the others.

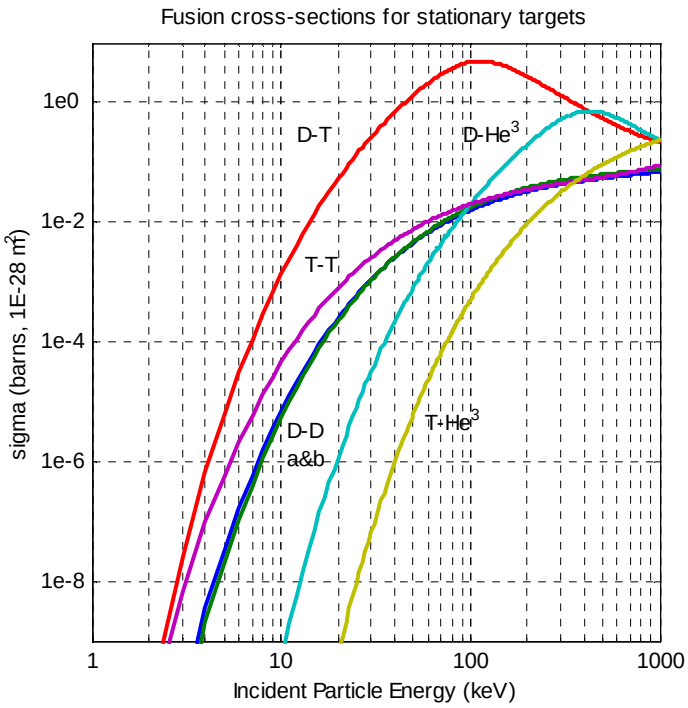

Figure 2.2, Target particle fusion cross-sections as a function of incident particle kinetic energy [21]

2.4 Beam-beam reaction in the device core

The beam-beam interaction can be divided into two parts, 1) in the dense core, and 2) in the 'spokes' formed by the counter-streaming beams, as shown in Figure 2.3. The dense core can be modeled as a region of 'overlap' of many converging beams, each with a specific radius. Given the long mean free paths for fusion and ion-ion scattering cross-sections at fusion relevant energies (greater than 25 keV), the beams will only weakly couple via collisions. A quick estimate of the ion-ion collision mean free path can be taken by using the standard expression for thermal ion-ion collision frequency. Using high estimates of deuterium ion density of 10^{20} m^{-3}, energy and temperature equal to 25 keV and a Coulomb logarithm of 15 yields a mean-free path for ion-ion collisions of $5 \cdot 10^{5}$ meters. For a characteristic device diameter of 0.5 meters, this equals 1 million passes. Fusion mean free paths can be estimated with a density of 10^{20} m^{-3} and a peak

cross-section of 1 barn (10^{-28} m^{-2}), yielding 10^8 meters or 200 million passes through our characteristic device. Current state-of-the-art confinement is well below these levels, in the 10 pass area and this thesis deals with the effect of increasing that to 1000 - 10000 passes. Since this model looks to explain and extend the current state of the art, not exactly describe a break-even system, the ion-ion collisions can be taken to be a weak interaction mechanism.

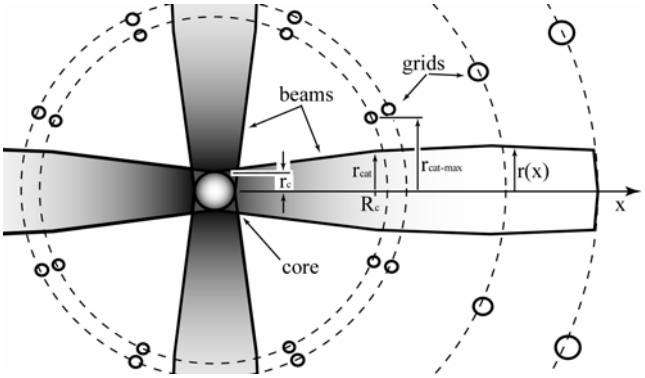

Figure 2.3, Model of 2 crossing ion beams and core size as a result of beam compression.

The other method of ion interaction would be space charge structures. In a device with no neutralization, the incoming ions will tend to produce significant regions of space charge, producing the alternating virtual anodes and cathodes called “poissors” as predicted by Farnsworth [5] and observed in experimental efforts [18]. In the current effort to reduce the defocusing effects of these space charge structures, an electron cloud is trapped within the cathode grid in order to neutralize the incoming ion beams. This innovation should greatly reduce the build-up of space charge at the device core, and allow the core regions to be simply modeled as a region of beam overlap. The overall applicability of this model to prior experiments is still good due to the fact that no prior IEC experiments have found evidence of significant beam-beam fusion reactions, so most of the important relations for prior work reside in the beam-background term. Given a

sufficient number of constant density profile beams, the core is well modeled as a uniform density region with a spherical boundary, radius = 'r_c'. The total fusion reaction rate in the core volume is given by:

$$\dot{r}_{beam-core} = \frac{4}{3}\pi r_c^3 \cdot \frac{n_{core}^2}{4}\left\langle \sigma_{fus} v \right\rangle_c \tag{2.8}$$

Substitute the core density Equation (2.4) into Equation (2.8) and simplify:

$$\dot{r}_{beam-core} = \frac{i_{in-tot}^2 \left(\#\, p\right)^2}{3\pi e^2 r_c v_c^2}\left\langle \sigma_{fus} v \right\rangle_c \tag{2.9}$$

In the core an isotropic velocity distribution exists where every ion has the same radial velocity evenly distributed across all angles. The non-radial components of velocity are assumed to be zero for each ion in the core. The fusion cross-section must be averaged since the relative velocity of ions varies from head-on to glancing collisions. This value is given by averaging over all the target ions, which are spread uniformly over a sphere in velocity space, as shown in Figure 2.4.

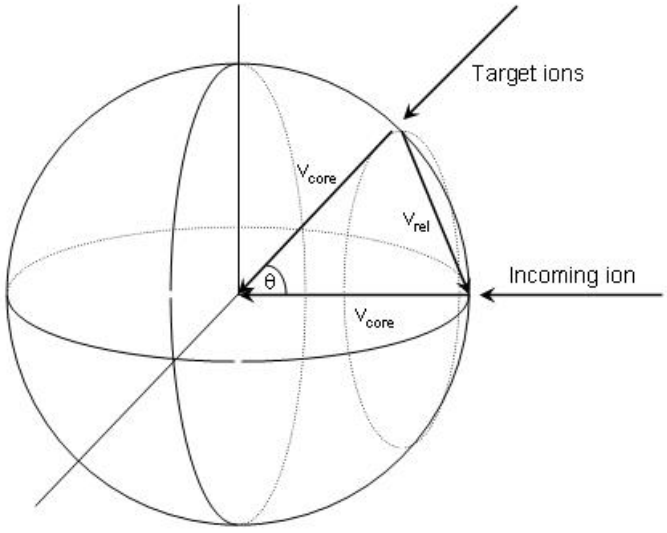

Figure 2.4, Diagram of collisions in a uniform core, for averaging over core population.

The relative velocity between the incident and target particles of equal kinetic energy is found by applying the law of cosines, with the mass ratio of the incident and target particles defined as 'μ'.

$$v_{rel} = \sqrt{\frac{2eE_i}{m_i}\left(1+\mu^2-2\mu\cos\theta\right)}, \qquad \mu = \frac{m_i}{m_t} \tag{2.10}$$

The calculations presented here follow from the NRL Formulary and the cross-sections fitted by Duane coefficients provided there [21]. The cross-section is defined in terms of the kinetic energy of the incident particle hitting a stationary target field.

$$\begin{aligned} &\left\langle \sigma_{fus} v \right\rangle = \frac{1}{SA}\int \sigma v dA = \frac{1}{2}\int_0^{\pi} \sigma\left(\frac{1}{2} m_i v_{rel}^2\right) v_{rel} \sin\theta d\theta \\ &for\ \mu = 1, \quad v_{rel} = 2v_{core}\sin\left(\frac{\theta}{2}\right) \\ &\left\langle \sigma_{fus} v \right\rangle = v_{core}\int_0^{\pi} \sigma\left(4E_i \sin^2\left(\frac{\theta}{2}\right)\right)\sin\left(\frac{\theta}{2}\right)\sin\theta d\theta \end{aligned} \tag{2.11}$$

where the fusion cross section is a function of the proper energy in units of keV, and the case of identical particles yields a simpler expression. The core averages for D-T, D-D (the tritium/proton branch), and D-He^3 are shown in Figure 2.5. The maximum '<σv>' for the D-T reaction was found to be $1.05 \cdot 10^{-21}$ m^3/sec at a core potential of 84 keV. The maximum '<σv>' for the D-He^3 reaction was found to be $2.90 \cdot 10^{-22}$ m^3/sec at a core potential of 313 keV. The results agree very well with Rider's Ph.D. Thesis figures and tables (who used a similar approach) [27], and the peak values agree well with numbers presented in Nevins' paper [28], although at different core energies.

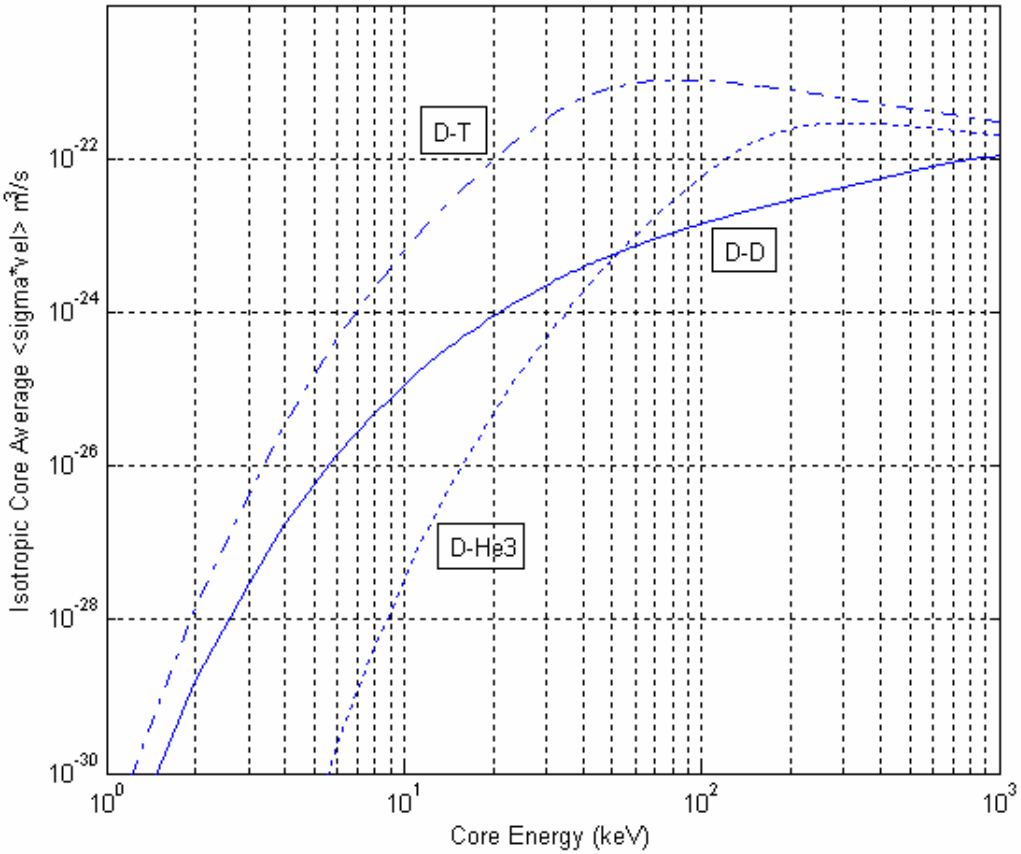

Figure 2.5, Core averaged product of cross-section and relative velocity for D-T, D-D, and D-He^3 reactions over a range of core ion kinetic energies.

2.5 Beam-beam reactions outside of the core

The beam-beam contribution from the spokes is found by integrating over the volume of a given spoke:

$$\begin{aligned} \dot{r}_{beam-spokes} &= 2N \int_{r_c}^{R_a} \int_{S} \frac{n_{beam}^2}{4} \left\langle \sigma_{fus}(x) v(x) \right\rangle_{beam-beam} dA dx \\ &= 2\pi N \int_{r_c}^{R_a} \frac{n_{beam}^2}{4} \sigma_{fus}\left(2v(x)\right) 2v(x) r(x)^2 dx \end{aligned} \tag{2.12}$$

where the beams are assumed to collide head-on with the relative velocity of a collision given by twice the single particle's velocity at that position, x, along the path. This is

valid for the non-relativistic acceleration of ions where a characteristic ion speed is ~$2 \cdot 10^6$ m/s for Deuterium at a kinetic energy of 50 keV. In the regime of a low number of passes, the ion velocity can be assumed to be only a function of the potential field and thus the path. Similarly, the cross-section can be evaluated at a given position with the relative velocity at that location. Here again, these simplifications would break down for ions undergoing enough passes so as to experience a few ion-ion scattering events and thereby lose energy and possibly gain significant non-radial velocity components, causing the ions to be no longer 'in' the beam. Also, the beam is assumed to possess a constant density profile and have a beam radius which varies with distance from the center of the sphere, *x*. Then substitute for the beam density, Equation (2.3), and simplify:

$$\dot{r}_{beam-spokes} = \frac{Ni_{in-beam}^2 (\#p)^2}{\pi e^2} \int_{r_c}^{R_a} \frac{\sigma_{fus}(x)}{v(x) r(x)^2} dx \tag{2.13}$$

Notice that the region immediately outside of the cathode can contribute to the fusion rate since ions are counter streaming there at high velocity, at essentially the same fusion conditions as immediately inside the cathode grid. Despite this fact, the rate quickly drops off as the potential outside the cathode rises, and for clarity, this region of fusion production will be ignored here as a conservative estimate. The upper limit of the integral in Equation (2.13) then becomes the cathode radius.

The effect of beam compression can be captured by considering the beam radius to be a linear function of axial beam position inside the cathode as shown in Figure 2.3. Beam compression or expansion could be produced by focusing properties of the

electrodes and the space charge of the beam, with the beam shaped as in a linear accelerator. The beam radius can then be written as:

$$r(x) = r_c + \frac{r_{cat} - r_c}{R_{cat}} x \tag{2.14}$$

Then let the beam radial focusing factor be the ratio of the beam radius at the cathode grid to the beam radius at the device center.

$$F = \frac{r_{cat}}{r_c} \tag{2.15}$$

If the region within the cathode is assumed to be at constant potential, the ions will drift through this region. This situation is assumed for ion beams that are adequately neutralized by an electron source within the cathode grid. A trapping potential difference exists on the cathode grids (grids #1 and #2 in Figure 2.1) first to contain streaming electrons and prevent them from being lost to the anode wall or grid [1], and secondly to confine a near-thermal neutralizing population of electrons. The neutralizing ability of these electrons is an ongoing area of research, with similarities to the neutralizers in Kaufman-type ion engines. This model for beam-beam interactions would not be strictly valid for most prior IEC devices because potential structures are allowed to develop within the cathodes as a result of charge imbalance and electrons were freely lost to the anode. As long as the trapped electron population remains near the grid temperature at standard densities (10^{15} to 10^{20} m^{-3}), the potential produced by this cloud will not have a significant impact on the ion velocities within the cathode. In advanced devices, especially those without grids, a trapped electron cloud that has gained significant temperature due to ion-heating could be made to produce its own confining well, with more complex ion dynamics. The drifting ion assumption thus allows the velocity and

cross section to be taken outside the integral as constants. By substituting Equation (2.14) into Equation (2.13) and simplifying, the beam-beam fusion rate in the spokes can be written as:

$$\dot{r}_{beam-spokes} = \frac{i_{in-tot}^2 (\#p)^2 \sigma_{fus}(4KE_o)}{\pi e^2 N v_{core}} \int_{r_c}^{R_c} \frac{1}{\left[r_c + \frac{r_{cat} - r_c}{R_{cat}} x \right]^2} dx$$

$$\dot{r}_{beam-spokes} = \frac{i_{in-tot}^2 (\#p)^2 \sigma_{fus}(4KE_o)}{\pi e^2 N v_{core}} \frac{1}{r_c r_{cat}} \frac{R_{cat} - r_c}{1 + \frac{r_{cat} - r_c}{R_{cat}}} \tag{2.16}$$

Substitute Equation (2.15) for the focusing factor, Equation (2.16):

$$\dot{r}_{beam-spokes} = \frac{i_{in-tot}^2 (\#p)^2}{\pi e^2 v_{core}} \frac{\sigma_{fus}(4KE_o)}{N r_{cat}} \frac{R_{cat}}{r_c} \frac{1 - \frac{r_{cat}}{R_{cat} F}}{1 + \frac{r_{cat}}{R_{cat}} \left(1 - \frac{1}{F} \right)} \tag{2.17}$$

If many beams are used (N>>1), the number of beams and the cathode radius can be related to the maximum beam radius at the cathode by writing a ratio of surface areas. Also, let the acceptance be the ratio between the beam radius and the beam opening radius.

$$r_{cat-\max} = R_{cat} \sqrt{\frac{2\Phi}{N}}, \quad r_{cat} = A_c r_{cat-\max} \tag{2.18}$$

where 'Φ' is calculated to be ~91.7% for a hexagonal packing of circles on a plane and the non-circle area taken to be the 'grid'. Another simple relation for the transparency of wires of diameter, 'd', in a hexagonal grid of side length ,'L', is given as $\Phi = 1 - \frac{2}{\sqrt{3}} \frac{d}{L}$. Greater transparencies are possible for non-circular beam-openings, for example, constructed of thin wires or tubes forming polygonal facets on a sphere. By substituting

these relations into Equation (2.17), assembling and simplifying the complete reaction due to all the rate components, Equation (2.17), Equation (2.9), and Equation (2.7), the total rate is:

$$\dot{r} = \frac{i_{in-tot}(\#p)\cdot 6.436\cdot 10^{22}\cdot p_{torr}}{e}\sigma_{fus}(KE_o)R_{cat} + \frac{i_{in-tot}^2(\#p)^2}{\pi e^2 v_{core}}\frac{1}{R_{cat}A_c\sqrt{2\Phi}}\left[\frac{\langle\sigma_{fus}v\rangle}{3v_{core}}F\sqrt{N} + \frac{\sigma_{fus}(4KE_o)}{A_c\sqrt{2\Phi}}\frac{1-\frac{A_c}{F}\sqrt{\frac{2\Phi}{N}}}{1+A_c\sqrt{\frac{2\Phi}{N}}\left(1-\frac{1}{F}\right)}\right] \quad (2.19)$$

The first term in Equation (2.19) is the reaction rate due to beam-background interactions. The second term in the equation shows the combined beam-beam reaction rate due to beam-core and beam-spoke interactions, respectively. Notice that only the core beam-beam rate term scales strongly with the focusing factor, while the beam-background and spoke contributions are unaffected by focusing. Also, the core has a fairly important square root dependence on the number of beams, but the spokes are only weakly dependent on the number of beams. The input current and confinement for the beam-beam term have a quadratic dependence. This strong scaling has been the historical impetus for high current pulsed experiments, as it is hoped that the fusion rate will increase faster than the ion losses with favorable scaling laws. As for geometry, the beam-background term scales linearly with the device size, specifically the cathode radius. The beam-beam terms however can be rewritten to show that the key geometrical scaling is an inverse relation to core size. For a given focusing factor, the beam-beam reaction rate is then inversely related to cathode radius. This would suggest that if focusing cannot be easily controlled, it would be easier to produce highly reactive cores in smaller devices.

2.6 Relative importance of beam-background to beam-beam reactions

The ratio of beam-background fusion reactions to beam-beam fusion reactions can be calculated,

$$\frac{\dot{r}_{beam-back}}{\dot{r}_{beam-beam}} = \frac{6.436\cdot 10^{22}\cdot p_{torr}\pi e R_{cat}^2 v_{core} A_c \sqrt{2\Phi}}{i_{in-tot}(\#p)\cdot F\left[\frac{\langle\sigma_{fus} v\rangle}{\sigma_{fus}(KE_o)}\frac{\sqrt{N}}{3v_{core}} + \frac{\sigma_{fus}(4KE_o)}{\sigma_{fus}(KE_o)}\frac{1}{A_c\sqrt{2\Phi}}\frac{1-\frac{A_c}{F}\sqrt{\frac{2\Phi}{N}}}{1+A_c\sqrt{\frac{2\Phi}{N}}\left(1-\frac{1}{F}\right)}\right]} \quad (2.20)$$

For the favorable beam-beam reaction scaling to dominate the reaction rate, this ratio must be less than 1. This condition is met by decreasing the operating pressure, making the device smaller, increasing the input current, increasing the ion confinement, and increasing the focusing, '*F*'. The ratio is a weaker function of the cathode potential and number of beams. While this suggests that high power, pulsed experiments may be a viable way to explore the beam-beam scaling, the ion confinement term will be shown later in this chapter to be inversely dependent on the input current when the space charge of the beams becomes important. In order to examine beam-beam interactions while avoiding this limiting mechanism, it seems favorable instead to operate at lower pressures with better confinement.

2.7 Distribution of beam-beam fusion rates

The distribution of beam-beam fusion reactions between fusion in the core and the spokes can be found by looking at the ratio of these two terms.

$$\frac{\dot{r}_{beam-core}}{\dot{r}_{beam-spokes}} = \frac{\langle\sigma_{fus} v\rangle}{v_{core}\sigma_{fus}(4KE_o)}\frac{\sqrt{N}A_c\sqrt{2\Phi}}{3}\frac{\left[1+A_c\sqrt{\frac{2\Phi}{N}}\left(1-\frac{1}{F}\right)\right]}{1-\frac{A_c}{F}\sqrt{\frac{2\Phi}{N}}} \quad (2.21)$$

This ratio describes the relative reactivity of the core and how well the device approximates a point source. When expressing the right hand side as a product of three fractions, the first and third fractions in the above expression are of order 1, and the most important variable in the second fraction is the square root of the number of beams. When the number of beams is low, as on many experiments to date, the beam-beam fusion rate is spread out over the cathode volume. However, this effect was not observed in prior experiments to date since the background rate swamped any signal from the beam-beam fusion rate. As '*N*' gets large, the beam-beam fusion is more localized to the core, which should be generally desirable for designing low-loss energy conversion systems where streaming reaction products are least likely to impact grids before exiting the semi-transparent system.

2.8 Break-even operation

Working from the reaction rate expressions, there appear to be two main methods to increase the fusion rate, 1) a large system geared towards beam-background operation, and 2) a small, low-pressure system geared towards beam-beam reactions. The system gain, the ratio of fusion energy produced to input energy, '*Q*', will be the deciding factor between these two approaches. It will be shown that the confinement time for this model is the key variable for determining the system gain, and that only the low-pressure system will lead to a viable, high '*Q*' device.

The two main loss mechanisms for a gridded IEC are ions impacting the cathode grids and electrons streaming to the anode grids. Ions impacting the cathode act to raise the potential of that grid, and some energy must be expended to remove that ion's charge

and maintain its potential. Also, the impacting ions can cause the emission of secondary electrons, which are then lost to the anode. While the secondary emission of electrons has been an important loss mechanism in IEC experiments to date, the electron trapping grids used in this concept are assumed to eliminate the electron streaming loss. This effect was experimentally observed in Hirsch's work, in which a secondary cathode grid biased to a potential on the order of 1 kV effectively halted the streaming electron current[1]. Many different mechanisms deviate the ions from purely radial paths and cause them to impact the cathode grid. These include tangential forces from the grids themselves, tangential forces from the ion beam space charge, ionization and charge exchange with the background neutrals, high angle scattering collisions with other ions, ion thermalization within the beams, and direct impact of ions unfortunate enough to be produced on a path leading directly to a grid. A simple expression for the gain can be written looking at the frequencies and associated energy losses for these mechanisms in comparison to the fusion reactions, assuming the electron loss can be effectively halted by the trapping grids.

$$Q = \frac{P_{elec}}{P_{in}} = \frac{\eta E_{fusion}}{E_{cat}} \frac{\dot{r}_{fusion}}{\left[\frac{i_{in-tot}}{e} - \frac{i_{fusion}}{e} \right]} \tag{2.22}$$

where the fraction of input current that fuses is found by acknowledging that each fusion reaction consumes two ions:

$$\frac{i_{fusion}}{e} = 2\dot{r}_{fusion} = f \cdot \frac{i_{in-tot}}{e} \tag{2.23}$$

Solve for the fraction of ions that fuse:

$$f = \frac{1}{\frac{1}{2Q}\eta \frac{E_{fusion}}{E_{cat}} + 1} \simeq \frac{E_{cat}}{E_{fusion}} \frac{2Q}{\eta}, \; for \; Q \le 10 \tag{2.24}$$

Table 2-1 shows the calculation of the fraction of ions that must fuse to maintain $Q = 1$ and $Q = 5$ for various fusion fuels, given an electrical conversion efficiency of 35%. The value of $\eta = 0.35$ is assumed here in all cases, although this value would be higher for direct electrical conversion of aneutronic fuels. Efficiencies of 48% were measured in tests of a direct converter system on the plasma leaking from the Tandem Mirror Experiment [4], and efficiencies of 60% and higher are predicted for more complex systems [3].

Table 2-1 Required ion fusion fractions for various fuels, $\eta = 0.35$

Fuel	E_{fusion}	E_{ion}	f, Q = 1	f, Q = 5
D-T	17.6 MeV	50 keV	0.0160	0.0751
D-D	3.65 MeV	100 keV	0.1354	0.439
D-He^3	18.3 MeV	100 keV	0.0303	0.135

The conditions for $Q = 1$ and $Q = 5$ are calculated, since a working system would need a gain considerably greater than 1 to account for overall system inefficiencies. These percentages range from 1% to 50%, indicating that the fusion time scale must be similar to, if not less than the loss time scales. In other words, if half of the input ions are to fuse, the time scale for fusion should be equal to the time scale for the loss routes. The limiting number of passes through the device can be found for each process in the system, including fusion, high angle ion scattering, and atomic processes such as charge exchange, ionization, and recombination. Simple collision cross-section models give these time scales as:

$$\tau = \frac{1}{n\sigma v}, \quad (\#\, p) = \frac{1}{2\int_0^{R_a} n_{t\,\mathrm{arg}\,ets}\,\sigma\, dx} \tag{2.25}$$

As a conservative approximation, the atomic processes can be assumed to cause irreparable damage to a candidate ion, rendering it unable to fuse by disrupting its energy and/or trajectory. In reality, some non-fusion reactions will act to gradually reduce the energy of an ion. The atomic processes then severely limit the lifetime of an ion due to the huge difference in cross-sections between fusion and atomic processes and the high background pressure in most of the experiments to date. The ratio of the fusion and atomic time scales is then given by:

$$\frac{\tau_{fusion}}{\tau_a} = \frac{R_a}{r_c}\frac{\sigma_a}{\sigma_{fusion}}\frac{n_{back}}{n_{core}} \tag{2.26}$$

where the geometrical scaling occurs because the majority of fusion reactions are occurring in the dense core (r_c), and atomic processes occur throughout the device volume (R_a). For this ratio to be less than one, core number density must outweigh the background density by the combined factors of geometry and cross-section. Even under these conservative approximations, for the fusion to dominate, the core density should be ~10 orders higher than the background. All IEC experiments to date have used operating pressures greater than 10^{-5} Torr, and have not operated near this state [1] [13] [22]. This also shows that increasing the beam-background reactions is not a viable way to increase '*Q'* since it relies on a high background density to achieve significant fusion output. In order to determine if beam-beam operation is viable, the prominent mechanisms limiting confinement are examined.

2.9 Pressure limited ion confinement

Recognizing that the atomic processes will often be the limiting factor for ion lifetime in experiments with relatively high background pressure, the number of passes

can be expressed as a path averaged expression of the atomic cross-sections and density in terms of pressure.

$$\#p = \frac{1}{2n_{back}\int_0^{R_a}\sigma_a(x)\,dx} = \frac{1}{2n_{back}R_a\langle\sigma_a\rangle_p} = \frac{1}{6.436\cdot10^{22}R_a p_{torr}\langle\sigma_a\rangle_p} \tag{2.27}$$

The atomic cross-sections for Deuterium are assumed to be identical to those of Hydrogen, plotted in Figure 2.6.

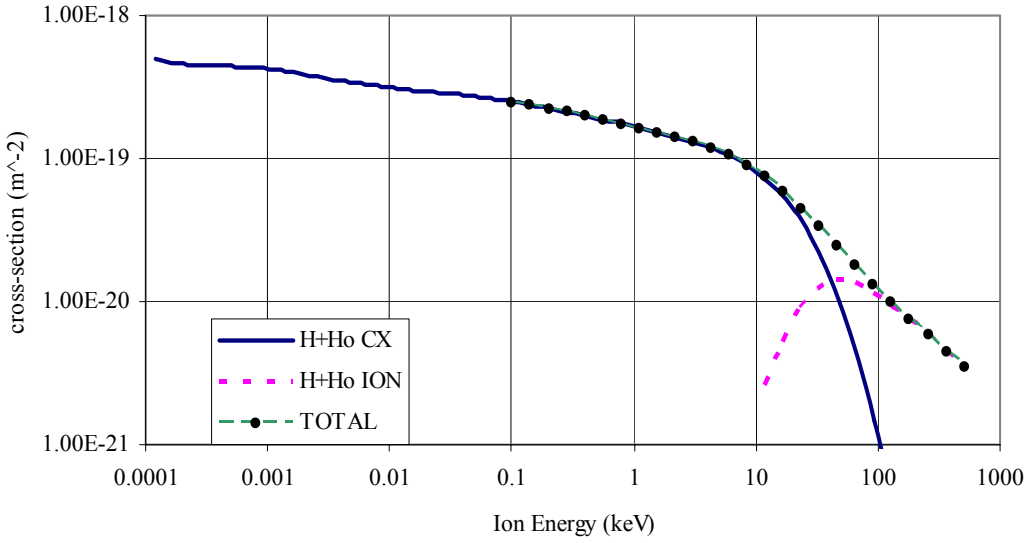

Figure 2.6, Charge exchange and ionization cross-sections for Hydrogen, H^+H_o, [20]

At thermal energies the cross section is about $5\cdot10^{-19}$ m^2 and is dominated by charge exchange. As fusion energies are achieved, ionization becomes more important and the cross section is reduced to about $1\cdot10^{-20}$ m^2. The path average of the cross-section depends on the velocities due to the specific device potential profile. The potential profile will be assumed to be constant (as shown in Figure 2.1) inside the cathode and approximated as $\frac{1}{r}$ between the anode and cathode.

$$v = \sqrt{\frac{2eE(x)}{m_i}} \quad E(x) = \frac{R_a R_c (E_{cat} - E_a)}{(R_a - R_c)x} + \frac{E_a R_a - E_{cat} R_c}{R_a - R_c} \tag{2.28}$$

The thermal velocity of the ions is assumed to be small, and the kinetic energy of the ion at the anode, 'E_a', is assumed to be equal to room temperature thermal energy of 0.025 eV. The effect of elevated wall or grid temperatures in eventual space reactors is small and favorable, slightly reducing the atomic cross-sections. Characteristic device sizes of a cathode radius of 10 cm and an anode radius of 50 cm are used. The total path-averaged cross-section can be numerically integrated to obtain $\langle\sigma_a\rangle_p \approx 1 \cdot 10^{-19}$ m^2 for Deuterium in a 50kV well and $\langle\sigma_a\rangle_p \approx 8 \cdot 10^{-20}$ m^2 for Deuterium in a 100 kV well.

IEC experiments to date have operated with a Deuterium-Deuterium reaction at fairly high pressures, ranging from 0.01 mTorr to 10 mTorr,[2,3] and anode radii of about 50 cm. From Equation (2.27), the atomic cross-sections discussed above, and typical parameters of p = 1 mTorr, 50 kV well, and 10 cm radii, ions make only 1.6 passes before being degraded by charge exchange and ionization. If the only limitation to the number of passes was atomic processes one could write the reaction rate, Equation (2.19), independently of confinement time by substituting Equation (2.27).

$$\dot{r} = \frac{i_{in-tot}}{e} \frac{\sigma_{fus}(KE_o)}{\langle\sigma_a\rangle_p} \frac{R_{cat}}{R_a} + \frac{i_{in-tot}^2}{\pi e^2 v_{core}} \left(\frac{1}{6.436 \cdot 10^{22} R_a p_{torr} \langle\sigma_a\rangle_p} \right)^2 \frac{F}{R_{cat} A_c \sqrt{2\Phi}} \times$$
$$\left[\frac{\langle\sigma_{fus} v\rangle}{3 v_{core}} \sqrt{N} + \frac{\sigma_{fus}(4KE_o)}{A_c \sqrt{2\Phi}} \frac{1 - \frac{A_c}{F}\sqrt{\frac{2\Phi}{N}}}{1 + A_c \sqrt{\frac{2\Phi}{N}} \left(1 - \frac{1}{F}\right)} \right] \tag{2.29}$$

This equation for purely pressure-limited confinement predicts that the beam-background term is independent of pressure and linear with current. Also, the beam-beam contribution is quadratic with current and is inversely related to the square of

pressure. Early results from Hirsch showed the reaction rate to increase with lower pressures, which suggested significant particle trapping in virtual anodes and cathodes [1]. However in the extensive follow-on IEC experiments to date, where the beam-background term is known to dominate the reactivity, the reaction rate is generally observed to decrease linearly with decreasing pressure [18][23], as is similarly described by Equation (2.19). Based on this model, these results suggest that the ion confinement in the experiments has not been limited by the pressure as in Equation (2.27), but rather by some other process which doesn't allow '*#p*' to increase with lower pressures. The limiting processes are most likely ion 'defocusing events' which are observed in raytracing resulting from asymmetries in the electric field due to high voltage grids and most importantly the stalk that supports the grid. In all the experiments to date, a single stalk supports the grids, but as will be shown in Chapter 3, an opposing 'dummy' stalk can help to make the fields more symmetric. Also, the reaction rate is observed to peak with increasing pressure and then decrease, corresponding to ions undergoing many atomic collisions before even reaching the cathode grid at higher pressure operation.

Table 2-2 Device parameters for proposed experiment, Deuterium fuel.

Device parameter	value
$i_{in\text{-}tot}$	10 mA
Cathode Potential	50 kV
R_a	20 cm
R_{cat}	8 cm
N	12 beams
F	1
Acceptance, A_c	100 %
Transparency,Φ	92 %
v_{core}	2.19e6 m/s
σ_{fus}(50 keV)	4.5e-31 m^2
$\langle\sigma_a\rangle_p$	6e-20 m^2
σ_{fus}(200 keV)	3.5e-30 m^2
$\langle\sigma_{fus}v_{core}\rangle$	5.5e-23 m^3/s

The reaction rate and expected number of passes from Equation (2.29) and Equation (2.27) are shown in Figure 2.7 and Figure 2.8 for a proposed lab experiment with only pressure limiting the confinement, which corresponds to results of ion tracing in a 3-D model of the standard 2 electrode system used in experiments to date. Listed in Table 2-2, the device parameters are chosen to represent a steady-state low-input power (500 W) device of similar dimensions to previous experiments. Conservatively, the focusing factor is chosen to be unity (no compression). Also, the acceptance is chosen to be 1, meaning the beams are expanded to fill the whole circular opening in the cathode grid. For these parameters, the reaction rate is predicted to vary with pressure as shown in Figure 2.7. Notice that the beam-background reactions are independent of pressure. The corresponding number of passes versus pressure is shown in Figure 2.8, as calculated from Equation (2.27). As pressure is reduced, the increased ion lifetime cancels out the reduced number of collisions with background particles to keep the beam-background rate constant.

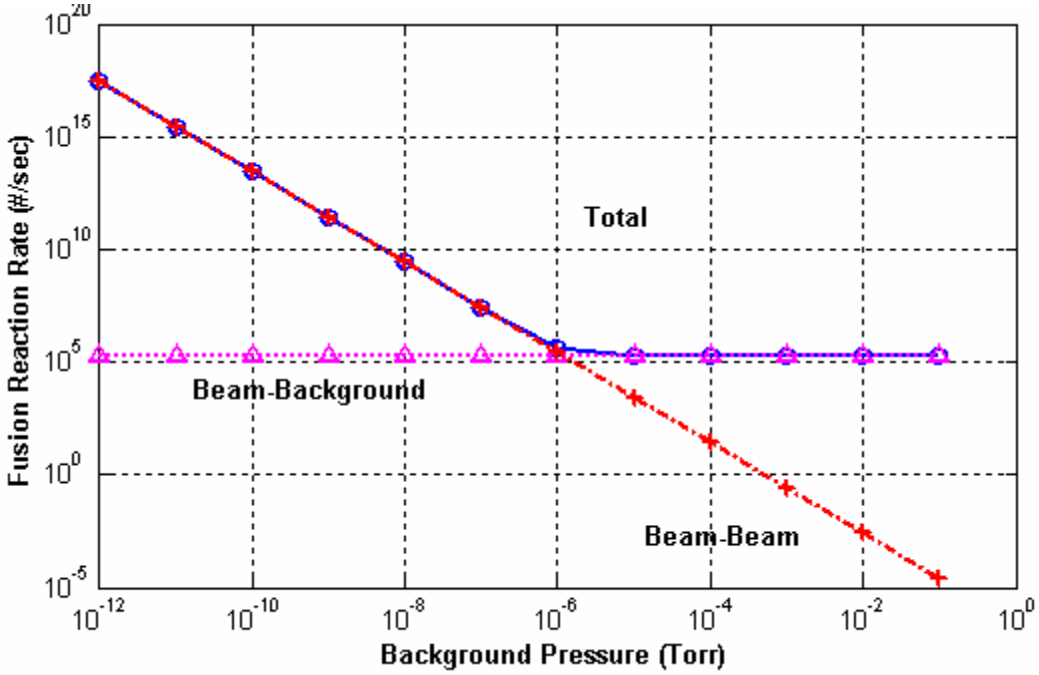

Figure 2.7, Reaction rate for pressure-limited ion confinement versus device pressure.

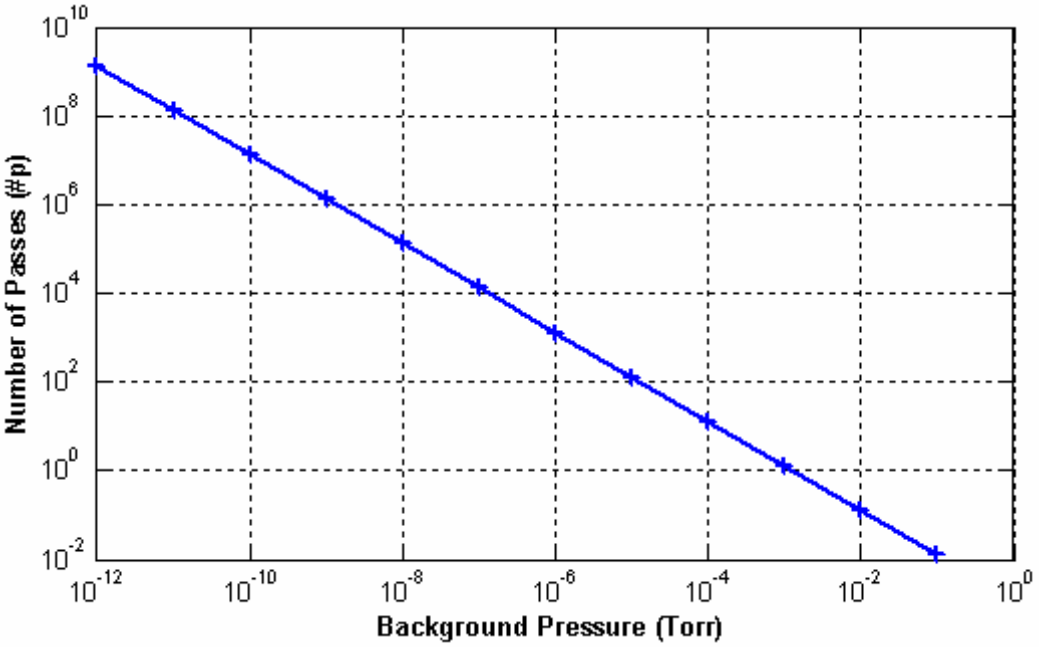

Figure 2.8, Number of passes versus device pressure.

Notably, in contrast to experimental data, Figure 2.7 shows the independence of reaction rate on pressure at high pressures, which correspond to the pressures used in

most previous experiments. Conversely, as the pressure is lowered beyond 10^{-6} Torr, the beam-beam reactions sharply increase. This happens as the corresponding number of passes goes above 1,000. However, as the confinement time increases, the assumption that the ions have little energy spread becomes less acceptable, and a more complex ion distribution should be considered.

2.10 Defocusing-limited ion confinement

If for the same device, the confinement is limited by ion focusing to only 10 passes, as suggested by ion particle tracing of simple one-grid cathode systems, the reaction rate varies with pressure as shown in Figure 2.9. The number of passes again varies with pressure as in Figure 2.8, but at lower pressures, is pinned at 10. Note also the number of passes required to enter the regime where ion-ion scattering and fusion reactions will dominate, as calculated earlier.

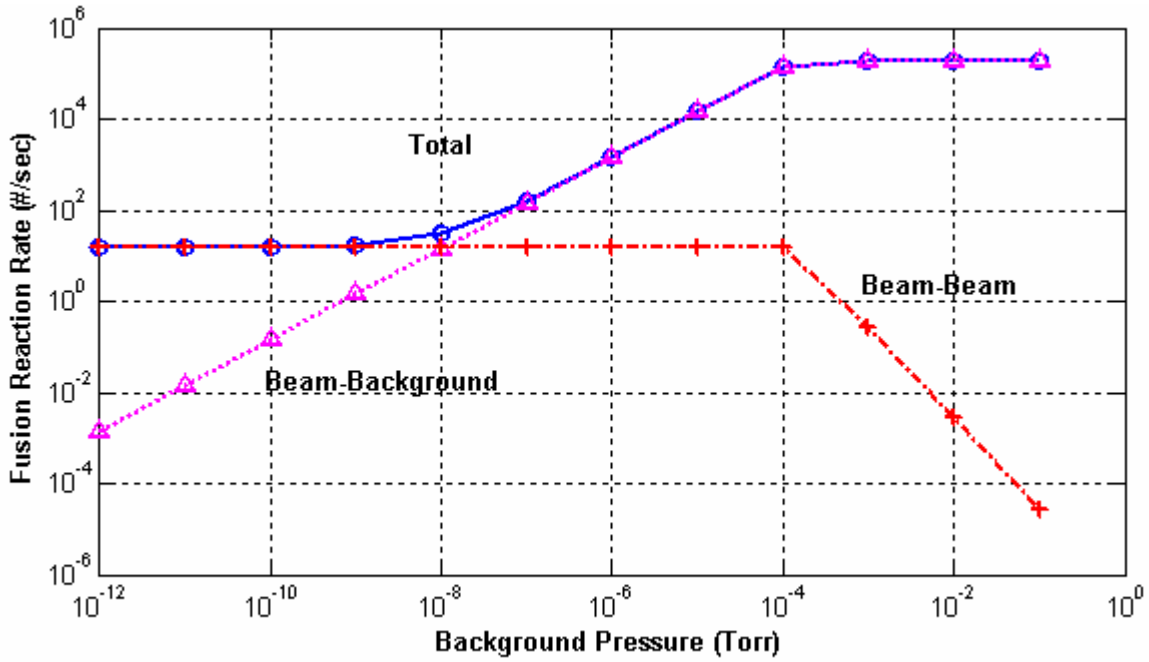

Figure 2.9, Reaction rate for defocusing-limited ion confinement versus device pressure, limited to 10 passes.

Now at high pressure, the reaction rate is still independent of the pressure. However, as the passes begin to be limited at ~10^{-4} torr, the rate drops off linearly with decreasing pressure. This linear relation matches experimental data, which suggests that the experiments have been confinement limited not by pressure, but by ion trajectories that are deflected by asymmetric and non-spherical grid potentials. Also, even though the beam-beam rate still eventually dominates the beam-background rate at low pressures, the total rate is almost negligible and at best levels off to be independent of pressure at very low pressures. From Equation (2.20), for a maximum of 10 passes, the beam-beam terms are found to dominate once the pressure falls below ~10^{-8} torr.

2.11 Improved defocusing-limited ion confinement

If the defocusing limit can be increased several orders of magnitude, the effect on the reaction rate behavior should be easily observable in a modest experiment of similar dimension to previous efforts. Shown below in Figure 2.10 is the reaction rate with the defocusing limit raised to 1000 passes.

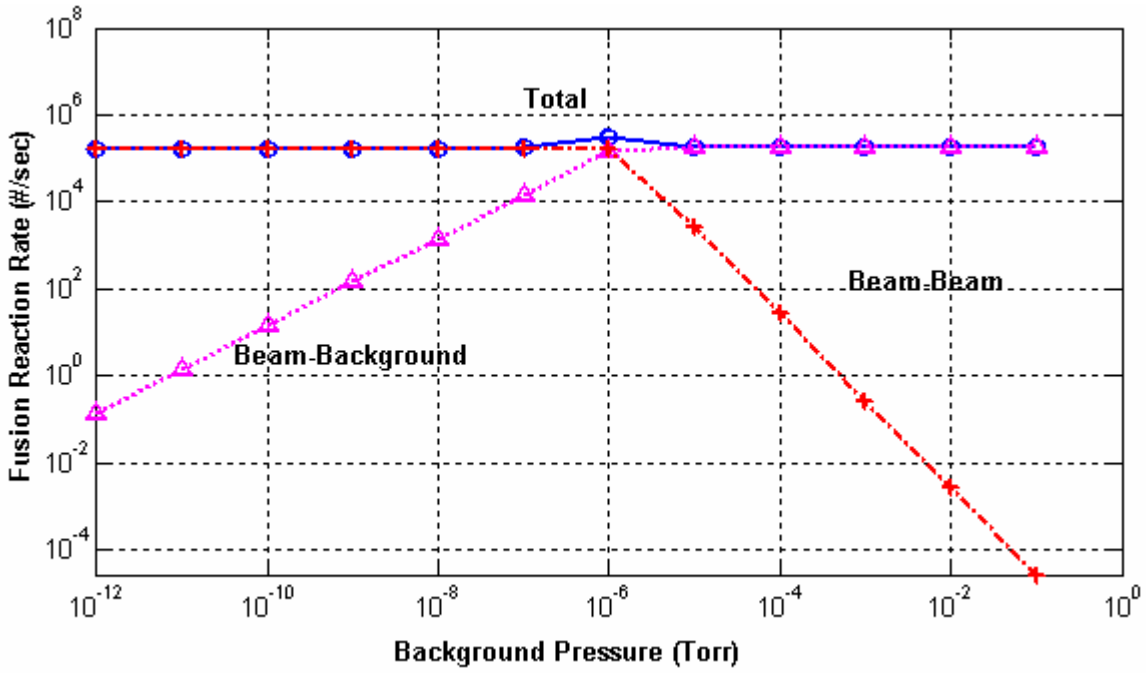

Figure 2.10, Reaction rate for defocusing-limited ion confinement versus device pressure, limited to 1000 passes.

Once again, as the pressure is lowered, the beam-beam terms become more important. From Equation (2.20), for a maximum of 1000 passes, the beam-beam terms are found to dominate once the pressure falls below ~10^{-6} torr. In contrast to the 10 pass limited case, here the total reaction rate is relatively independent of pressure. If the current or number of passes is increased further, the rate would actually increase with decreasing pressure.

2.12 Space charge limitations of focusing grids

The drastic increases in ion confinement from focusing grids have been predicted by ion particle tracing codes, but electrostatic lenses have limits. As the confinement time is increased, the ions create a larger and larger space charge in the beams due to recirculation, which eventually swamps the focusing properties of the electrostatic lenses. This limit can be estimated by equating the potential depth of the focusing lens to the

potential due to the recirculating ion beam. This represents the limit at which the lens would provide a focusing force on the beam. While the ion path confinement is a complex function of the whole geometry, the limit for a single lens can provide a useful first order approximation for electrostatic lenses.

Using a 2-D model for an infinite beam of charge, the radial field is given by Gauss' law,

$$E_r = \frac{e}{\varepsilon_o r(x)} \int_0^{r(x)} n_i(r) r dr \tag{2.30}$$

Assuming a constant beam density profile:

$$\begin{aligned} &for\ r < r_g(x), \quad E_r = \frac{e n_b r}{2\varepsilon_o} \\ &for\ r > r_g(x), \quad E_r = \frac{e n_b r_g^2}{2\varepsilon_o r(x)} \end{aligned} \tag{2.31}$$

The potential profile can then be calculated, defining the potential to be zero at the grid radius, '$r_{g\text{-}max}$', and integrating from the outside in,

$$V(r) = \int_{V_{g-\max}}^{V(r)} dV = \int_{r_{g-\max}}^{r(x)} -E_r(r)\, dr \tag{2.32}$$

Substituting the constant density beam electric field, Equation (2.31) yields:

$$\begin{aligned} &for\ r_g < r < r_{g-\max}(x), \quad V(r) = \frac{e n_b r_g^2}{2\varepsilon_o} \ln\left(\frac{r_{g-\max}}{r}\right) \\ &for\ 0 < r < r_g(x), \quad V(r) = \frac{e n_b}{2\varepsilon_o}\left[r_g^2 \ln\left(\frac{r_{g-\max}}{r_g}\right) + \frac{r_g^2}{2} - \frac{r^2}{2}\right] \end{aligned} \tag{2.33}$$

The voltage increases as the natural log outside the beam and is parabolic within the beam. This parabolic behavior matches well with the lens potential, which exhibits a

nearly parabolic profile. Substituting in for the acceptance, the central voltage drop can be evaluated,

$$V_{go} = \frac{r_{g-\max}^2 A_g^2 e n_b}{2\varepsilon_o}\left[1/2 - \ln A_g\right] \tag{2.34}$$

The bracketed term is most important when the grid acceptance is small, but is only a weak function of acceptance. For example, for a filament-type beam with an extremely low $A_g = 1 \cdot 10^{-8}$, the term equals only 38 times that of a fully expanded beam with $A_g = 1$. The leading term is constant if the amount of charge in the beam is constant, so that the lowest potential configuration is obtained by the beam spreading to fill the entire beam channel out to the grid.

Substituting for the beam density, the number of passes can be written in terms of the input current,

$$\# p = \frac{2\pi\varepsilon_o v_g V_{go} N}{i_{in-tot}\left[1/2 - \ln A_g\right]} \tag{2.35}$$

Using the experiment parameters in Table 2-2, a pinching grid which would be at -40 kV and have a lens depth of $V_g = 4$ kV (modeled numerically), the number of passes is limited to 1045. This is a very rough estimate, given the complex arrangement of lens and the drift regions between focusing and defocusing regions. The next level of complexity is to model all the lenses and the beam and to perform a self-consistent calculation to find the beam profile in such a system. This limiting mechanism forbids this simple electrostatic configuration of grids from supporting larger space charges. While this limit may or may not prove unbreakable, it still represents a significant improvement in efficiency.

2.13 Implications for pulsed high-power experiments

Recent experimental efforts have attempted to explore regimes of higher gain, not by increasing confinement time, but by drastically increasing the input current using a pulsed discharge [25]. Furthermore, the existence of particle trapping in poissors in these pulsed experiments is believed to enhance the fusion reactivity. While this analysis does not address the poissor question, the arguments about space charge build-up apply [Equation (2.35)] and the space-charge will act to severely defocus the ions, limiting the ion confinement to even less than what previous, steady-state defocused IECs achieved. Because of this 'hidden' scaling of confinement time with input current, the reaction rates will not follow a simple power law with current. Here, the space charge is a problem because as the confinement is improved, the recirculating current will increase along with the beam density. As this density becomes high enough for the beam's self-fields to internally counteract the externally imposed focusing forces, the device must transition into a more advanced mode of operation, where the space charge of the beams is somehow reduced or counteracted.

2.14 Streaming instabilities

Since an IEC system has very small current densities due to the recirculation of ions along the beams, electromagnetic instabilities are avoided, leaving only electrostatic modes. The two-stream instability is present for $v/\lambda < \omega_p$, and the growth rate is a maximum of about v/λ near the limit [24]. These values do not change much in our region of interest whether considering ion-ion, ions with cold electrons, or ions with hot electrons. This means that for a given streaming velocity, a minimum wavelength is

required to have an unstable mode, and the mode grows approximately at the plasma frequency. For laboratory devices with densities of 10^{15} m^{-3} and Deuterium streaming velocities of $2 \cdot 10^{6}$ m/s, the minimum wavelength is 6.8 centimeters, which is comparable to the device dimensions. For more advanced systems, say with densities of 10^{22} m^{-3}, the minimum wavelength is much smaller, only 21 micrometers. The OOPIC particle-in-cell modeling described further in Chapter 3 shows evidence of instability as density builds in the device. Disruptions from high density instabilities appear to be the ultimate life limiter of the ions. Also of concern is the low-speed anode reflection region, which appears to harbor regions of instability since the velocity drops so low there. An in-depth analysis of synchronizing, small-angle ion-ion collisions in the reflection region is presented in Chapter 4 of this text.

2.15 Caveats

The main limitation for using electrostatic lenses is the build-up of space charge, which is required for a high power system. Even if the background gas can be eliminated as a limiting mechanism, the space charge will still limit the focusing of the beams. The logical extension of increasing space charge is the Child-Langmuir limit, but the ion confinement will degrade severely before this limit is reached. The space charge counteracts the applied potentials, whether they are the main radial acceleration potentials or the secondary tangential focusing potentials. Since the focusing potentials are an order of magnitude smaller than the acceleration potential, it follows that space charge would affect the focusing potential before the main radial flow is affected greatly. This effect is shown in more detail in Chapter 3, where simulations show that the ion trajectories

become poorly confined as the ion charge builds, yet the background potential is barely affected by the ion space charge.

Another issue for a break-even system is the effect of ion thermalization as the confinement improves. The ion beams will undergo small angle collisions within the counterstreaming beams and within the core region. The redistribution of energy in transverse and radial directions provides an additional loss mechanism for ions as the residence time of an average ion increases. Thermalized ions will be lost to the grids as their trajectories become poorly confined.

The ability to produce and maintain a neutralizing electron population in the device center is another open question. Without neutralization, the converging ion beams will tend to decelerate and defocus due to their space charge. If enough electrons can be provided and allowed to travel with the beams in the core region, then the ions can be made to drift through the center and possibly even be focused by the electrons. The key to maintaining this electron population with low streaming losses is to create a trap within the cathode grid. It is hypothesized that cold electrons can be produced at the low work function emitting grid, populate the core region, and be contained by the trapping potential. As the electrons gain energy from the ions and heat up, they can form a potential well which could contain the thermalizing ions without letting those ions be in contact with any grids. For this to happen, though, the electron population must be in contact with the emitting grid, for which grid heating places limitations on the density and temperature of the hot electrons. A break-even reactor of reasonable dimensions and useful power levels (at least kW's) must be able to confine the higher densities resulting from the millions of passes a successful fusing ion must undergo. The behavior of

electrons in this configuration should be a main topic of investigation and may provide a way around the space charge focusing limitations of grids.

Other concerns for a breakeven IEC device include high angle ion scattering in the core, grid heating and sputtering, and direct energy conversion with aneutronic fuels. A high angle scattered ion from the core has a probability to directly impact a cathode grid, causing an energy loss. This reaction dominates fusion at low energy (<50 keV) and will likely set a minimum voltage for successful operation. Grid heating is a major concern and will set the dimensions of an IEC. For smaller devices, active cooling may prove too difficult, but radiatively cooled grids can handle much less heat input. Also, the sputtering of grids represents a life limiter for IECs. Since the sputter products are not in well-confined trajectories, they should quickly leave the system. The insulators will tend to be coated with these sputter products and are prone to arcing, but this could be minimized by clever design given that the sputter source locations are largely known and can be 'shadowed' from sensitive surfaces. The possibility of using direct conversion schemes with aneutronic fuels such as D-^{3}He and p-^{11}B is promising due to the decreased system mass and increased efficiency, but drawbacks include increased complexity and higher operating voltages for these fuels.

2.16 Conclusions of scaling analysis

The analysis of the importance of confinement on reaction rates shows that prior devices and experiments operated in a regime with limited ion confinement. This regime is characterized by a linear decrease of reaction rate with decreasing pressure and most of the fusion reactions occurring between the beams and the background gas. By enhancing

the focusing properties of the grids, the ion confinement can be allowed to increase as pressure is reduced, and the reaction rate will be independent of pressure. Furthermore, keeping device parameters constant, the enhanced confinement scheme should increase the confinement and reactivity by 2 orders of magnitude by increasing the confinement time at a given pressure, the most marked improvement at lower pressures.

The predicted increases in confinement and reactivity can be measured experimentally with a simple, low-cost apparatus. Experimental verification of these results will in the near term produce a much more potent, efficient IEC immediately marketable as an improved portable neutron source. Applications for an inexpensive and efficient neutron source are many, including radioisotope production for medical diagnostics and therapies, industrial bulk process quality control, landmine detection, well-logging, security screening, and neutron activation analysis [14]. Improving the IEC device from the '1-10 ion passes' regime up to the space charge limited regime of 1,000-10,000 passes will allow the study of collective behavior in the devices. More complex collective behavior and charge neutralizing schemes will be necessary to break the space charge-defocusing limitations of IEC devices. Only by further increasing the ion confinement can break-even operation be realized. Not only would a high power, breakeven IEC have enormous potential as a terrestrial power source, it would be a very lightweight method to harness nuclear power for fast, intrasolar system travel. This chapter has examined what can be achieved by an improved IEC, and the following chapter examines the details of a multigrid approach which allows the achievement of greatly improved ion confinement.

Chapter 3 Multi-grid IEC

3.1 Intro to improved IEC

The multigrid approach is an IEC innovation that provides the long-term confinement required to achieve higher efficiencies in IECs. The details of this innovation are presented in this chapter along with numerical modeling as evidence of the efficacy of this approach. The general picture is shown below.

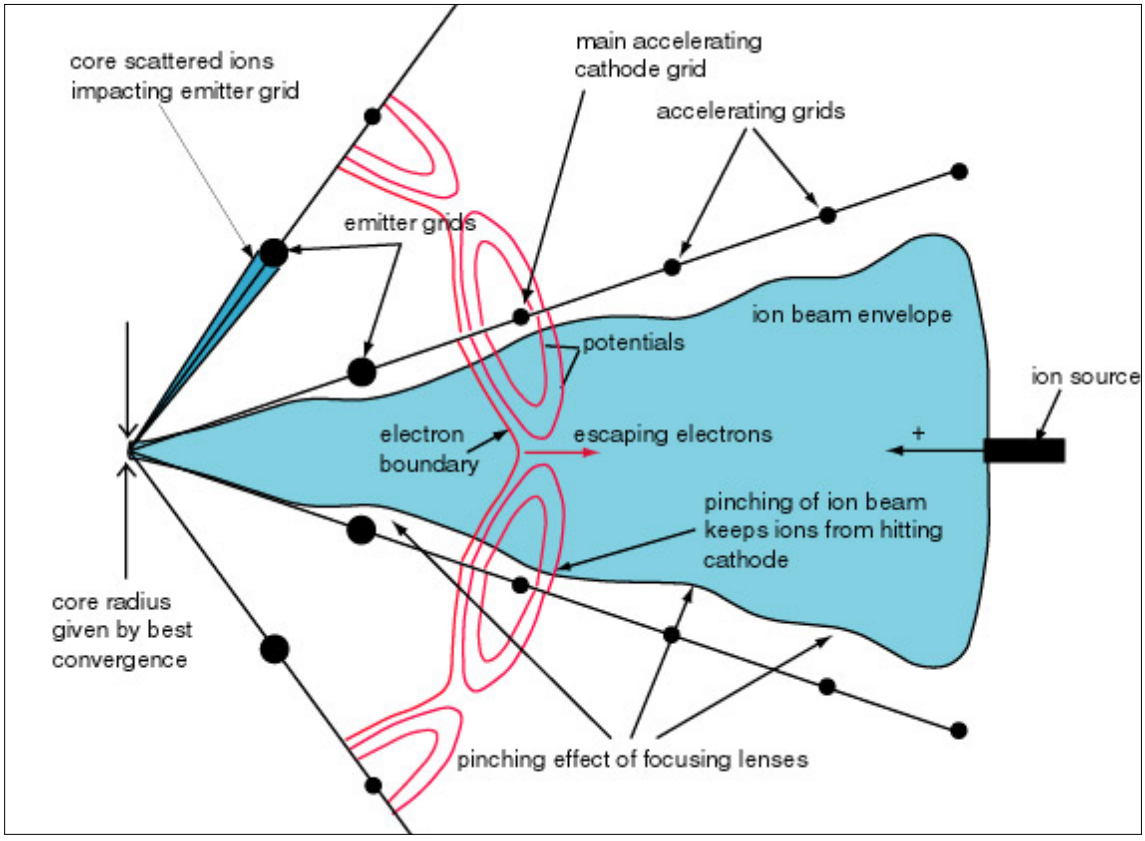

Figure 3.1 Generic picture of multiple grid confinement

An ion injector adds ions to the recirculating ion beam so that beam builds from a relatively small source. The grids effectively shield out non-radial asymmetries in the

background field. The multiple grids also create a focusing channel for the recirculating ion beam. The general effect on the beam envelope is shown above, where the cathode grid pulls the beam away from its radial motion, but the other grids redirect it back into the center of the channel. The voltages of the grids can be set to control the level of beam focusing. The high angle scatters are shown to be only lost to the inner most grid if they are deflected directly into those grids, otherwise they are deflected onto other confined beams. Also, the ions are most likely to impact the innermost grid and cause it to emit electrons. These electrons are prevented from streaming to the anode by the field structure created by the multiple grids. The various elements of this improved IEC are discussed in this chapter, including focusing, high angle scattering, electron suppression, and finally particle-in-cell simulation of multigrid IECs and limitations on confinement and density.

3.2 Focusing limits for a single recirculating ion beam

It is supposed that increased focusing in the core of the IEC will lead to increased fusion output. In the absence of neutralizing effects in the core, the space charge of a single beam will determine how tightly a recirculating beam may be focused. The non-neutralized beam is of immediate interest, since a proven method to neutralize the core of an IEC in the low-pressure regime has yet to be demonstrated. Further, the beam is assumed to be laminar with zero thermal content for this 'best case' analysis of focusing. Also, the assumption of a recirculating beam primarily affects the boundary conditions and is consistent with increasing ion lifetimes to boost IEC efficiency (the beam slope must be zero at the core for symmetry). A single beam will be a close approximation to a collection of beams if the core overlap region is small (i.e. focused cores). If, however,

the focusing is minimal, say of order unity, the space charge from the other beams will significantly affect the single beam and would require a more complex model.

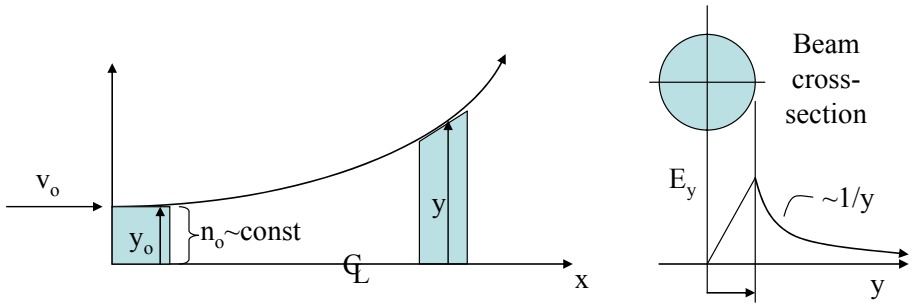

Figure 3.2 Axisymmetric beam model and transverse electric field

The beam is modeled as axisymmetric, traveling at constant velocity in the x-direction, shown in Figure 3.2. The beam's space charge will then expand the beam radius from its initial core radius of 'y = y_o' at 'x = 0' to some new value at a future x-position. Recall Figure 2.3, where here we are dealing with just one of the overlapping beams. As the beam expands in the 'x' direction, the cathode opening radius and cathode grid position can then be used to define a beam end point and beam radius limit. The region within the cathode is assumed to be field-free, but the region between the cathode and anode grids can form lenses which can dynamically contain the beam's space charge. The transverse electric field responsible for beam self-expansion is found from applying Gauss's law.

$$\int E \cdot dS = \frac{q_{enclosed}}{\varepsilon_o} \Rightarrow E_y = \frac{e}{\varepsilon_o y(x)} \int_0^{y(x)} n_i(y)\, y dy \tag{3.1}$$

where 'y' is the radius of the expanding beam. With a constant density, top-hat shaped beam cross-section, the electric field as a function of beam radius is:

$$E_y = \frac{en_b y}{2\varepsilon_o}, \quad y < y_b$$
$$E_y = \frac{en_b y_b^2}{2\varepsilon_o y(x)}, \quad y > y_b \tag{3.2}$$

where 'y_b' is the beam envelope radius in the transverse direction.

The differential equation describing the beam envelope is given by the acceleration of an ion at the beam edge due to the electric field at that point.

$$\frac{d^2y}{dt^2} = \frac{q}{m}E_y = \frac{e^2 n_o y_o^2}{2m\varepsilon_o}\frac{1}{y} = \frac{A}{y} \tag{3.3}$$

Multiply both sides by 'dy/dt' , integrate, and apply a zero slope boundary condition at 't = 0' to yield an expression for the beam envelope slope.

$$y'(0) = 0 \quad \Rightarrow \quad \frac{dy}{dt} = \sqrt{2A\ln\left(\frac{y}{y_o}\right)} \tag{3.4}$$

One can then separate variables and integrate from '$t = [0 \;\; t]$ *and* $y = [y_o \;\; y]$'. By making a few substitutions and applying the definition of the imaginary error function, the time as a function of beam envelope is found.

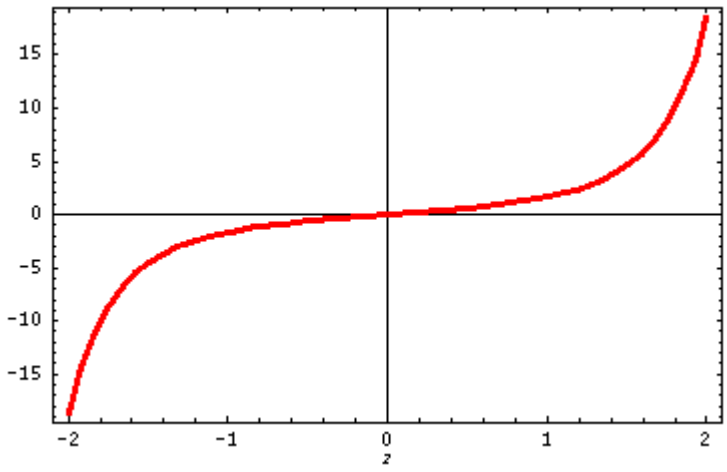

Figure 3.3 Imaginary error function, erfi(z) vs. z

$$Erfi(z) = \frac{2}{\sqrt{\pi}} \int_0^z e^{t^2} dt = \frac{2}{\sqrt{\pi}} \sum_{k=0}^{\infty} \frac{z^{2k+1}}{k!(2k+1)} \tag{3.5}$$

$$t = y_o \sqrt{\frac{\pi}{2A}} Erfi\left(\sqrt{\ln\left(\frac{y}{y_o} \right)} \right) \tag{3.6}$$

Since we really are interested in the beam envelope geometry, substitute 'x_{cat}/v' for time elapsed in the field free region and take the inverse of the imaginary error function to get the beam size at the cathode grid. The ratio of the beam envelope radius at the cathode over the core value, 'y_o', is defined as the focusing factor, 'F'.

$$F = \frac{y_{cat}}{y_o} = e^{\left[Erfi^{-1}\left(\frac{ex_{cat}}{v} \sqrt{\frac{n_o}{\pi \varepsilon_o m}} \right) \right]^2} \tag{3.7}$$

The maximum non-neutralized achievable core density can then be written as a function of the focusing factor and the number of overlapping beams.

$$n_{core} = \frac{2\pi\varepsilon_o E_{i_{eV}} N_b}{ex_{cat}^2} \left[Erfi\sqrt{\ln F} \right]^2 \tag{3.8}$$

where the beam energy, 'E_i' is given in electron volts. The density scales linearly with the beam energy and the number of beams, and scales inversely to the cathode size. Since the density and thus the power both monotonically increase with increasing core energy, the core averaged reactivity for D-T, D-D, and D-He3 is evaluated at a single characteristic core energy of 100 keV. Also, characteristic MIT laboratory device parameters of 12 beams with 'x_{cat} = 5 cm' and 'y_{cat} = 3 cm' are used.. A workable reactor may operate at higher energies to boost output, but will unlikely be any smaller than the stated lab values. Figure 3.4 below shows that the core density increases monotonically with increasing focusing ratios, as one might expect.

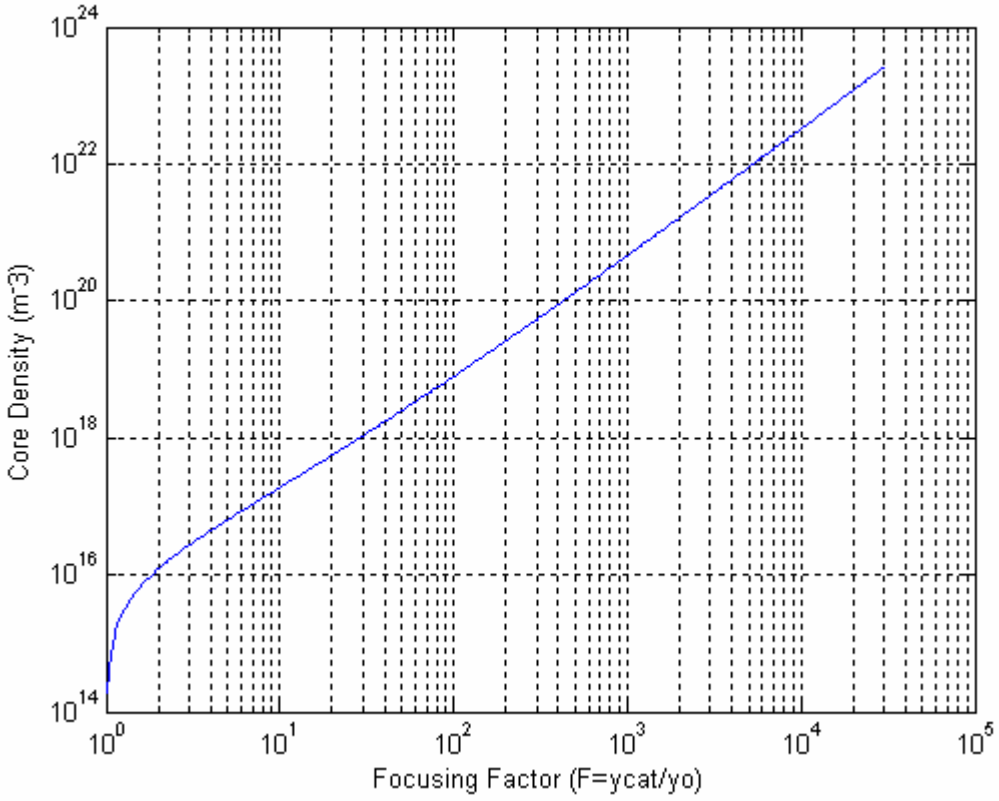

Figure 3.4 Core density for 100 keV beams as a function of focusing factor

The core density quickly rises as the focusing factor goes from 1 to 2, but then steadily rises with further focusing. The density at the cathode is somewhat more interesting. The expression for cathode density follows from continuity.

$$n_{cat} = \frac{n_o}{F^2} = \frac{2\pi\varepsilon_o E_{i_{eV}}}{ex_{cat}^2} \frac{\left[Erfi\sqrt{\ln F} \right]^2}{F^2} \tag{3.9}$$

Similarly the cathode density scales linearly with beam energy and inversely to cathode size. However, as can be seen in Figure 3.5, the cathode density peaks at a focusing factor of 2.33. At larger focusing factors, less and less cathode density is needed to achieve higher and higher core densities. Since transverse confinement of high

beam densities near the anode is problematic, the reduction in density allowed by better focusing would be welcome.

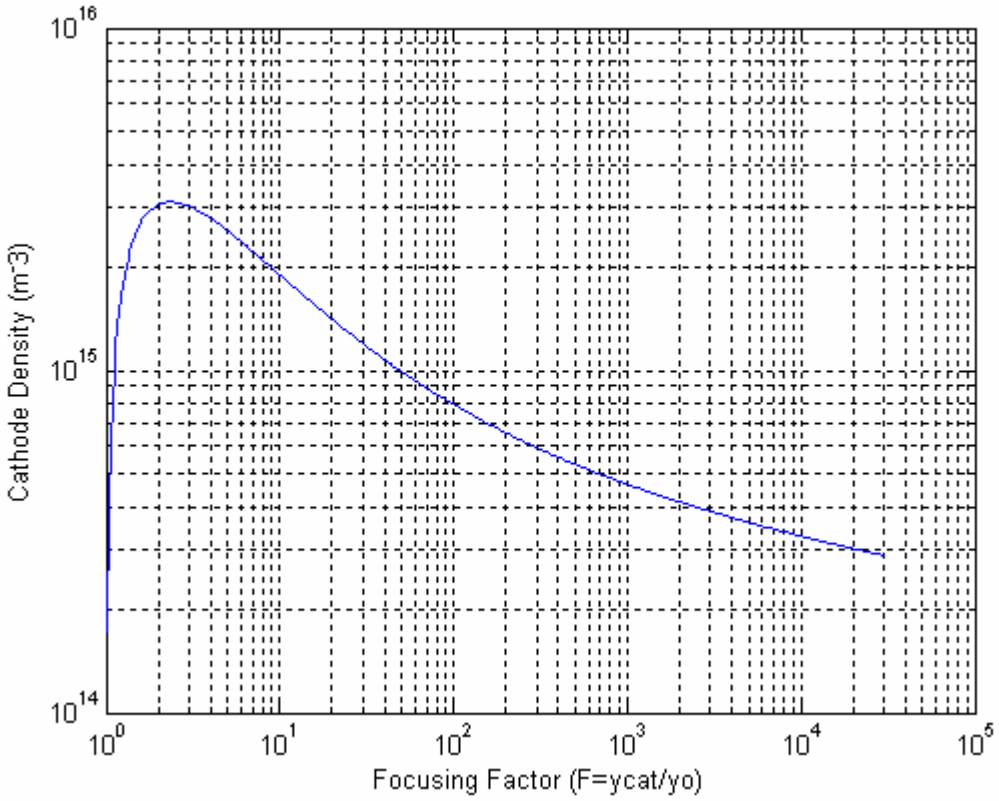

Figure 3.5 Cathode density for 100 keV beams as a function of focusing factor

The fusion power produced in the core is given by:

$$P_{core} = \frac{4\pi^3 \varepsilon_o^2}{3e} \frac{1}{x_{cat}} \left[E_{i_{eV}}^2 \langle \sigma v \rangle_c Q_{f_{eV}} \right] N_b^2 \left(\frac{y_{cat}}{x_{cat}} \right)^3 \frac{\left[Erfi\sqrt{\ln F} \right]^4}{F^3} \qquad (3.10)$$

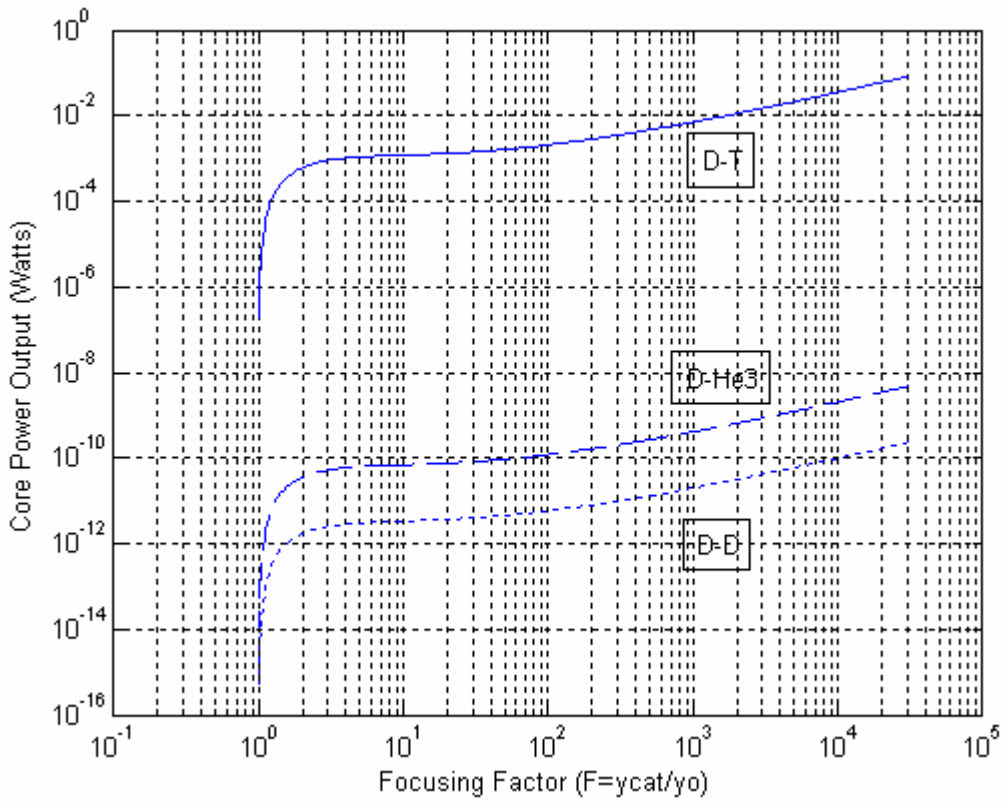

Figure 3.6 Core fusion power for 100 keV beams as a function of focusing factor, (D-T, solid line; D-He^3, dashed line; D-D, dotted line)

The main point to be made is that the overall power production is quite small for very high focusing ratios even with this ideal situation of negligible beam thermal spread. The non-neutralized beam simply undergoes too much space charge expansion to allow the higher core densities required for significant power production. Another important thing to note is that a 4-order increase in power output is obtained by increasing focusing from 1 to only 3. While further focusing is beneficial, increasing the power by another order requires ~1000 times better focusing! A focusing factor of only 3 seems technically feasible with multiple grid IEC devices, and the predicted boost in core density should be observable in laboratory experiments with variable focusing. Despite the low predicted powers, the huge boost in reaction rate for near-term neutron producing IECs is impressive and is shown below in Figure 3.7. While initial particle-in-cell

simulations show that a multigrid system allows for some control over the focusing factor, the detailed tuning of electrodes to produce different focusing factors is a topic for future numerical and experimental study.

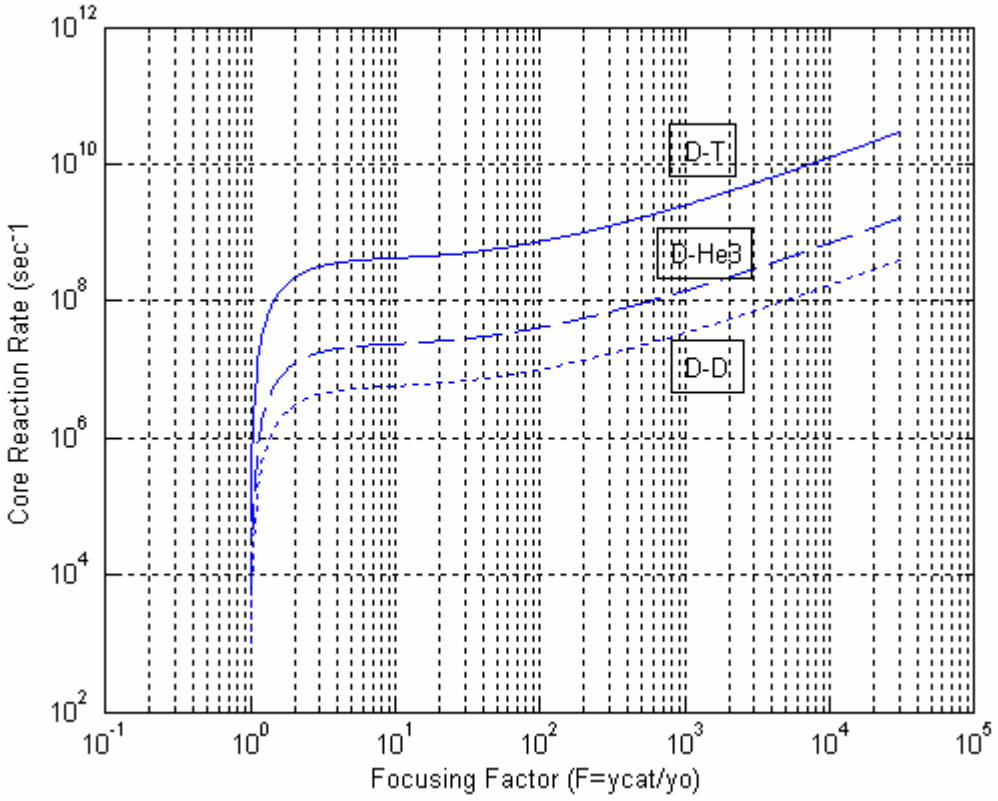

Figure 3.7 Core reaction rate for 100 keV beams as a function of focusing factor, (D-T, solid line; D-He^3, dashed line; D-D, dotted line)

3.3 High angle scattering of ions in the dense core

Ion-ion collisions tend to occur on a faster time-scale than fusion at the ion energies of interest for an IEC. The majority of collisions occur in the dense core of the device. Small-angle deflections are the most common and result in the ion beam thermalization, but do not greatly impact the confinement of the individual ions or the beams in general. High-angle scatters on the order of tens of degrees are much less

frequent but are of grave concern due to ion impacts on the grids. Any ion hitting the inner grids constitutes an energetic loss and should be limited if possible. On the plus side, only a fraction of the high angle scatters will impact grids, the rest being deflected into other ion beams since the collisions happen mostly in the core. This effect is quantified below using the Rutherford differential cross-section result to estimate the collision cross-section for ion-ion scatter into a 'ring' of solid angle which represents one or a set of grid wires. The cross-section can then be used to compare against the fusion cross-section and is useful for designing a low loss grid system.

The nomenclature and derivations follow from Mitchner and Kruger, 1973 [26]. Ion-ion collisions between identical singly charged ions are assumed. The collision cross-section is given by the integration of the differential cross-section over the full solid angle.

$$Q_{12} = \int_{4\pi} I_{12}(\chi, \phi) d\Omega \tag{3.11}$$

where 'χ' is the scattering angle and 'φ' is the polar angle. We will make the assumption that the characteristic ion is traveling centered in the ion channel, directly into the device center. The cross-section can then be simplified using axisymmetry to integrate in the 'φ' direction.

$$Q_{12} = 2\pi \int_{\alpha_1}^{\alpha_2} I_{12}(\chi) \sin\chi \, d\chi \tag{3.12}$$

where the grid 'ring' occupies the solid angle between 'α_1' and 'α_2'. The Rutherford differential cross section for coulomb scattering is given by:

$$I_{12}(\chi) = \frac{\left(\frac{b_o}{2}\right)^2}{\sin^4\left(\frac{\chi}{2}\right)} \tag{3.13}$$

where 'b_o' is the impact parameter for ninety degree scattering, which for identical particles of kinetic energy 'E_{eV}' is given by:

$$b_o = \frac{e}{16\pi\varepsilon_o E_{eV}} \tag{3.14}$$

The field particles are assumed to be stationary, which approximates the isotropic nature of the velocities in the core. This assumption is crude, but is sufficient for the purposes of generating a rough estimate of the high angle scattering cross-section. A more detailed approach would average the cross-section of a distribution of colliding ions accounting for the grids over a distribution of field particles also accounting for grids. The detailed approach becomes very complex due to the complex description of the three dimensional grids required. As a note, the very specific calculation of a colliding ion with a target ion with an exactly opposite velocity vector results in a cross-section of half of the result obtained here. Using the stationary field particle assumption, the integration gives the cross-section for scattering into a ring from the stationary field particles as:

$$Q_{\alpha_1,\alpha_2} = 2\pi b_o^2 \left[\frac{1}{1-\cos\alpha_1} - \frac{1}{1-\cos\alpha_2}\right] \tag{3.15}$$

The total cross section for a set of 'rings' is obtained by adding the individual 'ring' cross sections. The above expression can be rewritten in terms of an average ring position angle, 'α' and a wire diameter, 'd', assuming the wire diameter is small in comparison to the distance from the core to the grid, 'R_{cat}'.

$$Q_\alpha = \frac{e^2}{128\pi\varepsilon_o^2 E_{eV}^2}\left(\frac{d}{R_{cat}}\right)\frac{\sin\alpha}{(1-\cos\alpha)^2} \tag{3.16}$$

The above expression concisely shows the major scaling dependencies. Notice that mass shows no dependence. The cross section scales with the inverse of the square of particle energy and the inverse of the relative wire size 'd/R_{cat}', and increases drastically as average scattering angle, 'α' becomes small. To minimize this loss, the ion energies should be increased, the grids made thin, and the grid openings made relatively large. The argument for smaller grid openings (which corresponds to more beams) is somewhat confused by the assumption that the ions all begin centered in the ion channel. A more accurate derivation would include an average of a distribution of ions across an ion beam scattering onto a non-symmetric beam surface, but the complexity of this calculation is analytically prohibitive.

Example values of the cross-section can be calculated for deuterium at 100 keV, using device sizes for the laboratory device at MIT with a cathode radius of 5 cm and wire diameter of about 1 mm. The cathode grid has 12 beams, with 24 grid openings that measure 45 degrees across. The cross-section is then estimated by summing the contributions from 4 rings, at angles of 22.5, 67.5, 112.5, and 157.5 degrees. The results are shown in Table 3-1 below.

Table 3-1 Characteristic calculation of high angle scattering cross section

Wire #	α (degrees)	Q (barns, 10^{-28} m^{-3})	% of total
1	22.5	1.0756	95.6
2	67.5	0.0395	3.5
3	112.5	0.0079	0.7
4	157.5	0.0017	0.2
total		1.125	

Note is that the majority of the cross-section comes from scattering into the closest grid, which would suggest that a greater number of beams would be detrimental as it would greatly increase this term. The characteristic calculations show that the cross section is much larger than the fusion cross-section for deuterium-deuterium fusion specifically and is comparable to most fusion fuel reactions. The situation is not so bad, though, as higher energies and larger devices can drive the high angle cross-section well below the fusion cross-section. For example, a 200 keV system with a 15 cm radius cathode will have cross-section less than a tenth of a barn.

3.4 Suppression of electron streaming

In standard single cathode IEC experiments electrons constitute a significant power loss. Electrons are liberated as a result of ionization collisions and are released as secondaries when ions impact the cathode grid or stalk at high energies. These electrons then move through the system according to the local fields, so they end up streaming up to and eventually impacting the anode wall or anode grid. An electron hitting the anode wall streaming from the cathode to the anode constitutes a loss in energy equal to the voltage of the cathode grid in eV (-50 kV cathode grid equals a 50 keV loss per electron). Since almost every ion ends up impacting the cathode and creates a few electrons, the power loss due to ions is multiplied a few times by the electron loss! Fortunately this electron loss can be suppressed with the multiple grid scheme as shown in Figure 3.1. The ions impact the inner most grid, which is at a higher potential than the cathode grid. Secondaries produced in this reaction are thus prevented from streaming out to the anode and are confined to the core of the device. The highest electron densities will thus be

local to the innermost grid, which we will refer to as the ‘electron trap grid’. This grid also plays a key role in focusing the ion beams, as will be shown later.

The idea of suppressing the electron streaming is not unprecedented. Indeed the seminal experiments of Hirsch incorporated a version of this solution. The experiment produced the highest rates of any IEC experiment to date and relied on ion guns to introduce ions into the system. The experiment used a solid cathode grid with ports placed in front of the ion guns to allow ions to enter the device center. The experiment was run with deuterium tritium mixtures at voltages over 100 kV and required operation in a radiation safe cement pit.

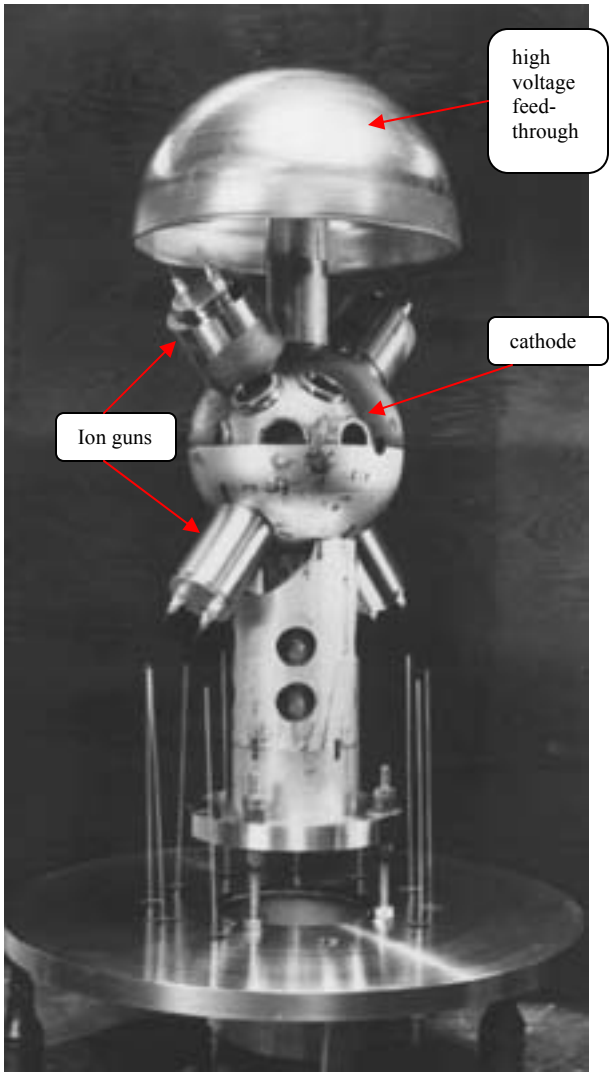

Figure 3.8 Hirsh ITT experimental set-up, ion guns and cathode labeled

Hirsch noticed that the electron streaming loss was rather high and his experiment allowed for an easy solution. A close-up of the cathode port shows that port is covered by a pair of wire meshes. The meshes can support a significant voltage between them, and Hirsch found that a bias of about a kilovolt was all that was necessary to eliminate the electron streaming from the cathode to the anode. The electron trap grid in the multiple grid IEC is capable of easily creating this level of bias and should effectively suppress the electron streaming losses.

Figure 3.9 Hirsh experiment cathode and close-up of electron streaming suppressor screens.

3.5 Multigrid confinement and the OOPIC code

The improvements to the IEC concept are verified in this thesis using a Particle-in-Cell plasma simulation code. First, let me say a few words on the general usage of numerical simulation as a scientific technique as opposed to experimentation and analytical models. The burgeoning field of direct simulation of plasma and other materials has been made possible by the explosion of computer processing ability, especially for personal workstations. In the past, there has been a significant gap in the development process between high-level global analytical models and experimental vetting of a design. In the design of general systems, and specifically plasma devices, the cycle of design and test can stall if there isn't a way to examine the inner workings of a

device and its physical processes. For example, the use of probes to measure plasma parameters can disrupt the very things one is trying to measure. In other cases, the test phase may agree poorly with design predictions and available diagnostics may not suggest straight forward corrections. The use of numerical simulations can fill this gap by allowing a higher-order model to emerge from base physical laws and allowing the user to diagnose the system at that smaller scale. For example, a plasma device can be simulated by a statistically representative group of thousands of macroparticles which interact via physical laws inside a specified geometry. The properties of the plasma can then be examined at all locations in the device at any time. With numerical simulation one can quickly examine effects of device parameters and geometry, allowing the traditional analytical and test cycle to converge more quickly. The simulations of course have limitations and are dependent on accurate implementation of all important microscopic phenomena and accurate field solutions.

Initial multi-grid modeling, other techniques

Several other techniques were tried before settling on the OOPIC code for modeling the IEC. The OOPIC code's main benefit is that it couples the field solution with the particle mover, whereas most of the other techniques explored had to jump between two separate codes for this. The other complication is the addition of non-symmetric geometries. A short description on these analyses is provided here, including a 2D analytical field solver and particle mover, 2D FEM field solver, 3D finite difference field solver and particle mover, 3D FEM field solver, and 3D Fokker-Planck distribution mover. These techniques provided understanding of the focusing properties and correct

field solutions for the gridded fields with asymmetries. Ultimately, the quantitative results of the thesis were provided by a commercial Particle-in-Cell modeling tool, which will be discussed in much more detail.

Firstly, the starting point for the research work was to look at the confinement characteristics of the standard IEC with a single cathode grid. For this simple grid configuration, a 2-D planar approximation of the geometry lets one solve exactly the electrostatic field between any number of circular grids by using complex functions. The analytical nature of the field solver allows a highly accurate particle mover to be easily implemented in Matlab. The particle mover is totally decoupled from the field solver, essentially a low-density approximation. Also, there are no collisions, so background effects are not included. Still, this technique verified that the single cathode grid behaves as a defocusing electrostatic lens and particles are quickly deviated from initially radial paths. Additionally, this technique showed that the multigrid scheme indeed creates electrostatic lenses that keep the particles moving on radial trajectories. The mechanism can be visualized as a rubber sheet model, with the cathode grid creating 'holes' which attract ions, but the other grids raise the potential relative to the local, background field, creating 'mountains' which deflect ions. By sandwiching the cathode grid with these 'mountains', the ions are steered away from the cathode grids and focused.

The electrostatic field is represented in 2D complex space as:

$$
\begin{aligned}
& z = r\,\mathrm{e}^{i\theta} \\
& \Phi = \sum_{a=a,b,c\ldots}^{\#grids} k_a \left[\ln\left(z^{N_a} + R_a^{N_a} \right) - \ln\left(z^{N_a} + \left(\frac{R^2}{R_a} \right)^{N_a} \right) \right] \\
& \frac{d\Phi}{dz} = -E_x + iE_y
\end{aligned}
\tag{3.17}
$$

All points in Cartesian space are described by the complex variable 'z'. Each set of grids sits at radius such as 'R_a' with a number, 'N_a', of evenly spaced wires. The charge constant for each set of grids is given by 'k_a'. The anode grid is assumed to be solid and sits at a radius of 'R'. Each set of grids contributes a set of source terms and a set of reflections terms which establish a circular boundary condition at the anode. The total potential is given by the sum of the contributions of each set of grids. The potential at a particular grid is affected by it charge constant, 'k_a', but is ultimately dependent on the other grid contributions to the potential field. Thus, one can not directly set the potential on a particular grid with this method, but one can vary the k values until the desired potential field is obtained. The electric fields anywhere in the device are found by taking the real and imaginary components of the derivative of the complex potential. An equivalent description of this model is given by R.W. Moses in [19]. This model is quite powerful and easily provides field data for individual ions and in beam envelope modeling. An example solution showing a multiple grid system is shown below in Figure 3.10.

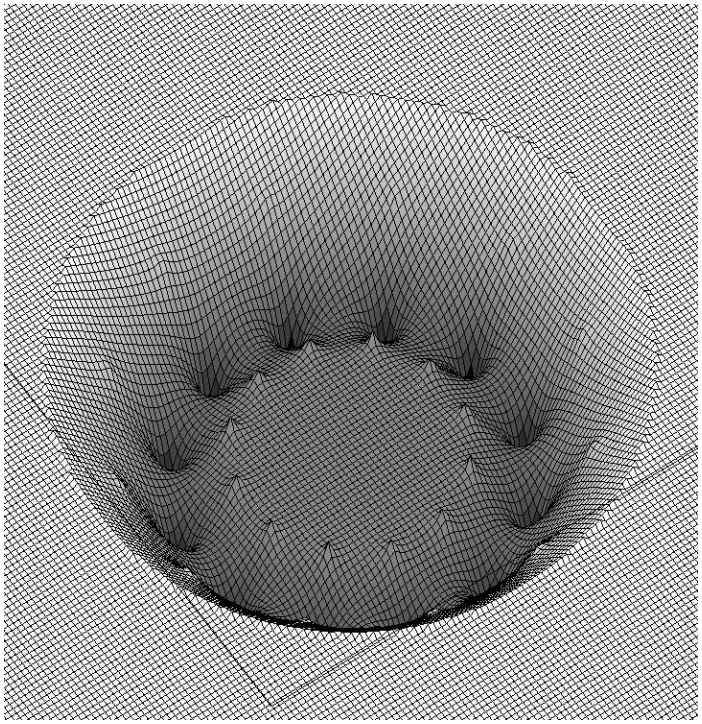

Figure 3.10 Electric potential solution for analytical 2D model of 5 grids and solid anode.

The simple ion ray tracing algorithm was implemented in Matlab and showed that ion trajectories could be stabilized by multiple grids for a wide range of grid configurations. An example of a well confined ion trajectory is shown in Figure 3.11.

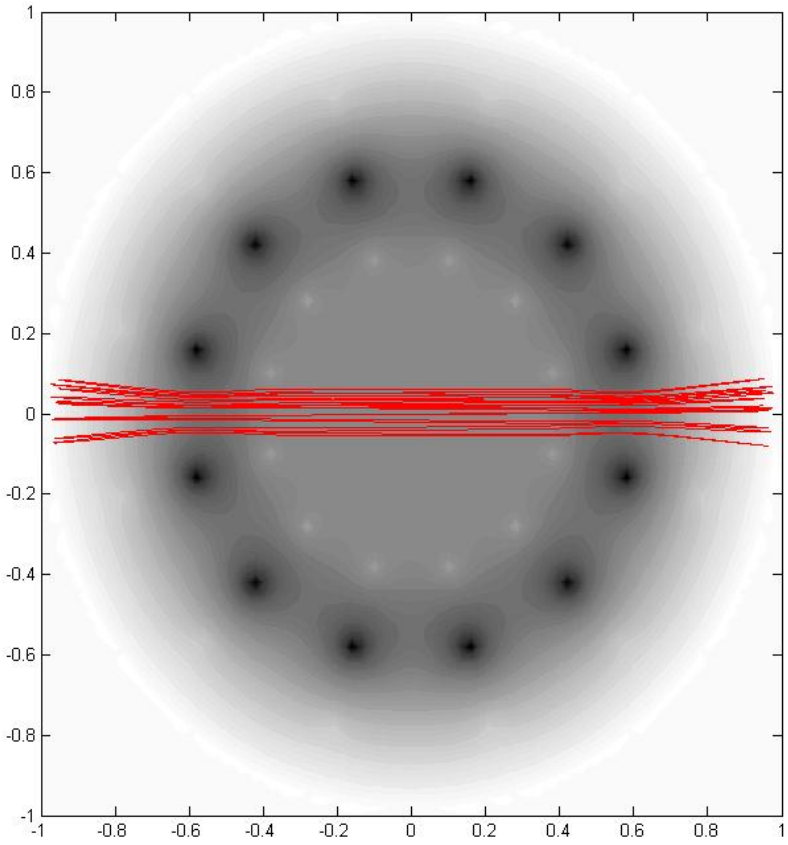

Figure 3.11 Confined particle trajectory (red) superimposed on electric potential solution for analytical 2D model of 5 grids and solid anode (darker is lower potential).

The electric field components along the center of a grid wire opening show why a single grid system does not generally allow for stable, recirculating ion trajectories. The top panel of Figure 3.12 shows the radial potential for a cathode potential of -50 kV and a fairly sparse number of grids (~10). The bottom panel shows the second derivative of the potential, which scales directly with the transverse acceleration of the ion. The large positive spike shows the attraction of an ion towards the cathode grid as it passes by the cathode. In the device center, the symmetry of the field is very good and there is very little off-axis acceleration. At the anode, the transverse acceleration is actually somewhat

negative, so that the ions tend to be pushed back towards the center of the ion channel. This combination of the defocusing and focusing regions results in trajectories that are only generally stable for ions which start directly on the center of the ion channel.

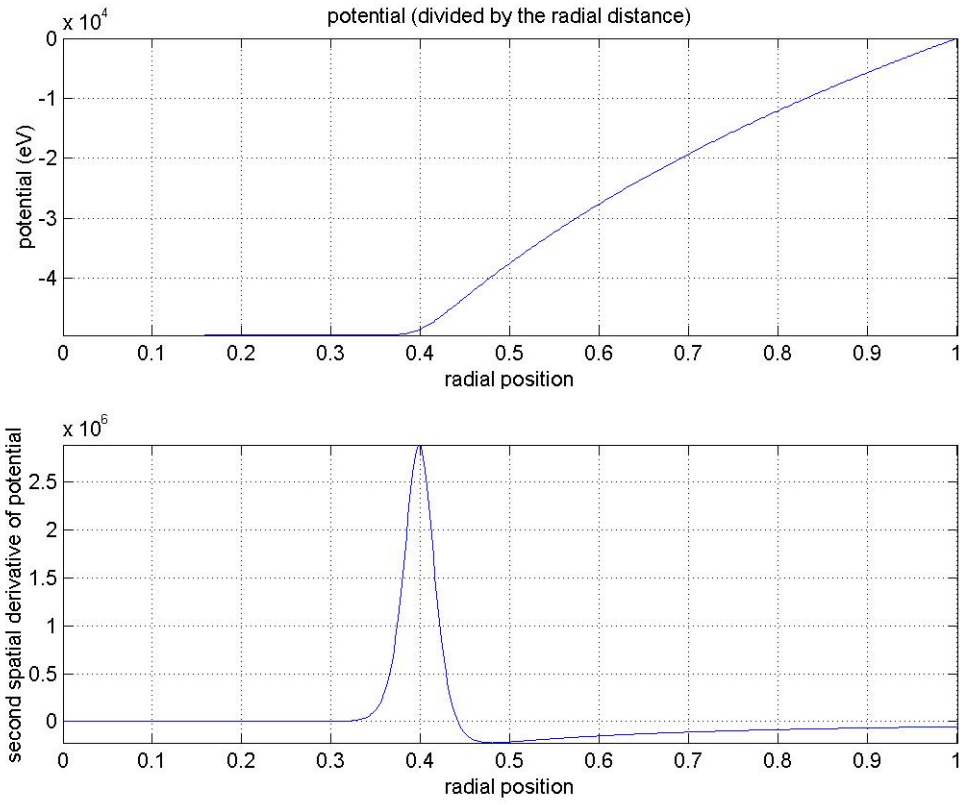

Figure 3.12 Top: potential solution along center of radial path for analytical solution of standard single cathode grid model with solid anode. Bottom: second derivative of potential along radial path, or negative of second derivative perpendicular to the ion path, corresponding to transverse acceleration of beam.

A multiple grid configuration is shown in Figure 3.13. Observe that the central potential is now somewhat higher at -40 kV. The cathode grid is actually about twice as defocusing, but it is now surrounded by much larger regions of focusing. The deceleration grid provides a very large focusing acceleration, but the outer grids are just as important because the velocities are lower in this region and accelerations in these regions integrate over a longer time. Ion trajectories are observed to be stable over a

much wider range of initial velocities and positions relative to the center of the beam channel.

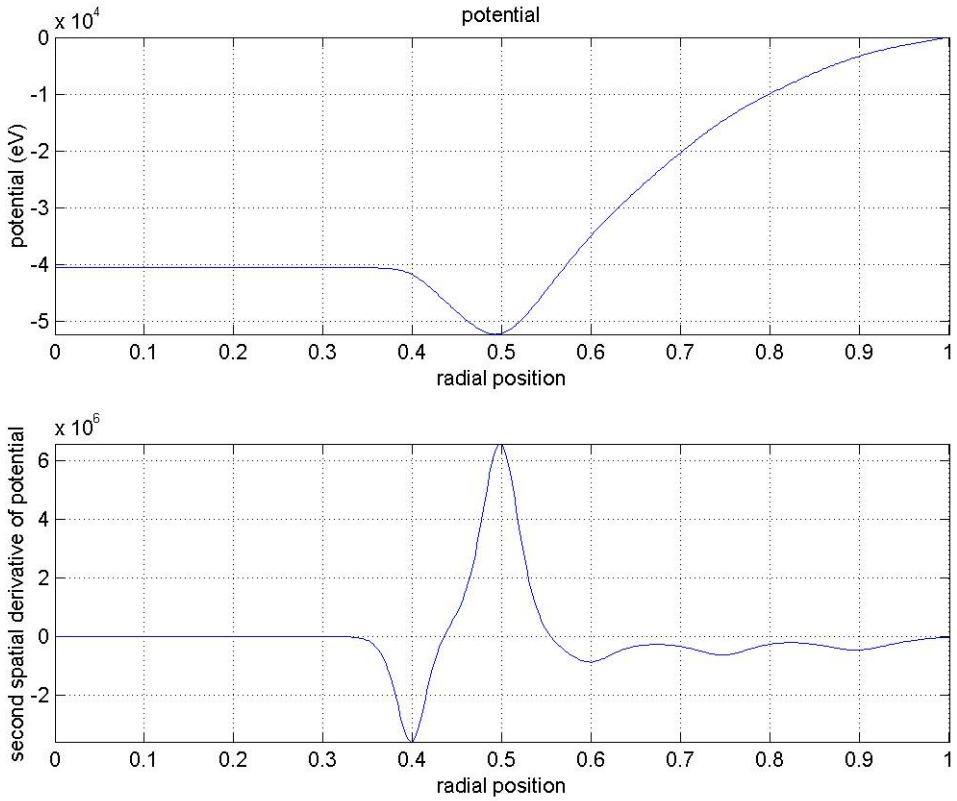

Figure 3.13 Top: potential solution along center of radial path for analytical solution of 5 grid model with solid anode. Bottom: second derivative of potential along radial path, corresponding to transverse acceleration of beam.

Considerable effort was devoted to using the analytical field description as a background field solution for a paraxial ray, self-consistent description of the beam envelope. It was hoped this would be useful to describe the focusing properties of the various grid configurations. Unfortunately, a laminar beam approximation is necessary, but questionable in the context of the real IEC system, especially in the core region where focusing can result in beam cross-over instead of necking. A non-laminar beam could experience cross-over if the transverse kinetic energy of an ion exceeds the space-charge

potential of the overall beam. Several numerical techniques for field solutions were subsequently explored in anticipation of a more accurate way to describe the beam behavior in the IEC.

Two Dimensional Finite Element Model (FEM) Solvers

In addition to the self-consistency issue of space charge and the uncertainty over beam flow properties, the other problem with the analytic model was the symmetry enforced by the model. Any incorporation of real-life asymmetries such as high voltage stalks or anode protrusions requires a numerical model. Several finite element model (FEM) solvers were used with varying degrees of success. A simple 2D model with wedge symmetry is shown below in Figure 3.14.

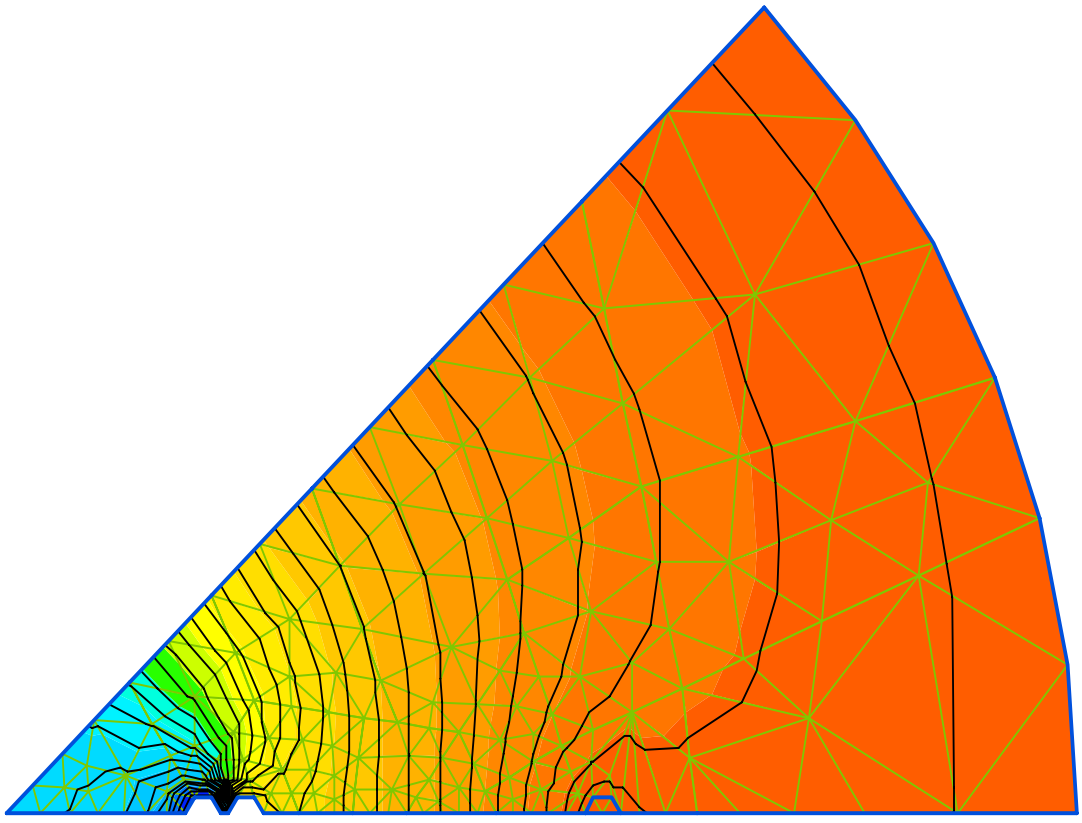

Figure 3.14 Grid triangles and potential solution for 2D FEM wedge model of three grids

The solution accuracy was found to be quite good for a relatively simple model, even for multiple grids. A quadrant model of a dual grid immersion lens is shown in Figure 3.15. An immersion lens is simply two apertures situated along the beam path with a potential difference between them. Subsequent grids in an IEC device behave as a system of these electrostatic lenses.

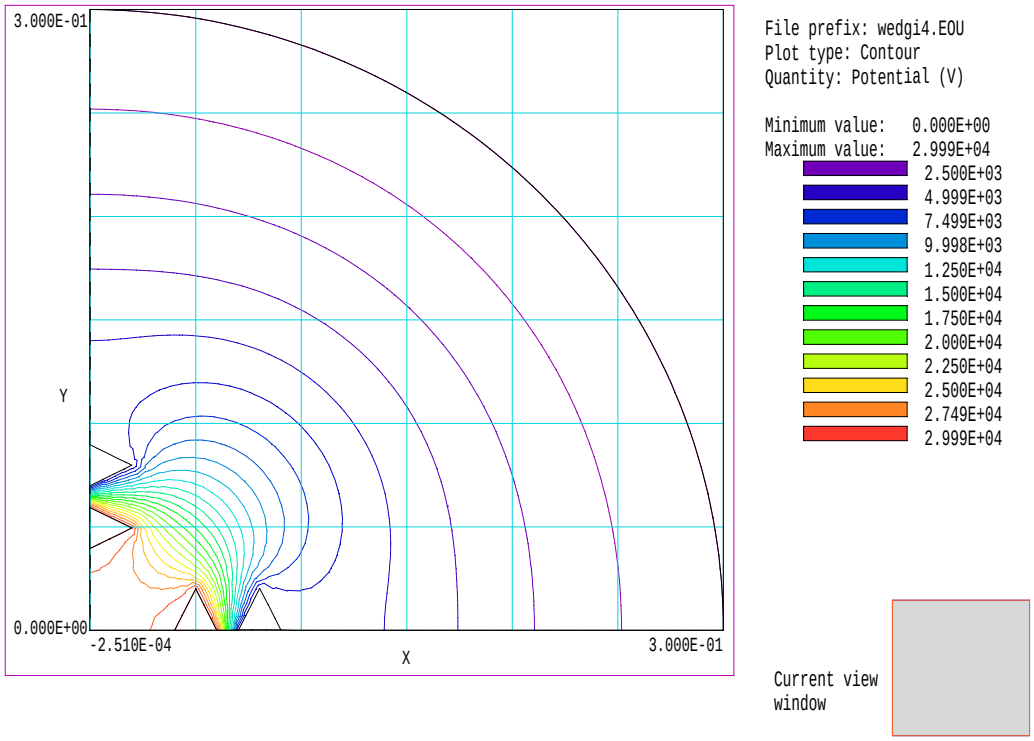

Figure 3.15 Electric Potential of cathode immersion lens, 2D FEM model

Several commercial packages were used, including Quickfield and Maxwell. The next model shows a much more complex geometry created to observe the effects of a high voltage stalk. A gridded anode is also modeled, as is the high field region where the high voltage stalk enters through the anode grid.

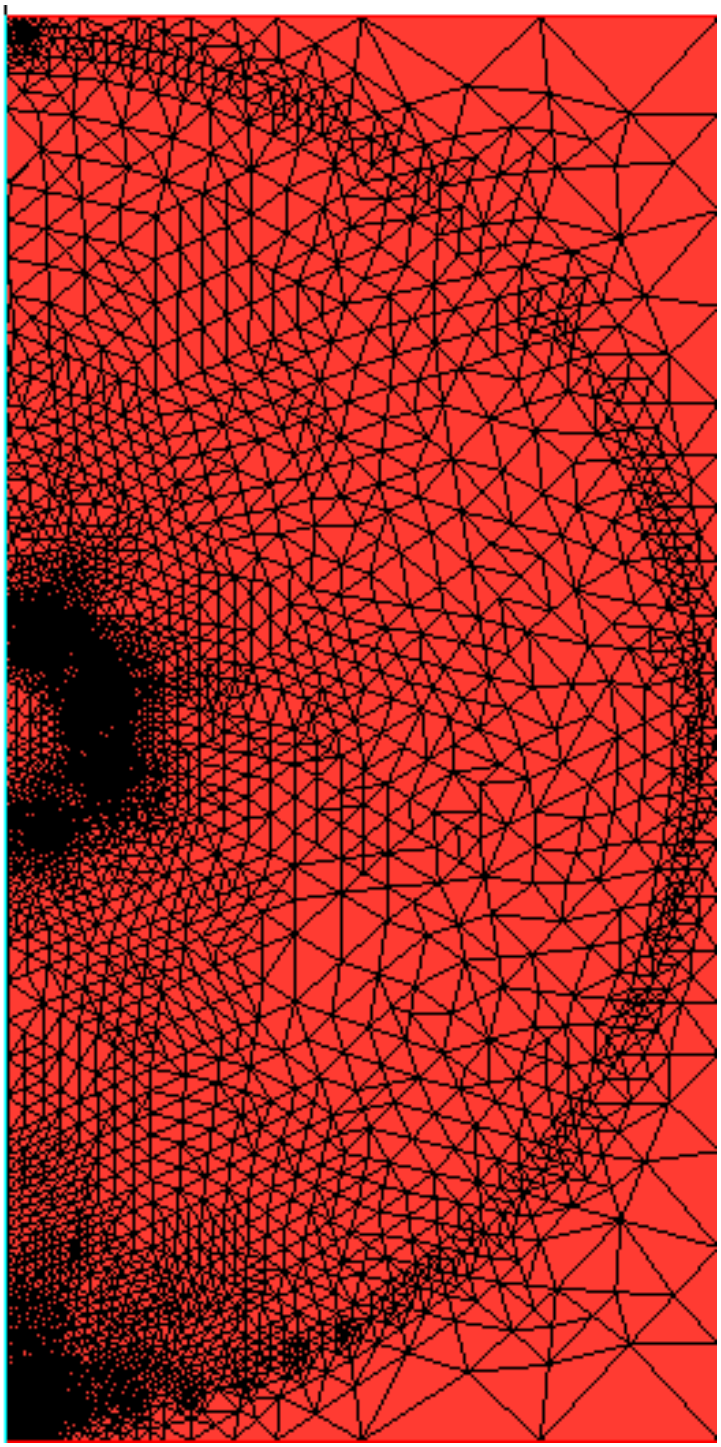

Figure 3.16 Grid geometry for 2D FEM model including high voltage stalk and gridded anode wall.

The codes systematically adapt the grids to provide higher accuracy. The regions near the cathode and stalk/anode interface are the most complex. In general these field

solutions are much more accurate in these important regions than a regular finite differenced grid we will see later.

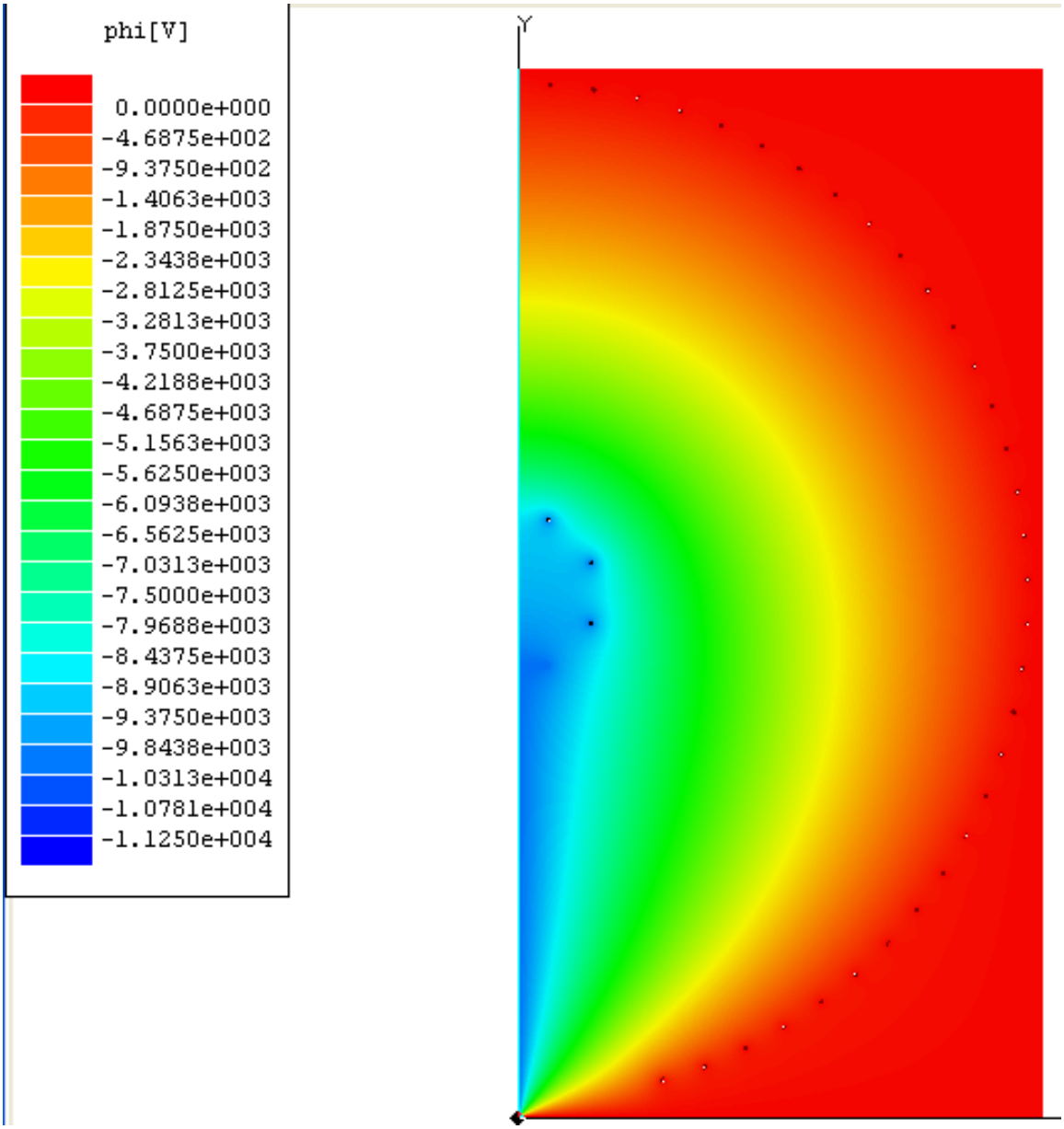

Figure 3.17 Electric potential solution for 2D FEM model including high voltage stalk and gridded anode wall.

Notice the strong asymmetry caused by the high voltage stalk. The field asymmetry local to the cathode grids is also easily visible. The anode grids provide a much better approximation to a spherical boundary than might be expected. There is still

localized field scalloping here as well, and is more easily seen in the plot of electric field, Figure 3.18.

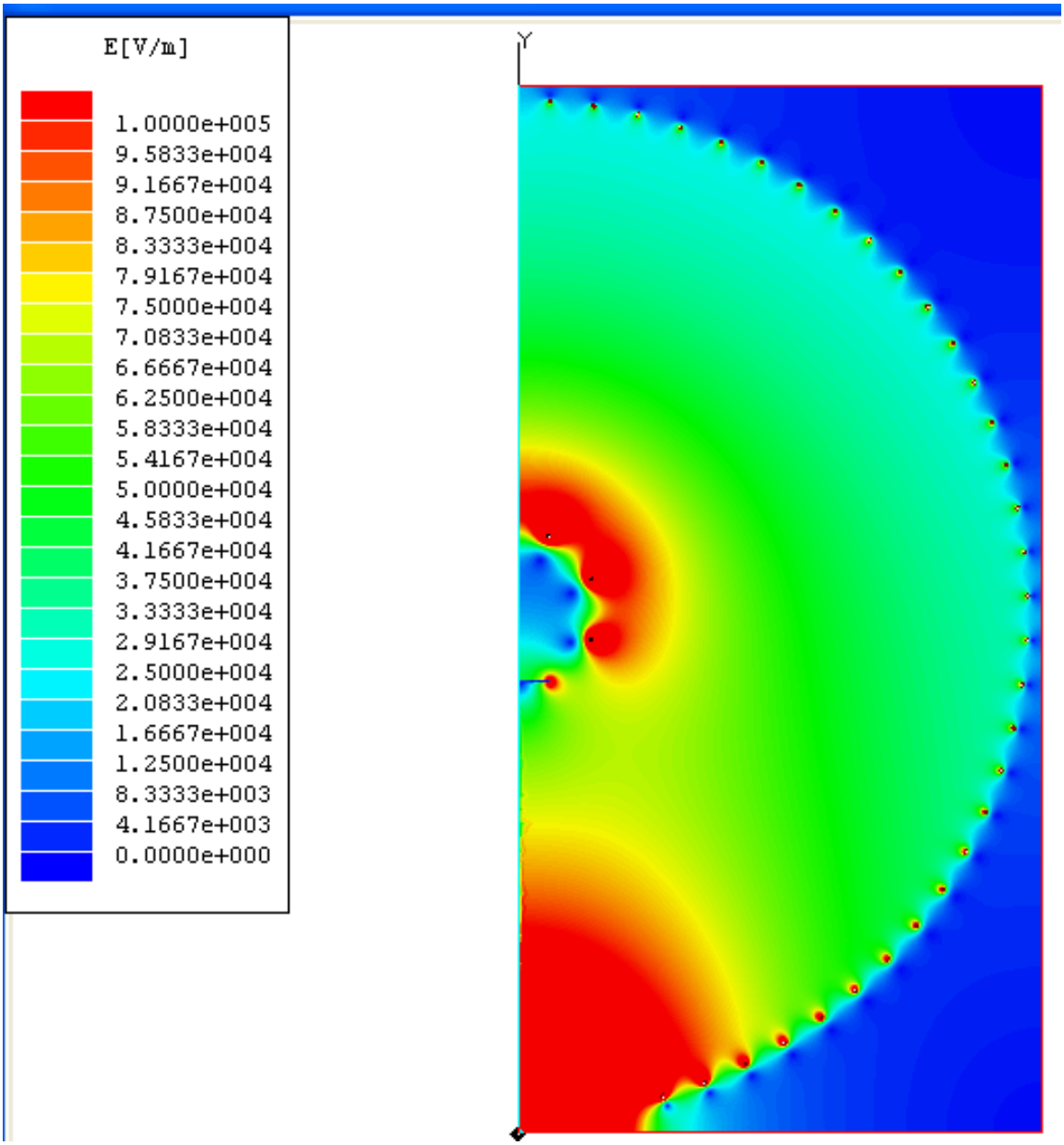

Figure 3.18 Electric field solution for 2D FEM model including high voltage stalk and gridded anode wall

The plot of electric field shows that the stalk/anode interface produces accelerations as strong as the cathode grid. It will be shown that this strong asymmetry is the major cause of poor ion confinement in single cathode IECs. This 2D model was

very good for background field calculations, but unfortunately didn't have a way to incorporate the space charge of ions into the model. Also, at the time it was difficult to export the field data in a form that could be used in a particle tracer.

SIMION field solver and particle tracer

The SIMION program is a 3D finite difference field solver and particle tracing program. The best 3D IEC model of multiple grids is shown in Figure 3.19. Here the grids are represented by shells with polar apertures removed for the beam line.

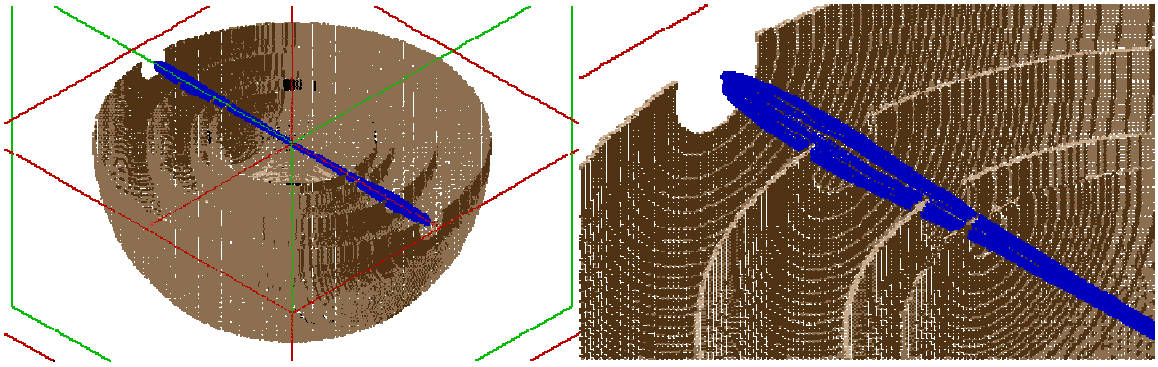

Figure 3.19 Ion recirculation in nested shell SIMION IEC model, left-cutaway view, right-zoom.

The SIMION model is a finite difference solver on a regular grid. It is difficult to get the desired grid structure, but the program has a good built-in particle mover. It is too difficult to create a full 3D grid representation, but a cylindrical symmetry can be exploited to get fairly good results for a single beam line. 2D planar models agreed with the higher fidelity FEM models, and allowed for particle tracing. Several ions can be propagated simultaneously to investigate the envelope of a beam, but the program doesn't treat the beam self-charge accurately. This model was useful for validating the particle trajectories in the general geometry, but unfortunately could not be used to investigate the effects of space charge on the ion confinement.

Three dimensional finite element model

The most complex field model was created using AutoCAD's solid modeling routines and solved in Maxwell on a UNIX workstation. A system of three grids was created that exhibited 3 planes of symmetry, with separate voltage stalks for each grid. The tetrahedral grid is shown drawn on the symmetry planes near the two inner cathode grids in Figure 3.20. Notice the computational grid is not as fine as in the 2D model, especially near the wires.

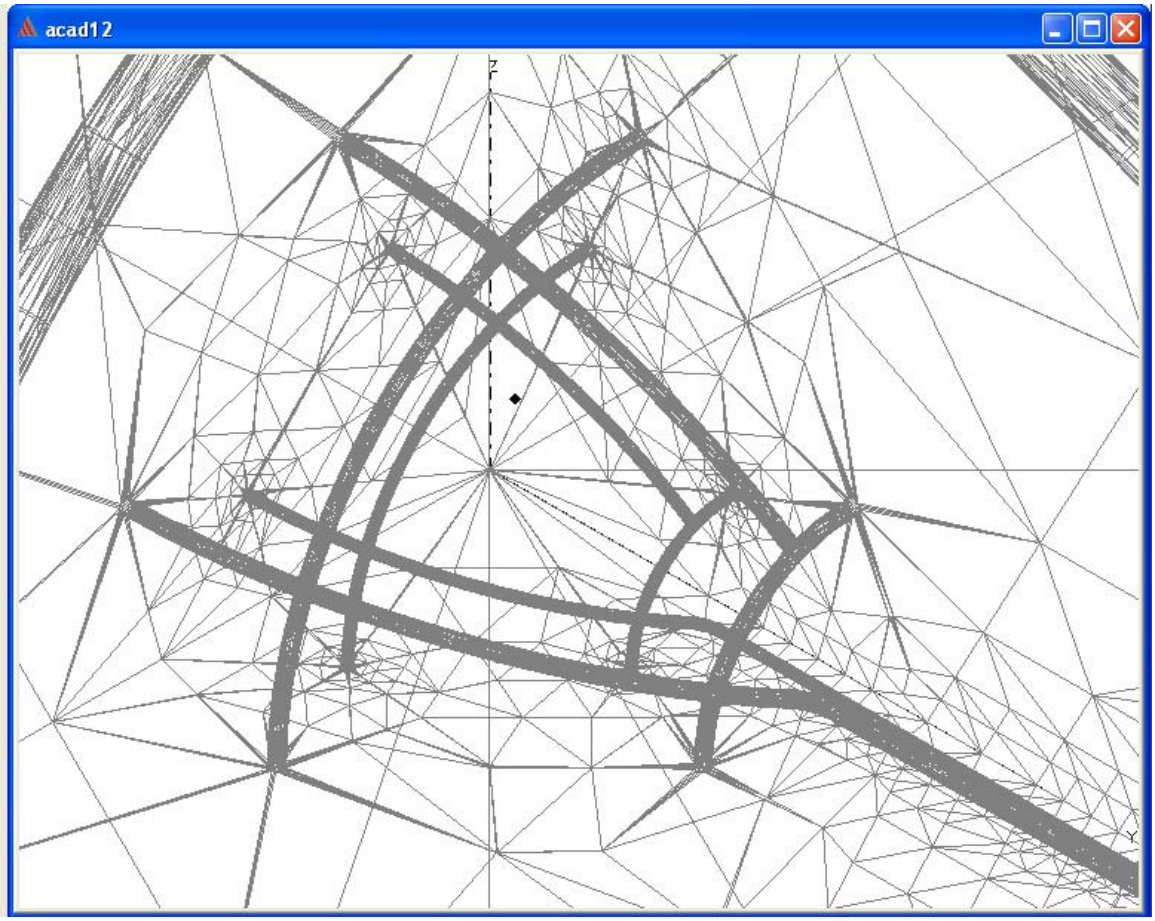

Figure 3.20 Tetrahedrons on symmetry boundaries for 3D FEM model near double cathode.

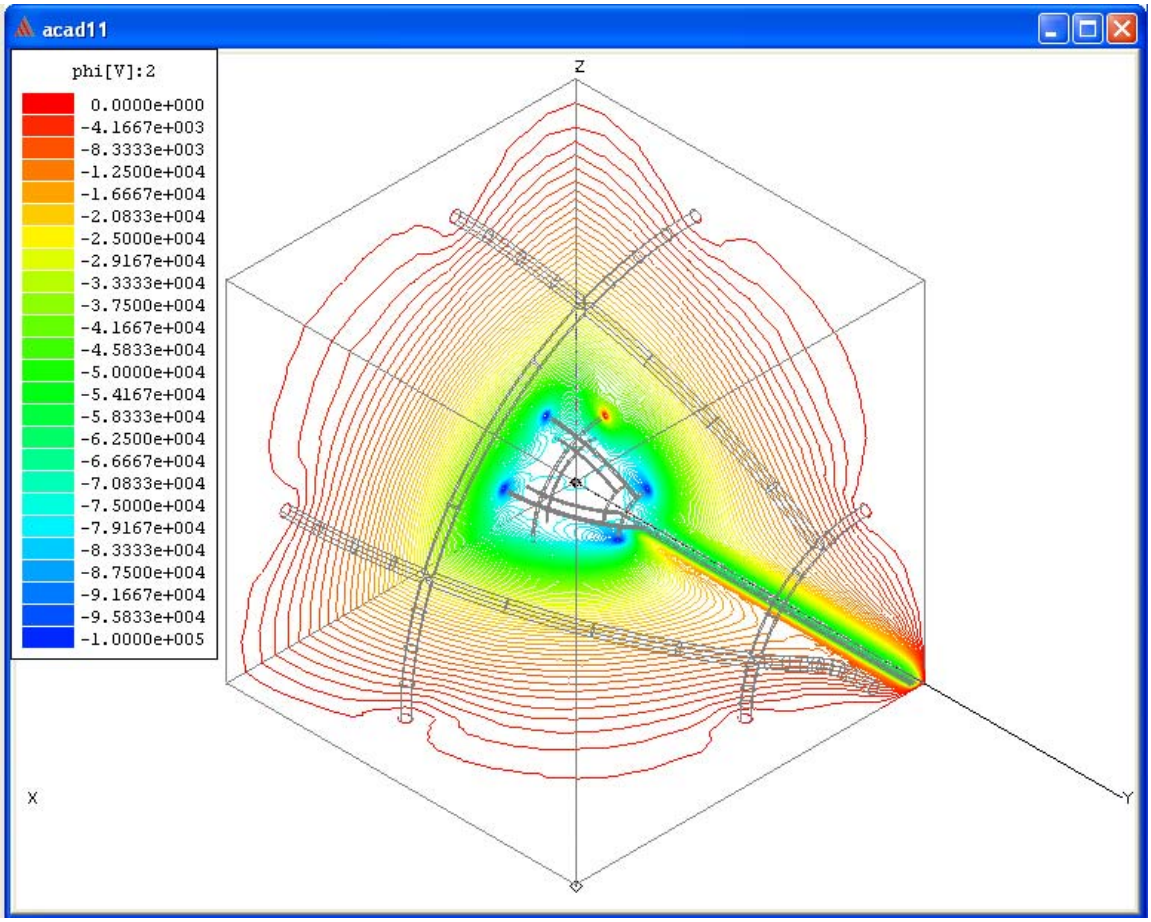

Figure 3.21 Electric potential for 3D FEM model with double cathode grid, anode grid and high voltage feeds, peak voltage, -100 kV.

The potential field solution is shown in Figure 3.21. The model includes 100,000 tetrahedrons and this solution has less than 12% error. The model is essentially too complex to run efficiently on a workstation. More crude grids exhibit even higher errors, and this run took several hours to execute. Finer grids crashed the workstation. Still, the information gleaned from this model is quite interesting and useful. On can see that the electric potential 'balloons' well outside the anode grids. Thus, if one would like to approximate a spherical potential surface at the anode, a finer grid is required. The three dimensional model also shows the real potential one gets from a system of grids instead of the idealized 2D model. The system of longitudinal and lateral wires forms quasi-

rectangular grid openings. As Figure 3.22 shows, the electric potential inside this quasi-rectangular surface quickly forms a more ellipsoidal shape approaching the center of the ion beam channel. The electric potential field is plotted on a spherical surface with a radius slightly outside the innermost grid.

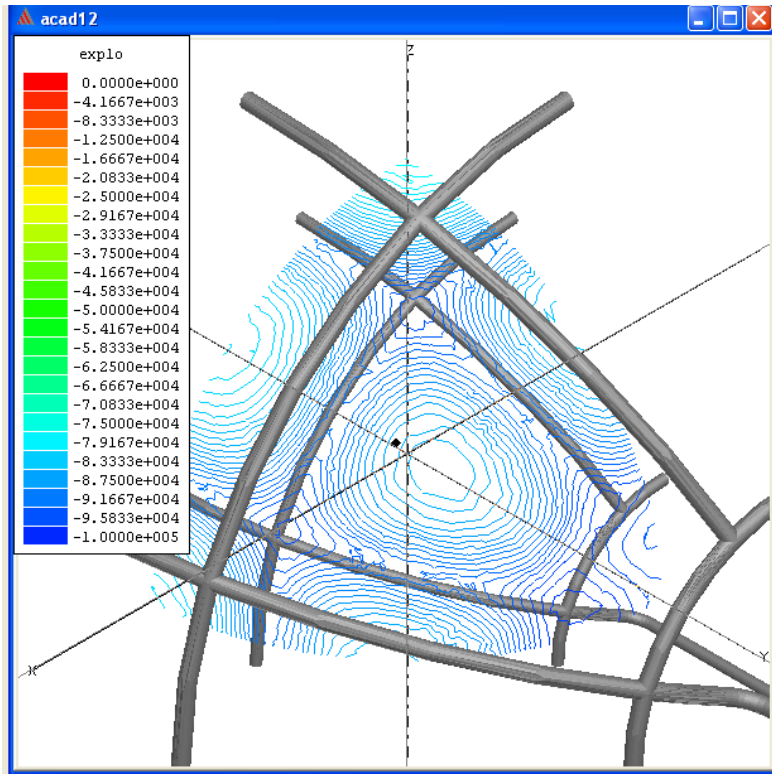

Figure 3.22 Electric potential near cathode grid for 3D FEM model

Another open question was the field penetration of the ellipsoidal field towards the device core. Figure 3.23 shows how the ion channels look on a spherical surface well inside of the innermost grid. The ion channel is still clearly visible centered in the grid opening, despite being far from the grid. Notice also how the intersection of the grid wires appears as a localized raised region in potential. This means that ions that are deflected in the core towards the grids or grid intersection will be accelerated away from the grids line somewhat by this field penetration.

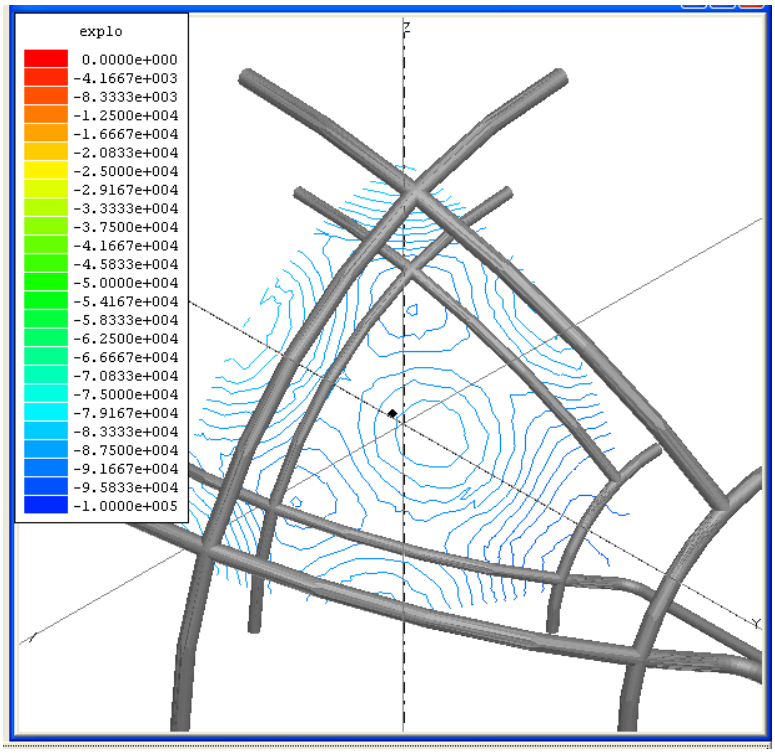

Figure 3.23 Electric potential inside cathode grid for 3D FEM model

While these results were quite exciting, the inability to export the field solutions and the slow runtime of the code limited its uses. Ideally, the space charge of ions could be included back into the field solver and this could be done in an iterative manner. Unfortunately, the model was much too complex for this to be done efficiently.

Quasi-3D polar model

In order to have a fast field solver with ion space charge included, a custom finite difference solver was written in Matlab. Wedge symmetry was used to approximate a 'slice of pie' shaped region from the device center to the anode. The model used circular grid openings a mapping technique to allow solution of the field on a rectangular grid. The model provided good field solutions for multiple grid systems, as shown in Figure 3.24. The potential is plotted over the wedge where the polar distance measures the

distance along the beam path and the transverse distance measures the distance from the center of the beam channel to the grid wires.

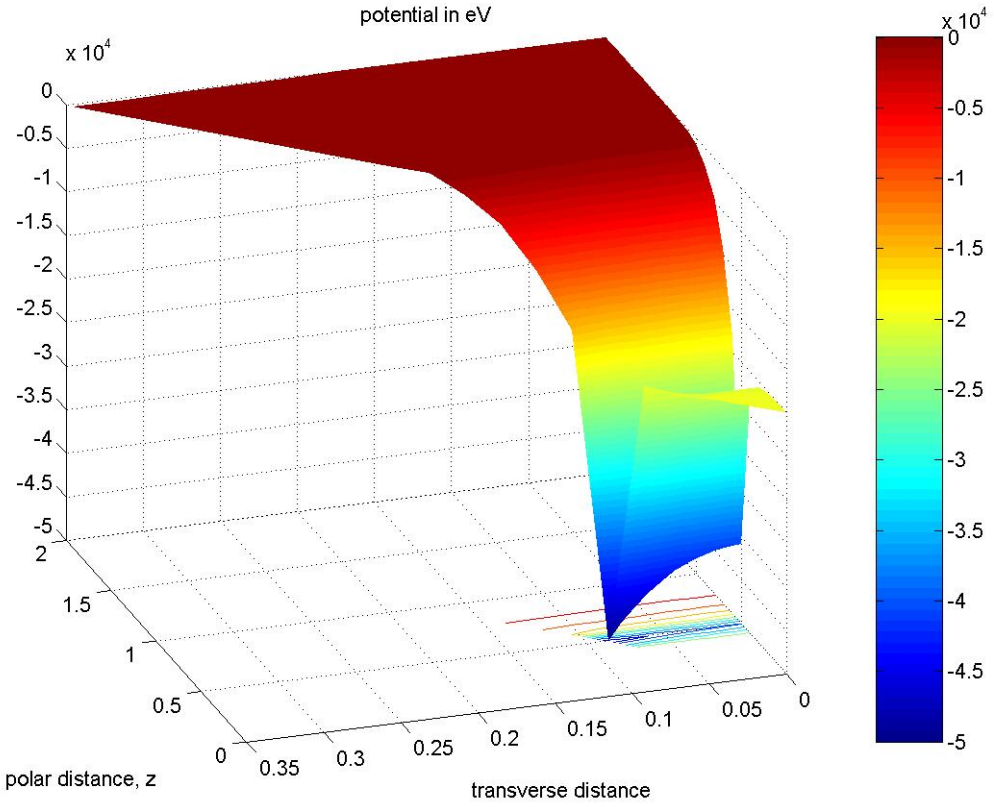

Figure 3.24 Electrostatic potential of focusing lenses for the 3D wedge model with cathode grid at -50 kV. Polar distance is the radial dimension and transverse axis is perpendicular to the radial direction.

This model allows the user to quickly find the shape of the electric potential in between the grid wires. The depth of the focusing ion lenses can then be diagnosed, as is shown in Figure 3.25. The horizontal axis shows the distance from the center of the beam channel to the grid. The top panel shows the defocusing cathode grid, while the other tiles show the focusing grids. One can see that the depths of the potentials of the outer lenses are much smaller than that of the cathode grid.

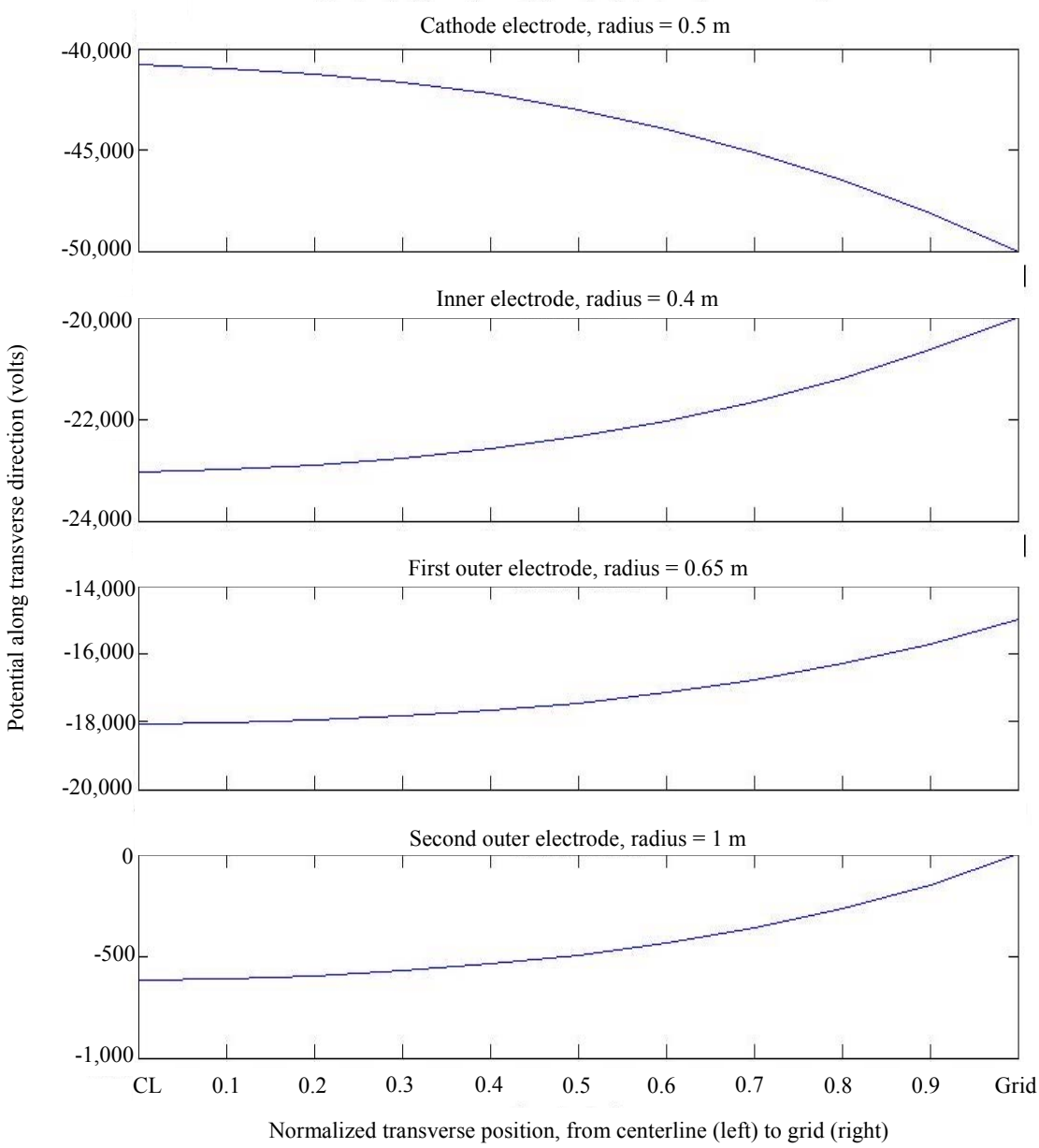

Figure 3.25 Lens potentials transverse to the beam line, top is cathode grid, 2nd is inner grid, 3rd is the third grid, and the bottom plot is the outer grid. The potential is in volts and the horizontal axis starts at the beam centerline (left) and stretches to the grid location (right).

The primary purpose of this model was to investigate the role of the ions on the shapes of these focusing lenses. The intention was to find the amount of space charge required to remove the lens and thus find the space charge limitation for ion beams in the system, since without the lenses the ions would be unconfined. The problem then

became how to properly model the ion beam. Unfortunately, one needs to essentially 'know' the end state of the beam to load a proper ion beam. This leads to using the field model to model the self-consistent transient to 'build' up the beam naturally without presupposing a particular beam structure. This becomes considerably difficult if one tries to model the ion beam by some analytical description. Essentially, with every step the model becomes more generalized and thus more computationally intensive. The last step was to meld the field solver with a model of the ion distribution function discretized in velocity and position. Despite the symmetries of the wedge model, there are simply too many dimensions to discretize accurately and still run the model efficiently. At this point, we considered custom coding a Particle-in-Cell model which can more efficiently model systems with many degrees of freedom. Fortunately, Suman Chakrabarti, a colleague at NASA Marshall Research Center, pointed us to a commercial PIC code that happened to be just about perfect for this application.

OOPIC Pro Particle-in-Cell model

The Particle-in-Cell technique is used in the OOPIC Pro code, a Windows-based version of XOOPIC, a plasma code developed by the Plasma Theory and Simulation Group at the University of California Berkeley [31][32]. In this code, a collection of macroparticles is tracked through a grid geometry representative of the device being modeled. The collection of particles is large enough to be statistically representative of the plasma at all locations in the device. The particles are then used as source terms to solve Maxwell's equations for the electromagnetic fields on the grid. These fields are then interpolated to move particles across the device, and the process continues for as long as the simulation runs. Details on the technique are provided in several references,

the author of which helped to develop the kernel of the code used here [29][30]. The XOOPIC code implements an object-oriented scheme that allows the user to easily change code parameters, geometries, and boundary conditions without re-writing the code. It also provides an easier architecture for the developer to add features to the code, but this was not necessary for the work presented here.

The Tech-X Corporation ported the code to windows and is marketing it as a general plasma and beam simulation tool. The capabilities of the code, taken from a product white sheet from the company's website reads, "OOPIC Pro simulates physical systems including plasmas; beams of charged particles with self-consistent and externally generated electric and magnetic fields; multiple species; low-to-moderate density neutral gases; and a wide variety of boundary conditions. OOPIC Pro has electrostatic and electromagnetic field solvers for 2D geometries in both x-y (slab) and r-z (cylindrical) coordinates, and includes Monte Carlo collision and ionization models." The data sheet continues to say that the OOPIC physics kernel has been used around the world since 1995 to study a variety of problems including plasma displays, the plasma environment for ion implantation, microwave devices, and particle acceleration concepts [32].

An OOPIC input file was created to describe the geometry of IEC devices in a two dimensional planar model. An example of the ion map for this model is shown below in Figure 3.27. An example input file and description is given in Appendix A. In this model, the charged particles behave as infinite rods. Ideally a three dimensional model would be used, but it is too computationally expensive and not useful as a design tool. Also, a three dimensional code would have to be coded from scratch, as one is not public available to the author's knowledge. The geometry doesn't make use of any

symmetry planes because they would impose an artificial symmetry to the unsteady behavior which emerges. Initial models included a single high voltage stalk, but later models included a second stalk to increase symmetry in the system, which is easily implemented in real-life. Ions are created at 6 emitters, 4 along the diagonal beam lines, and 2 along the equatorial cut. The ion current is set before each run, and can be commanded off at a given time to watch the decay of particles in the system. The emitters provide a more realistic and simpler particle loading scheme than pre-loading the beam as a region of plasma. While at first this might seem favorable, it is difficult to know before hand what a beam will look like in terms of shape and velocity profile for any given set of parameters. By starting the simulation as a transient, we can observe how the beams build-up over time and how the shape of the beams changes with increasing space charge or instability. Also, it matches the experimental procedure of oscillating the guns on and off with a set square wave to determine ion decay lifetimes.

The anode grid is represented by a ring of grid 'squares' which are made up of anode segments. The anode grid is required to approximate the spherical symmetry without needlessly increasing the computational domain, which would greatly slow the simulation. On almost all surfaces, ions that impact the surface are lost and kick off electrons. In all the low pressure cases presented here, these secondary electrons simply stream to the anode because the background pressure is simply not high enough to generate new ions by electron bombardment. The only exception is at the emitters, where ions are reflected from this surface to model the port of a real ion gun. Now it is true that ions are emitted at a finite velocity (1 eV here) and have a chance to come back and strike the source, but this assumption can be relaxed and similar behavior is observed in all the

runs. A fraction of the ion current is lost, but it merely has the effect of reducing the effective input current of the gun, since some of the current does not return to hit the source. It misses the source due to either deflections from particles or its trajectory simply doesn't return to the middle of the channel, where the source only occupies a small portion of the ion channel.

The pressure in the runs presented in this thesis is set to $1 \cdot 10^{-10}$ Torr in order to eliminate the background effects from the simulation. This also reflects the lowest pressure we stand to see in the lab device here at MIT. The model can be run at higher pressure though, and the glow discharge results of standard IECs are reproduced. This code is not ideal for this application though, since only the voltage to the grids is set. Without a current limitation, an excessive current is drawn from the grids in the form of secondary electrons and ion impacts. The code could probably be adapted to help design ion guns in the future, but has some limitations with regard to accurately modeling the steady behavior at high pressures.

The time step is chosen so that at maximum velocity, an ion takes more than 2 steps to traverse the cell size. This is a coarse discretization, but the field solutions are found to vary smoothly, even near the grids, which are the smallest model features. This time step is adjusted to match the ion species and domain size used in the particular run. The standard domain size is an 80 by 80 grid which represents a 40 cm square, so that the smallest features are 5 mm across. While this is somewhat larger than the grid wires used for this size IEC, this cell number provides an acceptable number of field points (8 in most cases) in between the cathode wires to model the field curvature there. Running the model on more cells seriously slows the simulation to the point where it cannot be run

efficiently on a desktop PC. A characteristic run will use 50,000 ion macroparticles, with about 400 time steps for an ion to traverse the device. Running the simulation to 100 passes (40,000 steps) can take anywhere from 10 minutes to an hour. Using fewer particles speeds the simulation, but starts to reduce the statistical accuracy of the representation. There are 6,400 cells in an 80 by 80 grid, and an even distribution of particles would yield fewer than 8 particles per cell. Many of the cells are empty in a run, however, and perhaps only 10% of the cells actually have particles, which raises the particle per cell number to 80, which is much better, but still noisy. The size of macroparticles was varied for given model conditions to investigate the effect of macroparticle number on fluctuations in the ion number density in the beams, and it was found that simulations of greater than 10,000 particles are essentially equivalent. The PC desktop used had 2 gigabytes of memory and successfully simulated greater than 5 million particles, although the simulation ran quite slowly.

As was discussed earlier, for a single cathode grid, the high voltage stalk asymmetries in the electric fields cause the ions to deflect off radial paths. Multiple grids serve a few different purposes, the first of which is to shield this stalk asymmetry from the radial paths. Multiple grids also make tunable electrostatic immersion lenses which can focus the beams and keep them on generally radial trajectories. Multiple grids can also stop the electron streaming to the anode by forming a potential barrier of a few kilovolts around the core region.

As in most complex systems, the geometry and voltages of the multigrid system are chosen with specific goals in mind. First, the main cathode grid must provide enough acceleration to ions so that they achieve sufficient energies to fuse in the device core.

The other grids main purpose is to change the local potential so that it provides a focusing curvature to ions on radial paths. To this end, the voltages on these grids are set to be somewhat higher than the local background potential produced by the main cathode grid. Further, the additional grids must be separated by a significant distance (cm's) so that arcing on the feedthrough is less problematic. The actual positions and voltages presented here are a product of extensive trial and error using the OOPIC program. The goal was simply to produce well-confined ion beams, not to optimize the system for fusion production per se. An optimization project using simulated annealing is a topic of current research in the lab at MIT. The grid locations used here are generally evenly spaced with an outer anode size sized to fit in the MIT vacuum system, a radius of 25 cm. The innermost grid is at least 10 cm in diameter since welding a smaller grid is difficult. Also, OOPIC uses a regular computational field grid and it is computationally expensive to increase the number of cells, so a smaller cathode would not have enough cells in the core region to get good results.

A series of OOPIC models is presented here. The first figure is a single cathode grid without the high voltage feed through. The next model adds the feedthrough and each successive model includes an additional grid. The first model shows good confinement of ions, but observe that when the feedthrough is added the confinement for a single grid is quite poor, with many of the ions impacting the cathode stalk. A second grid stabilizes the equatorial grid, but doesn't shield the anode region of the diagonal beams enough to stabilize them. A third grid improves the situation, but a fourth grid allows the diagonal beams to be completely confined. Complete confinement means that absent of space charge build-up, an ion will oscillate in the system indefinitely. A single

grid cathode without the stalk asymmetry will still be unstable, with a maximum lifetime of about 10 passes for an ion starting almost in the center of the ion channel.

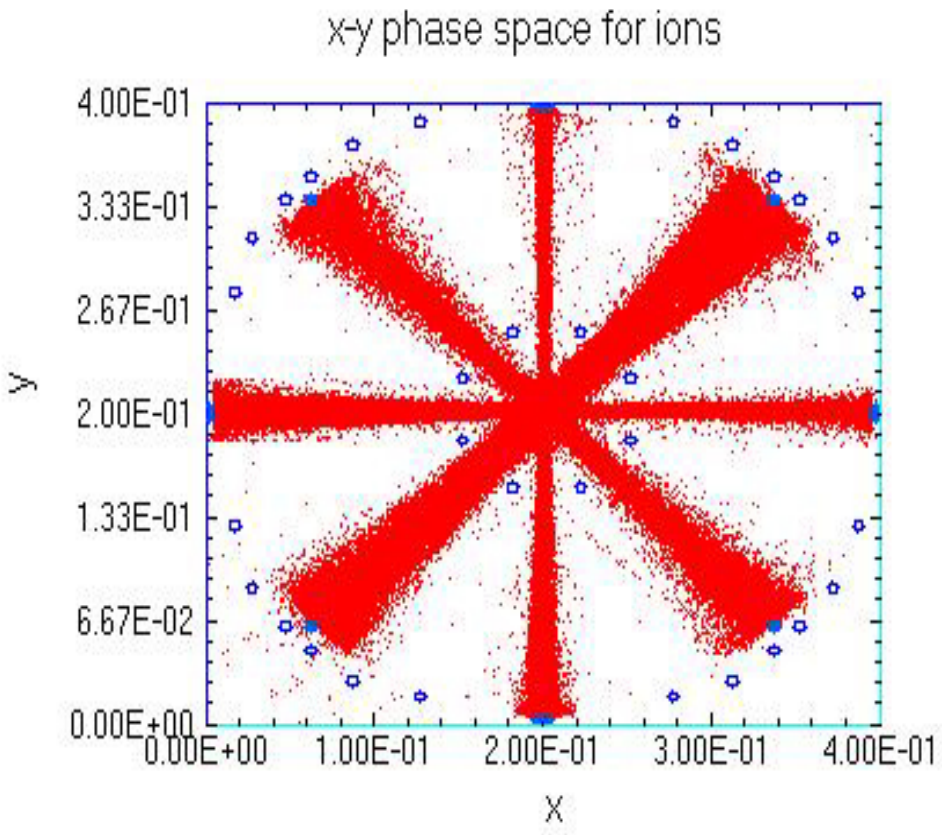

Figure 3.26 Single grid IEC, OOPIC model with no feedthrough stalk, shows good confinement of all beams

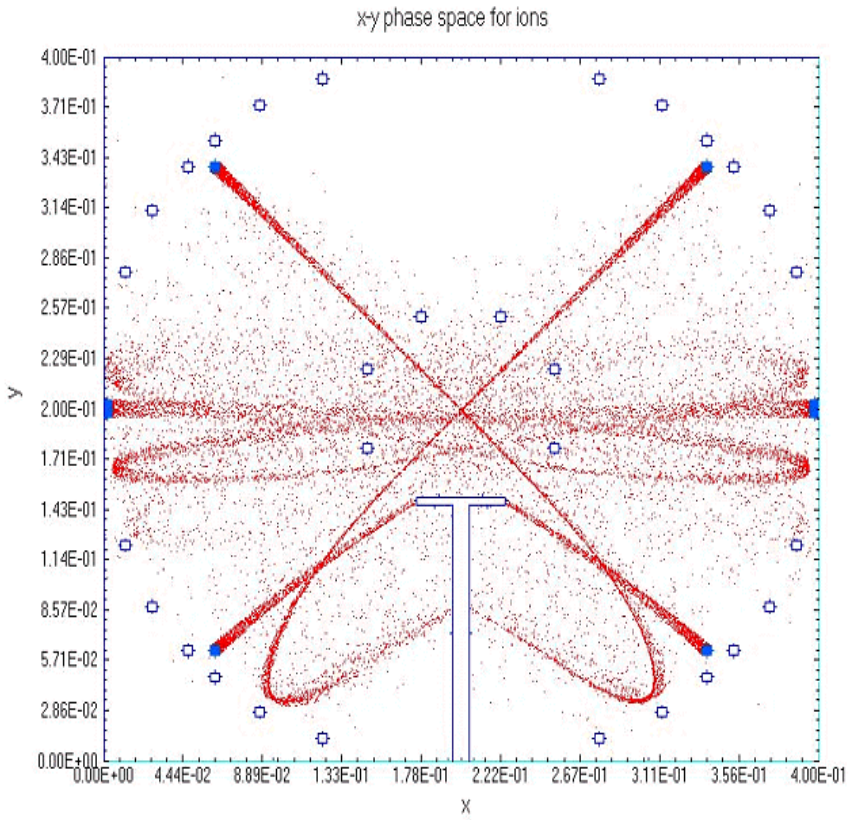

Figure 3.27 Single grid IEC, OOPIC model, shows poor confinement of all beams.

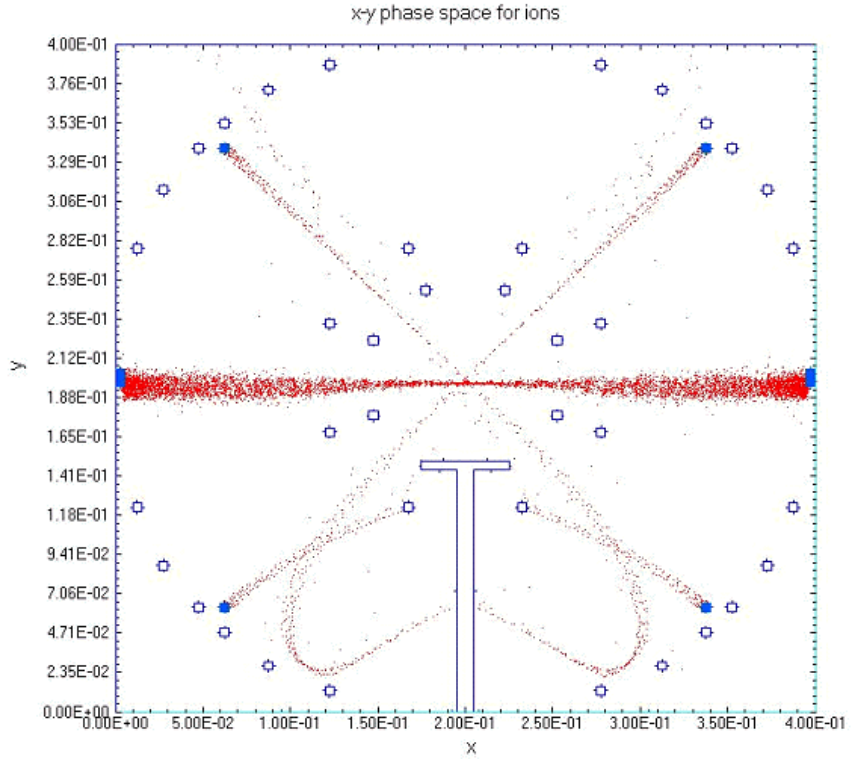

Figure 3.28 Double grid IEC, OOPIC model, shows good equatorial confinement.

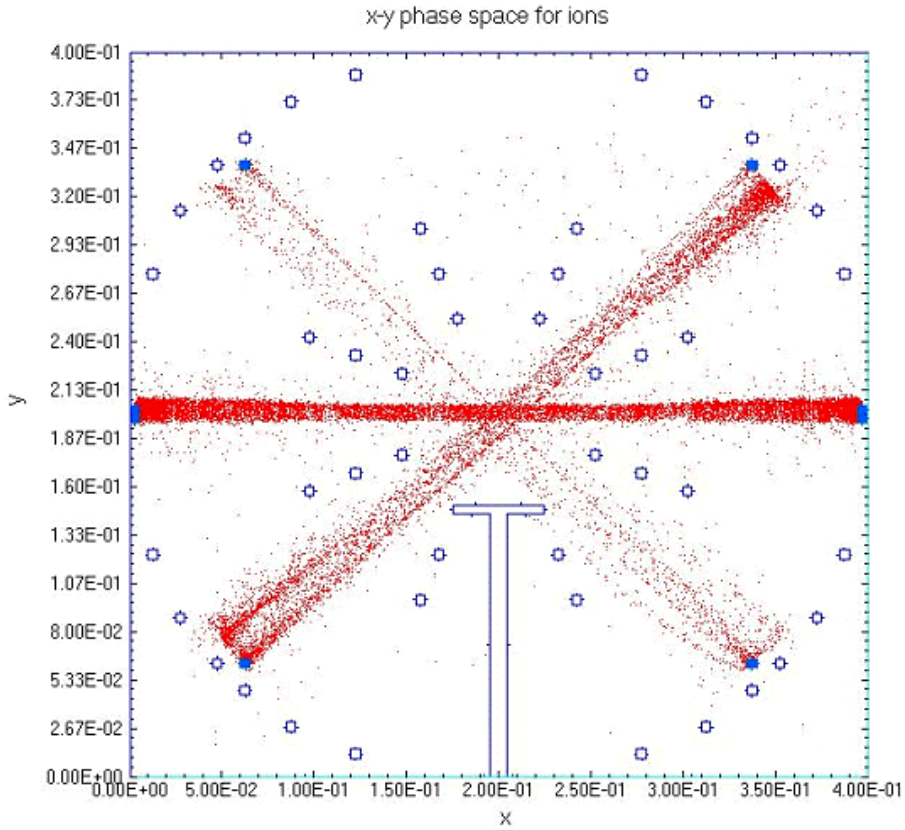

Figure 3.29 Triple grid IEC, OOPIC model, shows better confinement in all beams.

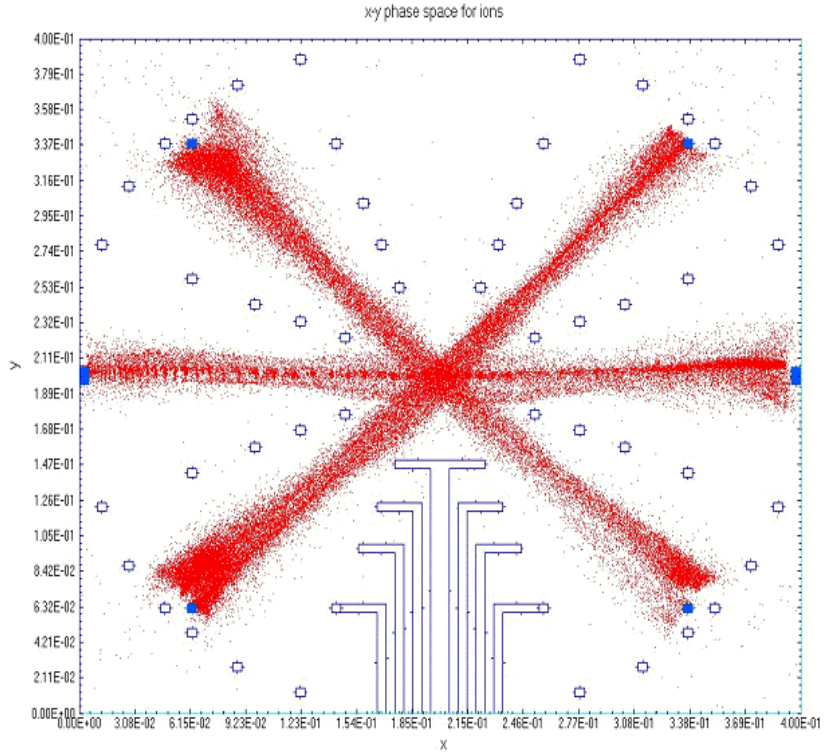

Figure 3.30 Quad grid IEC, OOPIC model, shows complete confinement.

The shielding effect can be seen more clearly on a plot of the potential. In Figure 3.31, the asymmetry caused by the high voltage stalk is clearly causing a sink for ions, causing them to 'roll' into the stalk instead of the device center. In Figure 3.32, observe how the additional grids localize the stalk disturbance, so that any given ion channel now looks more or less symmetric. Further, the field resembles more of a bobsled run as opposed to the 'bowl' potential assumed by an idealized spherically symmetric potential. These channels are still conservative fields, so they do not dissipate components of ion kinetic energy. They do, however, remove the restriction of conservation of angular momentum relative to the device center on the convergence of ion paths. The use of angular momentum conservation appears often in prior theoretical work on the space charge structures called 'poissors', and it is clear that conservation of angular momentum applies only far removed from grids as in a gridless system or possibly locally to the core. Further, the particular grid voltages shown result in a central potential much less negative than in the single grid case, but this is not a general result. Field penetration from the main cathode still lowers the central potential despite the presence of a decelerating innermost grid. The central potential can then be set to a desired value by adjusting the main cathode grid.

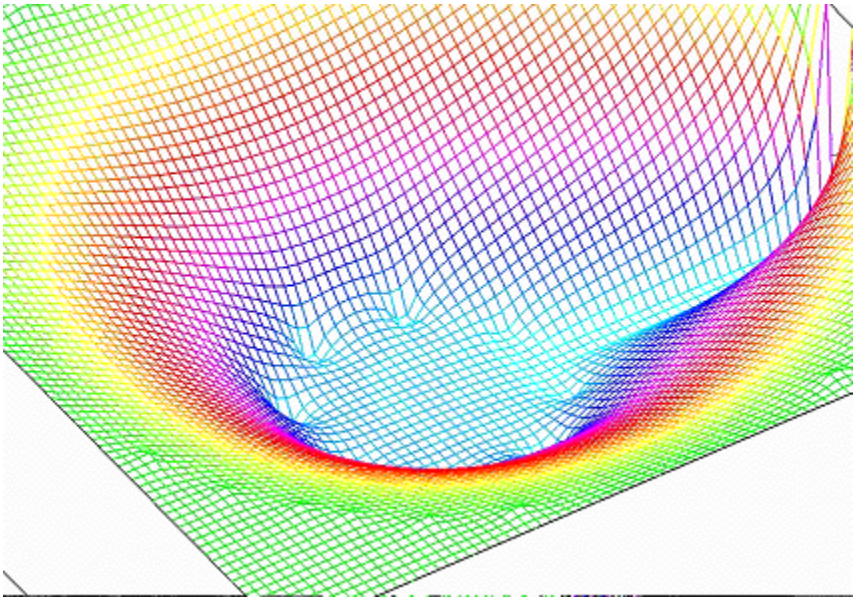

Figure 3.31 Electric potential for a single cathode grid IEC, OOPIC model

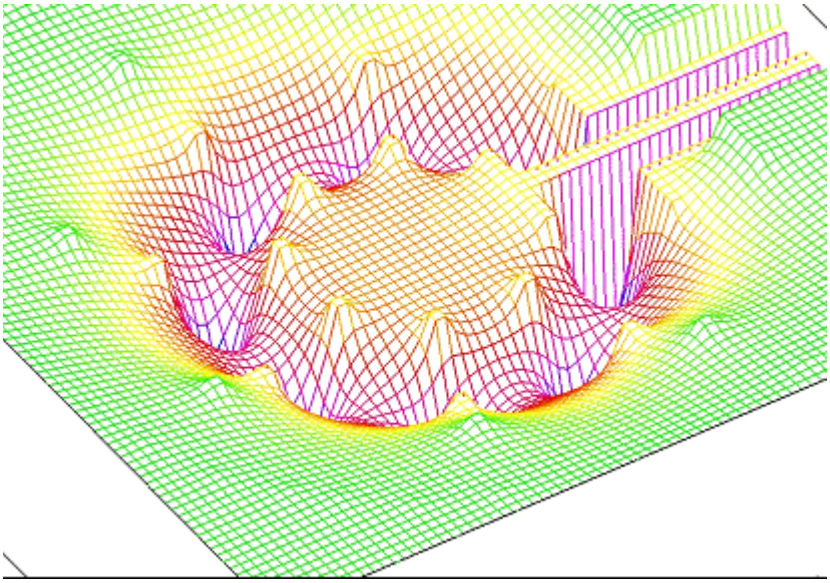

Figure 3.32 Electric potential for a multi-grid IEC, OOPIC model

Alternative confinement schemes

The potential set-up shown in Figure 3.32 is the baseline confinement scheme and will be used through most of this thesis. It features deceleration grids inside of and outside of the main cathode grid. Additional grids are added outside of the central assembly, with potentials above what would otherwise be the local potential. Finally, the

anode is represented by another grid as opposed to a solid wall. There are at least a few other options which will be discussed only briefly.

First is the 'anode trap' configuration. In this case, the innermost deceleration grid is removed so that the cathode grid is now on the inside. The rest of the grids are evenly spaced between the cathode and anode, each slightly above the local potential to form a focusing channel. The 'anode trap' provides good ion confinement, but does nothing to stop electrons streaming from the core. Further, high-angle scattered ions from the core impact the lower energy cathode as opposed to the decelerating grid at a higher potential. This means that these ions will cause a much larger power loss.

Another variation is the 'dual trap', which is basically the same as the baseline case, but the inner most grid is moved much farther out towards the anode. This has a couple of advantages, one of which is easier cooling for the cathode grid. It also has higher grid transparency due the relative size of wires compared to the grid opening. Most interestingly, the increased core volume for a given device size should make it easier to try and produce a confined electron cloud in the core. A confined electron cloud will behave as a gridless cathode, but it must be itself confined. The increased volume would make it easier to install electron guns or emitters at the device perimeter instead of jamming them into a compact core region. Also, the larger volume allows a lower electron density to achieve the virtual cathode potentials needed for accelerating the ions to fusion energy. This type of trap is not used for this thesis because the confinement properties were not as good as the baseline case. The longer drift region in the core makes the confinement properties more sensitive to the lens potentials. The baseline case was ultimately chosen because the increased confinement resulted in the collective

plasma behavior, and it was decided to study this phenomenon further. The collective behavior is characterized as a instability that results in the ions in the system bunching together and oscillating together so that each bunch reaches the center of the device at the same time. This phenomenon is termed synchronization in this thesis. Before discussing synchronization, we will further characterize the behavior of the multi-grid IEC OOPIC models.

Scaling of behavior with device size

One of the main questions we seek the model to answer is what ion densities can be achieved in the system. With the recirculation, the ion density gradually builds. This eventually stops as the ion space charge causes the ion trajectories to deflect into the grids. In many cases, the particles will bunch and eventually this pulsing can deflect particles into the cathode grids or even the anode grids. In either case, the steady state ion density mostly depends on the voltages and geometry, not the injection current. There is a dependence on the injection current, but it is much less than linear and will be explored in much more detail in the next section. The scaling of the device dimension is very strong, as smaller devices can support much higher ion densities for a given cathode voltage. This scaling is important as eventually one would like to optimize the device for fusion rate. For the investigation of size scaling it is enough for now to know that the bunching phenomenon creates a center density that oscillates in time, with a sharp maximum. This peak central ion density will be used as a characteristic density to compare three different device scale sizes. The first is the baseline device with a diameter of 40 cm, along with devices of 20 cm and 80 cm diameters. The time step must be adjusted accordingly, and the injection current is adjusted to produce steady-state

populations after about ten passes. A realistic reactor might trickle ions into the system to achieve higher lifetimes, but as will be shown in the next section, the highest density for a given system occurs when ions are 'flooded' into the system. The overall behavior of each model is similar, including the steady-state synchronization oscillations. The confinement properties for the different scales are similar and the core size thus roughly scales linearly with the device size. The density scaling is shown below in Figure 3.33. Assuming that the core, beam-beam reactions dominate in the low pressure regime, the reaction rate varies as the square of the density times the core radius cubed, as in Equation (2.8). The density scales as the inverse of the square of the device diameter, the overall beam-beam fusion rate scales inversely with device size.

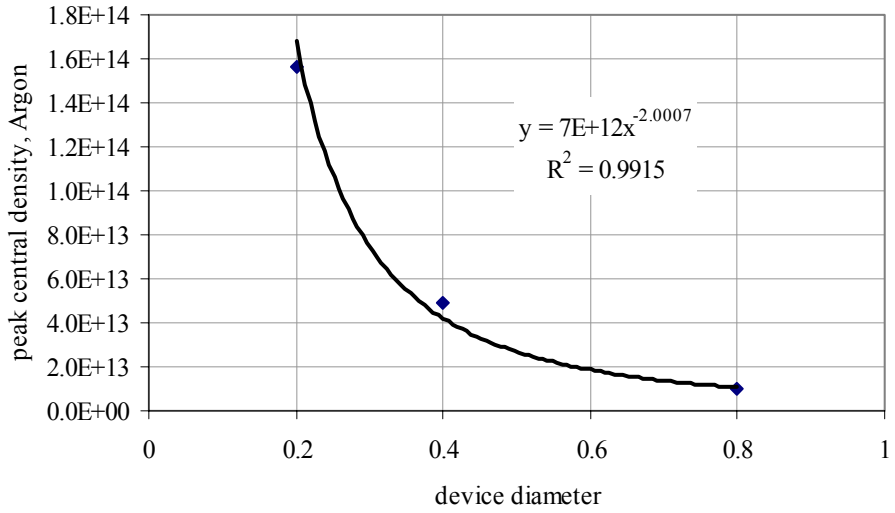

Figure 3.33 Peak central density versus device diameter for Argon, cathode voltage of -10 kV, central background voltage of -2.61 kV.

The above results show the highest density that can be achieved in steady state for any injection current. It will be shown in the following section that using a lower injection current reduces the peak density only slightly and shows more ordered behavior.

Scaling of long-term peak potential versus input current

Based on the above results, one might suppose that the steady-state ion beam density is limited by a total space charge limit. As ions are well-confined, they will simply recirculate and the ion beams grow in strength until a limit is reached. Different injection currents would just change the amount of time required to reach this steady state. This section describes a parameter study that tests this conjecture. In this study, both Argon and Deuterium ions are injected at various currents and the model run until a steady-state behavior is achieved. In all cases the system exhibits some degree of oscillations and bunching, so the peak central ion density is used as a convenient measure of space charge in the system. An understanding of the mechanisms by which the particles self-organize into bunches, what I call synchronization, is presented in Chapter 4. The general behavior is characterized by a bunching instability in the initially uniform beams. Bunches start off with small wavelengthes but gradually coalesce into larger bunches. At long times, the system settles into a system with 2 opposing bunches on each ion beam, moving so that they reach the device center at the same time, hence the term 'synchronization'.

Here we are simply interested in the steady-state behavior of the device. The time required to achieve the steady-state population level gives an estimate of the ion lifetime in the system. Diagnostic routines from the OOPIC program are used to plot and output time histories of various quantities, including the potential at any location in the device. The general behavior exhibited in this study is shown in the figures below and the results plotted for both species in Figure 3.38.

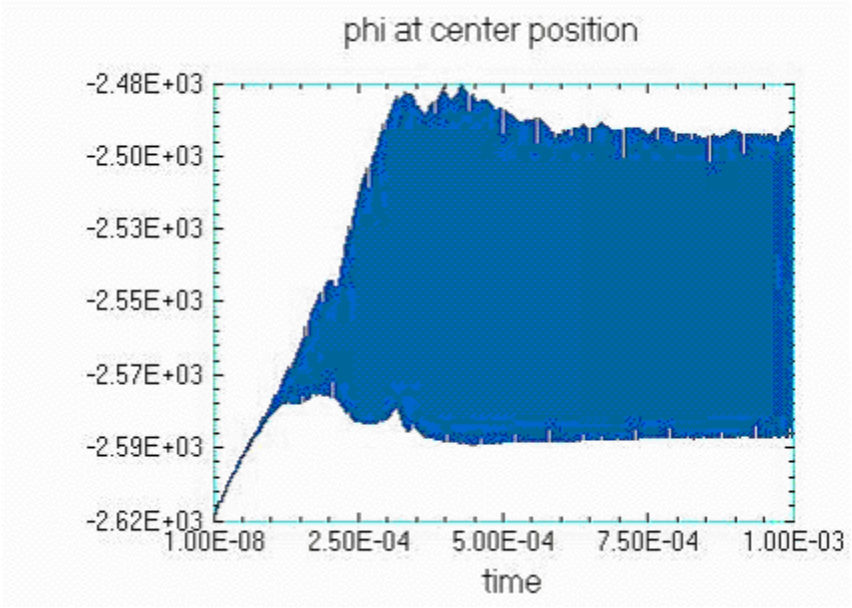

Figure 3.34 Central Potential in volts for low input current of 10 μAmp per beam for Argon.

The above figure is characteristic for low levels of constant injection of ions. The plot shows the potential in the device center as the charge in the system builds. Initially the value of the potential is that of the background fields and as ions build this value rises about 140 volts at peak. Initially, the space charge builds steadily, corresponding to the uniform beams growing in strength. As instability drives the system into the synchronized state, the space charge oscillates and the maximum and minimum is easily seen. At steady state, the frequency of this sinusoidal oscillation is the bounce frequency of individual ions in the system. The synchronization takes some time to develop, but settles into a steady state behavior at a rate that depends on the level of current injection. This rate dependency is explored in a following section. For a given level of injection, the peak space charge present in the device center is recorded. The value of the potential is less noisy, but somewhat harder to translate into a peak density so the charge density is used instead. At higher levels of injection a few things change. First, the steady-state is

achieved more quickly. Also, the peak density and potential are slightly higher. Figure 3.35 shows that increasing the current by a factor of ten from 10 to 100 microamps increases the central potential from 140 volts to 260 volts. This trend reaches a limit, however, as eventually the confinement becomes poor and the peak density starts to fall. One can see that in Figure 3.35 the oscillation envelope is much smaller than in the lower current case of Figure 3.34. As the current level increases, the ion lifetime decreases. Eventually the lifetime is short enough that a given ion doesn't have enough time to synchronize with the rest of the group before it is lost. Thus a significant portion of the ions are still in the 'uniform beam' state instead of the fully synchronized state. In the low current case, the oscillation minimum is close to the base background space charge level, indicating that almost all of the ions are synchronized. At very high injection currents, synchronization does not occur, but the instabilities violently eject particles from the system, preventing any recirculation of beam current. This realization is important for traditional IEC systems which have tried to reach high fusion rates with extremely high pulsed injection profiles.

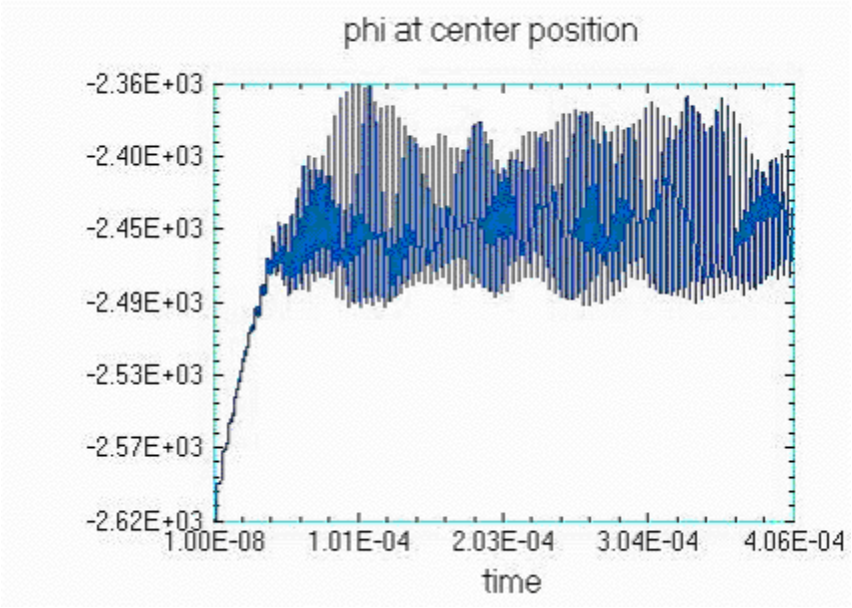

Figure 3.35 Central Potential for high input current of 100μAmp per beam for Argon.

To understand why the space charge puts a limit on the confinement of the system, observe the ion maps in Figure 3.36 and Figure 3.37. The first figure shows a relatively low level of ion injection of 1 milliamp per beam for a deuterium system. The system is in steady-state oscillations at 500 passes. The majority of ions are synchronized and the bunches are each near the anode in their respective beam paths. One can still see that some of the uniform beams are present. In this mode of operation, the dominant ion loss is at the anodes, where ions are upscattered on to the 'uphill' side of the injectors where they are lost.

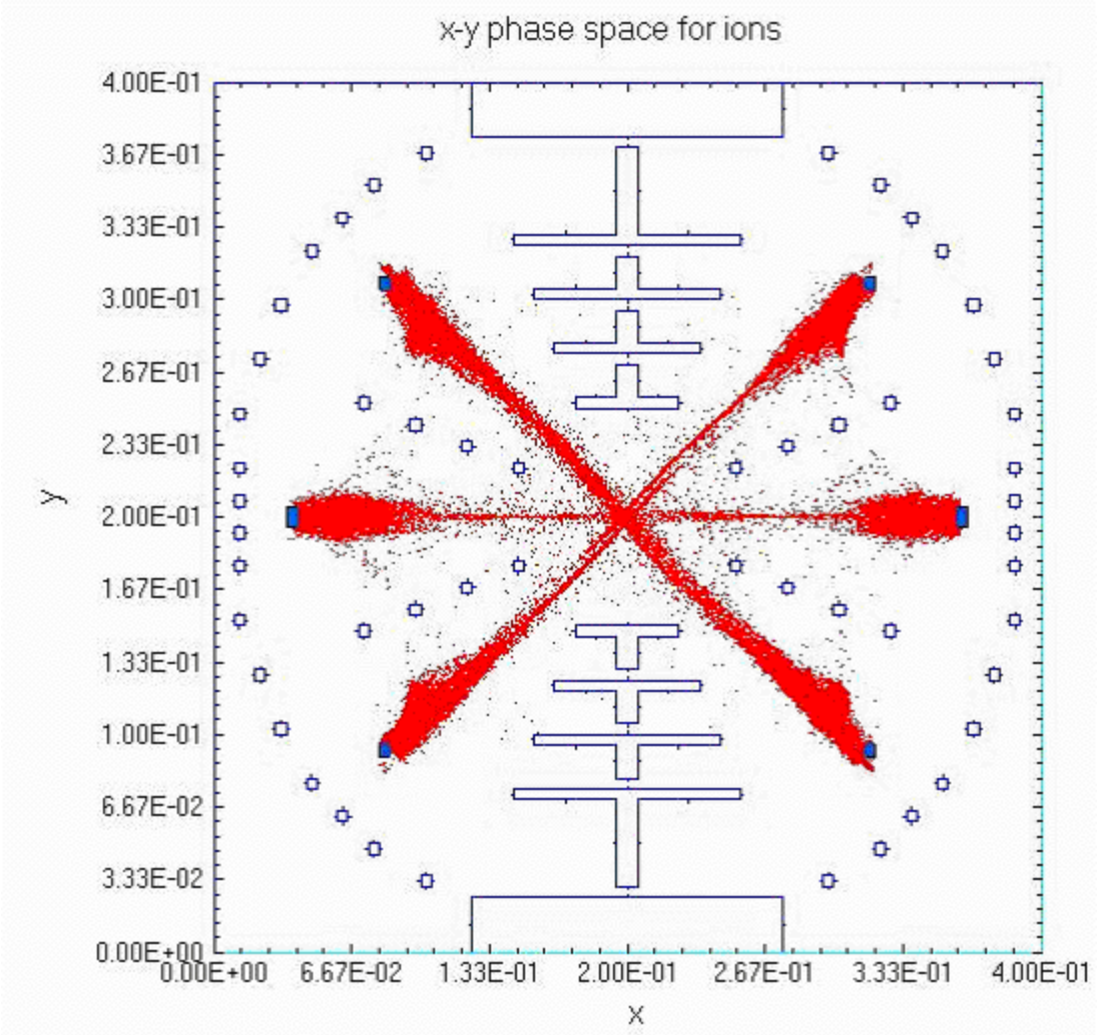

Figure 3.36 Ion map for low input current of 0.001 Amp per beam for Deuterium at 500 passes (steady-state behavior).

Losing ions to the injectors is much less problematic than having the ions lost to the minimum potential grid, which for this case is the second grid, set to -200 kV. Ions lost to the injector system represent a power loss on the order of their ionization energy, ~100 eV. This is a three order of magnitude difference in the main power loss of the system. The high current case is shown below in Figure 3.37.

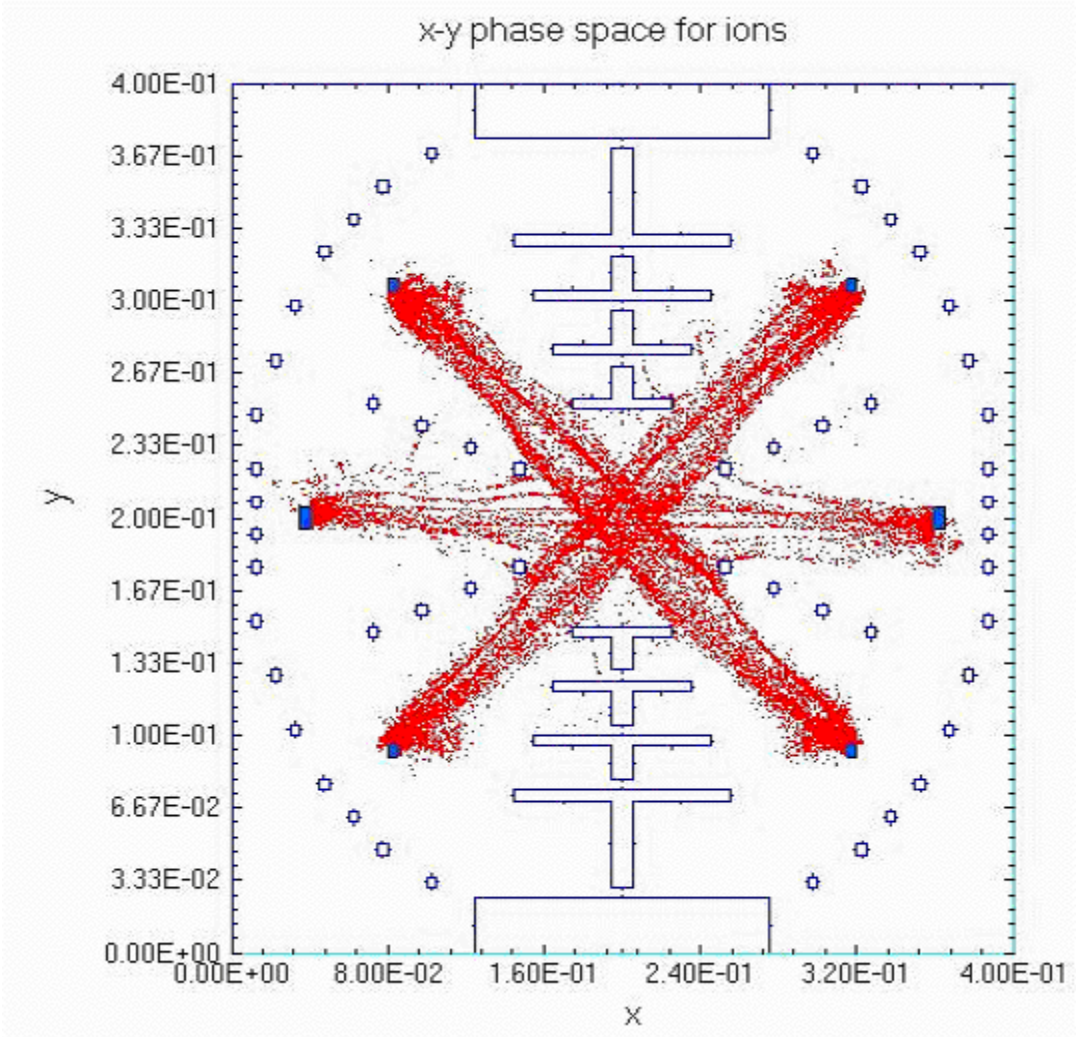

Figure 3.37 Ion map for high input current of 0.1 Amp per beam for Deuterium at 50 passes (steady-state behavior).

One can see that the system is generally less ordered. The ion beams through the center of the device have filamented, so that the ions no longer recirculate through each other. This 'two-lane road' is less efficient at packing charge into the ion channel as the two filaments push each other apart. This increased beam width causes the ions to impact the innermost grid, so that the average ion is lost at this energy. For the study here, this grid is set to -40 kV, considerably higher than the cathode which is set to -200 kV. So not only is the total density in the system less at high currents, the ion power losses are

much higher. These trends are shown for Argon and Deuterium in Figure 3.38. Keep in mind that the voltages for the Argon and Deuterium cases are considerably different in magnitude, but the potential distribution among the grids is essentially the same, resulting in similar confinement behavior. The Argon runs were limited to -10 kV, characteristic to laboratory experiments at MIT. The Deuterium runs were run at much higher voltages of -200 kV, characteristic of eventual fusion reactors.

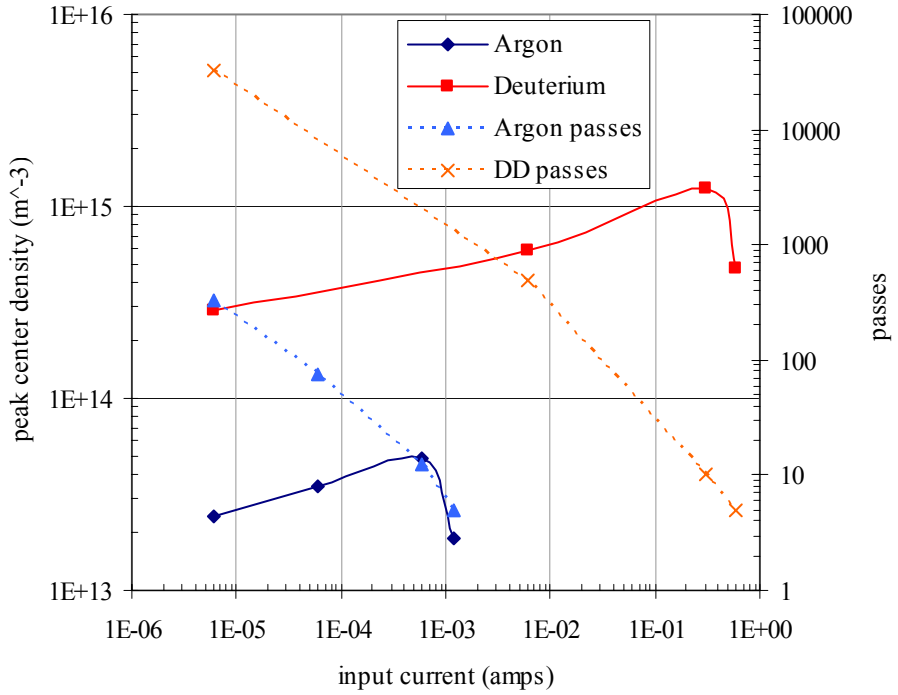

Figure 3.38 Steady-state center peak density in m^{-3} and confinement time in passes versus input current in amps for Argon and Deuterium

The density versus input current for deuterium peaks near a total injection current of only 0.3 amps. The peak density at lower currents scales as '$i^{0.13}$'. The peak lifetime measured in number of passes varies as '$i^{-0.76}$', a lower power law than the inverse linear relationship one might expect. The data on the left side of the chart becomes increasingly difficult to collect, as the simulation time becomes very large. The Deuterium model for

6 μAmp total injection reached steady state at 33,000 passes, ~13.3 million time steps and 2 weeks of continuous computer time. Patience and computing power thus become the driving factors in obtaining simulated lifetimes longer than this with the current OOPIC models. Argon is included as it is the gas of choice for follow-on laboratory testing. Interestingly, the peak density for each species occurs when that species executes 10-20 passes. The lower densities for Argon are mainly due to the difference in voltages. In any case, the trends are clear and can be used to estimate the fusion rate for deuterium plasma in the synchronization regime.

Fusion rate estimates, density pulse shapes

Before a rate can be estimated, the pulsed nature of the core ion population must be addressed. With operation in the low-pressure regime, beam-beam reactions in the core will dominate the fusion reaction rate. The steady-state density pulse shapes in the core for the deuterium cases are shown in Figure 3.39 and Figure 3.40. The core rate depends on the square of the density. The integrated value of density squared is calculated for the low and high current cases and compared to the value of the peak density squared in these two cases. The pulse shape is slightly different between the two. The high input current case in Figure 3.39 looks more like a sawtooth waveform and has an average to peak ratio of 33.5%. This ratio simply multiplies the peak density squared to get the average core density squared. The low current case in Figure 3.40 shows a more symmetric sinusoidal pulse shape with a ratio of 26%. As a conservative estimate, the lower ratio of 26% is used for the fusion rate estimate.

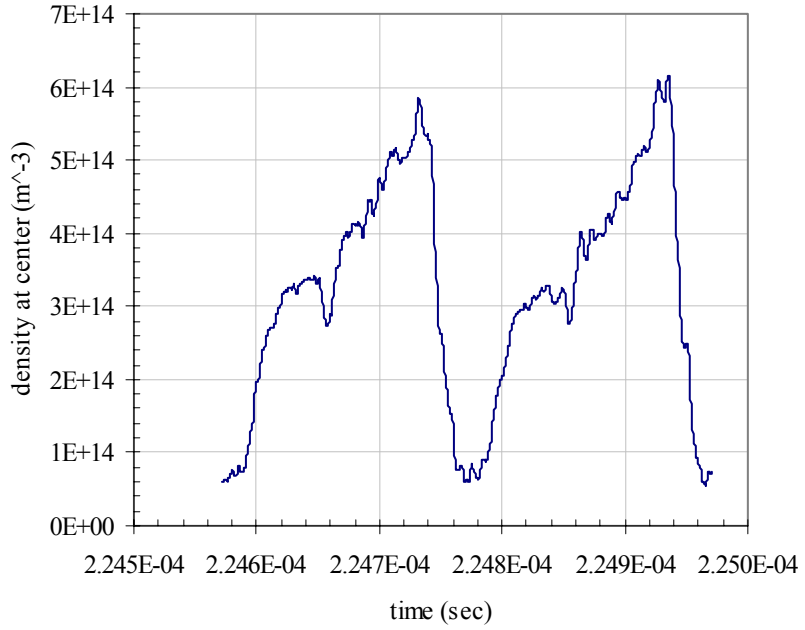

Figure 3.39 DD steady-state fusion test, 1 milliAmp injection x6 beams, 33.5% average to peak n^2 ratio, ~500 pass lifetime.

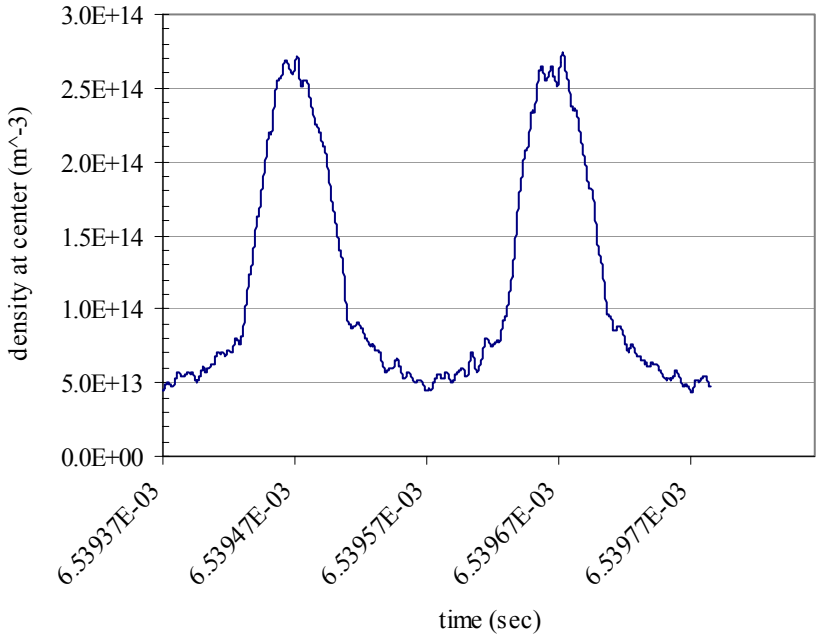

Figure 3.40 DD steady-state fusion test, 1 microAmp injection x6 beams, 26% average to peak n^2 ratio, ~33,000 pass lifetime.

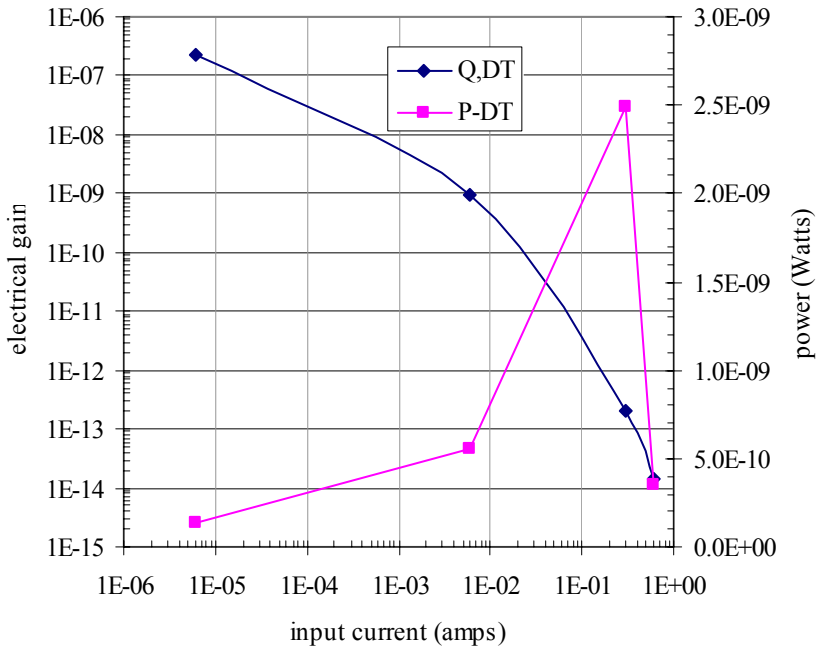

Figure 3.41 Projected DT fusion gain and electrical power production versus input current, 40 cm diameter device with -50 kV central potential.

Equation (2.8) is used to estimate the core fusion rate. The core radius is observed from the OOPIC runs to be about 1 cm for the device size of 0.4 m diameter. The core averaged value of the product of the fusion cross-section and velocity is taken as 10^{-21} m^3/sec for DT from Figure 2.5. The peak density values for the Deuterium runs are used to approximate the DT plasma behavior. Electrical conversion efficiency between thermal and direct conversion was chosen as 50%. Further, the pulsing factor of 26% is included. One can compare these results to the analytical model results of Figure 2.10 and observe that the predicted rates are much lower than the analytical model. This is mostly due to the differences in core size and cathode radius, which combine to give a smaller fusing volume in the OOPIC estimate. Also, the OOPIC estimate does include contributions from the spokes, which was shown to be significant in Chapter 2. The

fusion rate is shown to peak at a few nanoWatts and then fall off slowly as input current is reduced.

The fusion gain is calculated simply in Figure 3.41 as the ratio between the fusion electrical power produced divided by the ion power loss. The electron losses are assumed to be small in this configuration. The ion power loss for the two higher injection currents of 50 milliAmps and 100 milliAmps is assumed to be 40 keV per ion, as ions end up hitting the innermost grid held at a potential of -40 kV. The two lower input current cases of 1milliAmp and 1 microAmp assume a power loss of only 100 eV per ion since ions in these cases end up impacting the injectors. These injectors are near ground, so the only power loss is the ionization energy required to produce them given a 100% efficient gain. One can see that the power gain increases dramatically as the current is reduced, with the roughly the same scaling as the ion lifetime. There does not appear to be any barrier to increasing the ion lifetime and fusion efficiency by reducing the input current to a mere trickle. This makes sense, since in an ideal system, new ions would be introduced only as the old ones fuse.

The prospect of a break-even fusion reactor is fabulous, but the fusion rates shown above are unimpressive. Some improvement could be made by reducing the overall size of the device as discussed earlier, but this becomes very difficult due to the complexity of the grids and the high voltage gaps. In order to make useful amount of fusion however, the densities must be increased. For the near-term application of IECs for portable neutron production, one could run in a 'hybrid' mode. By operating at a background gas pressure in between the ultra low pressures assumed above (10^{-10} Torr) and the pressures used in IECs operating in the glow discharge regime (10^{-3} Torr), the

rates can be increased by beam-background collisions, but with at least an order of magnitude improvement in confinement time so that the devices are more electrically efficient. The remainder of this thesis will investigate the physics behind the synchronization phenomenon so that it can be exploited fully.

Chapter 4 Synchronization

Before we begin, let me detail the organization of this somewhat lengthy chapter. The first section describes the synchronization phenomenon as observed in particle-in-cell simulations. The remaining 4 sections seek to build an overall understanding of the phenomenon. The second section describes prior experimental, numerical, and analytical work by other researchers on a similar system. The third section derives the two-stream instability and applies the lessons learned to understand the initial growth of the phenomenon. The fourth section describes a 2-body collision model which is used to shed light on the microscopic processes which are responsible for the synchronization not only on a single beam but any crossing beams. Information gleaned here is used to estimate how quickly the system progresses from its initial uniform state to the saturated, synchronized state. The last section describes an N-body model in order to understand how bunches of particles on many different beams can all become synchronized together. This model shows and quantifies how synchronization breaks down at too low and too high densities. All together, the chapter's purpose is to build an understanding of the phenomena observed in the numerical experiments.

4.1 Synchronization in OOPIC models

In the OOPIC models, the simulation begins as ions are injected into the device. The beams are initially well-confined and as they reflect and circulate, the density of each beam grows. As the density grows large enough, the individual uniform beams break up

into many bunches which counter stream through each other. Eventually these coalesce into 2 opposing bunches for each beam line. On a slightly slower time scale, bunches on each separate beam path become synchronized with all the others. If the injection is terminated, the stable state is then 2 opposed bunches per beam line with all bunches collapsing into the device center at the same time and reaching the anode at the same time. The amount of time required for this process varies according to the input current level and can occur as quickly as 25 passes. At higher densities, particles are first ejected from the simulation by a violent instability and then the bunching develops at about the same rate. The progression from uniform beam to totally synchronized bunches is shown graphically in the following figures.

Progression of instability on equatorial beam

Figure 4.1 shows how waves travel back and forth along the equatorial beam. The charge density (Cm^{-3}) along the equator is plotted for consecutive time steps, over a tenth of a pass. The various plots show snapshots as time advances up to 50 passes. In these plots the presence of the diagonal beams is evidenced by the central spike caused by the overlap of the beams.

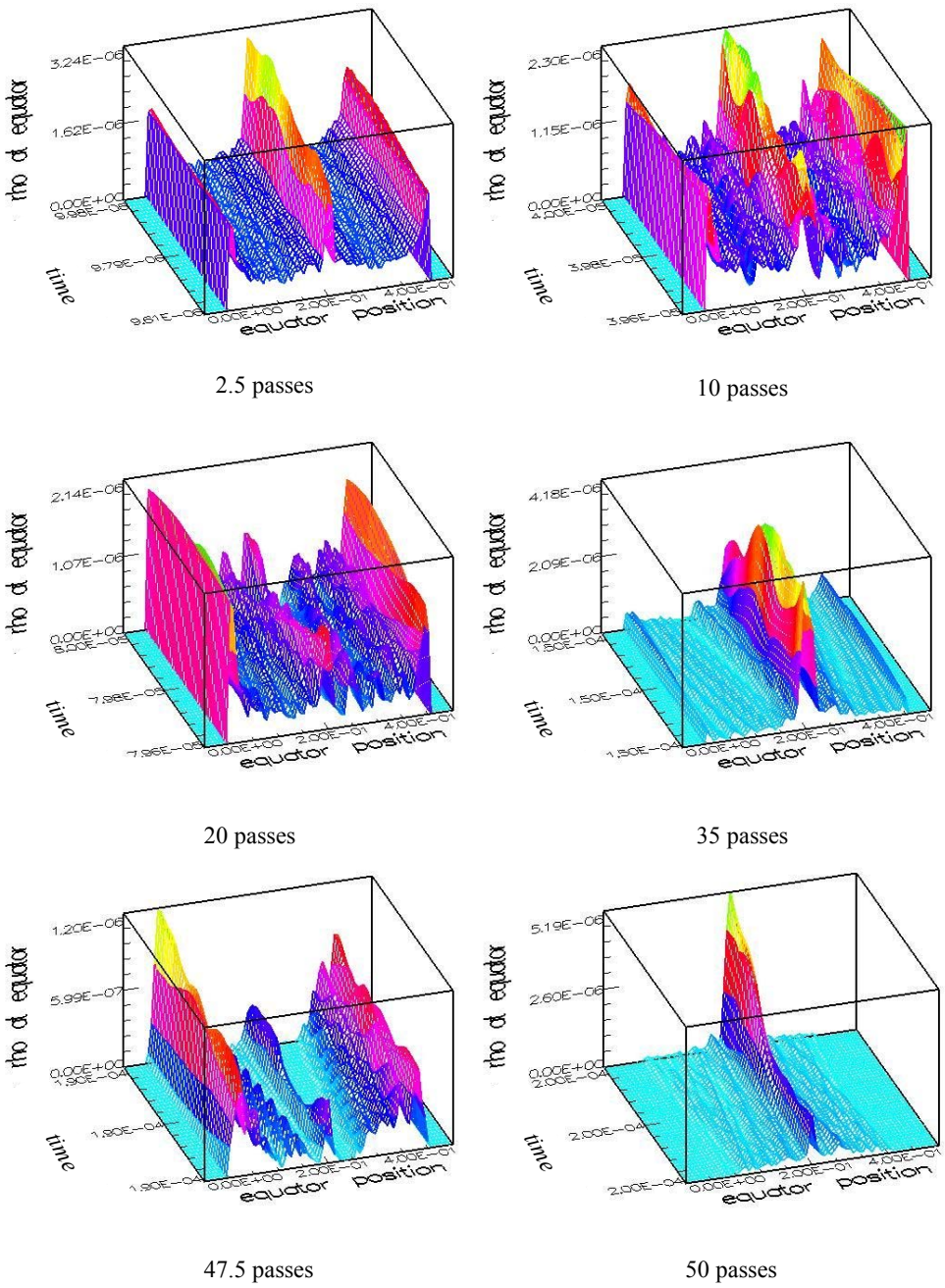

Figure 4.1 Progression of synchronization, localized space charge (vertical axis) vs. equatorial position vs. time. Each tile spans a tenth of a pass in time and plots the space charge specifically along the equatorial beam line.

One can see that early on after an elapsed time of 2.5 passes, the density profile looks as one would expect. At the anodes there are peaks due to the low velocities, and at the center there is peak due to the overlap of the diagonal beams and the equatorial beam.

Waves traveling along with the beam are visible as ridges in the acceleration region between the edges and the central peaks. Injection is terminated at the 5 pass mark, and ions just recirculate inside the system after this time. At the ten pass mark, there are still peaks, but the waves have grown considerably in strength. By 20 passes, the bunching has grown strong enough so that the central peak is almost gone, indicating that the beams are no longer overlapping, uniform beams. The synchronization continues to grow stronger so that by the 50 pass mark, the central peak easily dominates the density profile as the bunches pass through the center of the device. Also, the waves are reduced in strength relative to the main bunches since the smaller bunches have conglomerated into a synchronized pair of ion bunches for each beam, all colliding in the device center simultaneously.

Progression of instability on diagonal and equatorial beams

A more intuitive picture of this process is shown in Figure 4.2, where the ion positions are plotted every 2.5 passes, from the beginning of injection to 50 passes. A relatively high injection current is used to illustrate a fast progression from the uniform to synchronized state. The well-ordered beams in the first tile become considerably 'thicker' and filamented in the second tile, which coincides with injection termination. The filamentation of a recirculating ion beam is observed at high injection currents and forms when the reflected beam has enough space charge to repel the oncoming beam. The pair of filaments then spread out across the ion channel much more than the individual beams otherwise would. Regardless of filamentation, smaller bunches are soon seen to form and gradually give way to the final state of two opposing bunches on

each beam path. The last two tiles show the synchronized state in its steady form with the bunches all at the anode and the device center, respectively. One can also see that the shape of the bunches is roughly spherical at the anodes and stretched into elongated ellipses in the device center.

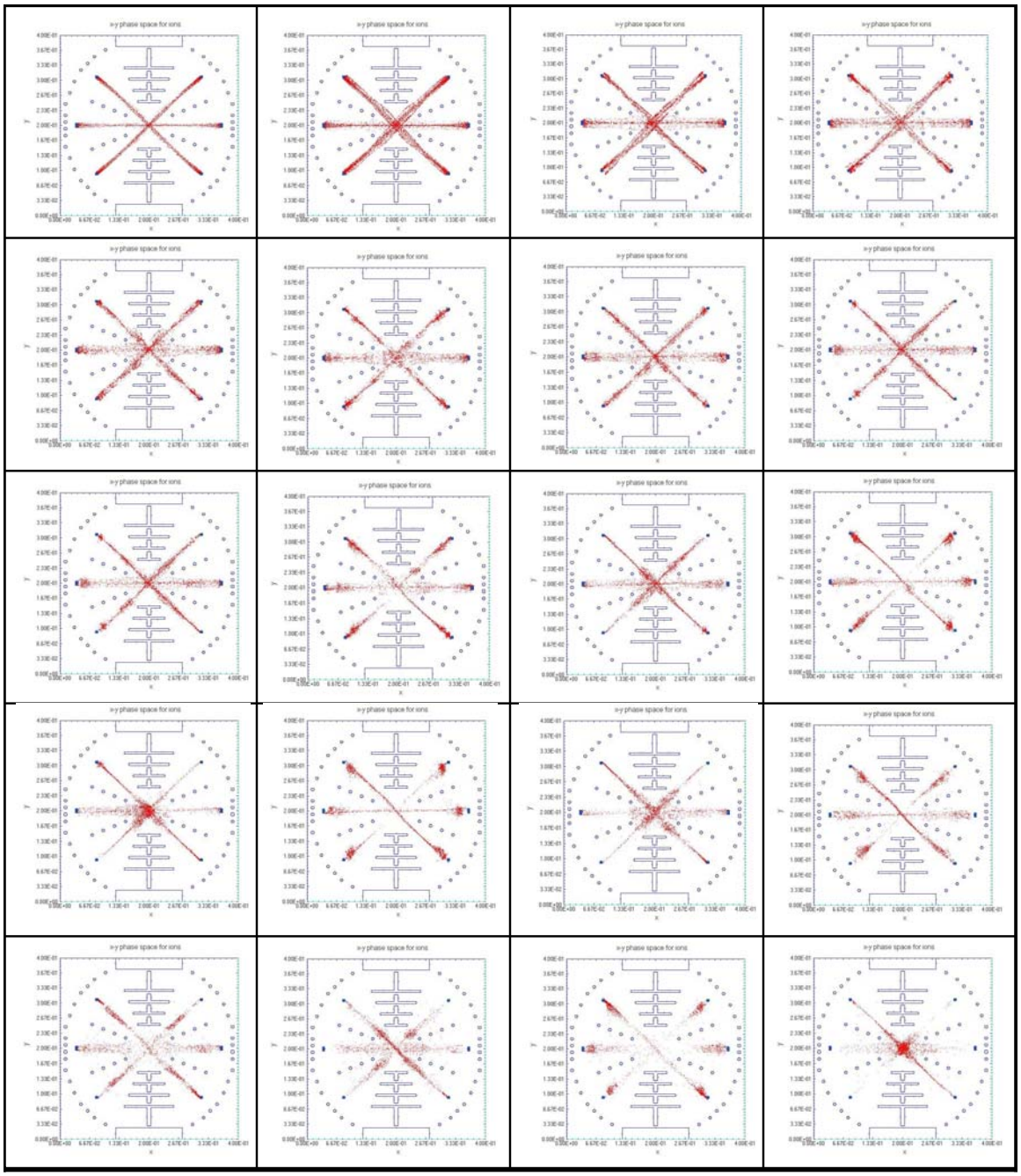

Figure 4.2 Progression of synchronization, ion maps. Starting in top left, time runs left to right, with each slide jumping about 2.5 passes forward, covering 50 passes total.

The synchronization effect is seen in almost all of the OOPIC simulations which have increased ion confinement. The exception is at very low ion injection currents and densities, where the beams are observed to be well-ordered and recirculate and grow in density for as long as injection is continued. The boundaries for the onset of the phenomena and the growth rate as a function of density are examined next.

Growth Rates for OOPIC simulations

The OOPIC model can be set up to allow measurement of the growth of the overall bunching. The standard model of 6 injectors on 3 beam lines is used here, with the injection continuing for only 5 passes. This brief period of injection serves to load the particles in a realistic manner without lasting long enough to confuse the injection and the instability processes at fairly high densities. Since we would like to try to measure the progress of the instability, it is better not to have brand new particles being injected while the existing particles have had many passes to interact. The input current is varied between runs as the most direct way to control the beam densities. In each case, the simulation is allowed to run for 100 passes, or $4 \cdot 10^{-4}$ sec. The quantity measured to determine growth is the potential above the background, measured in the device center, where the beams overlap. An example run is shown in Figure 4.3 for an injection current of 15 μAmp per beam.

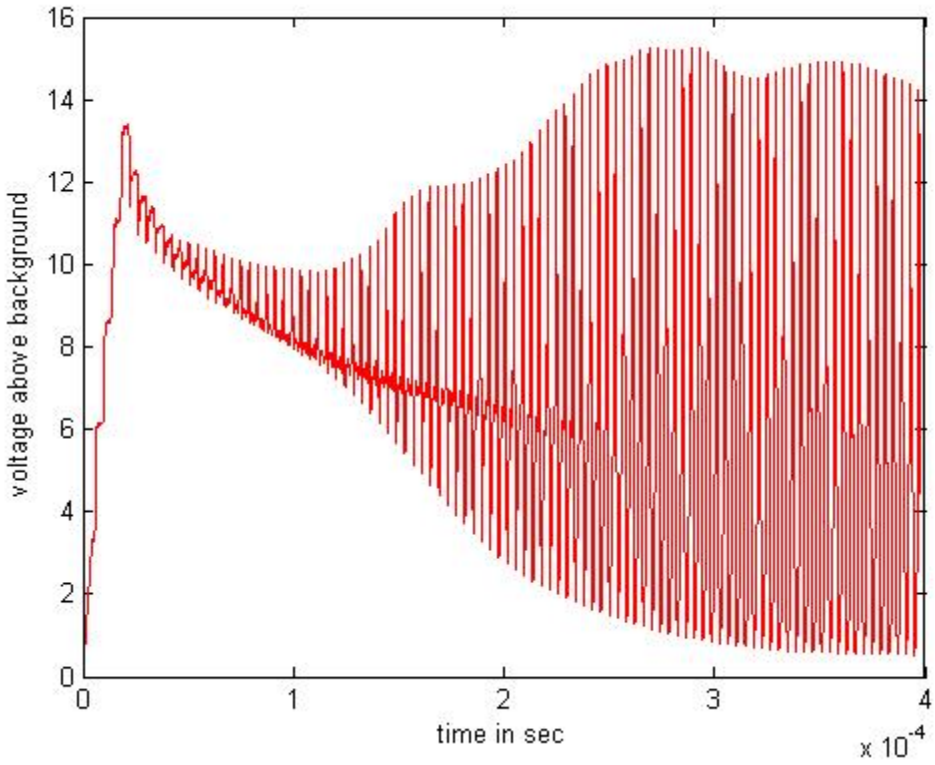

Figure 4.3 Central potential above background vs. time for 15 μAmp per beam

The potential trace is somewhat noisy, but the overall envelope between local maxima and minima is easily visualized. The oscillations are clearly more complex than a simple sinusoid, and this will be examined further later in the chapter. For now, though, we are concerned with the overall strength of the bunching. A zoomed in view of the above trace is shown in Figure 4.4. Observing that the actual data trace in red shows an overall periodicity at the bounce frequency, a moving window at this period is used to define local maxima and minima. The average of these two values at each time point gives a measure of the average beam strength in the device center. The difference between the maxima and the average, divided by the average value gives the percentage strength of the overall oscillation. The growth must be normalized to the average value since particles are continually being lost from the system so the 'baseline' density is

reduced with time. When this ratio reaches 1, or 100%, the bunching will be completely dominant and the uniform beams will have essentially disappeared. This ratio is plotted versus time in the lower plot of Figure 4.4. A complete time history is shown in Figure 4.5.

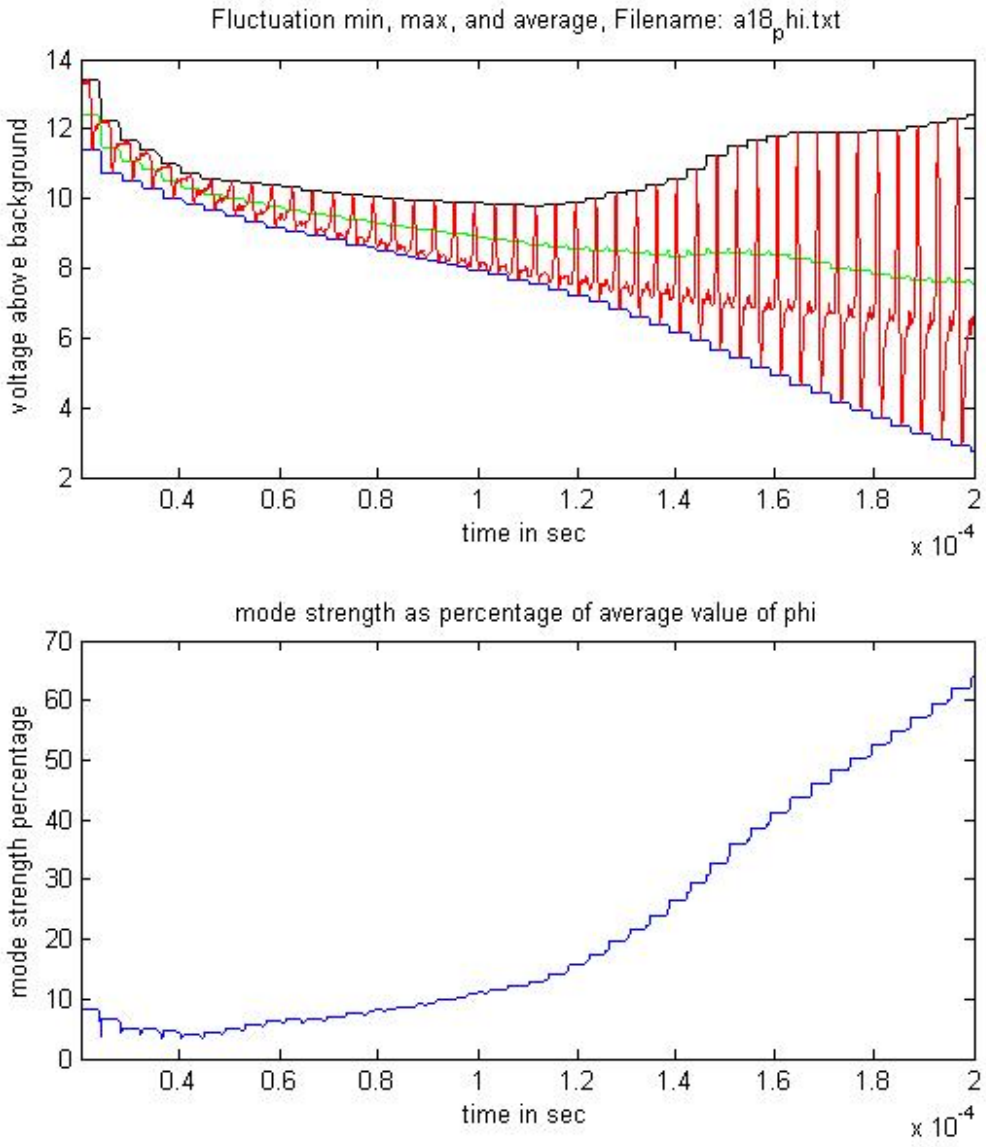

Figure 4.4 Zoomed view of central potential trace for 15 μAmp case. Top: red curve is the actual trace, green is the average curve, black is the maximum curve, blue is the minimum curve. Bottom: relative strength of fluctuation vs. time.

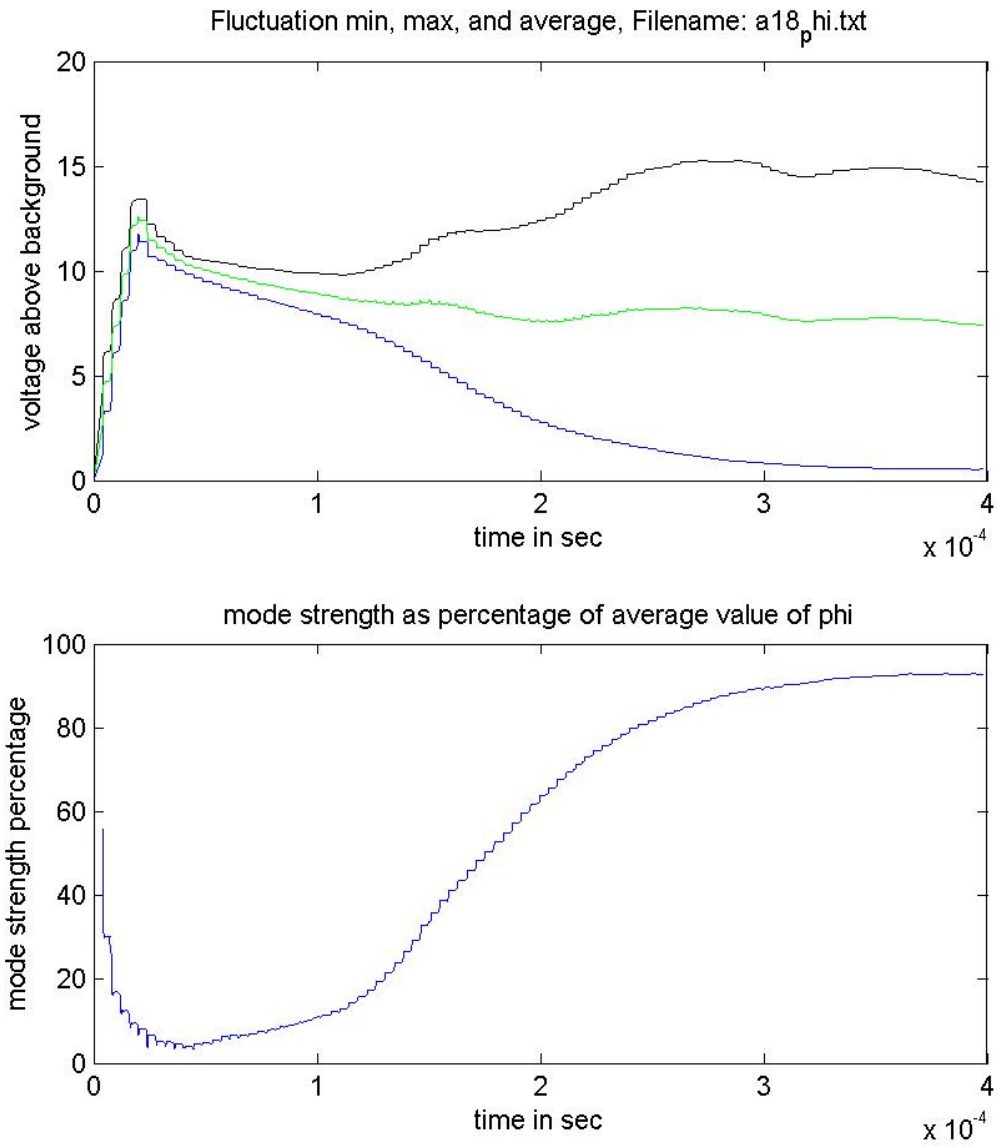

Figure 4.5 Central potential trace for 15 μAmp case. Top: green is the average curve, black is the maximum curve, blue is the minimum curve. Bottom: relative strength of fluctuation vs. time.

The growth trace in Figure 4.5 is characteristic of the various runs. Ideally, the trace would start at zero growth and some initial growth period could be used to estimate an exponential growth rate. As shown above, the injection process confuses our zero, and the growth rate isn't exactly exponential or linear since it levels off. It saturates as

we would expect at long times. The compromise chosen is to calculate an average linear growth rate using the time elapsed between mode strength of 10% to 60% as an approximate to an exponential growth rate. This works reasonably well for most data points, but at low and high densities, the situation becomes more complex. The percentage increase per pass is plotted as a function of the input current per beam in Figure 4.6.

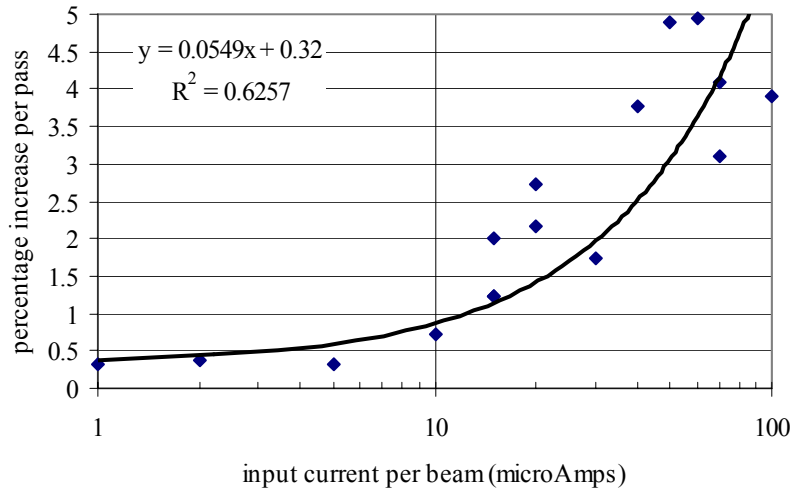

Figure 4.6 Growth rate vs. input current per beam

At very low densities, the growth rate calculated by this method does not disappear as expected. The growth rate tends to bottom out at a value of 0.32% per pass. While this is curious, the beams remain quite uniform and not bunched. The signal is just a result of a residual signature from the injection process and the general particle decay over time. The residual signature from the stepped injection and injection termination tends to remain constant, while the overall particle number is dropping in time, getting weaker.

Runs at high density on the other hand show violently unstable growth of the bunching modes. Instead of actually bunching more quickly, particles are expelled from

the system due to the violent instability. Particles are ejected until the density is reduced to a density plateau and bunches then grow as for lower densities. The growth rate is observed to plateau at about 5% per pass, which stands to reason since this is the growth rate for the cases with the same particle density after ejection.

The growth rate data from this method is quite noisy with a significant spread in results for multiple runs of the same initial conditions. Nevertheless, a clear trend can be seen. In order to later relate these results to the 2 stream instability models, the beam density is found for a given input current. This is somewhat problematic since the beam density varies significantly between the anode, cathode and central overlap regions. A value of density taken in the acceleration region should be characteristic of the individual streaming beams. The charge density vs. equatorial position for the 20 μA case is shown in Figure 4.7, where the horizontal axis spans the device diameter of 40 cm. The anode and central spikes are clearly visible, and the acceleration region value of charge density is blue.

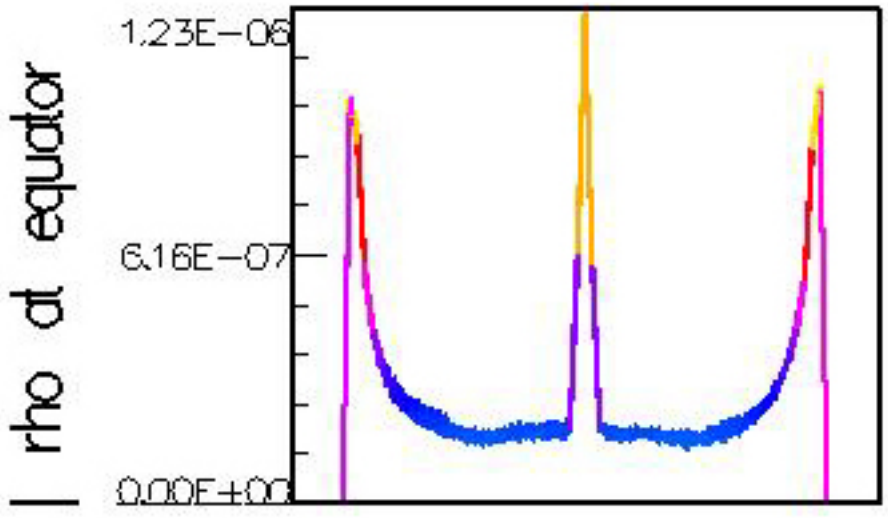

Figure 4.7 Equatorial charge density (Cm^{-3}) vs. equatorial position (spans 40 cm) after 5 passes with 20 μA injection.

Several of the data runs were used to compute an average value for this factor. The growth rate data in Figure 4.6 can thus be related to beam density by a factor of $5.6 \cdot 10^{10}$ $m^{-3}/\mu Amp$, and these data are included in Figure 4.31.

This analysis only examined the growth of the overall instability. The role of higher order bunches and the progression from uniform beams to fully bunched motion is examined further using Fourier transform analysis of the central potential data.

Fourier transform analysis of synchronization

Ideally, we would like to know exactly how the system transitions from the uniform beam state into the stable steady-state oscillations. The behavior is simply too complex to answer this question by merely watching the ion motions over time. A discrete Fourier transform analysis was used to peer through the noise and complexity. The Fourier analysis is able to identify the unstable modes and compare the relative frequencies of those modes at different times. Observations of the OOPIC models suggested that higher frequencies would be fairly strong initially, eventually giving way to a dominant mode at the bounce frequency of ions in the device. In order to assess this, the electrostatic potential in the device center is recorded at every time step in the OOPIC runs. The unstable modes show up as oscillations above the background potential due to the space charges in the local vicinity of the device center. The measurement of the central potential inherently provides a more smoothed signal than the actual ion density in the device center. A characteristic OOPIC run was chosen with 6 ion guns each injecting singly-charged Argon ions at 10 μAmps for $1 \cdot 10^{-4}$ sec. This injection profile

yields relatively uniform beams at the termination of injection with an anode density of about $2.5 \cdot 10^{13}$ m^{-3} and a peak central density of about $1.2 \cdot 10^{13}$ m^{-3}. Four cathode grids are used. Starting with the outer grid moving inward, the voltages on the grids are: -200, -2000, -10000 volts, and -2000 volts. The anode grid is held at 100 volts. The system of grids results in a one pass period of $4 \cdot 10^{-6}$ seconds. This bounce period corresponds to a frequency of 250 kHz. The injection is then terminated at $1 \cdot 10^{-4}$ sec, about 25 passes, and the simulation is allowed to continue to $4 \cdot 10^{-4}$, about 100 passes total. The time step of $1 \cdot 10^{-8}$ sec gives 40,000 total time steps. The complete time history of the central potential is shown below in Figure 4.8.

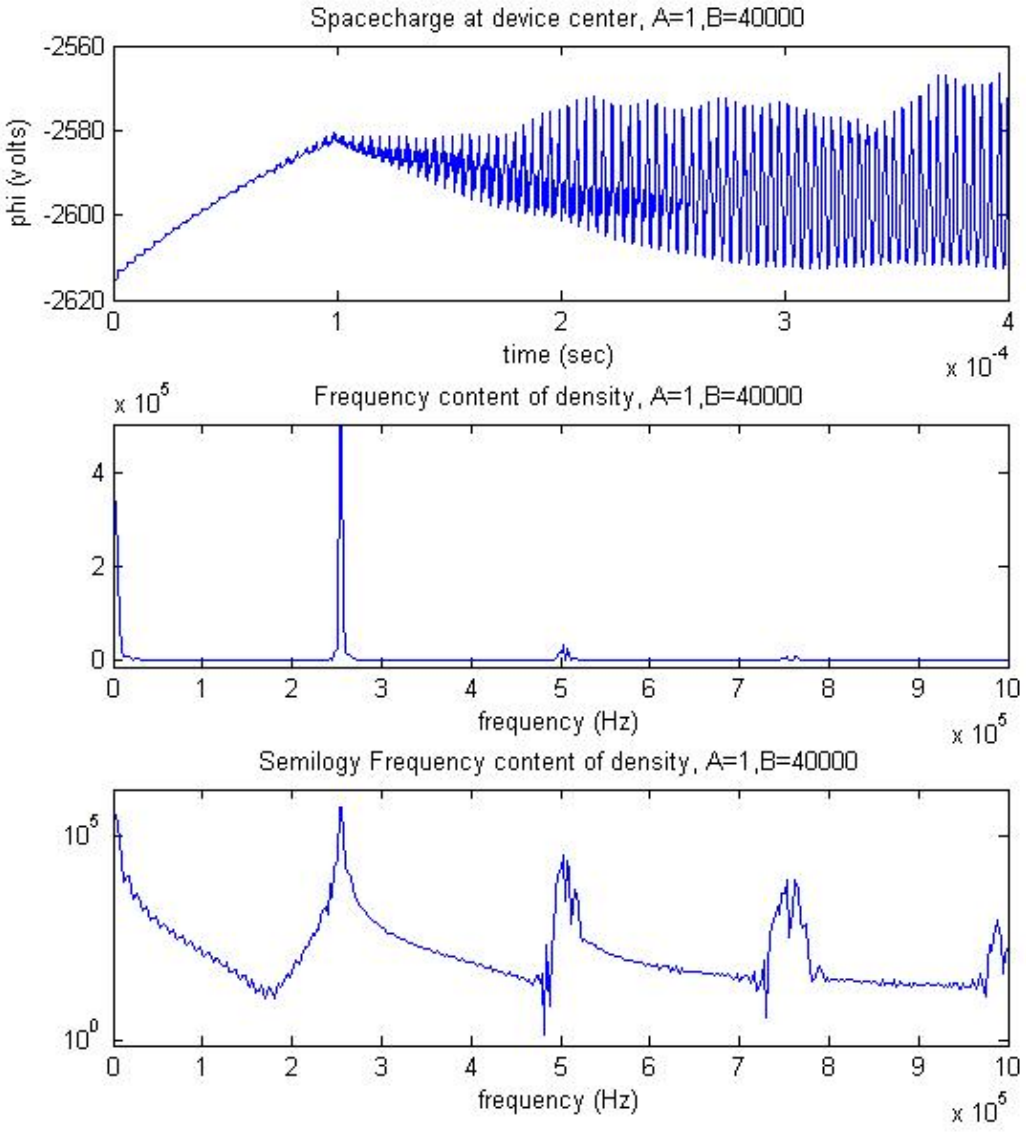

Figure 4.8 Data for characteristic OOPIC run, 6x 10 μAmp injection for $1 \cdot 10^{-4}$ sec. Top: central potential (volts) vs. time. Middle: FFT of central potential from t = 0 to t = $4 \cdot 10^{-4}$ sec (100 passes). Bottom: semilog plot of FFT in middle frame

The top pane of Figure 4.8 shows the central potential building in an almost linear manner with time until the injection stops. The instability builds and completely dominates by the end of the run. A discrete FFT of this entire time history is shown in the lower two panels. The strongest mode is at 250 kHz and shows evidence at higher

harmonics with the strength decreasing with higher frequencies. There are more spikes at even higher frequencies, but all are at harmonics of the fundamental bounce frequency and are progressively weaker. There is also a significant spike at zero frequency which is due to the transient rise in signal due to injection. When a smaller time window is used outside of the injection regime, this zero frequency signal disappears. The specific response at harmonics of the bounce frequency suggests that the device size indeed provides a significant boundary condition on the allowed oscillations in the system.

The development of the synchronized state can be seen by looking at smaller time windows. The initial 5 passes are shown below in Figure 4.9.

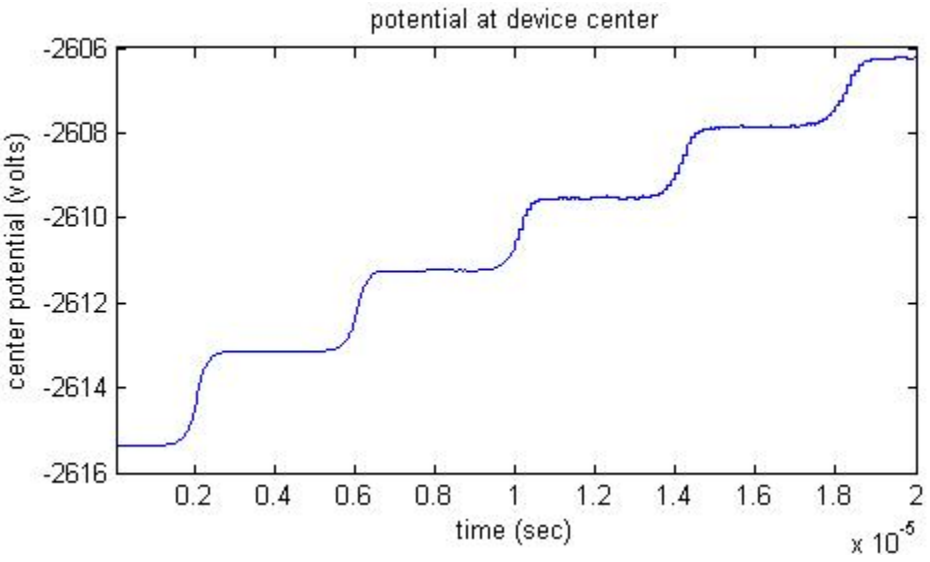

Figure 4.9 Central potential (volts) for characteristic OOPIC run, first 5 passes

Notice that the central potential initially follows a stepped profile and exhibits very little noise. Each pass initially increases the central potential about 2 volts over the background. Also notice that the step is somewhat smoothed since this is a measurement of potential not density. The instability in the signal gradually builds and by the time the

injection is terminated the instability is strong enough to grossly distort this step pattern, as shown in Figure 4.10.

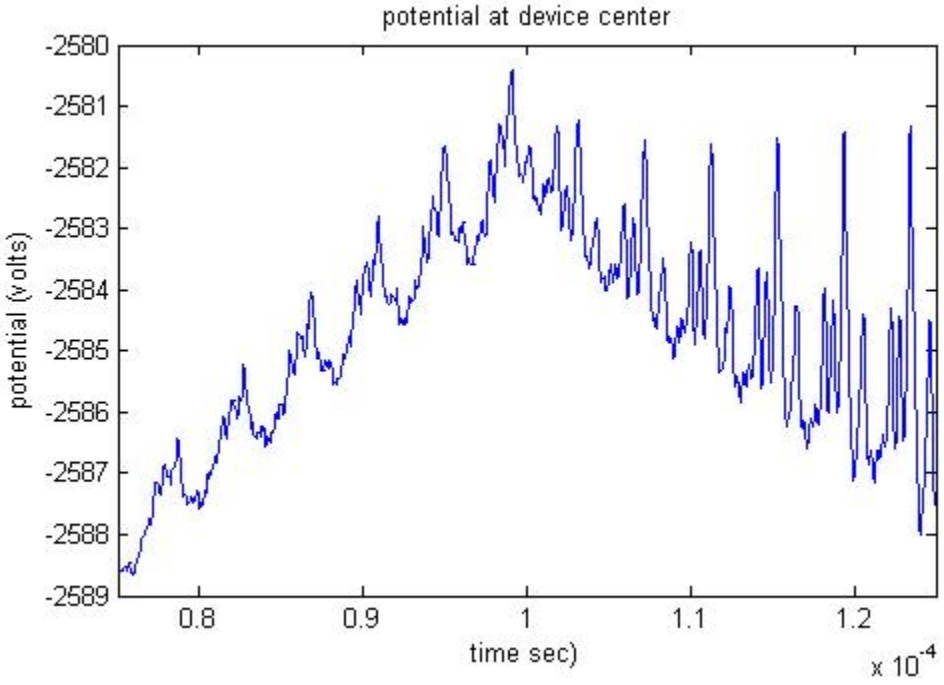

Figure 4.10 Central potential (volts) at injection cut-off of $t = 1 \cdot 10^{-4}$ sec, 25 passes elapsed

Figure 4.10 shows about 5 passes before and after turning the ion guns off. Before termination, the peak potential is increasing about 1 volt per pass as is the local minimum. After termination, the peak potential maintains its level, but the local minimum drops at about 1 volt per pass. The number of particles in the system immediately drops significantly at termination, so the maintenance of the peak potential is rather interesting. Also, qualitatively, one can see that there are many harmonics on top of the main oscillation frequency. This signal seems rather noisy already, but overall, the beams are still uniform as shown in Figure 4.11.

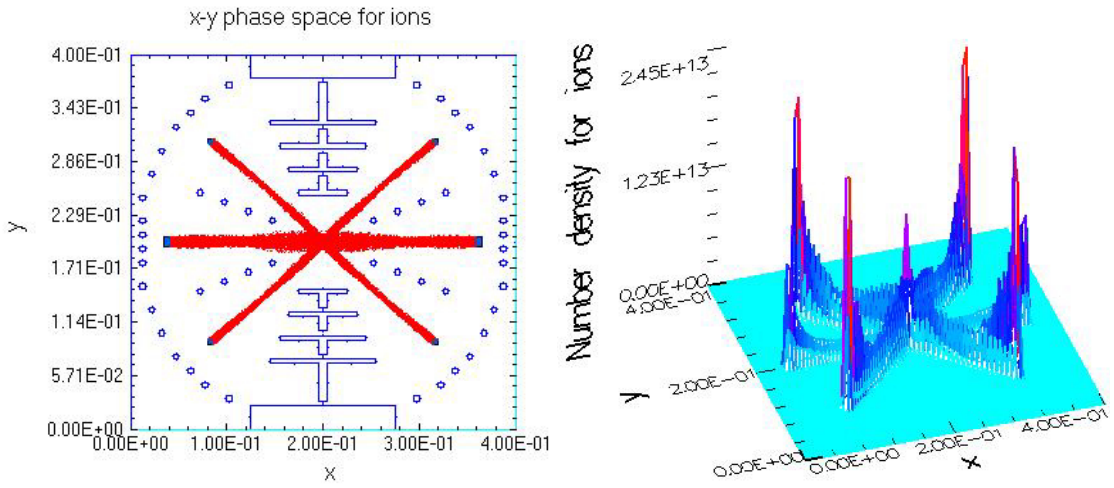

Figure 4.11 Ion positions and density map at termination of injection, $t = 1 \cdot 10^{-4}$ sec

Over time, the instability dominates and the higher harmonics are relatively lost compared to the strength of the main peak. At the end of the run the potential trace shows that the noise in the signal is gone, shown below in Figure 4.12. Instead of causing local maxima or minima, the higher harmonics now serve to merely shape the main spike.

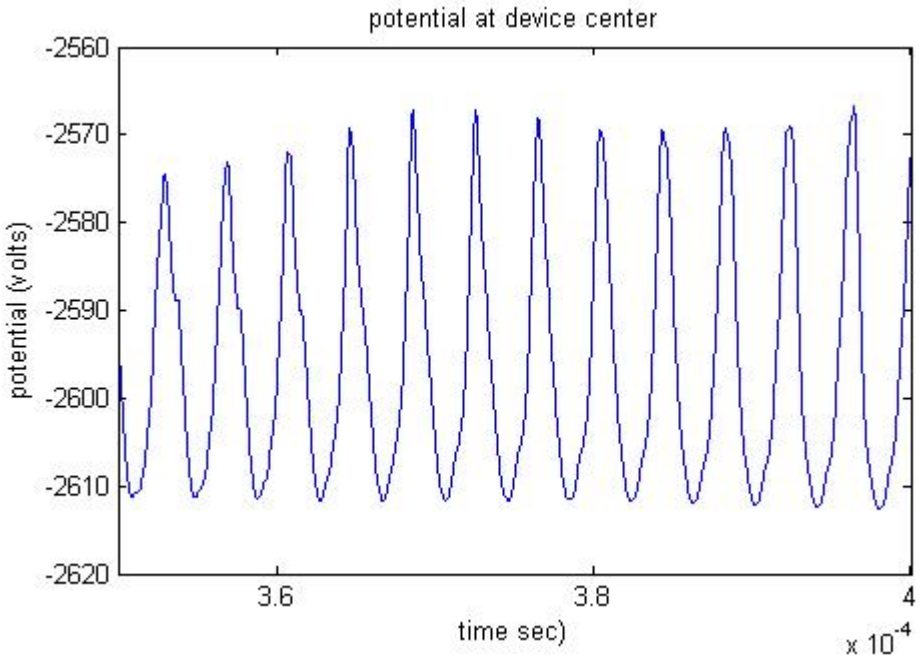

Figure 4.12 Central potential (volts) at end of run, 100 passes elapsed, $t = 4 \cdot 10^{-4}$ sec

The Fourier transform is performed over a subwindow of 10 passes in order to determine the growth of the various harmonics over time. The results in Figure 4.13 show the relative strength of the bounce frequency and the next 3 harmonics on a log scale. The strength is the magnitude of the Fourier transform at the given frequency.

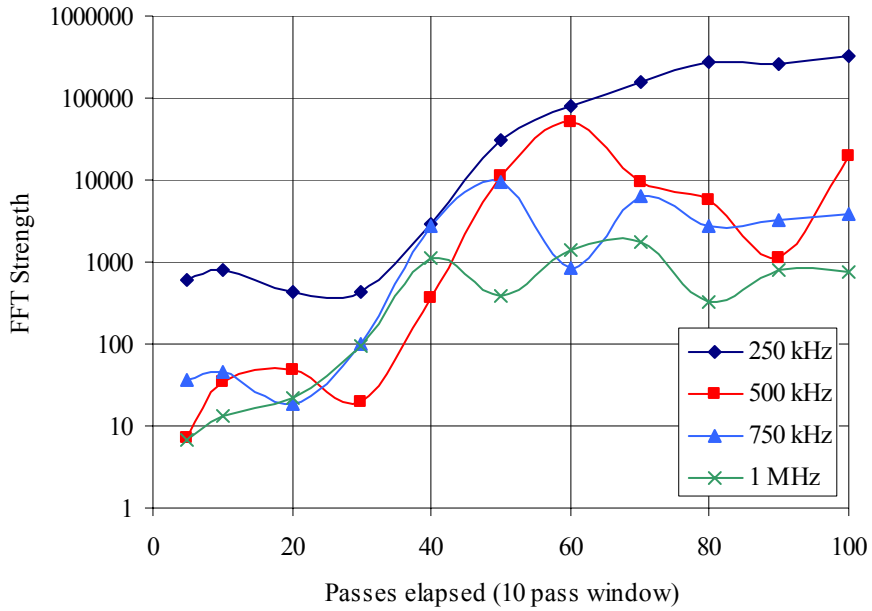

Figure 4.13 Strength of dominant modes vs. elapsed time.

In Figure 4.13, observe that the bounce frequency of 250 kHz is dominant over the other modes at the beginning of the simulation and remains in that position, growing over the entire 100 passes. The harmonics, however, grow over a time but then plateau. The highest frequency mode, 1 MHz, actually grows the fastest but plateaus at about 40 passes. The 750 kHz harmonic peaks at about 50 passes and is somewhat stronger than the 1 MHz mode. The 500 kHz reaches its peak at about 60 passes and then fluctuates somewhat. After 100 passes, the bounce frequency is a full order of magnitude stronger than the next strongest mode. These observations agree with the general behavior of

growth rates for the 2-stream instability, with higher frequencies having correspondingly higher growth rates for a certain range of wave numbers. The 2-stream instability is examined in much more detail later in this chapter.

Another curious detail in the FFT results is that the instability appears right away, well before it is observable just by looking at the ion positions. Also, bounce frequency is immediately stronger than the other harmonics, which suggest that the modes are being initially tripped somehow. An idealized injection profile was created by taking the actual profile in Figure 4.9 and making the transitions completely step-like while maintaining the level of the steps, shown in the top frame of Figure 4.14. The Fourier transform of this idealized stepped injection is shown in the middle frame and is also shown in a log-scale in the bottom frame. It features a strong zero frequency peak as one would expect since the overall signal is growing. More importantly, the bounce frequency of 250 kHz appears prominently. The first and third harmonics are almost zero, but the second harmonic appears, although less strongly than the bounce frequency. This agrees very well with the actual data, where the bounce frequency and its second harmonic are initially much stronger than the other frequencies. Over time, all the harmonics still grow, as this idealized step behavior is quickly lost at the densities in this characteristic run. The important thing to note is that the transient nature of the injection process produces disturbances at harmonics of the bounce frequency, providing a natural seed from which instability can grow.

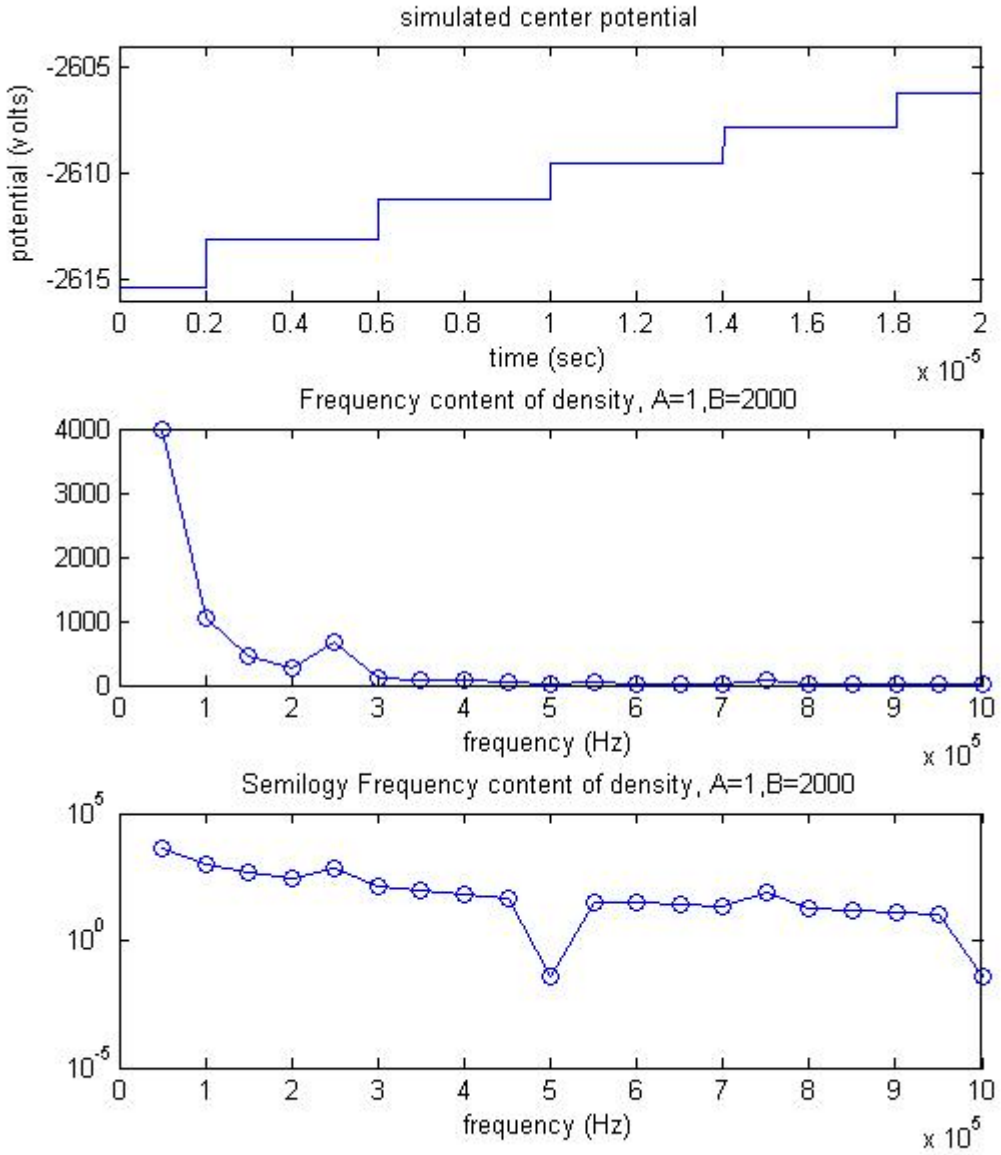

Figure 4.14 Data for simulated OOPIC run, stepped central potential for $2 \cdot 10^{-5}$ sec. Top: central potential (volts) vs. time. Middle: FFT of central potential from t = 0 to t = $2 \cdot 10^{-5}$ sec (5 passes). Bottom: semilog plot of FFT in middle frame

Complete saturation, steady state behavior

The characteristic run used for the FFT analysis can be allowed to run for many more passes in order to assess the lifetime of ions in the trap. After 100 passes, the

uniform beams have been largely transformed into a set of 6 synchronized bunches, 2 on each beam path. The general behavior is shown in Figure 4.15.

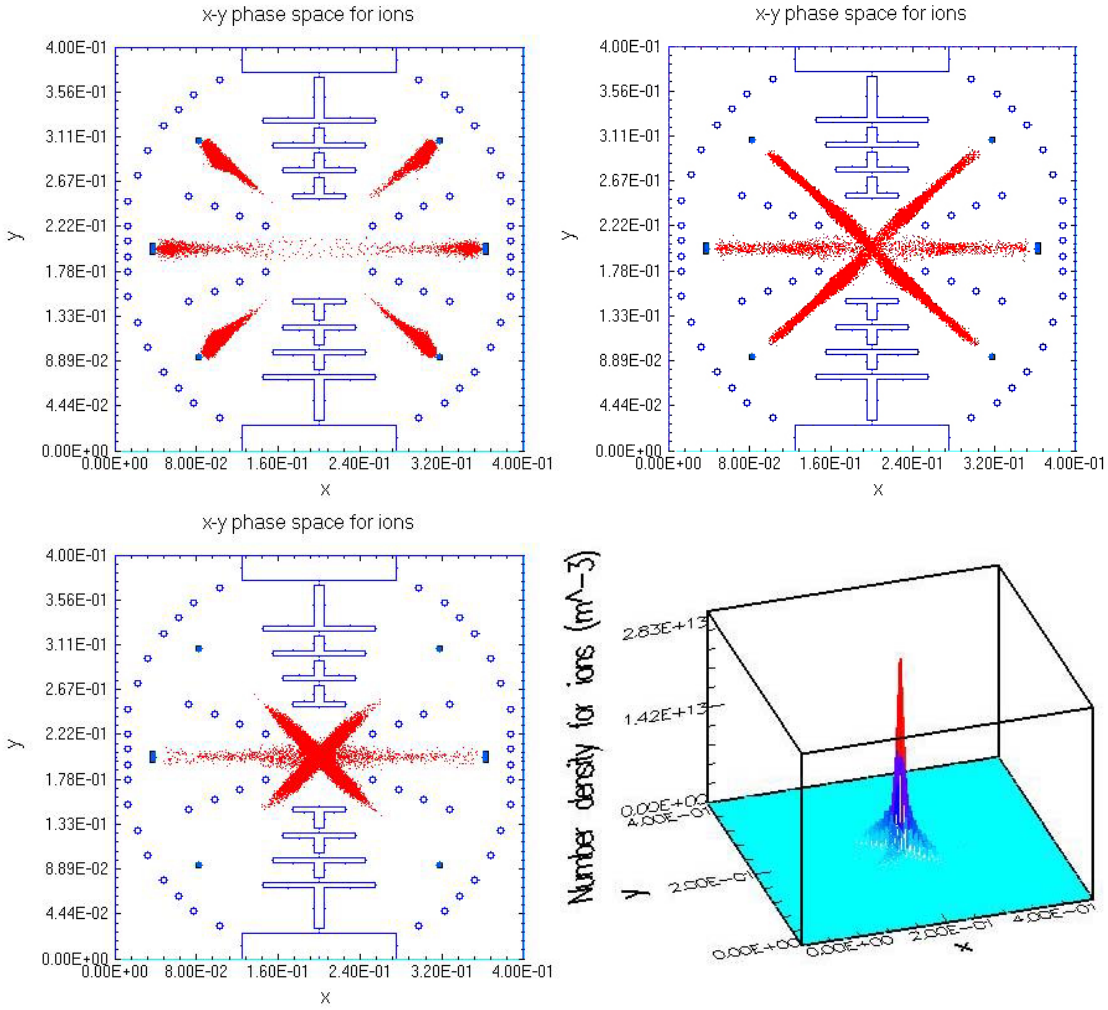

Figure 4.15 Long-lived, stable synchronization. Tiles depict the characteristic OOPIC run at 0.01 sec, 2,500 passes elapsed. Top left: ions approaching anode region. Top right: ions approaching the device center. Bottom left: ions in center at peak density. Bottom right: ions density profile at peak central ion density.

From Figure 4.15, the bunches can be seen to stretch as they depart the anode at about 2 cm in diameter and by the time they meet in the device center, the bunches are ovals about 10 cm long by about 2 cm wide. Individually, bunches are somewhat Gaussian shaped and the collective central peak in density is quite sharp. The simulation

was allowed to continue to 0.09 seconds, which corresponds to 22,500 passes. Shown in Figure 4.16 for comparison sake, the central potential at this advanced time is still 30 volts above the background compared to a maximum value of about 60 volts at about 500 passes.

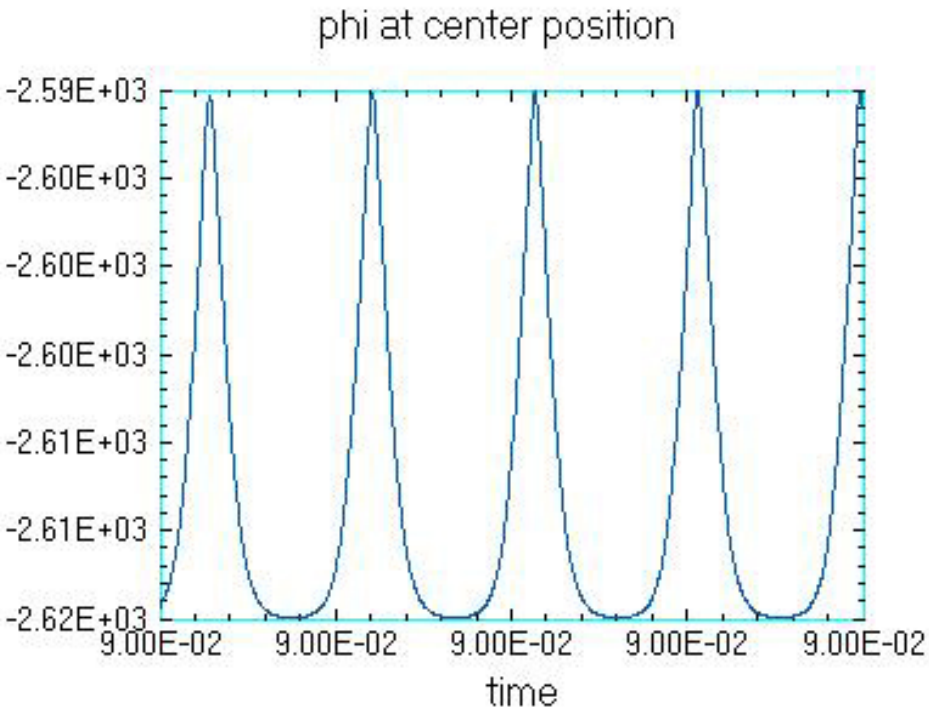

Figure 4.16 Central potential for characteristic run at t = 0.09 seconds, 22,500 passes.

The bunches are still stable and rate of particle loss at this advanced stage actually is decreasing. The particle number history is shown in Figure 4.17. The initial particle loss is quite rapid and the first 2 milliseconds of the particle number history are shown in Figure 4.18. Curiously, the longer the simulation runs, the 'lifetime' of the remaining particles gradually grows. This can be seen trying to fit an exponential decay curve to the particle number history. A single exponential decay for the entire history is quite a poor fit. Over smaller time windows, the fit can be quite good. The time constants for a

number of fits are shown in Figure 4.19, with the first 10 ms divided into 1 ms windows and the last 80 ms divided into 10 ms windows.

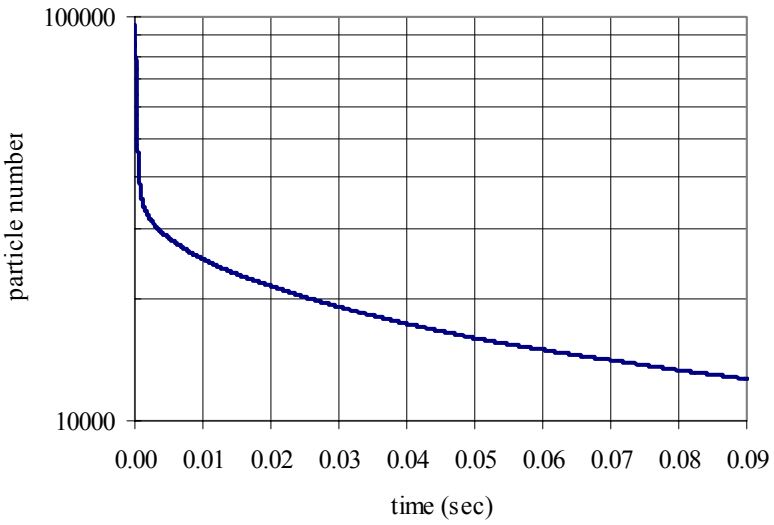

Figure 4.17 Particle number vs. time for long-lived OOPIC run

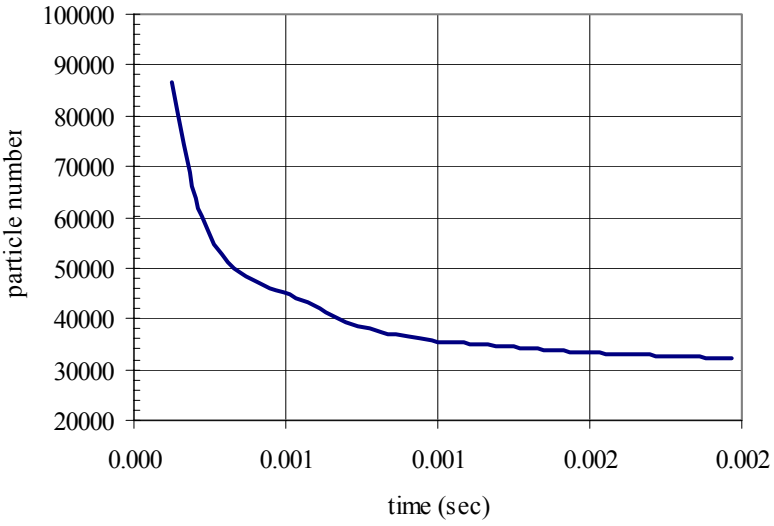

Figure 4.18 Particle number vs. time for long-lived OOPIC run, first 2 milliseconds

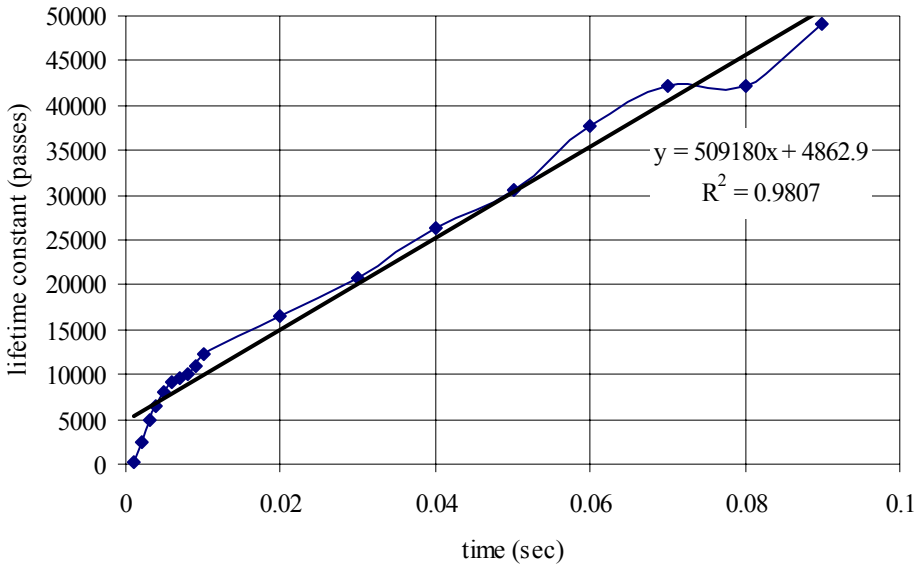

Figure 4.19 Fitted exponential decay time constants vs. simulation time. 1 ms fit window for t < 10 ms, 10 ms fit window for t > 10 ms.

The particle loss is clearly quite rapid at the beginning of the simulations, and this is most likely due to the instability of the synchronization process. These particles are mostly lost to the emitter surfaces at the anode when bunches coalesce near the anodes. The model is set-up to reflect any particles that happen to come back and hit the emitters. However, when ions are kicked onto the backside of the emitters, the boundary is treated as a particle sink and the ions are removed. This process should continue over the whole of the simulation. Initially, some particles are lost to the cathode grids, but the densities in this run do not cause the beams to intersect the grids once the synchronized state is achieved.

Also, under these long run times, the containment in the equatorial beam is observed to be significantly worse than the diagonal beams lines. At 0.09 seconds, the equatorial bunches are still present, but the diagonal bunches have a higher peak anode

density by about an order of magnitude. This is most likely due to the granularity of the field model used in the simulations.

From Figure 4.19, one can see that the lifetime 'constant' quickly climbs to about 12,000 passes at 10 ms, and then linearly increases with time. The time constant for the last 10 ms of the run is about 50,000 passes. This is quite an improvement over the 10 passes for a traditional IEC one grid system. This gradual increase in lifetimes suggests 2 scenarios. The first is that there is an initial mix of particle lifetimes, the ions don't really mix over time, and the short-lived ones are simply lost earlier. The second is that the ions mix over time and bunches as a whole grow more stable as they shed particles over time. In either case, the physical cause of particle removal from the system appears to be an artifact of the model, not an actual process such as striking the cathode grids or upscattering in energy and leaving the simulation region. This suggests that if emitters can be properly designed not to be impinged by the beam, lifetimes of greater than tens of thousands of passes should be achievable at the modest densities allowed in a non-neutralized system.

4.2 Synchronization background

The discovery of such a peculiar phenomenon as self-organization necessitated a return to the library. Surely similar behavior must be present in other experiments or in other fields of study. The general study of synchronization has a rich and quite old history, stretching all the way back to the times of Huygens and the quest for accurate clocks. A very accurate clock would allow navigators to determine their longitudinal position, making trans-Atlantic crossings safer and naval engagements a much more

exact art. In 1656, Huygens invented the pendulum clock, a breakthrough in accurate timekeeping. As a side note, while it worked well on land, the pendulum was susceptible to disturbance accelerations from the ship motion, leaving the thorny problem of sea-based timekeeping unsolved for another century. While Huygens was developing his sophisticated clocks, he noticed that the pendula would become in sync with each other, despite being physically separated. The very same clocks would drift apart if they were located farther away, say in another building. The slight perturbations caused by each of the clocks transmitted through the floor and wall was apparently enough to keep them swinging together. Specifically, the clock pendula were found to oscillate perfectly asynchronously, so that a disturbance on the connecting wall produced by one would cancel out the other.

Examples of naturally occurring synchrony are abundant in nature. A poignant example most people have experienced is the coherence of cheering and clapping of hands at sporting events. People can quite naturally perceive the errors in phase and pitch from their neighbors and adjust to match them. A more sophisticated version takes place in a choir. This 'choir' effect is also seen in other animals, including the nighttime calls of frogs and cicadas. The phenomenon of synchrony is also observed on the microscopic scale, where neurons have been shown to act together and show collective behavior [33].

The Zajfman trap

While searching the literature for plasma instabilities that would tend to show this self-organizing type of behavior, I found the work of a group at the Weizmann Institute of Science in Rehovot, Israel. The group built a cylindrical, electrostatic ion trap to study

laser-ion beam interactions. The trap features a single beam line with focusing electrodes and mirrors at the ends of the trap and a long field free region in the device center, schematically shown in Figure 4.20. Small bunches of ions were injected into the trap and then allowed to bounce back and forth. A centrally located ring yields a capacitive signal as ions pass through it. The bunch is expected to spread out over time due to the slight differences in ion energies. The capacitive signal was expected to be initially periodic and then gradually smooth out. However, they found that for certain electrode potential settings, the signal would remain periodic and stable over very long timescales, with a typical lifetime of 0.27 seconds (90,000 oscillations). Additionally, stable bunches were observed for times longer than this and longer times were assumed possible [38]. The group has produced a series of papers presenting the experimental results and theoretical explanations of the observed behavior [34]-[42].

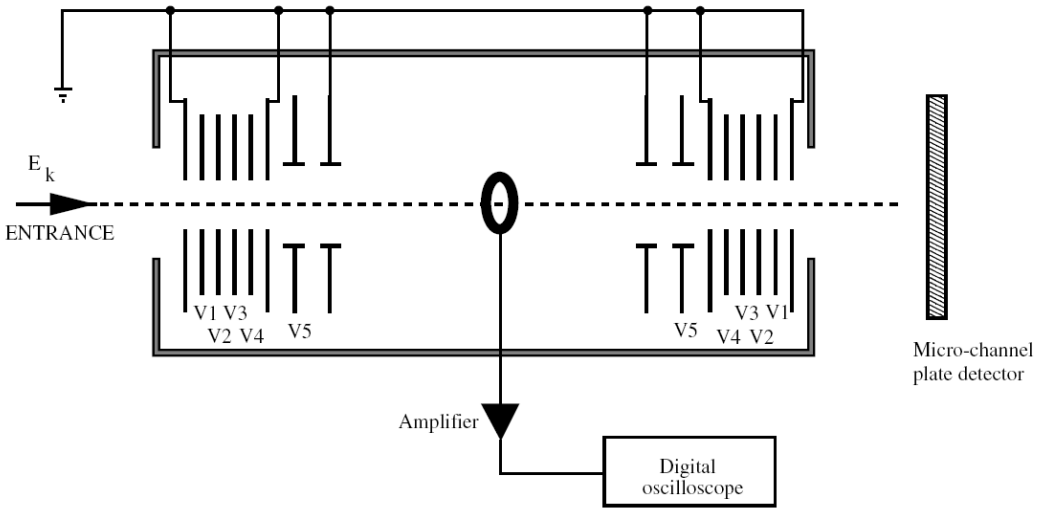

Figure 4.20 Schematic view of the Zajfman trap, Figure 1 from Pedersen, et al., 2002 [37]

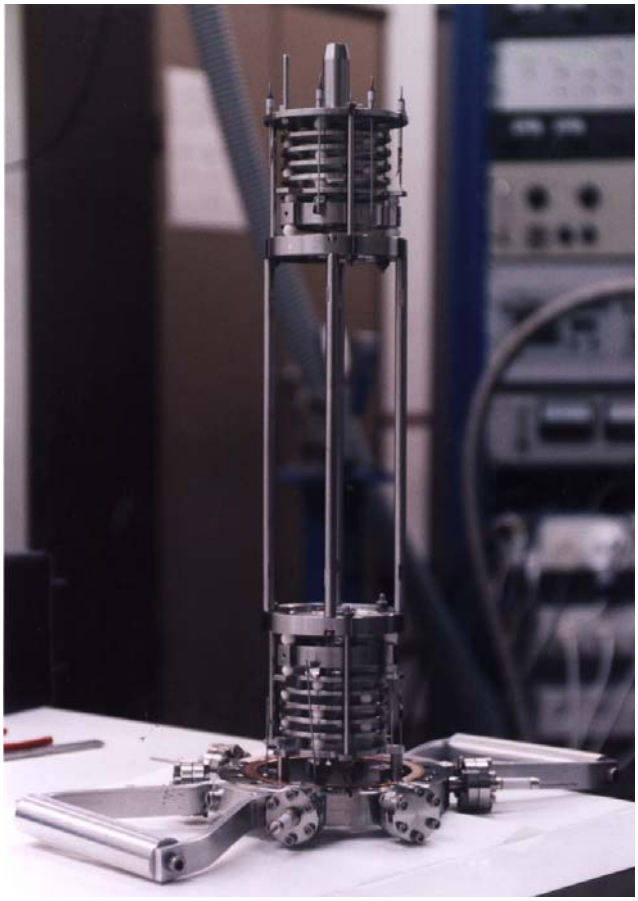

Figure 4.21 40 cm long Zajfman trap, photo credit D. Zajfman, Weizmann Institute of Science

In this text I will refer to the Weizmann group's ion trap as the Zajfman trap as he is the first author on the first paper on the topic and the name is used in popular articles about the work. Certain aspects of the actual ion trap are very similar to an IEC device, while some are quite different. The trap was envisioned for storage of fast ion beams, and the ions travel through the center at keV energies and above. Most of the papers presented Argon ions at about 4 keV. The scale sizes are similar to IECs as well, on the order of half a meter to a few meters in length. The pressures are much lower however, on the order of 10^{-10} Torr. This is to extend the lifetime of the ions limited by neutralization. Predicted pressure limited lifetimes are on the order of a second for a

variety of gases [35]. Of course, this assumes that the ion trajectories are confined over such long time scales. The introduction of Einzel lenses to confine the ions is functionally equivalent to using multiple grids in an IEC device, except that access to the grids is much easier in the cylindrical geometry. The cylindrical geometry is similar to the "C-device" IEC at the University of Illinois at Urbana-Champaign [18]. Improving the C-device with the Einzel lenses and mirrors would allow the device to operate at low pressures and produce a line source of fusion products in the central region. The multigrid-spherical device we propose is essentially the product of 'overlapping' many of these stable beam lines through a mutual central point.

There are also significant differences with the Zajfman trap and an IEC device. The method of ion injection is quite different due to the extremely high vacuum involved and the desire to look at a variety of interesting ions produced external to the device. The need to 'open' and 'close' the trap means that the ion injection process is inherently discrete. Most IEC experiments use a continuous injection scheme internal to the device, so that a continuous beam is a more natural situation. This continuous injection behavior is modeled in OOPIC, and the synchronous behavior was observed to arise from an initially uniform state. As was shown in the beginning of this chapter, a hybrid of the two situations was used to produce a clear picture of the emergence of bunches from the uniform beams. The Weizmann studies do not speak to this initial process, but they do present a compelling framework for understanding the stability of the long-lived bunches.

Criteria for synchronization

Several analyses are used by the group to explain the phenomenon, including optical models, 2-body simulations, N-body simulations, and a periodic mapping technique. The main explanation of the synchronization is that the ions undergo Coulomb interactions in the mirror regions which effectively redistribute energy in the bunch so that the ions orbit around near each other in phase space. They found 3 main criteria to hold experimentally and theoretically to achieve synchronization.

The first and perhaps most important criterion is that the period of an ion in the trap should increase as the energy (more generally the momentum) of the particle increases. This 'Kinematic Criterion' is simply stated as:

$$\frac{dT}{dE} \geq 0 \tag{4.1}$$

A parabolic potential well produces a value of zero for this criterion, as the period is independent of energy. An example of unstable geometry would be the simple 'square well' potential, with the faster particles simply taking less time to cross the well. The IEC geometry tends to easily satisfy this criterion, with more energetic particles traveling farther out of the well near the anode, extending their period relative to the slower ions. The kinematic criterion ensures that the more energetic particles will tend to migrate to the rear of the bunch. This re-organization in phase space forces the collision process to be a structured process instead of a random one. The general effect of collisions is to always transfer energy from the aft particles to the leading particles. By itself this would yield a random, diffusive re-organization of energy. Coupled with the kinematic criterion, collisions produce a closed orbit in the relative phase space of an ion and the bunch center of mass.

The second criterion is that the ions should be sufficiently focused in the mirror region, so that the ions occupy the same physical space as each other and thus undergo Coulomb collisions. Loosely stated, the criterion is that the axial and radial extent of the bunch should be equivalent at the anode turning point.

$$\Delta z_t = R_t \tag{4.2}$$

'Δz_t' is the axial size of the bunch and 'R_t' is the radial size of the bunch, using the notation from [38]. It will be shown that for the OOPIC IEC simulations, this criterion is less meaningful since ion bunches interact on distances on the scale of the device, as opposed to the microscopic collisions considered for individual ions.

The third criterion is that the collision rate must be just right to get the desired effect. Too few collisions and the ions will naturally spread out due to small initial differences in energy, although they will still be re-ordered in velocity space according to the device kinematics. Too numerous collisions will violently scatter the ions out of the group, effectively spreading the bunch. The high density limit is found by estimating the characteristic amount of energy transfer between particles in a given pass and limiting the density so that the scattered particles will still be within the bunch after they are re-ordered in the mirror. [38] calculates that for their characteristic experimental bunch density of 10^{12} m^{-3}, the range goes from about an order of magnitude less in density to about 2 orders greater in density. Their experimental values were always in this range given that lower densities didn't produce a strong enough signal and the particular ion source didn't allow greater densities. This is in contrast to the OOPIC simulations and experiments where the densities can build slowly due to the recirculation effect, with the

experiment crossing into the stable synchronization regime when enough density is built-up.

Microscopic picture of synchronization and Poincare sections

In addition to the original trap applications, several papers discuss the exploitation of the synchronization effect as a high resolution mass spectrometer [36] [39]. In support of this serendipitous invention a more sophisticated microscopic description of the synchronization mechanism was put forth in [40]. This mapping technique describes the ion motion through the various sections of the trap with mapping functions that include the effect of collisions as time delays. The paper finds that this approach closely reproduces the exact trajectories simulated for two particles in the trap.

A Poincare section is used to visualize the synchronized behavior in the relative phase space of two trapped particles, shown in Figure 4.22. The curves of the Poincare section here are the locus of data taken periodically in the system, specifically as the particles pass through the center of the device. A totally uncorrelated motion would emerge as a cloud of random points, but structure suggests that organized behavior is taking place. The top panels show the results of the 2 ion trajectory numerical simulations. Each curve represents different initial conditions with the vertical axis the relative momentum and the horizontal axis the relative position of the particles. The top-left panel shows the results for a satisfied kinematical criterion, where the curves are mostly closed orbits (synchronized motion). The exception is the chaotic layer around very small values of relative momentum and position, where the curves are not orbits but rather fill in randomly within the layer structure. The top-right panel shows the results

for a trap where the kinematic criterion is almost satisfied, but not quite. Most of the orbits are hyperbolic and the particles are separating in phase space from each other. There is still a synchronized, somewhat chaotic region for small initial relative positions which reportedly disappears as the kinematic criterion is less satisfied. The bottom two panels show the mapping results for the same kinematic criterion with the inclusion of the effects of collisions. The closed orbits are reproduced for the stable case as are the hyperbolic orbits for the unstable case.

The experimental and analytical results of the Weizmann group show that the synchronization effect is indeed real and for a single beam is relatively well-understood. The kinematics of the trap organizes the Coulomb interaction so that collisions redistribute the ion's energy so that ions orbit the center of mass of the total ion bunch. Further, criteria for the stability of the synchronized state are put forth and supported via several methods. The papers, however, do not address the emergence of the bunched behavior from a uniform state as in the OOPIC simulations. Also, the synchronization of several beams to each other is troublesome under the framework presented in these papers. The mirror collisions are thought to account for the synchronizing collisions, but in the OOPIC simulations, the bunches from separate beams only approach each other in the device center. The work of the following sections will build on the Weizmann papers and seek to explain the issues of emergence and inter-beam synchronization.

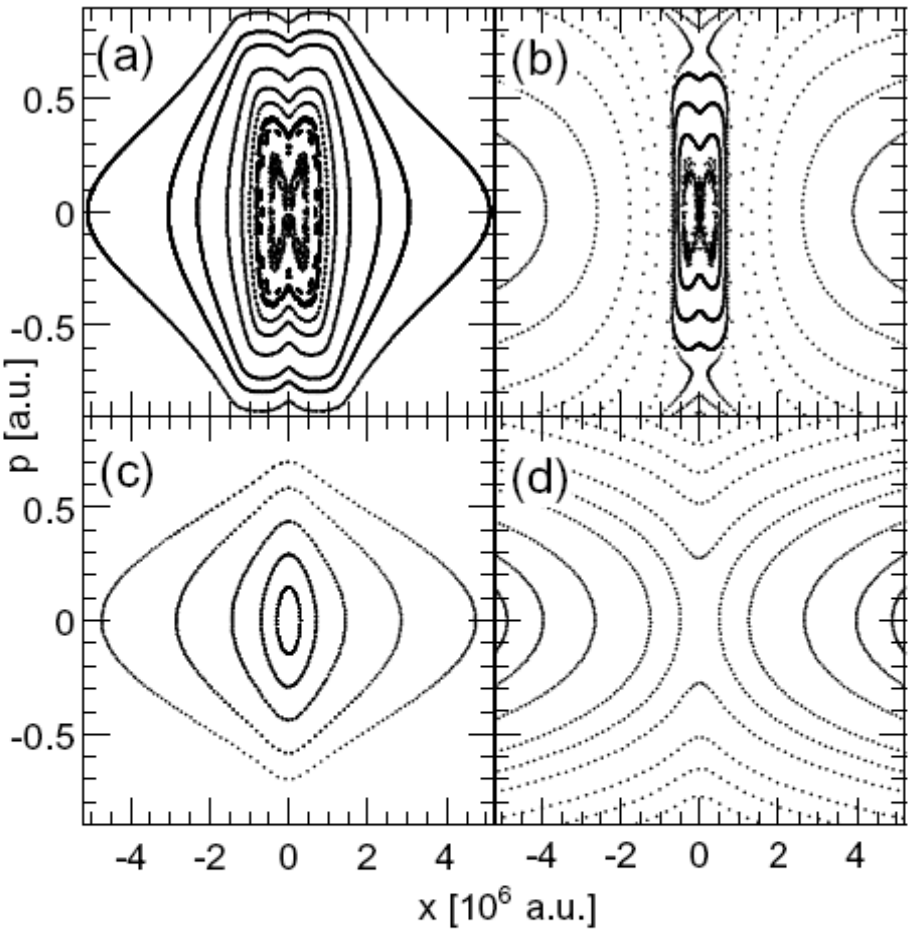

FIG. 9: Poincaré sections from trajectory calculations for the stable regime of $\alpha = 0.956$ (a) and for the unstable regime with $\alpha = 1.046$ (b). The lower row is the result of the repeated mapping $\mathcal{P}$ with a non constant τ_m from (39) for the same values of α as (a) and (b): (c) shows the stable and (d) the unstable regime.

Figure 4.22 Phase space Poincare sections for two-ion trajectory and mapping models, Figure 9 from Geyer and Tannor, 2002, [40]

4.3 2-stream instability theory

The results from the Weizmann group explain the synchronized stability of the initially bunched state. The behavior observed in the OOPIC models is significantly different in that the initial state is that of a uniform counter-streaming beam of increasing density. The cursory treatment of this instability in Chapter 2 is analyzed in more detail here in order to predict the growth rates for the unstable modes. First, the traditional 2-stream dispersion relation is derived, providing the result shown in [43]. Growth rates are found for an IEC by tracking the time evolution of decomposed disturbance waveforms. The dispersion relation is analyzed in 3-D space to understand the evolution of the instabilities in the non-uniform fields of an IEC.

Dispersion relation for two-stream instability in uniform field

Begin with continuity, momentum and one dimensional Poisson's equation for two identical particle species with different velocities.

Continuity
$$\frac{\partial n}{\partial t} + \frac{\partial}{\partial x}(nv) = 0 \tag{4.3}$$

Momentum
$$m\left(\frac{\partial v}{\partial t} + v\frac{\partial v}{\partial x}\right) = qE \tag{4.4}$$

Poisson
$$\varepsilon_0 \frac{\partial E}{\partial x} = \rho = qn \tag{4.5}$$

A first order perturbation is then introduced in density, velocity and electric field. The zeroth order terms are eliminated to leave the first order equations. The Poisson equation includes contributions from rightwards and leftwards propagating species. The continuity and momentum equations apply to both of these ion species separately, giving a total of five equations.

Continuity

$$\begin{aligned} \dot{n}_{1R} + n'_{0R} v_{1R} + n_{0R} v'_{1R} + n'_{1R} v_{0R} + n_{1R} v'_{0R} = 0 \\ \dot{n}_{1L} + n'_{0L} v_{1L} + n_{0L} v'_{1L} + n'_{1L} v_{0L} + n_{1L} v'_{0L} = 0 \end{aligned} \tag{4.6}$$

Momentum

$$\begin{aligned} v'_{0R} v_{1R} + v_{0R} v'_{1R} + \dot{v}_{1R} = \frac{q}{m} E_1 \\ v'_{0L} v_{1L} + v_{0L} v'_{1L} + \dot{v}_{1L} = \frac{q}{m} E_1 \end{aligned} \tag{4.7}$$

Poisson

$$\varepsilon_0 E'_1 = q\left(n_{1R} + n_{1L}\right) \tag{4.8}$$

Partial derivatives in time are denoted by dotted quantities and partial derivatives in space are denoted by apostrophes. The perturbations are assumed to follow a complex exponential wave form, and here we are interested in propagation along one spatial dimension.

$$\begin{aligned} E_1 = \tilde{E}_1 e^{i(kx-\omega t)} \\ n_{1R} = \tilde{n}_{1R} e^{i(kx-\omega t)} \; ; \; n_{1L} = \tilde{n}_{1L} e^{i(kx-\omega t)} \\ v_{1R} = \tilde{v}_{1R} e^{i(kx-\omega t)} \; ; \; v_{1L} = \tilde{v}_{1L} e^{i(kx-\omega t)} \end{aligned} \tag{4.9}$$

Substitute the exponential form, Equation (4.9), into the continuity relations, Equations (4.6), to yield expressions for densities in terms of velocities. Also assume that a field-free region implies that spatial derivatives of the zeroth order density and velocity are zero.

$$\tilde{n}_{1R} = \tilde{v}_{1R} \frac{n_{0R} ik}{i\left(\omega - k v_{0R}\right)} \; ; \; \tilde{n}_{1L} = \tilde{v}_{1L} \frac{n_{0L} ik}{i\left(\omega - k v_{0L}\right)} \tag{4.10}$$

Substitute the exponential forms, Equations (4.9), into the momentum relations, Equations (4.7), to yield expressions for velocities in terms of electric field.

$$\tilde{v}_{1R} = \tilde{E}_1 \frac{\frac{q}{m}}{-i\left(\omega - k v_{0R}\right)} \; ; \; \tilde{v}_{1L} = \tilde{E}_1 \frac{\frac{q}{m}}{-i\left(\omega - k v_{0L}\right)} \tag{4.11}$$

Substitute Equations (4.11) into Equations (4.10) to give the density variations in terms of the electric field variation.

$$\tilde{n}_{1R} = \frac{\frac{q}{m}\left(n_{0R} ik\right)}{\left(\omega - kv_{0R}\right)^2}\tilde{E}_1 \; ; \tilde{n}_{1L} = \frac{\frac{q}{m}\left(n_{0L} ik\right)}{\left(\omega - kv_{0L}\right)^2}\tilde{E}_1 \tag{4.12}$$

The rightward and leftward traveling species are assumed to be equal mass and have equal densities moving at opposite velocities. Equations (4.12) are then simplified.

$$\begin{aligned} n_{0R} = n_{0L} = \frac{n_0}{2} \quad & v_{0R} = v_0 \\ m_R = m_L = m \quad & v_{0L} = -v_0 \end{aligned} \tag{4.13}$$

$$\tilde{n}_{1R} = \frac{\frac{q}{m}\left(\frac{n_0}{2} ik\right)}{\left(\omega - kv_0\right)^2}\tilde{E}_1 \quad \tilde{n}_{1L} = \frac{\frac{q}{m}\left(\frac{n_0}{2} ik\right)}{\left(\omega + kv_0\right)^2}\tilde{E}_1 \tag{4.14}$$

Now substitute Equations (4.9) and Equations (4.14) into Poisson's Equation (4.8), and rearrange to obtain the dispersion relation in terms of the ion plasma frequency.

$$\omega_p^2 = \frac{e^2 n_0}{\varepsilon_0 m} \tag{4.15}$$

$$1 = \frac{\omega_p^2}{2}\left[\frac{1}{\left(\omega - kv_0\right)^2} + \frac{1}{\left(\omega + kv_0\right)^2}\right] \tag{4.16}$$

With the goal of separating the frequency and wave number, make the following substitutions.

$$\Omega = \frac{\omega}{\omega_p} \quad K = \frac{kv_0}{\omega_p} \tag{4.17}$$

$$2 = \left[\frac{1}{\left(\Omega - K\right)^2} + \frac{1}{\left(\Omega + K\right)^2}\right] \tag{4.18}$$

The bi-quadratic equation provides 2 solutions for 'Ω^2'. After simplification, the equation is as follows.

$$\Omega^2 = K^2 + \frac{1}{2} \pm \sqrt{2K^2 + \frac{1}{4}} \tag{4.19}$$

Assuming that K is real, there are four branches to the solution and these are separated into the real and imaginary parts below in Figure 4.23. The imaginary solution corresponds to exponential growth or decay of a mode and the real component describes the spatial frequency of the oscillation and the velocity of the wave.

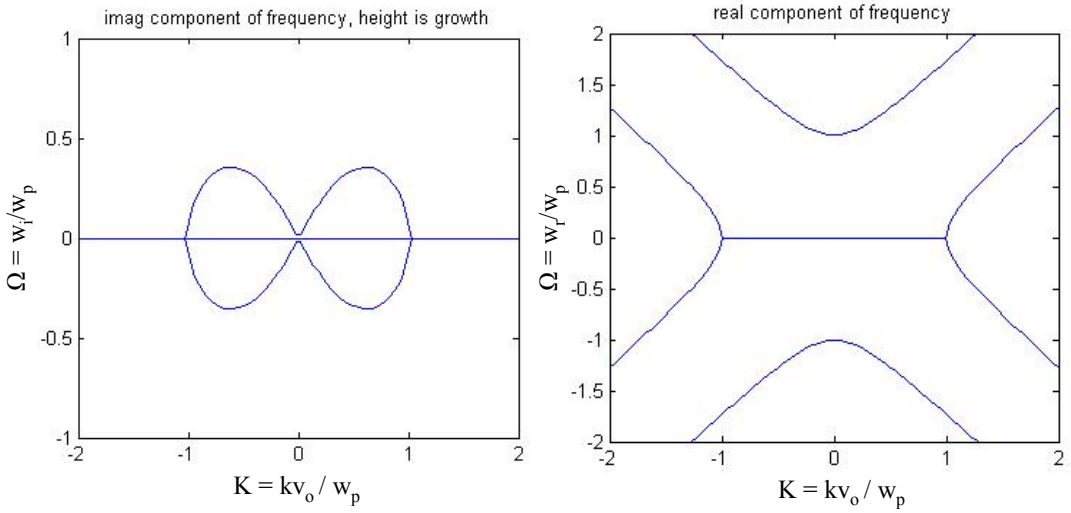

Figure 4.23 2-Stream dispersion relation, imaginary (left) and real (right) solutions, w=ω

For $K^2 > 1$, there are 4 purely real roots to Equation (4.19), a 'fast' and a 'slow' wave traveling in both directions. The 'fast' and 'slow' waves have phase velocities $\left(v_\phi = \frac{\Omega}{K} v_o \right)$ above and below the streaming velocity, 'v_o', but approaches 'v_o' as $K \to \infty$. Note also that the group velocity, '$d\omega_r/dk_r$', also asymptotes to the streaming velocity for large 'K'. There are 2 purely real and 2 purely imaginary roots for $|K| < 1$. The purely

real solutions describe neutrally stable, traveling waves at the given wave number. The purely imaginary solutions describe non-propagating waves ($\omega_r = 0$) that exponentially grow and decay with time. The transition from stable to unstable wave numbers sets a condition for minimum density at which to expect instability.

Two-stream instability conditions for OOPIC model

The values from Table 4-1 of nominal OOPIC model characteristics are used here to find a minimum density for instability.

Table 4-1 2-stream parameters for nominal OOPIC model

One Pass Period	$T = 4 \cdot 10^{-6}$ seconds
Bounce Frequency	$f = {}^{1}/_{T} = 250$ kHz
Bounce Angular Frequency	$\omega_1 = 2\pi f = 1.57 \cdot 10^{6}\ {}^{rad}/_{sec}$
Streaming Velocity	$v_o = 1.6 \cdot 10^{5}\ {}^{m}/_{s}$
Smallest Wave Number	$k_1 = {}^{\omega}/_{v_o} = 9.38\ m^{-1}$
Largest Wavelength	$\lambda_1 = 0.67$ m

$$k < \frac{\omega_p}{v_o}, \quad n_{\min} > \varepsilon_o m \left(\frac{k v_o}{e} \right)^2, \quad k_1 = \frac{\omega_1}{v_o} = 9.38\, m^{-1}, \quad n_{\min} > 5.69 \cdot 10^{13}\, m^{-3} \qquad (4.20)$$

The lowest wave number, k, which corresponds to the largest possible wavelength fluctuation in the device, is estimated as the streaming oscillation frequency divided by the streaming velocity. The resonant nature of the device sets the boundary condition on this largest wavelength, but it is confusing because the streaming velocity slows approaching the anode. One's first instinct would be to fix the wavelengths at fractions of the device diameter, but waves are compressed near the anode, so the effective largest wavelength is larger than the device dimensions. The OOPIC device diameter

(wavelength for one pass) is only 0.4 meters, but the effective wavelength value used here is calculated as 0.67 meters. Equation (4.20) gives the minimum density at which this largest possible wave will be unstable. Smaller wavelengths thus require larger densities before they become unstable.

Growth of localized disturbances

Instead of looking at a global disturbance wave, we would rather look at the response to a localized disturbance in the streams. This can be accomplished by writing a localized disturbance as a sum of component waves and then analyzing the growth of those components with time and space. At later times, the components are summed back together and the 'motion' of the initial disturbance can be seen. A Gaussian is a logical starting point for this exercise since its Fourier transform is simply another Gaussian distribution (for an infinite range). Further, a Gaussian can be arbitrarily localized and is well approximated by only a few terms in a Fourier series. The Gaussian would be characteristic of the disturbance due to the crossing beams in an IEC. The following series describes the spacetime evolution of the composite wave, written for a Gaussian centered at the device center.

$$\begin{aligned} n_{initial}(x) &= n_o + n_1 = n_o + \tilde{n}_1 e^{-\frac{x^2}{2\sigma^2}} \Rightarrow \hat{n}(k) = \tilde{n}_1 \sigma e^{-\frac{\sigma^2 k^2}{2}} \\ n(x,t) &= n_o + \frac{\tilde{n}_1 \sigma k_1}{\sqrt{2\pi}} \left(1 + 2\sum_{j=1}^{\infty} e^{-\frac{\sigma^2 k_j^2}{2}} \cos(k_j x) e^{\omega_i(k_j)t} \right); k_j = k_1 j \end{aligned} \tag{4.21}$$

where the base density is 'n_o' and the peak value of the disturbance density is '$\tilde{n}_1$'. Recall that the real component of the frequency is zero for the unstable waves we are interested in. For fairly broad disturbances, such as $\sigma = 2$ cm, the distribution is well approximated

by only 15 terms, as shown below in Figure 4.24. The distribution can be localized further, using 100 terms, a Gaussian disturbance with σ = 1 mm is shown in Figure 4.25. The peak of the disturbance is $^{1}/_{100}$ of the base density.

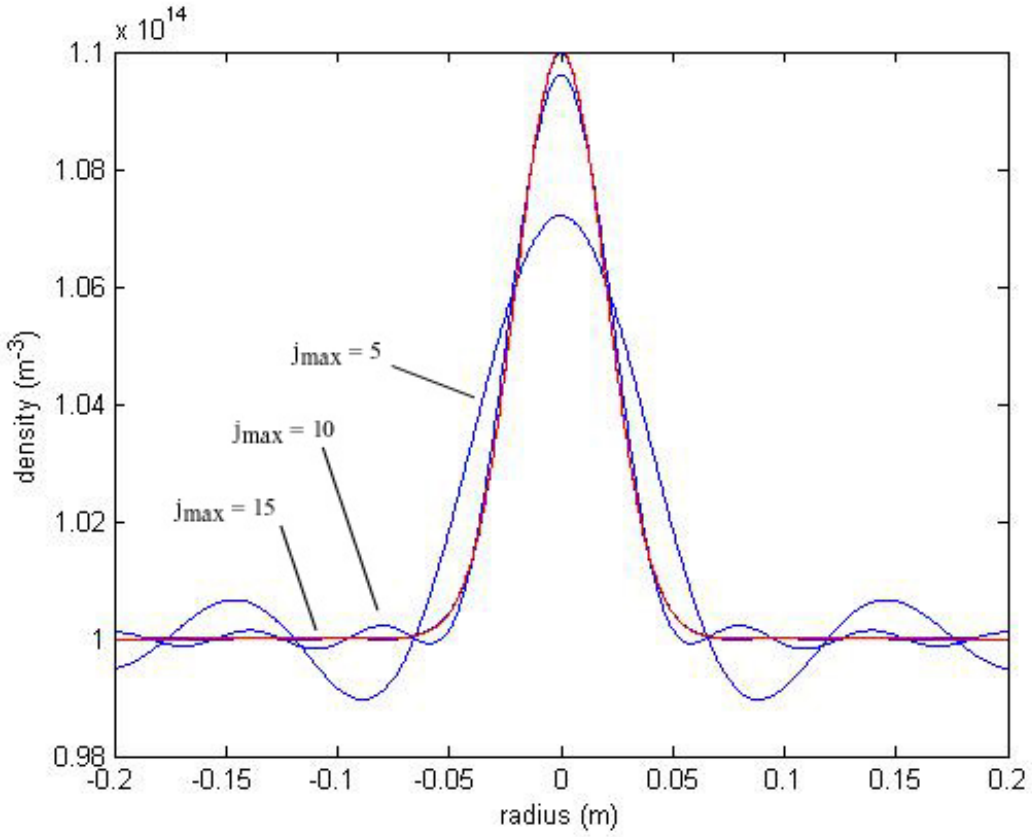

Figure 4.24 Fourier series approximations to the initial Gaussian disturbance, j_{max} = 5, 10, 15; σ = 0.02 m

As the width of the disturbance is reduced, the number of terms required to get a good approximation goes up. For a size of 1 mm, 100 terms is a good compromise between accuracy and required computation.

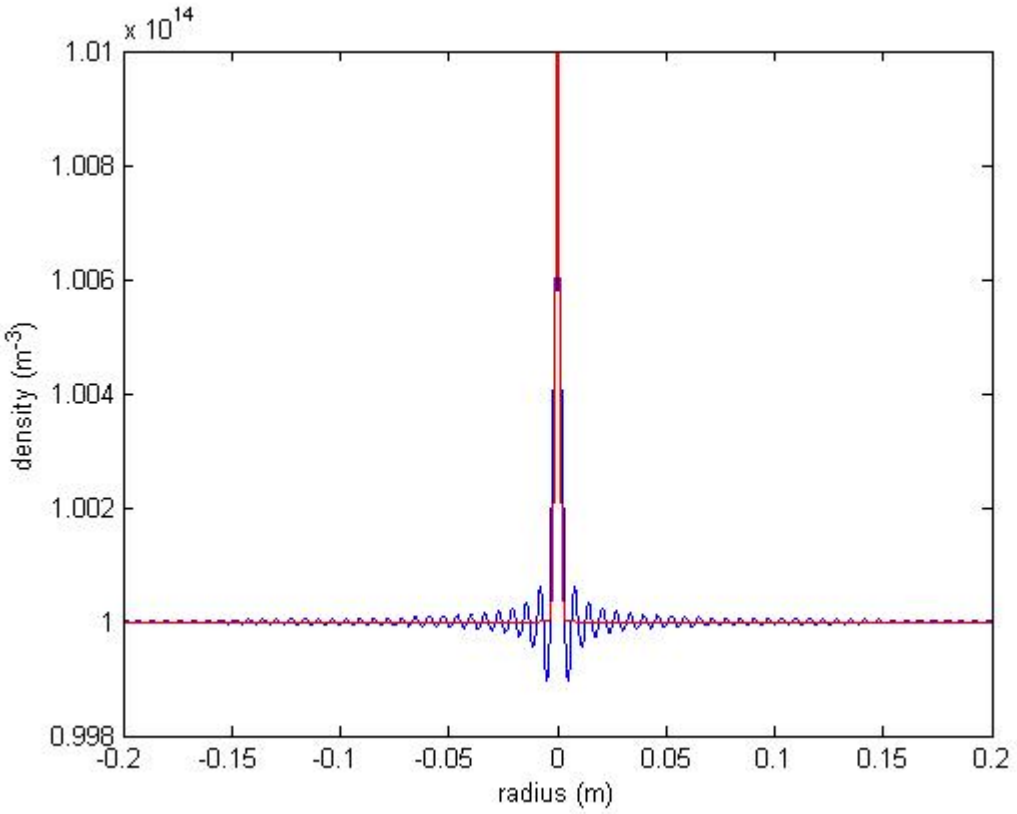

Figure 4.25 Fourier series approximation (blue), $j_{max} = 100$, compared to exact initial Gaussian distribution (red), $\sigma = 0.001$ m, $\tilde{n}_1/n_o = {}^1/_{100}$

From the dispersion relation, we see that only the smaller k's will be unstable, so that including even more k terms will have little effect on the time evolution of the disturbance. At the lowest unstable density, only the first wave number in the series will be unstable. Thus, the time evolution of the disturbance will increasingly morph into a global expression of this infinitely extending waveform. This type of case is shown in Figure 4.26 after slightly less than a pass has elapsed, for an initial beam density of $1 \cdot 10^{15}$ m^{-3}.

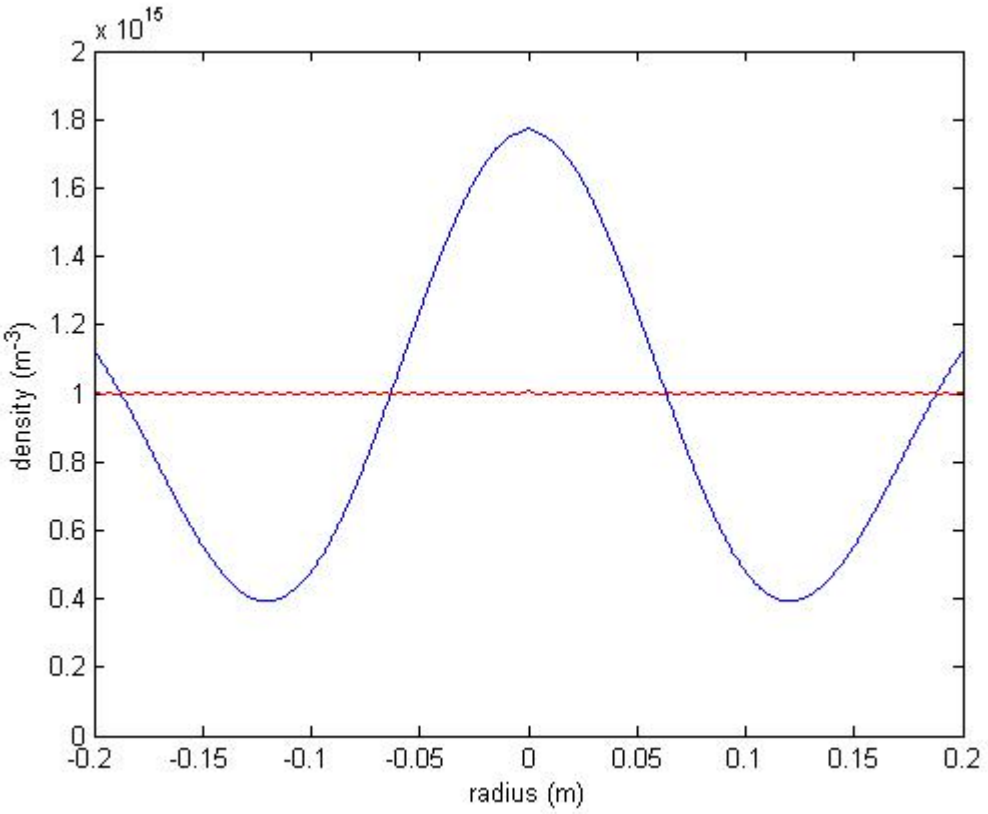

Figure 4.26 Evolution of Gaussian disturbance at t = 0.95T, $n_o = 1 \cdot 10^{15}$ m^{-3}

This waveform exhibits a slightly larger peak at the origin due to the inclusion of a few unstable modes in the series solution. As the density increases, more modes become unstable and the growth rate also increases, producing a more complex waveform of similar peak magnitude after only a quarter of a period, shown in Figure 4.27.

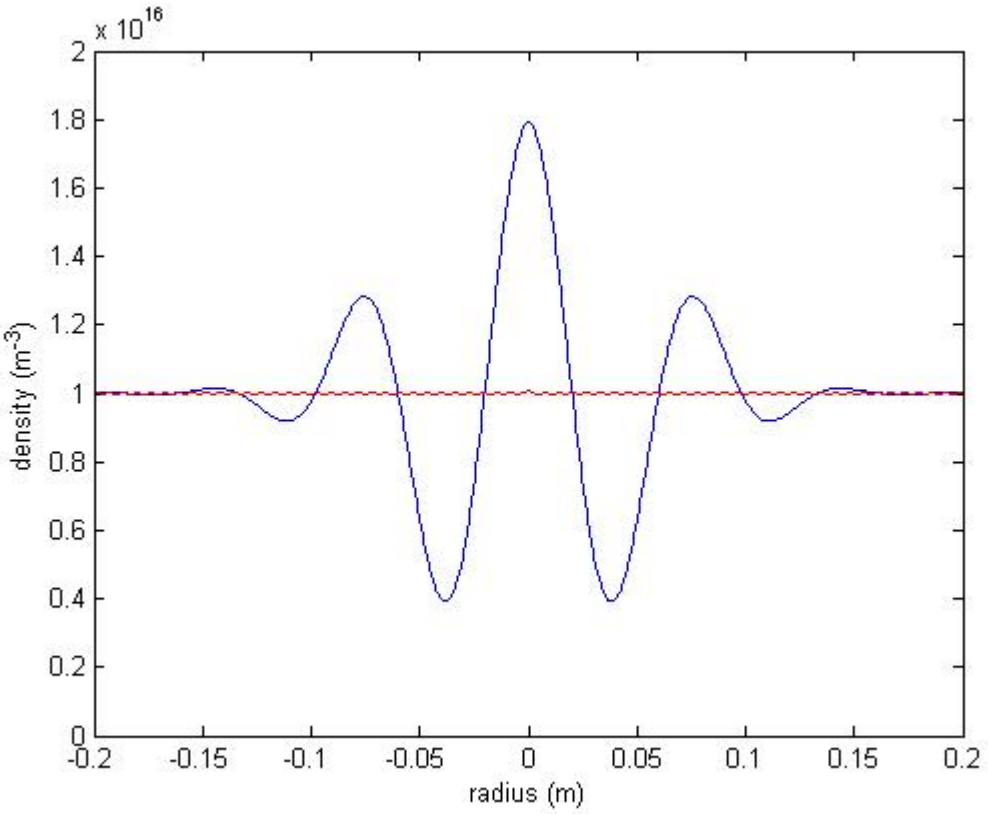

Figure 4.27 Evolution of Gaussian disturbance at t = 0.26T, $n_o = 1 \cdot 10^{16}$ m^{-3}

Now the disturbance appears to evolve from the origin, spreading outward. In reality, the wave is not traveling, but the amplitude increases fastest in the device center and less so further out, giving the illusion of an expanding ripple. Note that the central peak is much larger than secondary and tertiary peaks. Extending the simulation farther in time is unreasonable since the density is already approaching zero in some regions. However, if time is allowed to continue, the entire waveform grows in amplitude so that the entire device is affected by the localized disturbance.

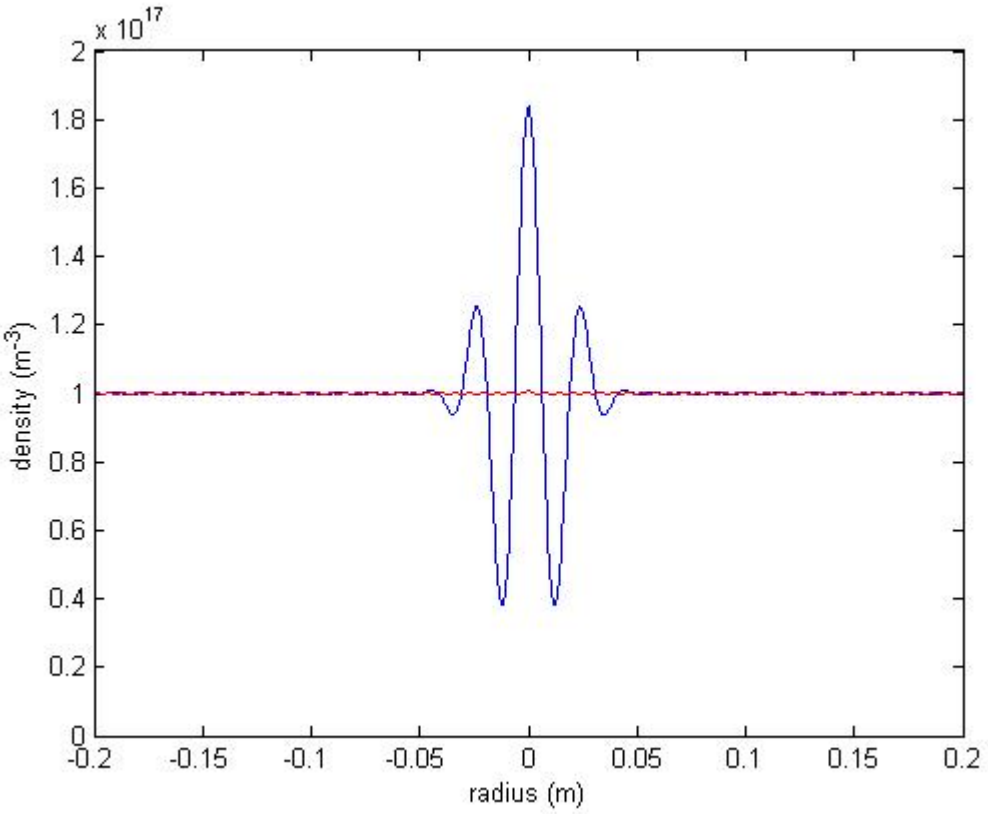

Figure 4.28 Evolution of Gaussian disturbance at t = 0.07T, $n_o = 1 \cdot 10^{17}$ m^{-3}

At even higher densities, the evolution is constricted further in space and reaches the 80% of base density growth mark much more quickly, in 0.07T. As shown in Figure 4.28, the disturbance is entirely localized within the center 10 cm of the device.

Step-shaped localized disturbance

Another disturbance of interest is the 'step' function. This disturbance appears because of the injection process where each beam is turned on and overlaps itself and builds up a recirculating current. The 'front' of this injected beam is well approximated by a Heaviside function moving at the streaming velocity. The 'step' disturbance analogous to the above Gaussian relation is shown in Figure 4.29. The function is more

of a sawtooth wave, rather than a perfect step. This is due to the enforcement of a minimum wave number in a discrete Fourier series expansion.

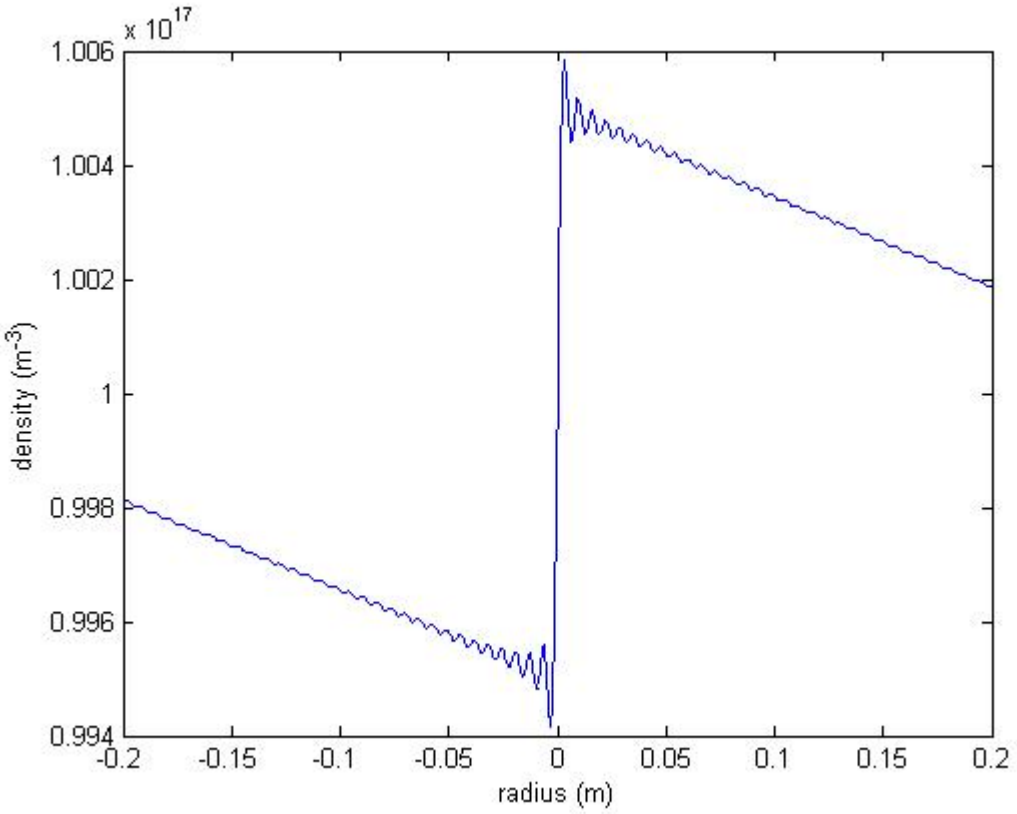

Figure 4.29 Sawtooth disturbance, $j_{max} = 100$, $\tilde{n}_1/n_o = {}^1/_{100}$

The time evolution of the composite waveform is as before, but now with a sawtooth function, H(x), a periodic function including a step from zero to one occurring at the origin. The Fourier series expansion now utilizes the sine function given that the disturbance is odd.

$$n_{initial}(x) = n_o + n_1 = n_o + \tilde{n}_1 H(x) \Rightarrow \hat{n}_1(k) = \frac{\tilde{n}_1}{2}\left[\delta(k) - \frac{i}{\pi k}\right]$$
$$n(x,t) = n_o + \frac{\tilde{n}_1 k_1}{\pi}\left(\sum_{j=1}^{\infty} \frac{\sin(k_j x)}{k_j} e^{\omega_i(k_j)t}\right) \tag{4.22}$$

The results for the sawtooth function are almost identical to the Gaussian disturbance, except for the odd vs. even nature of the two shapes. A typical case was chosen with density $n_o = 1 \cdot 10^{17}$ m^{-3} and plotted in Figure 4.30. One can see that for about the same simulation time, the waveform has grown in max amplitude and effective width as the equivalent Gaussian shown in Figure 4.28.

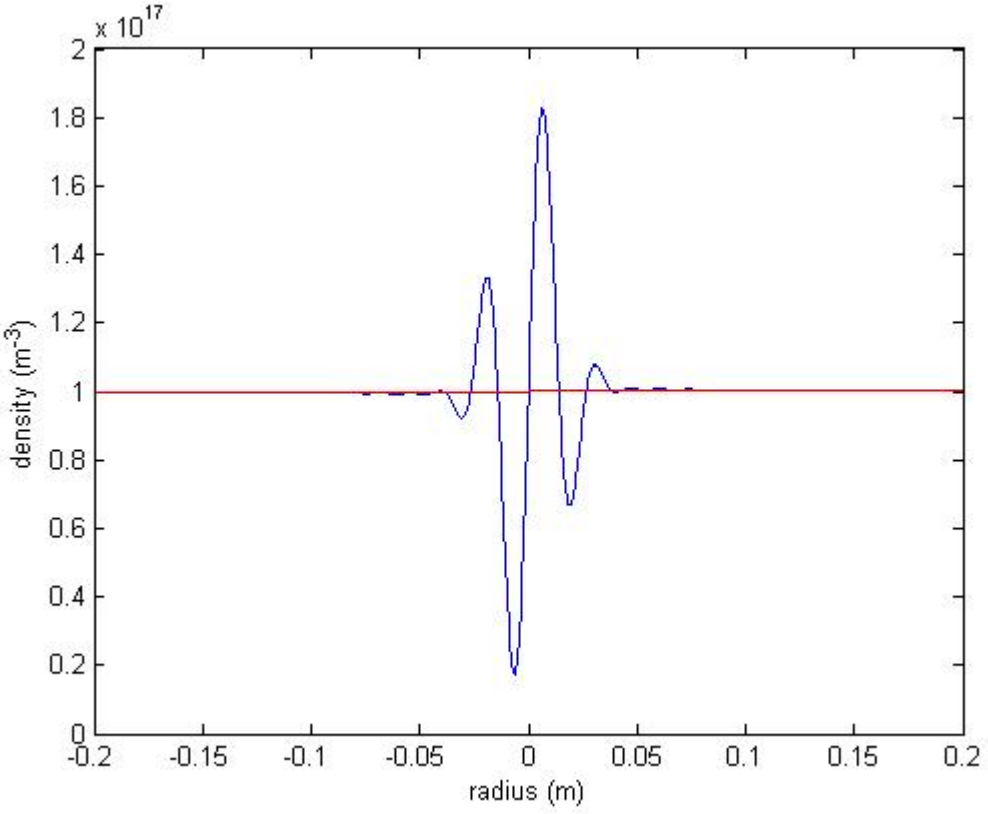

Figure 4.30 Evolution of sawtooth disturbance at t = 0.65T, $n_o = 1 \cdot 10^{17}$ m^{-3}

This similarity existed in all cases, so the Gaussian case was chosen for a parameter scan to find the growth rate of the overall mode shape as a function of density. For each case, the wave was allowed to evolve using the two-stream instability analysis growth rates until it had grown to about 80% of the initial uniform density. The initial disturbance was held at a hundredth of the uniform density with $\sigma = 0.001$ m. The

growth per pass through the device is then calculated and tabulated in Table 4-2 and plotted in Figure 4.31.

Table 4-2 Two-stream growth rate data for Gaussian disturbance, $\sigma = 0.001$ m

Initial Density (m^{-3})	Time in Periods (one pass)	Maximum Density (m^{-3})	% Density Increase per Pass
6.0E+13	9.00	6.89E+13	1.7
7.0E+13	5.40	1.13E+14	11.3
1.0E+14	3.30	1.69E+14	21.0
2.5E+14	2.00	3.86E+14	27.2
5.0E+14	1.30	7.20E+14	33.9
1.0E+15	0.95	1.77E+15	81.4
2.5E+15	0.55	4.01E+15	109.8
5.0E+15	0.38	8.57E+15	188.1
1.0E+16	0.26	1.79E+16	304.6
5.0E+16	0.10	8.21E+16	642.8
1.0E+17	0.07	1.84E+17	1198.6

The effective range of unstable density starts at the previously stated minimum unstable density of $5.7 \cdot 10^{13}$ m^{-3} and reaches 100% growth at a density of about $2.5 \cdot 10^{15}$ m^{-3}. The OOPIC simulations show instability at significantly lower densities than this, but keep in mind that this analysis doesn't treat the instability-prone anode regions. The growth per pass can be fit well to a power law.

$$\%_{per\ pass} = 10.675\left(\frac{n_o}{10^{14}}\right)^{0.7065}, \quad R^2 = 0.9124 \tag{4.23}$$

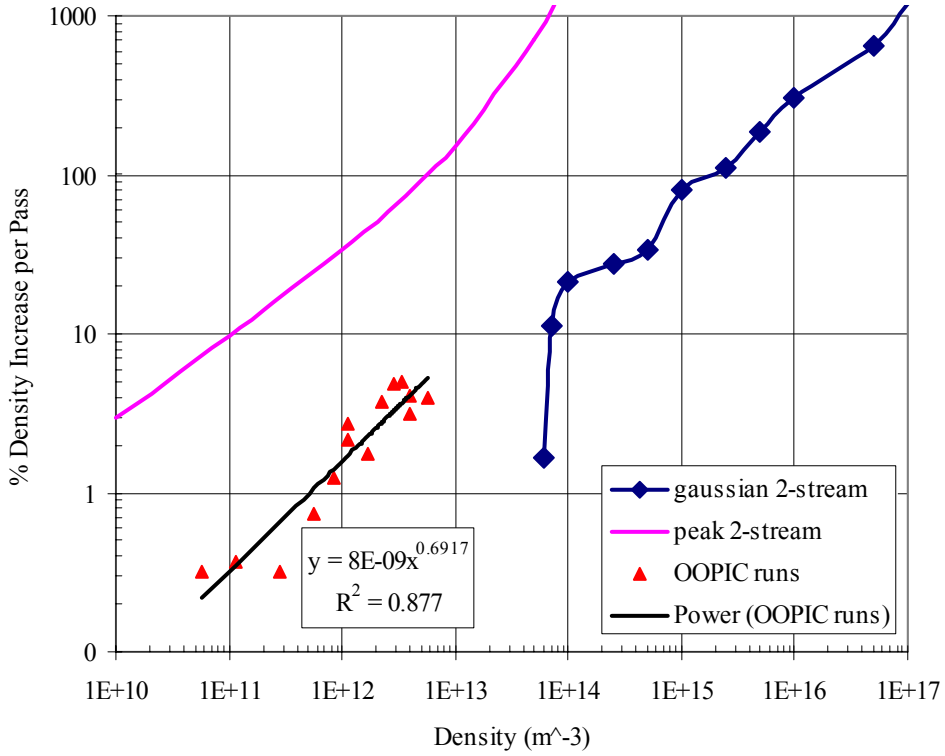

Figure 4.31 Growth rate per pass of central point, Gaussian disturbance (blue), peak 2-stream relation (magenta), OOPIC simulation data (red), and OOPIC power law (black) vs. initial uniform beam density

Alternatively, we can ignore the boundary conditions imposed by the recirculating nature of the system and simply find the maximum growth rate for a given density and streaming velocity. At low densities, this will correspond to wavelengths much larger than the device size. The growth rate per pass is shown below and is plotted in Figure 4.31.

$$\Omega_{i-\max}\left(K=\sqrt{\frac{3}{8}}\right)=\sqrt{\frac{1}{8}}$$

$$\omega_{i-\max}=\sqrt{\frac{1}{8}}\omega_p=\sqrt{\frac{1}{8}}\sqrt{\frac{n_o e^2}{\varepsilon_o m_i}}=0.074\sqrt{n_o}, \quad \textit{Argon Ions} \tag{4.24}$$

$$\frac{\%\ growth}{pass}=100\left(e^{2.94\cdot10^{-7}\sqrt{n_o}}-1\right)$$

The two-stream plots show a similar trend with density, but shifted by three orders of magnitude in density. Clearly, the center-of-device Gaussian description is wanting since such a sharp stability boundary is not seen in the OOPIC simulations. Also, the OOPIC simulations show instability at densities as low as 10^{10} m^{-3}, which would tend to agree more with the peak curve. On the other hand, the observed growth rates are about an order of magnitude lower than what the peak curve would predict. Now remember that OOPIC simulations peak at energy exchange of 5% per pass. At higher densities, the instability grows so quickly that it reaches a more complex saturated state before we can effectively measure the initial linear growth rate. Now if one extrapolates this power law to higher densities and energy exchange, it agrees well with the disturbance model. The disturbance did not include anode effects which would allow lower density instabilities, but it nonetheless appears to extrapolate to the observed behavior at lower densities. By analyzing the dispersion relation at the anode we can see how the smaller wavelengths are locally unstable and can produce computed results.

Differences in dispersion relations for cathode and anode

The real device doesn't have a constant background field, as the beams slow significantly in the anode regions and ultimately reverse their bulk motion. The beams also become more dense in the anode region. The OOPIC simulations found the velocities and densities to be practically limited to the values shown in Table 4-3 for a characteristic synchronized case. The local values can then be used to find the minimum stable wavelength corresponding to 'K = 1', and we find that the anode region can support wavelengths an order of magnitude smaller than the center. Note that this case

shows significant synchronizing behavior despite the minimum wavelength for cathode stability being larger than the device diameter. Also, the anode limit is 4.2 cm, which is still a large wave compared to the device size.

Table 4-3 Comparison of OOPIC cathode and anode 2-stream stability parameters

Center Velocity	$v_c = 1.6 \cdot 10^5$ m/s
Anode Velocity	$v_a = 2.0 \cdot 10^4$ m/s (~80 eV)
Center Density	$n_c = 1 \cdot 10^{14}$ m^{-3}
Anode Density	$n_a = 2 \cdot 10^{14}$ m^{-3}
Center Ion Plasma Frequency	$\omega_{p\text{-}c} = 2.1 \cdot 10^6$ rad/sec
Anode Ion Plasma Frequency	$\omega_{p\text{-}a} = 3 \cdot 10^6$ rad/sec
One Pass Bounce Frequency	$\omega_b = 1.6 \cdot 10^6$ rad/sec
Device Diameter	$2 \cdot R_a = 0.4$ meters
Minimum Unstable Wavelength	$\lambda > 2\pi v / \omega_p$
Cathode Stability Limit	$\lambda_c > 0.48$ meters
Anode Stability Limit	$\lambda_a > 0.042$ meters

Re-normalized dispersion relation for all locations in device

The dispersion relation can be written for these separate regions, but the problem is how to properly treat waves that propagate between regions of stability and instability. By renormalizing the parameters 'K' and 'Ω' of Equation (4.17) with the values of the streaming velocity and the plasma velocity at the device center as opposed to the local values, a sensible 3D dispersion can be pictured.

$$K^{**} = \frac{kv_c}{\omega_{p-c}}, \Omega^* = \frac{\omega_i}{\omega_{p-c}} \tag{4.25}$$

These 3D plots are a collection of the dispersion relations at various positions in the device, normalized to a single velocity and density. The plots do not describe how a

given wave would behave while traveling between two locations, rather the serve as a way to visualize how the dispersion relation changes for a given wave in different locations in the device.

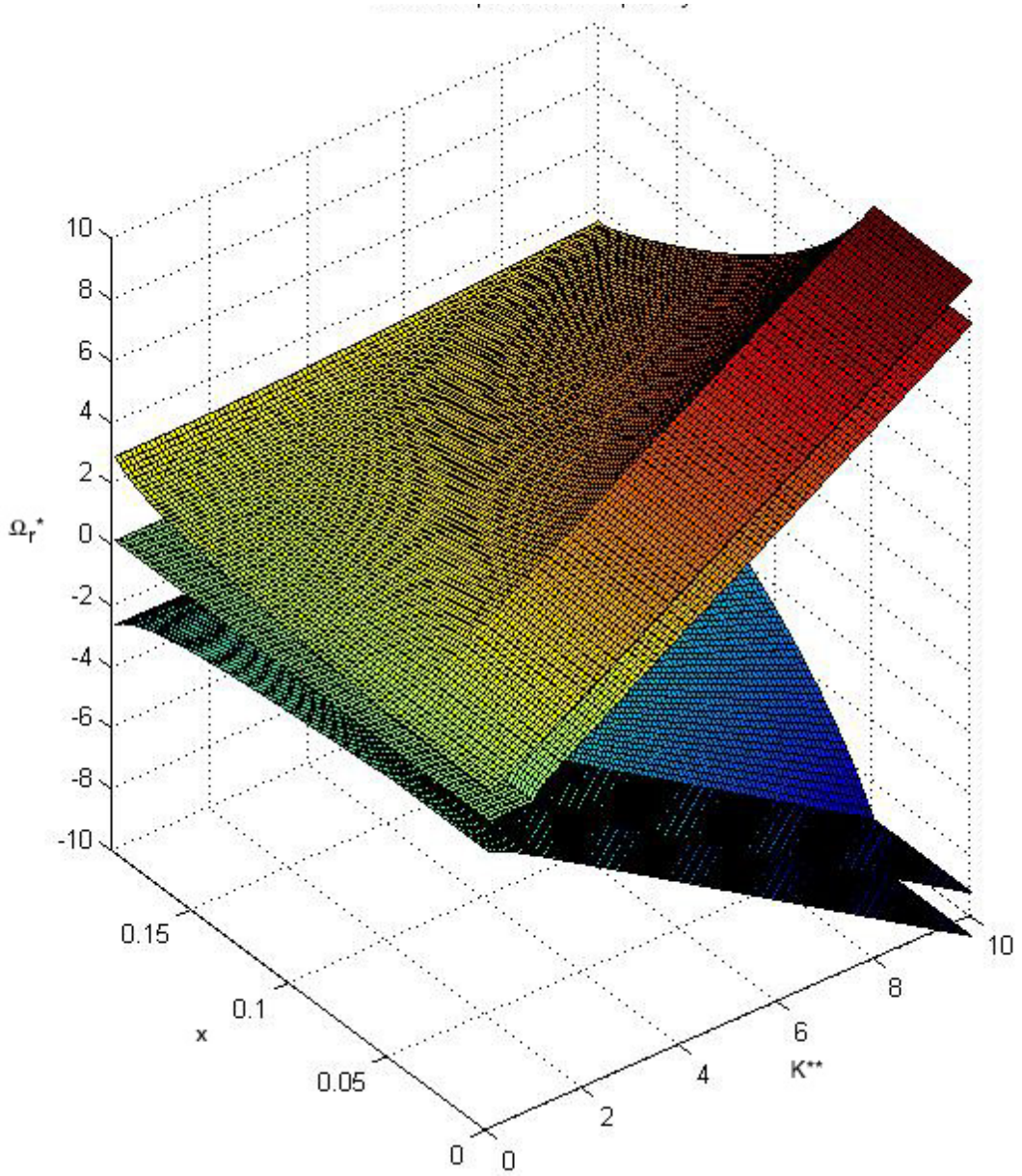

Figure 4.32 Re-normalized real frequency, Ω^*_r vs. re-normalized wave number, K^{**} vs. device radius (m), 4 solution manifolds

The real and imaginary plots of Figure 4.32 and Figure 4.33 assume the velocity varies with a spherically symmetric electric field with a field-free region out a radius of 5

cm, and a $^{1}/_{r}$ power law from 5 cm to 20 cm. The density varies with radius and is given by continuity. The three dimensional picture of the real frequency component shows how the speed of phase and group velocities generally decline near the anode of the device. The 'slow wave' manifold's intersection with the real frequency plane defines the maximum wave number for instability at that location. This curve can be seen in the imaginary plot, with K**(x = 0) = 1 and K**(x = 0.15) ~ 6. Thus, short wavelength waves which may be stable in the device center can be unstable near the anode. The shorter wave numbers will be more unstable closer to the anode, while the small K**, large wave numbers will be less unstable approaching the anode.

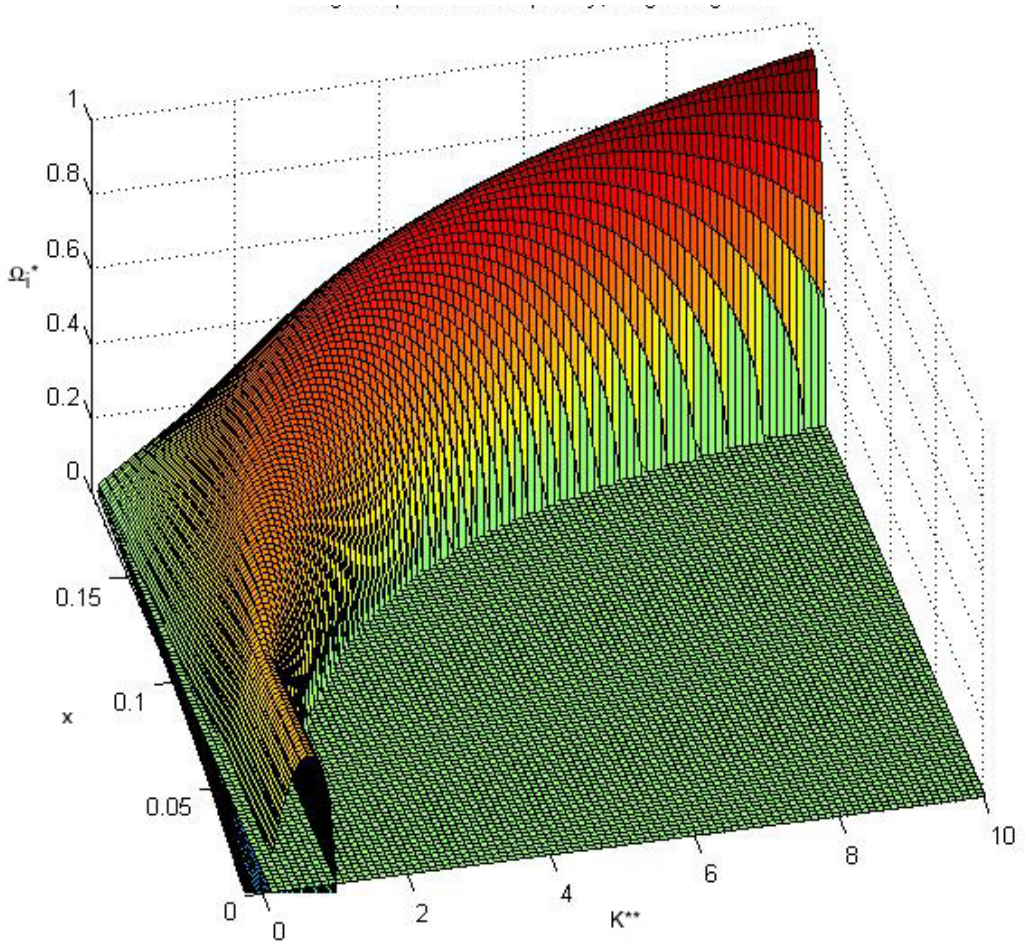

Figure 4.33 Re-normalized imaginary frequency, Ω^*_i vs. re-normalized wave number, K^{**} vs. device radius (m), unstable manifold shown

Based on observations of the anode region in the OOPIC simulations and the above analysis, it appears that the instability originates as disturbances near the anode. The unstable waves co-exist with and excite stable traveling waves. Thus, the unstable anode waves are able to travel across the device as stable waves, become unstable near the opposite anode and thus continue to build over time. Eventually the disturbance becomes non-linear as it dominates the original uniform streaming beams. The larger wavelengths will tend to grow and saturate more slowly than the smaller wavelengths. The longest wavelength disturbance allowed by the device boundary conditions eventually dominates and saturates itself to produce the counterstreaming bunches seen in the simulations.

Summary of 2-stream instability results

To summarize the main results of the 2-stream analysis, the general behavior of these localized disturbances can produce both the global waveforms and the localized bunches seen in OOPIC simulations. The crossing beams produce a large Gaussian-shaped disturbance and the injection process creates a step-function disturbance as was shown by the Fourier transform analysis of the initial density traces. The anode regions are susceptible to the counter-streaming ion instability and the predicted growth rate correlates well with the observed behavior. The progression from counterstreaming waves to bunches is the most complex part of the evolution and is well modeled only by the OOPIC simulation of tens of thousands of macro-particles. However, some understanding of this process can be gleaned by thoroughly examining why the end state of bunches on multiple beams is a globally stable configuration.

4.4 2-particle collision and dynamics models

The first step to understand the global stability is to examine the microscopic collisions specifically for this geometry. A two particle simulation was created to model the unconstrained central collisions in the field-free 2D planar space in an IEC device. Modeling results of Coulomb collisions between two ions and between two clouds of ions are presented in this section. The previous section shows how the large scale group synchronization behavior can evolve from an initially uniform state. Geyer and Tannor's mapping approach [40] was able to illustrate how the microscopic collision processes between two ions can produce the synchronizing behavior observed in the Zajfman trap [34]. Their treatment considered a single ion beam and showed two characteristic collisions, a mirror region collision and collisions in the central field-free region. The central collisions were determined to be unlikely causes of the synchronization behavior for two reasons. First, collisions between two trapped particles are more likely to occur in the mirror regions and second, synchronization from purely central collisions is shown to be unstable to perturbations. This presents a problem for describing the synchronization of multiple beams in the OOPIC simulations. These beams cross only in the center of the device and the collisions will be unconfined in the 3-D sense. We are thus motivated to examine these microscopic central collisions between neighboring beams (and their respective bunches) as a potential cause for interbeam synchronization.

A 2-particle simulation was created in Matlab to model the unconstrained central collisions in the field-free 3D space. The space is 3D, but the 2-body collision is inherently 2D with all motion taking place in a plane. The model is set-up so that collisions occur at the origin, and the particles are initialized a characteristic distance

away from the origin. The initial velocity vectors are directed so that non-interacting particles will pass exactly through the center. The motion traced by each particle represents the various paths in an IEC. The parameters of interest include the initial radial positions along the paths, the angle between the paths, the particle mass and charge, and the interaction force law for the particles.

The first force law is the simple Coulomb interaction. The 3-D representation of position and velocity allows the use of the force law with a singularity at a value of zero particle separation. Prior one dimensional studies have had to use an interaction potential with a minimal impact parameter to allow particles to pass each other along a constrained path [38]. A non-relativistic Eulerian first order scheme is employed as a particle mover with the interaction acceleration calculated every step. 500,000 steps are used to cross the characteristic path length of 2 nanometers, which yields a step size of 2 femtometers ($2 \cdot 10^{-15}$ m). A step size on the order of the nuclei size is necessary to produce the known behavior of head-on collisions where the particles turn each other away and effectively switch places, as shown below in Figure 4.34. The particles begin on 45 degree paths, which is characteristic of ions in the MIT laboratory IEC device.

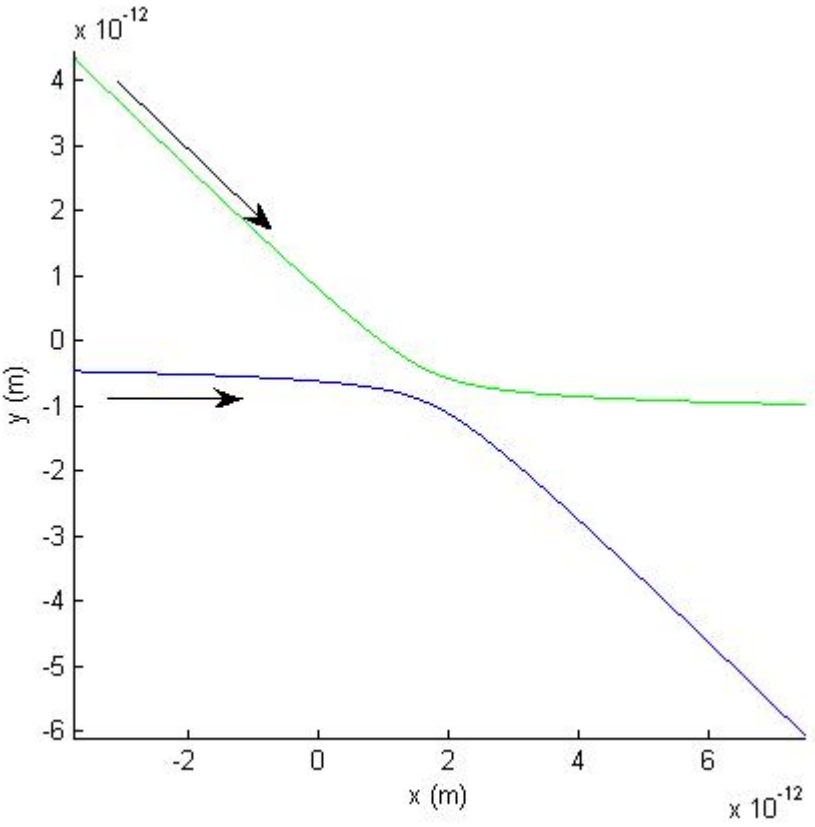

Figure 4.34 Head-on 45 degree coulomb collision, Argon ions ~5 keV

In the above figure, the horizontal, blue particle begins directed along the x-axis and the green starts at 45 degrees, both directed towards the origin. Notice that the collision occurs over a length scale of picometers and that the particle's center of mass at closest approach is displaced from the origin by a little more than a picometer. The start distance was chosen so that the interaction potential was minimal at the beginning of the simulation and the effect on the dynamics was negligible. The range of possible collisions is scanned by moving one of the particles inward so that the two particles reach the center at different times. This produces the family of curves shown in Figure 4.35. 'Beginning particle separation' is the amount of lead given to the horizontal particle measured along the radial path. Additionally, for this relatively simple case, the collision

process can be modeled analytically, and this derivation is presented for the interested reader in Appendix C.

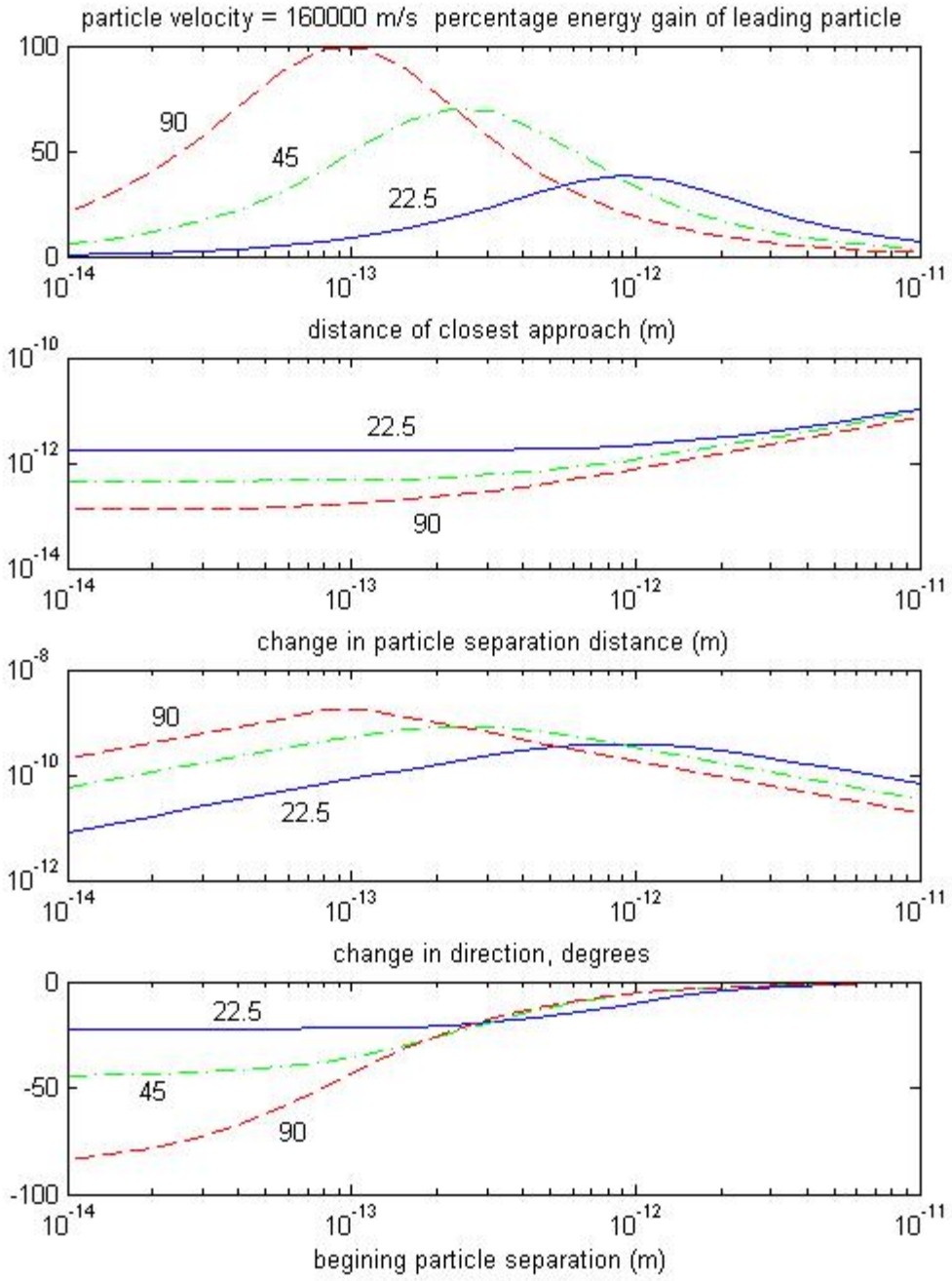

Figure 4.35 Effects of particle separation on central 2-body coulomb collisions vs. initial particle separation (90 degrees-red dashed, 45 degrees-green dashdot, 22.5 degrees-blue solid)

The three sets of curves are for different angular separations between the paths, 22.5, 45, and 90 degrees. The first subplot of Figure 4.35 shows the energy gain of the leading particle after the collision. The leading particle is always observed to gain energy in the interaction, irrespective of separation and angle. Notice that at the peak of the 90 degree curve, all of the energy of the lag particle is transferred to lead. The acute 45 degree collision is able to transfer more than half of the energy between the particles at peak. As the angle is reduced, the ability to transfer energy between ions is reduced. The curve is symmetric in semilog space, with small separation collisions having equal effect as the larger separations.

The second subplot shows that the closest approach asymptotes for the small separation, head-on collisions. The distance then monotonically increases as the separation grows to glancing collisions. For these glancing collisions the closest approach distance asymptotes to the beginning particle separation.

The third subplot shows the change in the difference between the two particle's radii from the beginning to the end as a function of the initial particle separation. It is also symmetric in semilog space, with the largest effect for each respective energy transfer peak case.

The last subplot shows the angular change of the trajectory of the lead particle. For small separation cases, the particles exchange places, which corresponds to the asymptote of initial beam angular separation. As the separation increases, the directional change asymptotes to zero for the glancing collisions. The angular change for the peak case is half the initial beam angle which corresponds to the lead particle carrying all the

momentum of the system along the original center of mass trajectory. This is also the inflection point for the plots in the last subplot.

So now we know that equal velocity ions will always transfer energy from the lag particle to the lead. The situation becomes slightly more complex when the initial velocities are slightly different. Similar studies were conducted and the energy transfer is still always from the lag to the lead. The position of the particles is the deciding factor as opposed to the relative energy of the particles. For example, when two particles begin at the same radius but one is slower than the other, the faster energetic particle will reach the center first and will gain energy from the slower particle. Now if the starting positions are altered so that the particles reach the center at the same time, the situation is similar to a head-on case where the particles exchange paths except that now some energy is exchanged to maintain the total system momentum. Since we wish to apply this to the problem of synchronization, only the glancing small angles are of interest to us where the total energy transfer is small and the probability of collision much greater. For these glancing collisions, the rule to take away is that the particle that reaches the center first takes energy from the lag particle. This is the key property which will combine with the trap dynamics to produce the synchronization. This study looked at the microscopic interaction, but is the group interaction between bunches on the beam paths strong enough to account for the synchronization? To answer this, the ions in the above code are replaced by Gaussian distributions of charge moving through a space corresponding to the IEC scale size.

Derivation of the two-dimensional particle bunch interaction law

A two-dimensional distribution of infinite rods was chosen to agree with the OOPIC modeling space and it is convenient that the two-body collision occurs entirely in a single plane. The electric field produced by a Gaussian-shaped particle bunch is derived by applying Gauss's law and integrating over the particle distribution. The dynamics model employed assumes that bunches retain their initial shape due to transverse focusing fields. Since the shape doesn't change, each ion in the colliding bunch must be accelerated by the electric force of the target bunch equally, with the acceleration being that of a test charge at the center of the colliding bunch. This model features an electric field which drops to zero at the bunch center, so that co-centric bunches would experience no acceleration. Clearly, the particles within the bunch would tend to fly apart, but the center of mass of the ions would stay stationary. The cloud model is thus meant only to deal with the synchronizing behavior between bunches and assumes the individual bunch shape is a separate behavior. If synchronization between bunches can be observed with this simple model, we can have confidence in the reason behind the synchronization. However, the removal of internal degrees of freedom within bunches may be too severe as it eliminates damping and dispersion in the simulations, so the model may be somewhat limited in scope as bunches cannot evolve. The two-dimensional electric field is given by Gauss's law.

$$\int E \cdot dS = \frac{q_{enclosed}}{\varepsilon_o} \quad \Rightarrow \quad E_r = \frac{e}{r\varepsilon_o}\int_0^r n(r)\, r dr \tag{4.26}$$

A gaussian distribution is assumed, defined in terms of the peak density and the variance of the distribution.

$$n(r) = n_o e^{-\frac{1}{2}\left(\frac{r}{\sigma}\right)^2} \quad \Rightarrow \quad E_r = \frac{e n_o \sigma^2}{\varepsilon_o r}\left[1 - e^{-\frac{r^2}{2\sigma^2}}\right] \tag{4.27}$$

As shown graphically in Figure 4.36, the electric field is equal to zero at zero radius, increasing to a peak near the standard deviation and then decaying away at increasing radius. The 'hollow core' of this field distribution suggests that collisions of bunches with little center of mass separation will exchange little energy. This provides a self-selection mechanism where bunches are 'jostled' via collisions until they happen to fall in line with the bulk synchronized population. Once co-located with the bulk center, the bunch will exist in the 'hollow core' of the interaction potential, essentially 'synchronized'.

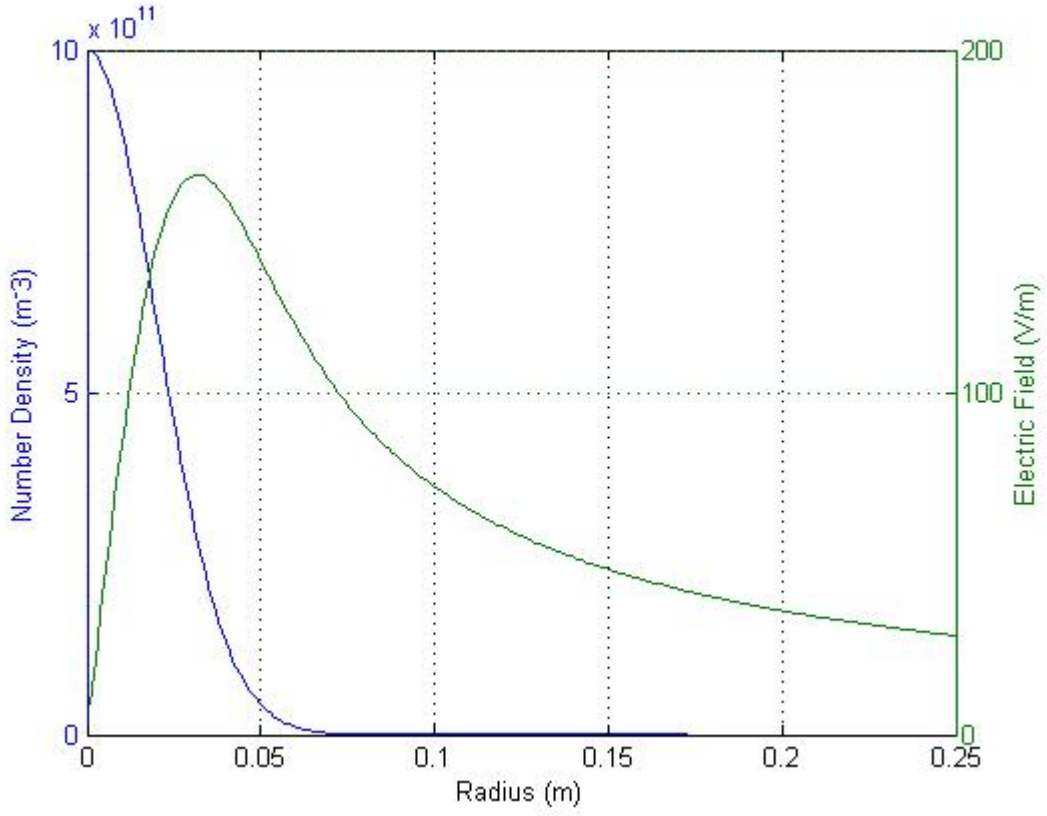

Figure 4.36 Two dimensional bunch interaction law for $n_o = 1 \cdot 10^{12}$ m^{-3}, $\sigma = 0.02$ m

2 particle cloud collision model

In this model 2 bunches are 'fired' toward the device center from a distance corresponding to the OOPIC and lab device sizes. Bunches interact the entire time via the force law derived in the previous section. The characteristic parameter values for the simulations include beam angle of 45 degrees, sigma = 0.02 m, initial starting radius of 0.4 m, and the lead particle is initialized inward of the start point. A non-relativistic Eulerian first order method uses 100,000 computational steps to traverse ~0.8 m for a step size of 8 micrometers. The step size was systematically reduced until the change in the trajectories was no longer observable on plots. An initial velocity of 160,000 m/s corresponds to the peak velocities achieved as singly charged Argon ions pass the cathode grid, as shown in Figure 4.42. The device size is assumed to be about 20 centimeters radius, and the start point is thus chosen to be outside of this with particles shot toward the center. The range of possible collisions is scanned by moving one of the particles inward so that the two particles reach the center at different times. There are no background fields in this model.

The bunch interaction falls off with increasing separation distance and is still significant at the very start of the simulation. This complicates the model since in the real version, bunches begin at rest at the anode and would be continually pushing against each other. If the arbitrary start distance of this model is too large, particles will interact longer than is realistic. On the other hand, a fairly large distance is required so that both bunches are sufficiently away from the center at the beginning of the simulation. The sensitivity to this parameter is shown in Figure 4.37.

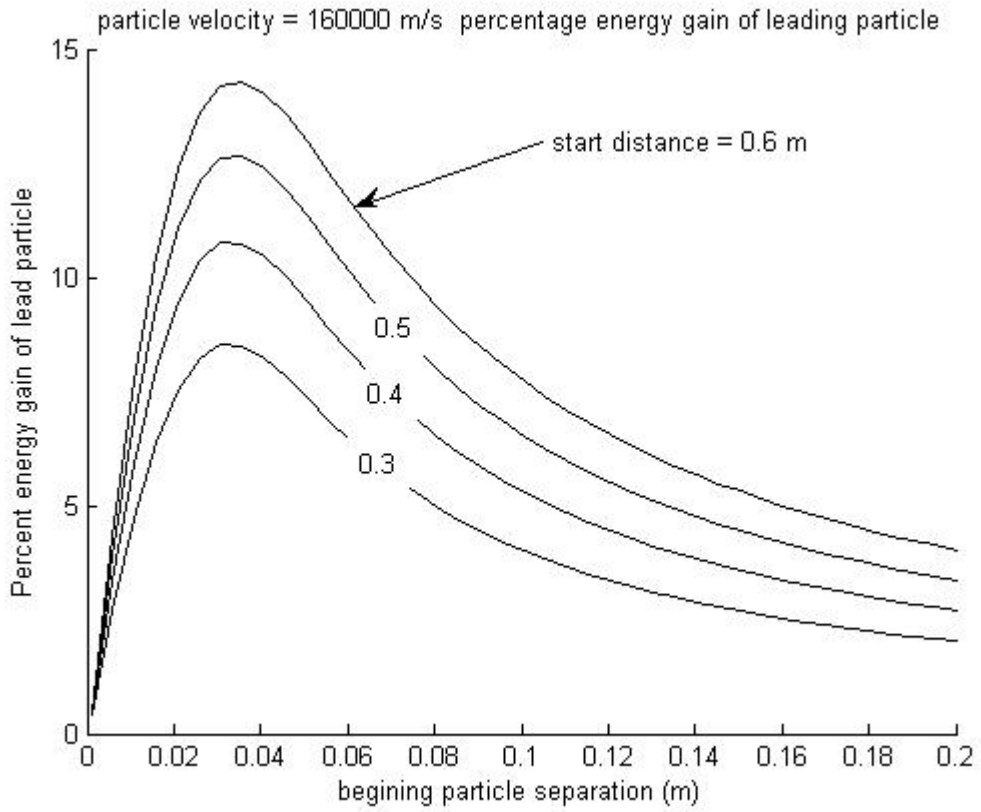

Figure 4.37 Percent energy gain for leading bunch vs. initial separation in 2-bunch collision model, various starting distances in meters, beam angle of 45˚, $\sigma = 0.02$ m, $n_o = 1 \cdot 10^{14}$ m^{-3}

As in the microscopic model, the interaction is measured by looking at the amount of energy gained by the lead bunch at the end of the simulation. The value of 0.4 meters was chosen as a nominal value since it is the smallest value where the two bunches can be separated from themselves and the device center by a full device radius of 20 cm. As is expected, increasing the start distance produces larger interactions due to the increase in interaction time. For the above range of values, the percent energy gain scales linearly with start position. This is a very strong dependence so while this model yields an enhanced understanding of collisions, the numerical values are not as precise as may be hoped. Similarly, the characteristic size of bunches also strongly affects the strength of the interaction.

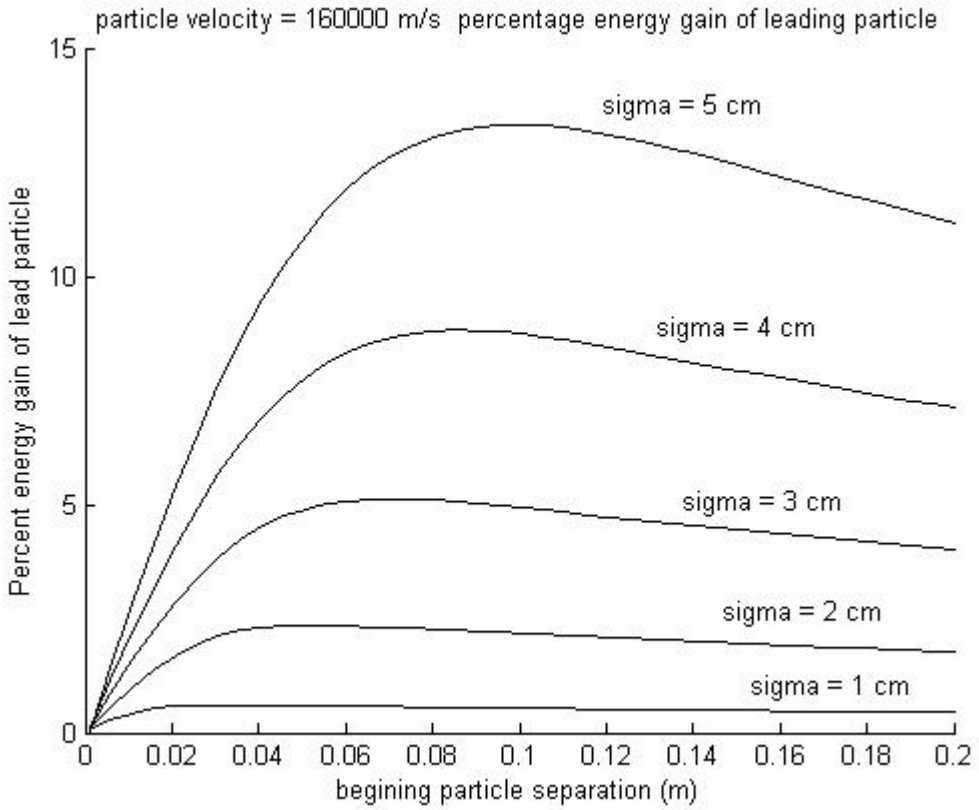

Figure 4.38 Percent energy gain for leading bunch vs. initial separation in 2-bunch collision model, various distribution sizes 'σ' in cm, beam angle of 45°, start distance = 0.4 m, $n_o = 1 \cdot 10^{13}$ m^{-3}

Figure 4.38 shows the variation in energy gain for different size bunches at the same peak densities. A large variation due to sigma size is evident. The OOPIC runs show that nominal bunch size near the anode is about 2 cm, but it spreads out significantly as it is accelerated into the center of the device. The above curves could be collapsed via a re-normalization to hold the total charge constant according to Equation (4.27). However, to better visualize the sensitivity to the chosen parameters, the above figure holds the peak density constant so that the sigma really changes the total amount of charge in the bunch, and consequently, larger sigmas show a bigger interaction. Again, this highlights a weakness in the model with respect to quantified predictions, but the results are useful in ascertaining behavior and scaling of the interaction. A more accurate

way to look at the effect of size would be to hold the total bunch charge constant instead of the density, but this was not necessary to proceed. Of primary interest is the amount of energy transferred for different peak densities over the range of possible collisions.

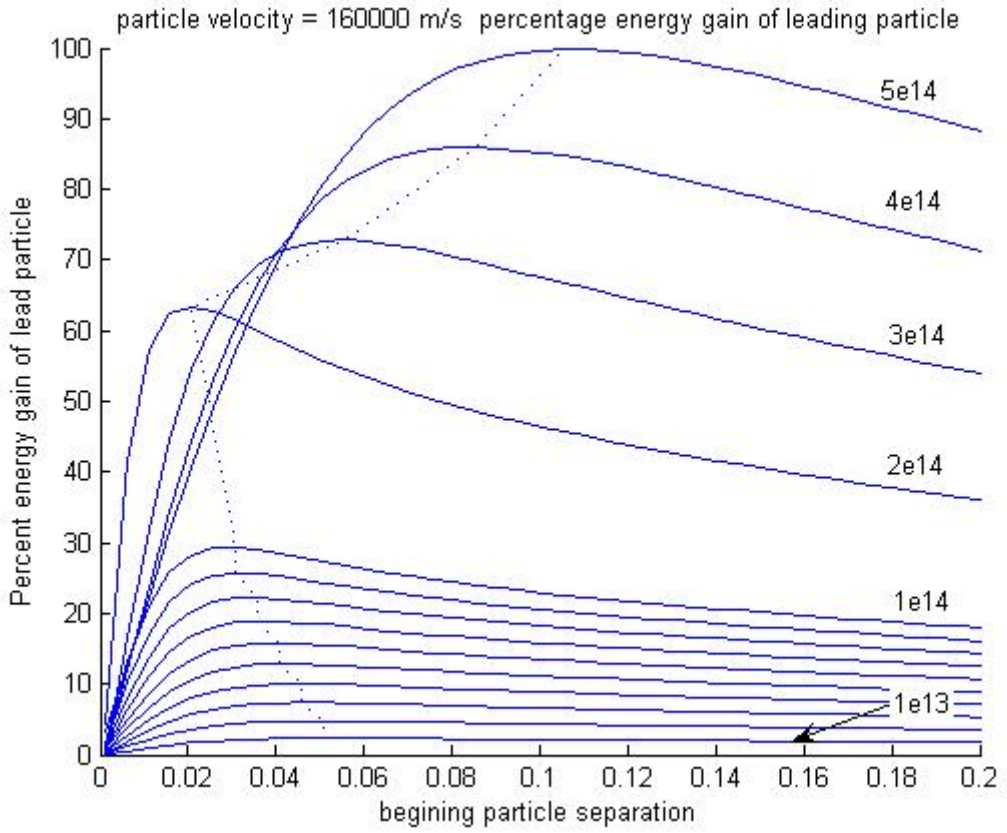

Figure 4.39 Percent energy gain for leading bunch vs. initial separation in 2-bunch collision model, Solid lines, $n_o = 1 \cdot 10^{13}$ m^{-3} to $1 \cdot 10^{14}$ m^{-3} by $1 \cdot 10^{13}$ m^{-3} and $1 \cdot 10^{14}$ m^{-3} to $5 \cdot 10^{14}$ m^{-3} by $1 \cdot 10^{14}$ m^{-3}, Dotted line is peak curve, beam angle of 45°, $\sigma = 0.02$ m, initial radius = 0.4 m

The family of density curves in Figure 4.39 shows the range of collision behavior. At lower densities, the amount of energy transferred between bunches is fairly uniform over the range of possible collisions (the x-axis). This is the essential, key behavior because it tells us that bunches will interact strongly despite being on separate beams and only 'crossing' in the device center. Furthermore, the interaction becomes quite large for even modest densities shown in the plot. This corresponds well with behavior of OOPIC

models, where severe disruptions are observed for peak bunch densities on the order of $n_o = 1 \cdot 10^{14}$ m^{-3}.

There are other interesting elements to note. First, as we expected, very small separations produce a small interaction due to the 'hollow-core' in the field. Non-intuitively, for a given separation, the larger density may not always give a stronger interaction. Also, for a given density, the peak energy transfer point is a separation always larger than the characteristic bunch size, σ. The peak (shown by the dotted line) moves inward with increasing density and then moves outward for very strong interactions. This peak line is quite interesting and is shown with another wrinkle below in Figure 4.40.

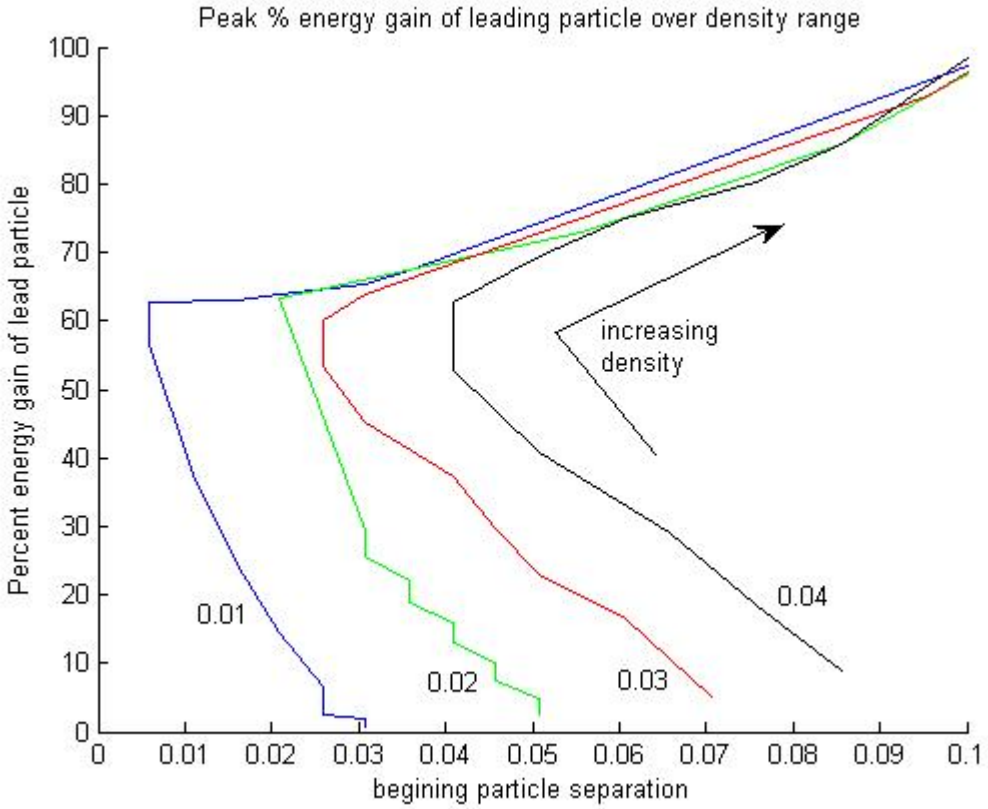

Figure 4.40 Peak energy gain of leading bunch vs. initial separation over density range curves for various distribution sizes, σ = 0.01, 0.02, 0.03, 0.04 m, beam angle of 45˚, initial radius = 0.4 m

Here the bunch size is varied and the peak line plotted for each one. Notice that as density is increased, the knee in the curve corresponds to the particular value of sigma. Also, after the knee on the curve is reached, the curves fall on top of each other. Thus for strong interactions the peak energy transfer collision is only a function of the initial separation. Using the above figure, we can say that when two Gaussian bunches on 45 degree beams interact with a separation of 5 cm, the energy transfer will never exceed ~70%. This value actually decreases for a 'closer' interaction which we would expect to have a greater energy exchange! Now most of the interesting non-intuitive behavior is for the stronger interactions where the bunch paths are severely disrupted by the interaction.

Calculation of time constant for development of synchronized state

While the strong interactions help to explain the instability observed at high densities, the weaker interactions can be examined to give a characteristic strength of interaction versus density. This can be then correlated to a time constant for the development of the saturated, synchronized state. The development will progress as follows: First, the amount of energy transferred in by a characteristic collision is found as a function of density, using the above collision model. The kinematics of the background field are then used to calculate the characteristic relative position change associated with a given energy transfer. Then a time constant will be defined as a bunch advancing a given distance in the system due to the energy transfer, all as a function of overall system density.

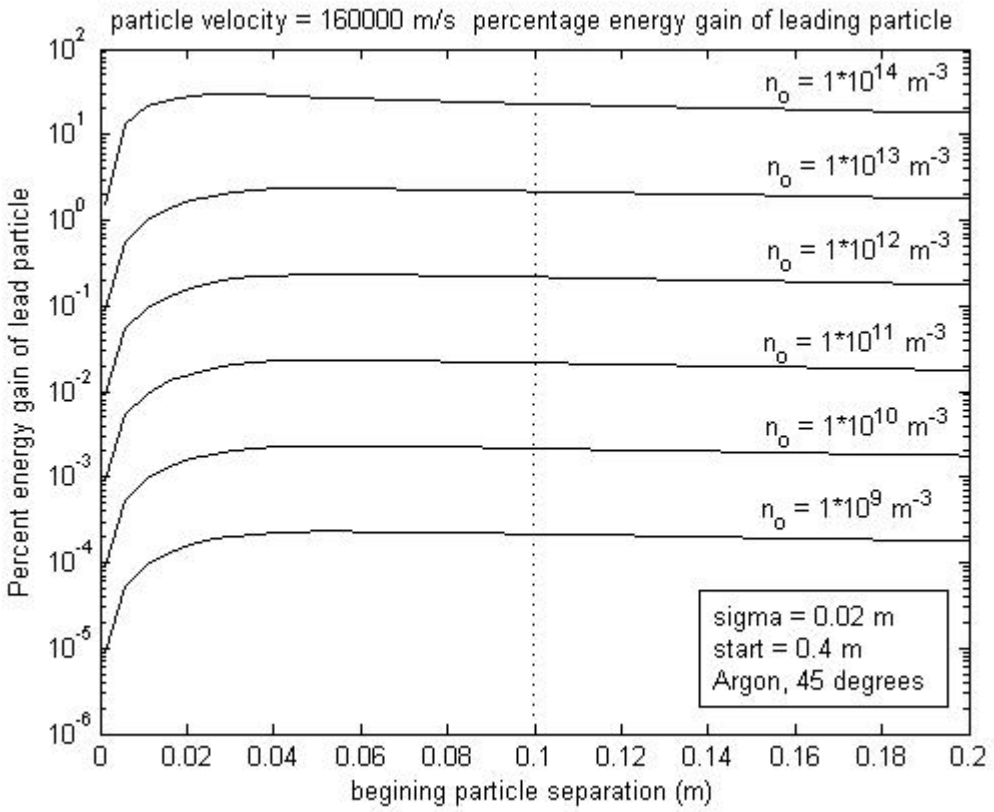

Figure 4.41 Peak energy gain of leading bunch vs. initial separation for various densities, dotted line defines values for calculating time constants, σ = 0.02 m, beam angle of 45˚, initial radius = 0.4 m

Using the 2-bunch collision model, the characteristic energy transfer for a given density is taken at a particle separation of 0.1 m. This is depicted in the semilog plot of Figure 4.41 as a dotted line. 0.1 m is chosen as a characteristic value as the interaction is relatively flat except for separations less than the sigma of 0.02 m, which would correspond to bunches which are already synchronized. The characteristic values define the growth rate per pass as a function of density, which is plotted in Figure 4.44, and is well approximated as a linear relationship. Now we know that as a bunch gains or loses energy, its period in the IEC will change. The change in period brings the two bunch centers physically closer on the next pass. This change in period defines the time constant for the interaction to bring two bunches into synchrony. To perform this

conversion, the relationship between period and energy for the IEC must be examined. The equatorial line potential for the OOPIC models is shown in Figure 4.42.

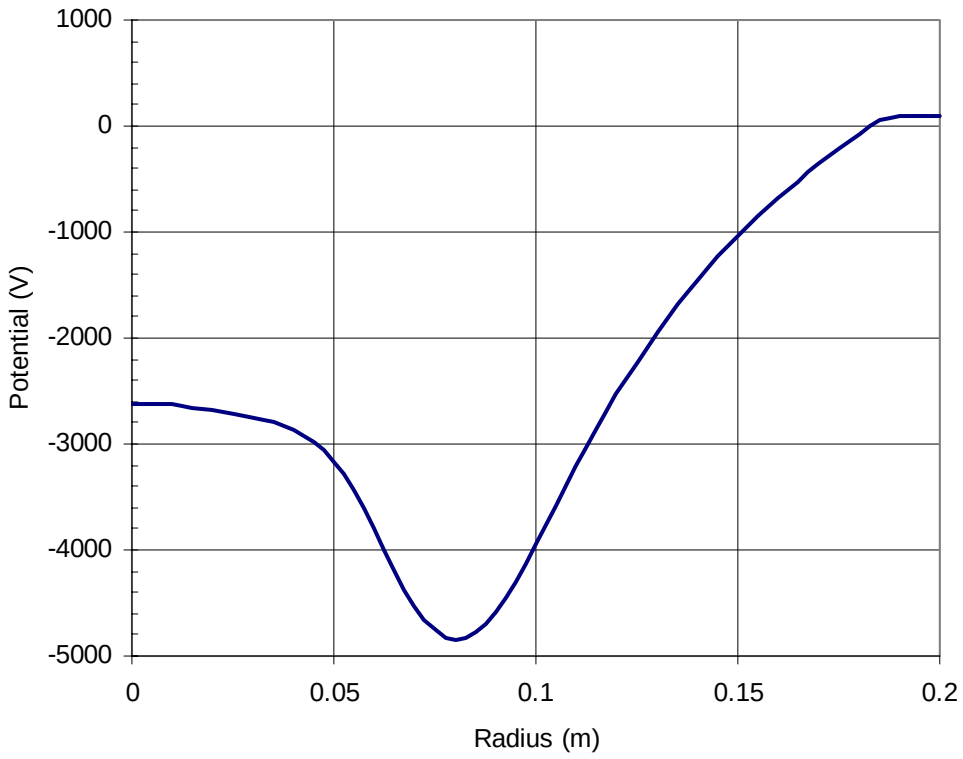

Figure 4.42 Equatorial line potential for OOPIC models and 2-bunch collision models with -2 kV grid at 5 cm, -10 kV grid at 8 cm and -2 kV grid at 10 cm, -200 V at 13 cm, and 100 V anode grids at 20 cm.

The above potential is used to derive the data via numerically measuring the period of bunches in a simplified OOPIC simulation. A very low density particle group is initialized in the device center with a particular streaming energy. The amount of time required for the group to travel to its reflection point and return to the device origin define the time for a pass, which is called the one pass period for this study. The usual starting condition for an ion in the OOPIC simulation is at 16 cm radius at only a few eV, so that the nominal energy in the device center is 1,927 eV. The peak ion energy is almost 5 keV, smaller than the actual cathode potential of 10 kV because the particles

move along the center of the beam path, away from the actual grid. The derivative of the period with energy is then found with a simple differencing scheme. This is shown in Figure 4.43.

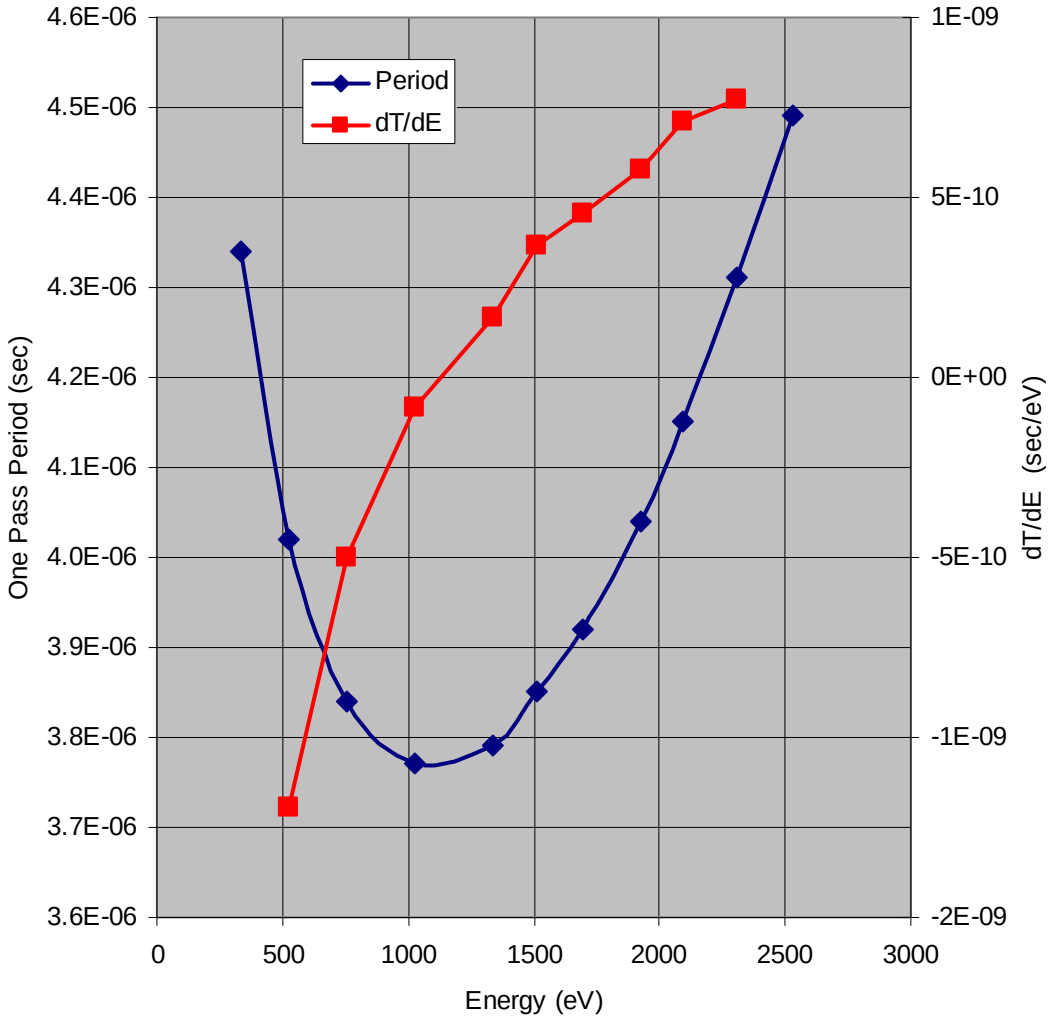

Figure 4.43 One pass period vs. core energy and derivative for OOPIC models

The derivative is positive for ions with core energies greater than ~1,100 eV. This implies that the kinematic criterion for synchronization is satisfied for the nominal case as well as a starting point as far down the well as ~14 cm. The derivative can be normalized by the nominal period and core energy, and fitted to a linear law for the

region of interest as in Equation (4.28). At the nominal ion energy of 1,927 eV and one pass period of $4 \cdot 10^{-6}$ sec, the value of the normalized derivative is evaluated as 0.276.

$$\frac{dT}{dE}\frac{E_o}{T_o} = 0.566\left(\frac{E}{E_o}\right) - 0.29, \quad R^2 = 0.9709, \quad 1{,}338\,eV < E < 2{,}306\,eV \tag{4.28}$$

The next step is to relate a given change in period with distance in the device:

$$\frac{\Delta x}{\Delta T} = \frac{r_a}{\frac{T_o}{2}} \Rightarrow \frac{\Delta T}{T_o} = \frac{\Delta x}{2r_a} = \frac{1}{2} \tag{4.29}$$

where the device radius corresponds to half of a pass. Thus the required change in period to move a bunch ahead one device radius in path distance equates to one-half of the total period. This factor of one-half is substituted into the value of the normalized derivative to find the amount of energy transfer required to bring a bunch into synchrony.

$$\frac{\Delta E}{Eo} = \frac{\Delta T}{To}\frac{1}{0.276} = 1.81 = 181\% \tag{4.30}$$

Now the time constant for synchronization in passes is calculated as the total amount of energy transfer calculated above divided by the amount of energy transferred per pass for a given density. This relation is portrayed as the secondary axis in Figure 4.44.

$$\tau_{synchrony} = \frac{1.81}{\left.\frac{\Delta E}{E_o}\right|_{per\ pass}} \quad [passes] \tag{4.31}$$

One can see that at the higher densities of interest for an eventual energy producing system, the synchronization occurs on very fast time scales. The high strength of the interaction is ultimately not compatible with a stable, gradual process of small energy transfers. This supports the observed high density behavior of large scale

disruptions which nonetheless exhibit a collective nature, i.e. the disruptions are manifested as waves of energetic, ejected particles.

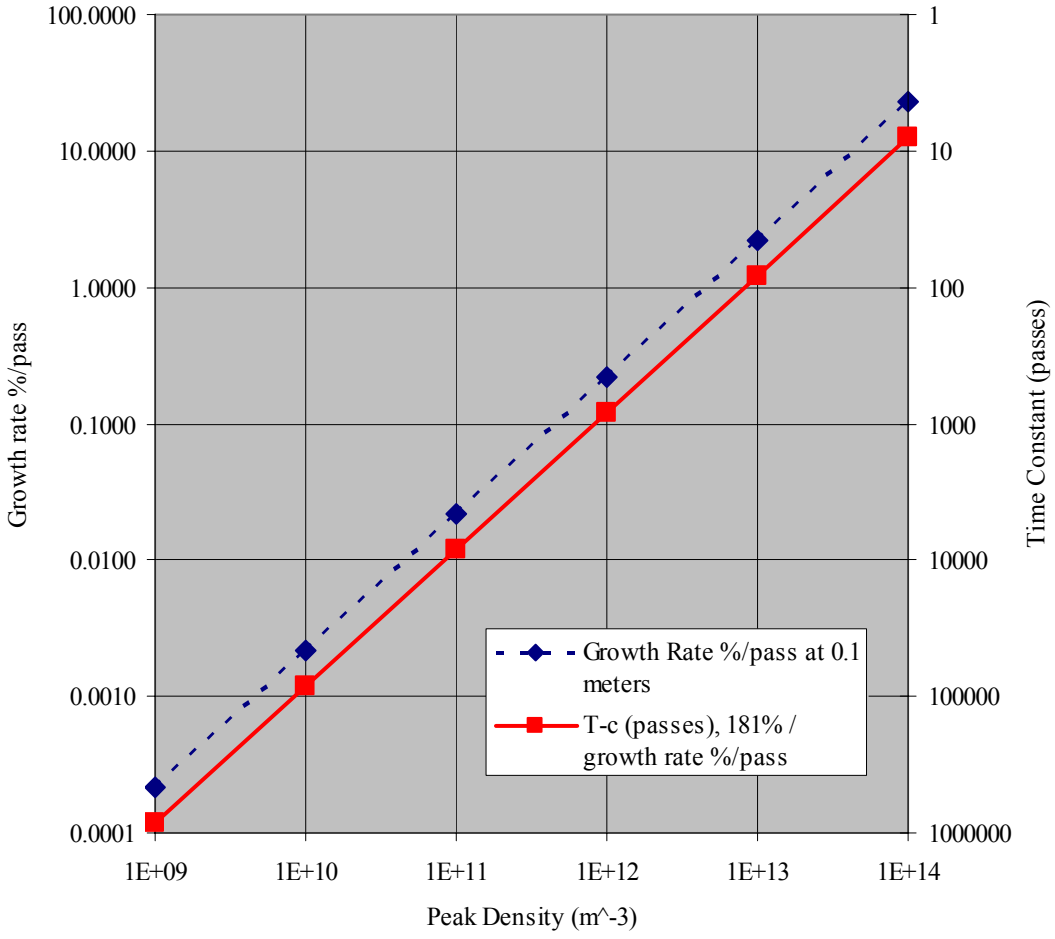

Figure 4.44 Growth rate percentage per pass vs. bunch peak density and time constant (passes) vs. bunch peak density

The above calculations show how the time for a synchronized state to develop varies with density. Ultimately, the same process which synchronizes 2 individual ions is shown to synchronize 2 bunches, even if they are on separate beams. The last section in this chapter will seek to expand this understanding to interactions of a full 3D system of many bunches.

4.5 3-D Cloud model of interbeam synchronization

The previous section shows that the collisions between two ions in the multiple grid IEC will tend to be synchronizing if the kinematics of the well is correct and the ions are confined transversely to the radial path direction. Does the same behavior result when we consider the more realistic three dimensional interaction of more than 2 bunches of ions? Also, the simple two-body study ignored the reflection region, which may significantly affect the interbeam interaction since bunches have a high residence time at a fixed position. The 3D cloud model presented here seeks to answer these questions.

The idea behind model is to create a simplified version of the OOPIC models that could more easily isolate the specific mechanisms responsible for synchronizing bunches between the various beams. The trick is make the right level of simplification, so that the behavior still appears while being simple enough to analyze. The cloud model consists of an N-body particle model with electrostatic accelerations from all the other bodies and a fixed background field. Further, the ion bunches are confined to radial paths. This assumption is justified by the transverse confinement provided by the multiple grids as observed in the OOPIC models. Also, the bunch sizes are assumed to be constant in time, so that the state of a bunch is defined solely by its radial position and velocity. The characteristic MIT lab device cases presented here follow a 'star' pattern of twelve intersecting beams with two bunches moving along each beam line. The grid pattern and beam paths are depicted below.

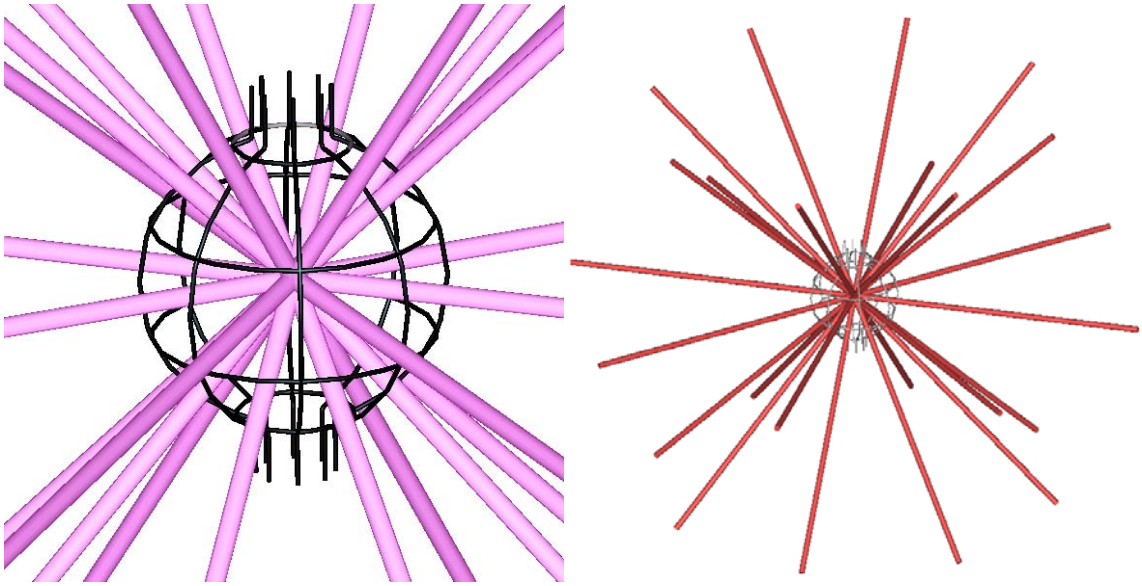

Figure 4.45 MIT grid model of 12 intersecting beams used in cloud model

Additional studies were conducted with bunches on a single beam line and 2-D planar patterns of fewer beams, which will be discussed further below. This model is simple enough to isolate the interaction between bunches, but it will not address the evolution of bunch sizes and the role of transverse confinement and energy build-up. These issues introduce enough complexity that the OOPIC model with its statistical approach on thousands of bodies provides a more accurate model to investigate those behaviors. The lack of those extra degrees of freedom means that the cloud model is better suited to examining the stability of the saturated synchronized state as opposed to the evolution of the synchronized state.

Algorithm and Force Law

The interaction acceleration for the three-dimensional model is derived similarly to the two dimensional model given by Equation (4.26).

$$\int E \cdot dS = \frac{q_{enclosed}}{\varepsilon_o} \quad \Rightarrow \quad E_r = \frac{e}{r^2 \varepsilon_o} \int_0^r n(r) r^2 dr \tag{4.32}$$

'r' is now the radial direction in spherical coordinates. As before, utilize a Gaussian bunch shape and integrate to obtain an expression for the electric field that now includes an error function. It is similar to the two-dimensional case, equal to zero at zero radius, increasing to a peak near one standard deviation and then decaying away at increasing radius.

$$n(r) = n_o e^{-\frac{1}{2}\left(\frac{r}{\sigma}\right)^2} \quad \Rightarrow \quad E_r = \frac{e n_o \sigma^2}{\varepsilon_o r^2} \left[\sqrt{\frac{\pi}{2}} \sigma erf\left(\frac{r}{\sqrt{2}\sigma}\right) - r e^{-\frac{r^2}{2\sigma^2}} \right] \tag{4.33}$$

The simulation algorithm is a simple integration scheme, where the initial positions and velocities are propagated forward in time using the fourth-order Runge-Kutta scheme implemented in Matlab. The acceleration on each particle is the sum of the background electric field and interparticle forces projected along the path. The centerline background field is shown below in Figure 4.46, with no variation in the transverse direction. The deeper potential well for the lab experiments was found via a simulated annealing routine developed by Carl Dietrich, details of which can be found in his doctoral thesis (projected graduation February 2007). The background potential values are determined via interpolation of a stored array of values, as a good-quality analytical fit was not found.

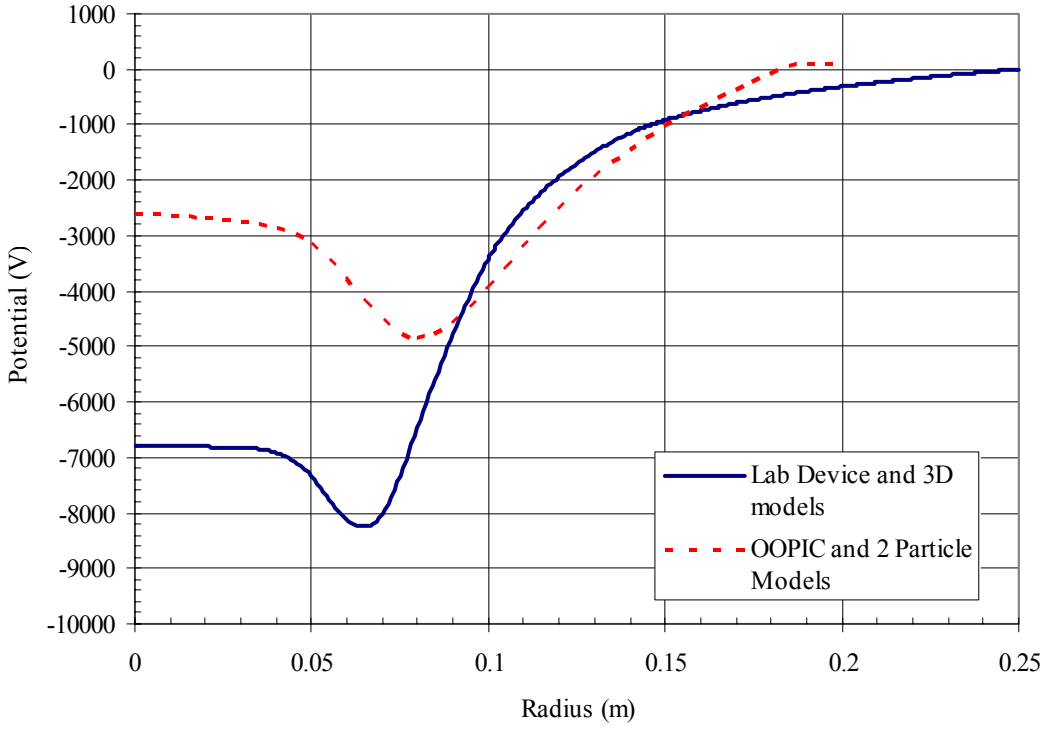

Figure 4.46 Solid line - Center line potential for characteristic MIT lab experiments with 10 kV cathode potential, used in three dimensional synchronization model, Dashed line – Equatorial line potential for OOPIC models and 2 particle collision models

The minimum potential is somewhat less than the cathode value of 10 kV due to field relaxation in the grid opening. Also note that the anode reflection region is relatively flat which serves to satisfy the kinematic criteria for synchronization. Bunches spend most of the time near the anode regions which is important since the inter-bunch forces are still strong there as opposed to short-duration, larger-force collisions near the device center.

The initial velocities of each bunch are calculated by assuming the bunch will have a kinetic energy equal to its potential energy at the specified initial position. The potential energies of the particles are defined so that all bunches start with a given turn-around location near the anode, in most cases at a radius of 18 cm. The turn-around

location must be down the potential well so as to allow for bunches to gain energy via collisions and still be confined. Bunches that gain enough energy so as to climb out of the specified potential are assumed to feel a constant background electric field equal to the value at the specified potential boundary at radii greater that that boundary (25 cm for all cases).

The main parameters investigated were the initial position spread of bunches, the individual bunch width, the peak bunch density, and the duration of the simulation. Studies of the stability of synchronization generally started all bunches near the anode, spaced randomly within a specified 'window'. For example, all bunches would start with a path position value between 17 and 18 cm. The duration of the simulation varied between 10 and 1000 passes.

The absolute and relative tolerance settings of the built-in Matlab 'ode45' integrator are both set to '1e-6' such that the total energy gain of a bunch per pass due to numerical errors is below 0.003%. This high level of accuracy is needed to produce reliable results over 100 passes. The error was determined by propagating the trajectory of a single bunch over many passes and examining the change in total energy, which ideally would be unchanged. Test simulations with inter-particle forces turned off at lower tolerances will show bunches moving relative to each other, which obfuscates the synchronization motion we are interested in. The two-body simulations showed that an interaction which changed the bunch energy on the order of only a few percent per pass was sufficient to account for the synchronization. The tolerance settings thus give error build up per pass values far below the amount of energy gained/lost due to inter-bunch interactions.

The simulation of 24 particles over 100 passes takes about 5 minutes to run on a 3 GHz pentium4, windows PC. The long-duration runs of 1000 passes take about an hour to execute at the same tolerances, but begin to suffer unacceptable error build-up. Increasing the tolerances for these long-duration simulations begins to push the run-time on the desktop to many hours or days, limiting its usefulness. The typical Matlab code for the N-body simulation is included in the appendices for reference.

Results

The first idea for the model was to reproduce the progression from an initially random multi-beam state to a synchronized situation. This, however, was not to be, as bunches would coalesce somewhat, but fell far short of the fully synchronized state observed in OOPIC. A wide variety of parameters were tried and the simulation run to 1000 passes, but the groups of quasi-synchronized bunches never fully swept in the remaining bunches. Several geometries were sampled, including the standard 24 bunch, 12 beam model, an 8-bunch, 4 equatorial beam model and a single beam path with varying numbers of bunches. The static nature of the bunch sizes and lack of transverse velocities are two possible reasons for the failure to synchronize in this simplified model. The model is still useful, however, as when the bunches are started in a synchronized state, they can continue to maintain that state if the bunch density is within an acceptable window and the initial state is sufficiently synchronized. The densities that show good synchronization were initially found via trial and error, and more extensive data on acceptable densities will appear at the end of the section. The effect of initial bunch spread will be discussed first.

Effect of initial spread in relative position on synchronization

If the initial spread is too large, synchronized bunches will tend to separate despite having the 'ideal' peak densities for synchronization. The following graphs show typical behavior of a bunch separated from the group after 100 passes for an initial 24-bunch, 12-beam group spread of 1.8 cm at the anode, 1/10 of the path radius. This means that all bunches were started close to the anode along each respective path, but at slightly different radii and velocities. For the synchronization to be steady on the order of hundreds of passes, initial separations on the order of 1/100 of the path radius near the anode are required.

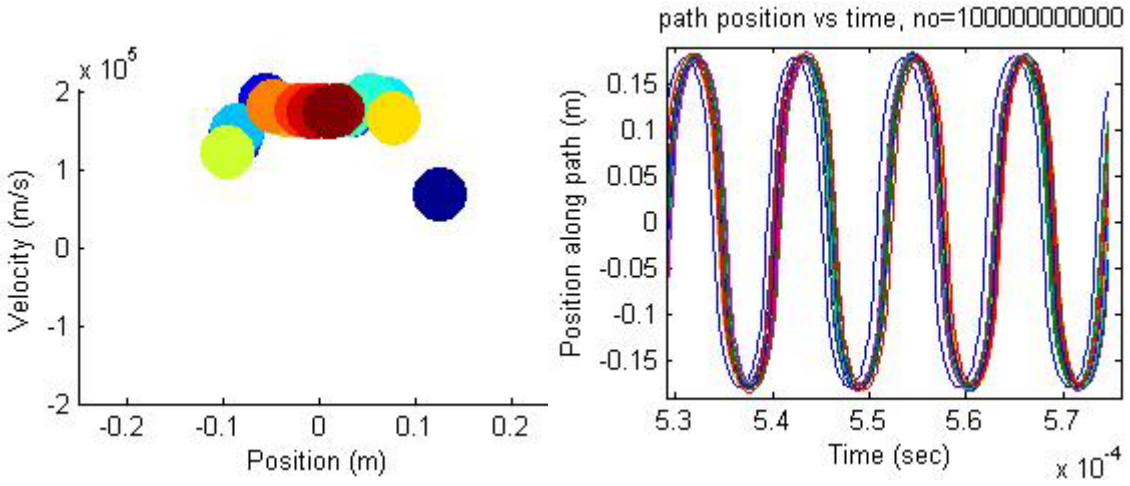

Figure 4.47 Particle ejection from an initially synchronized '1/10' state, $n_o = 1 \cdot 10^{11}$ m^{-3}, *left* – snapshot of path velocity (m/s) vs. path position (m), *right* - path position (m) vs. time (sec).

Notice that the total spread in radius varies widely from the anode to the center region. Although bunches all begin at the anode with a few centimeters of each other, as they pass through the center of the device the separation grows to tens of centimeters. This means that the distance between any given bunch and the group mean will be significant for a typical bunch. One may have expected a situation where the zero

in the electric field for a bunch at the bunch center would serve as a natural 'attractor', with the synchronized state such that as bunches pass through each other in the device center the forces would go to zero. The stretching of bunches through the center counteracts this by ensuring that the interbunch forces will be significant and energy will be exchanged on most passes through the device. Now a tighter initial configuration will reduce the interbunch forces and the associated energy exchange, and we see that for a given density the tighter initial conditions stay synchronized longer. Notice the difference in the spread of the bunch positions between Figure 4.47 and Figure 4.49.

Ideally we would like to visualize the relative motion of the bunches, discounting the base oscillatory motion in the potential well, so as to determine which particles are 'ahead' or 'behind' the group in position and velocity. If relative phase is examined continuously, the results are difficult to decipher. The picture is made clearer by only looking at the system when the background motion is the same every time we observe the system. Figure 4.48 shows the relative phase space for bunches, specifically plotted each time they are reflected at the anode. This plot is similar to the Poincare plots used to describe the 2-ion mapping results shown in Figure 4.22 from Geyer and Tannor, 2002 [40]. Each dot represents the state of that particular bunch at a given state, in this case turning at the anode. Specifically, when each bunch undergoes a radial velocity direction change, the mean location for all of the bunches is calculated and the relative position is calculated as the difference for these two values. This process is done for each individual particle. This picture is even more complicated because while one bunch is at the anode, the group mean may be at a greater radius due to energy differences between bunches, resulting in a positive relative position on the plot. One can see that some negative

relative positions are indeed plotted in Figure 4.48. The idea is to get a repeated picture of a system keeping some aspect of the oscillation constant between each pass. By 'connecting the dots', one can thus track the bunch as it changes its relative phase from pass to pass. Observe the asymmetry in the relative phase space. This plot shows that the runaway bunch is ahead of and slower than the mean group motion at the anode.

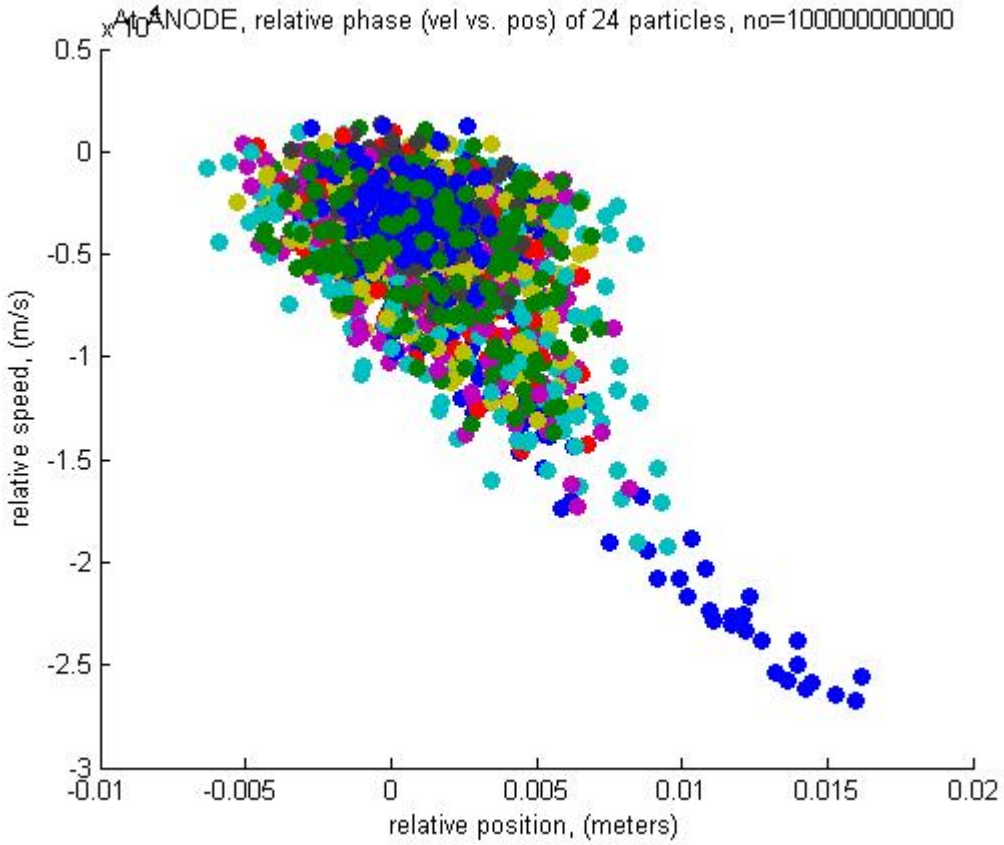

Figure 4.48 Relative speed vs. position for stable synchronization after 100 passes, $n_o = 1 \cdot 10^{11}$ m^{-3}, initial '1/10' spread of 0.018 m.

Now, instead of the symmetric cloud we would expect for long-lived situations, we see that the runaway orbit grows more funnel-shaped with consecutive orbits. Notice that besides the dark blue runaway bunch, several other bunches also show a non-circular orbit (depicted as separate colors).

Now we decrease the initial bunch separation to 1/100 of the path and the synchronization is stable after 100 passes, and the phase space cycling is observed to be more symmetric.

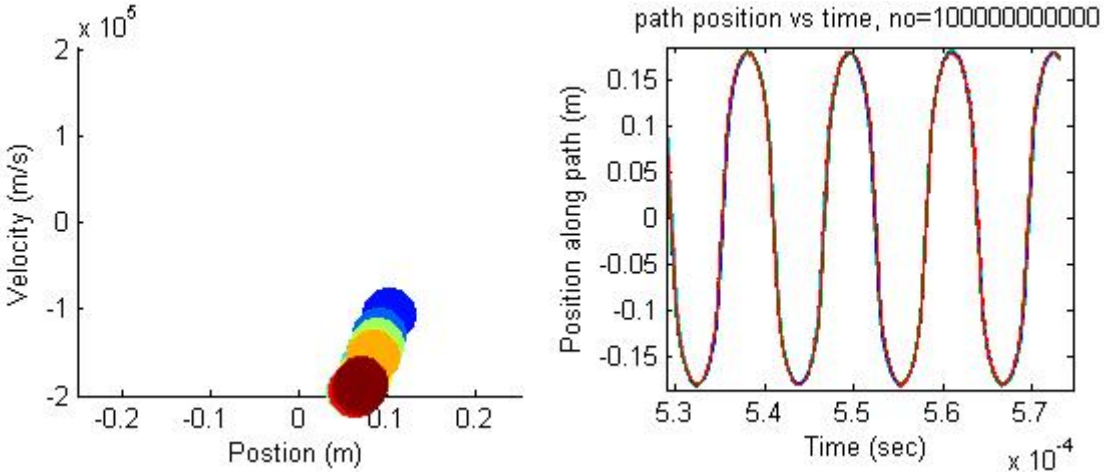

Figure 4.49 Steady-state synchronization from initially synchronized '1/100' state, $n_o = 1 \cdot 10^{11}$ m^{-3}, *left* - path velocity (m/s) vs. path position (m), *right* - path position (m) vs. time (sec).

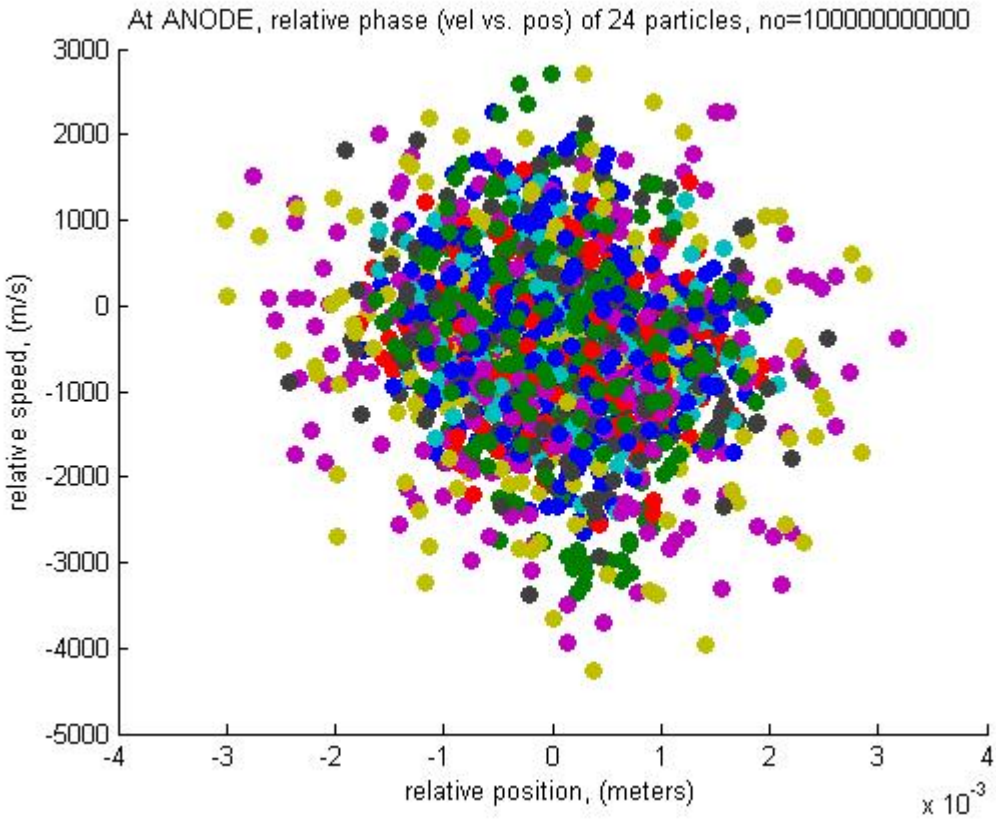

Figure 4.50 Relative speed vs. position for stable synchronization after 100 passes, $n_o = 1 \cdot 10^{11}$ m^{-3}, initial '1/100' spread of $1.8 \cdot 10^{-3}$ m. Phase plotted when each bunch reflects at anode.

The stability of the tighter group can be seen in the phase map of Figure 4.50. The steady-state size of the phase space 'cloud' is a function of the bunch peak density. Notice that the initial separation from the bunch mean is preserved with some color bunches residing close to the mean (red, blue), while others orbit at the edge (purple, tan). By picking out a few of the individual bunches and tracking the progress through phase space, the cycling behavior can be seen as crude orbits about the mean motion. The individual paths are represented in Figure 4.51 by different colors and roughly self-similar in terms of scale. This plot is similar to Figure 4.50 except that now successive orbits are connected by line segments, denoting the phase space motion from pass to pass. Remember that this is still a Poincare plot, a snapshot at of the relative phase when

bunches are at the anode. The orbit tends to be smoother when the relative speed is negative, corresponding to the bunch being slower than the mean. It tends to be more erratic when the relative speed is positive. Also notice that the orbit is slightly 'stretched' towards the bottom right of the graph, similar to the more exaggerated 'funnel' shape of phase space in Figure 4.48.

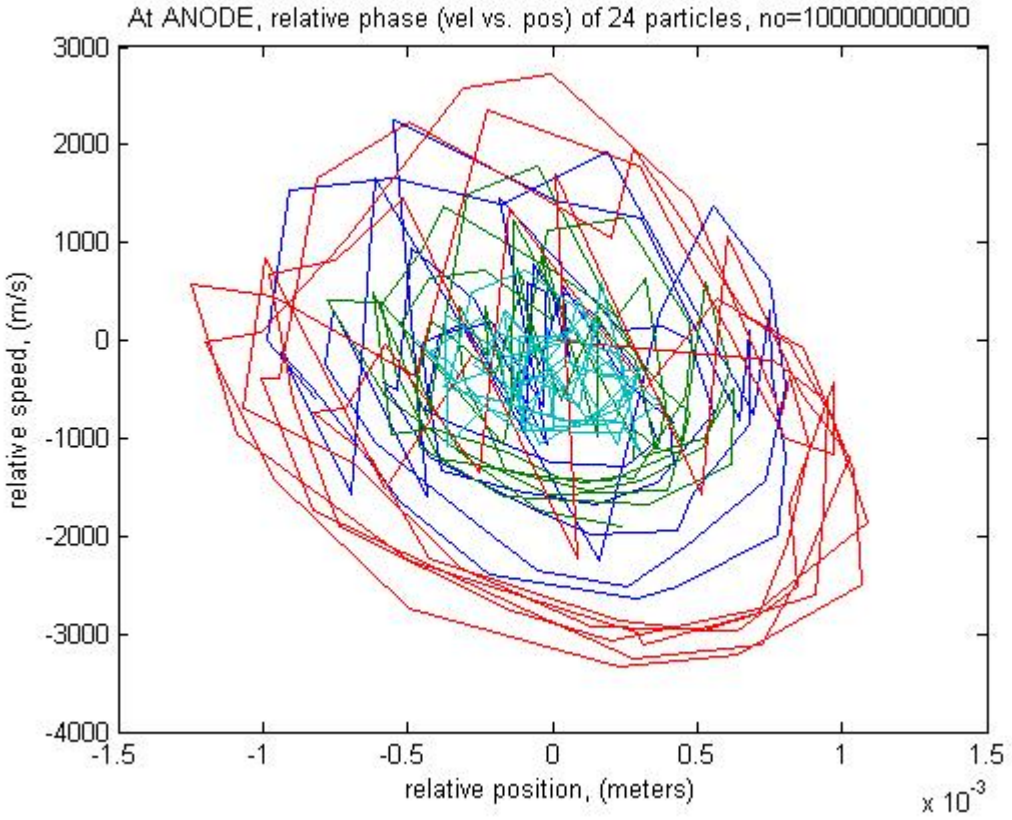

Figure 4.51 Relative speed vs. position for stable synchronization after 100 passes, n_o = $1 \cdot 10^{11}$ m^{-3}, initial '1/100' spread of $1.8 \cdot 10^{-3}$ m. Four separate bunch paths, phase plotted when bunches reflect at anode.

An alternative view of the cycling behavior is generated by keeping track of the order of bunches for consecutive passes near the anode, much like a leader board updated every lap in a car race. The following racetrack plot shows the 8 equatorial plane particles (out of 24 total) over the course of 14 passes.

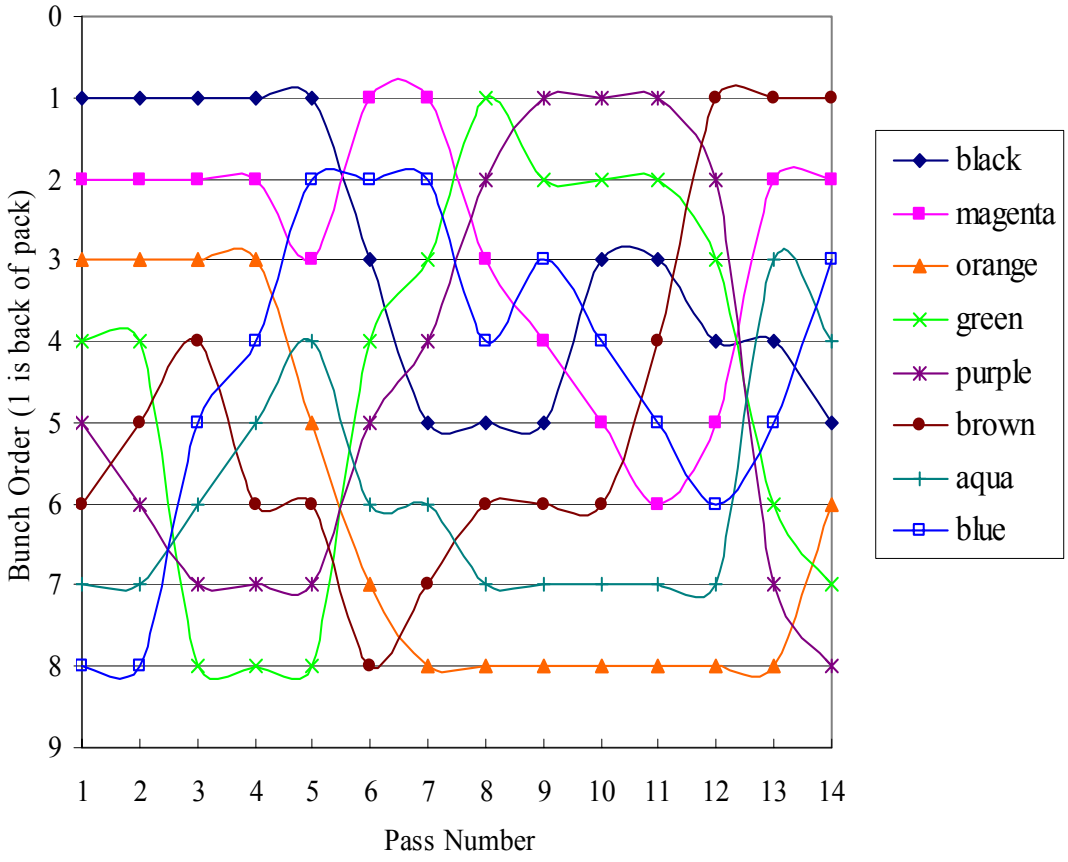

Figure 4.52 Racetrack plot of cycling behavior in three dimensional simulation of interbeam synchronization, position in pack versus pass number

This type of plot allows one to get an idea for the time constant associated with the cycling. In this case, bunches execute a cycle on the order of 10 passes and although it is somewhat disorderly, move back and forth around the middle of the pack.

Effects of density on synchronization

In addition to initial separations, the bunch density is another key parameter for the cycling behavior. The density of an already well-synchronized system is varied to find possible density limits and to examine the mechanism by which synchronization may be lost. The mechanism would be important if later steps must be taken to control the

synchronization phenomenon. A very tight initial grouping was chosen in order to minimize the effect of initial spread as understood from the results of the previous section.

The stability of the synchronized state is found to break down at higher bunch densities due to the high levels of energy exchange between bunches. As the density is increased, the system will tend to eject a single bunch from the group and as time and/or density are further increased, more bunches are ejected from the synchronized group. The overly-large energy exchange destroys the cycling behavior. A post-collision particle still is repositioned via the kinematics of the trap, but now it tends to overshoot and will be repositioned farther from the center of the bunch in phase space. The figures below show the break-down of the synchronized state for high density bunches with $n_o=1\cdot10^{13}\ m^{-3}$. The initial state is chosen to be highly synchronized, with an initial particle separation bracket of width $1.8\cdot10^{-4}$ meter, 1/1000 of the total path radius. The graph of position versus time in Figure 4.53 shows that only one pass is necessary for total break-down with a number of bunches being ejected far beyond the anode at 25 cm. In this model, the numerical potential well contains these ejectees, but this explains the losses to the anode grids observed in the OOPIC simulations. An operational IEC device will most likely contain these particles due to the high direct-conversion electric fields surrounding the core device, but the degree of collisionality may make it difficult to confine these ejectees transversely with purely electrostatic fields.

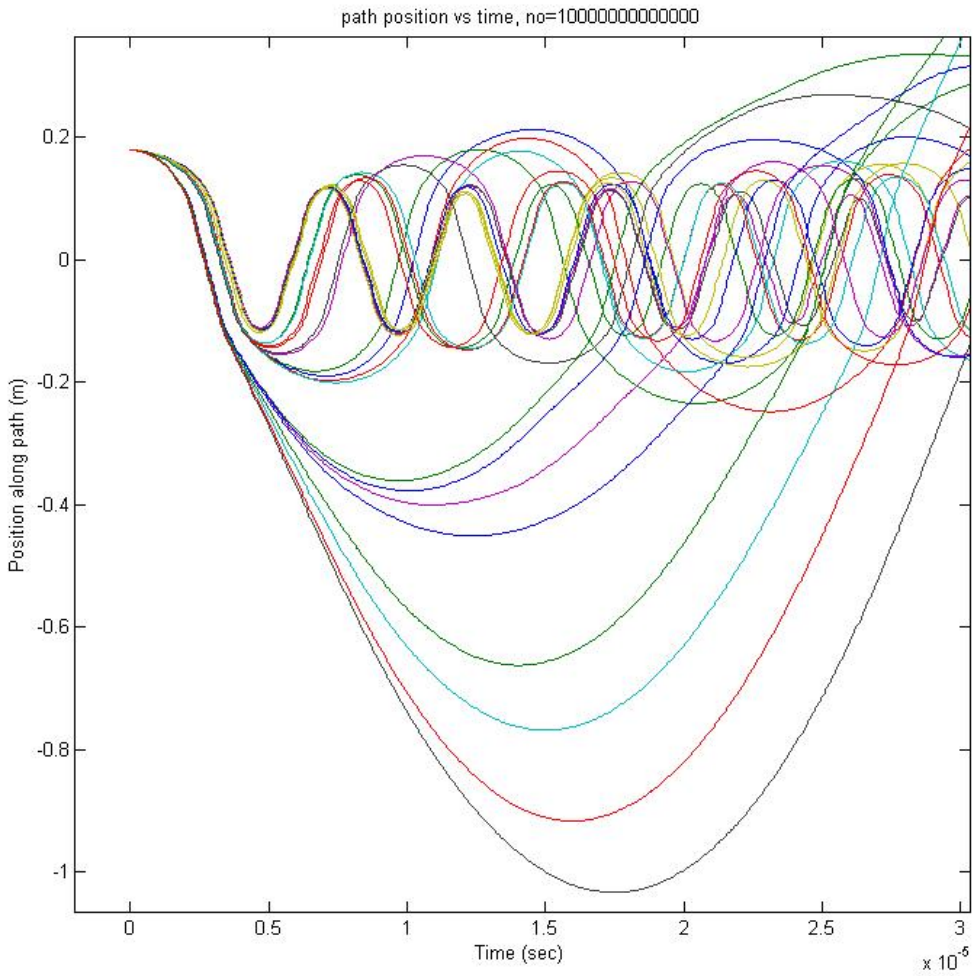

Figure 4.53 Desynchronization of high density bunches, position vs. time for peak bunch density of $n_o=1\cdot10^{13}$ m^{-3}, colors represent the 24 bunches

The velocity plot in Figure 4.54 shows that the synchronized bunches start at the anode with minimal velocity. Two groups immediately emerge, the first accelerated into the device core and the second delayed at the anode due to the space charge of the first group. As the first group descends into the core the second group follows it. We know that these leading particles will gain energy from the delayed particles, and sure enough this first group emerges from the core with much more energy, and they are carried out well past the anode. The second group continues on towards the anode after passing through the center of the device and then diverges in velocity as it approaches the anode.

The process continues with each pass and the system eventually becomes fully desynchronized.

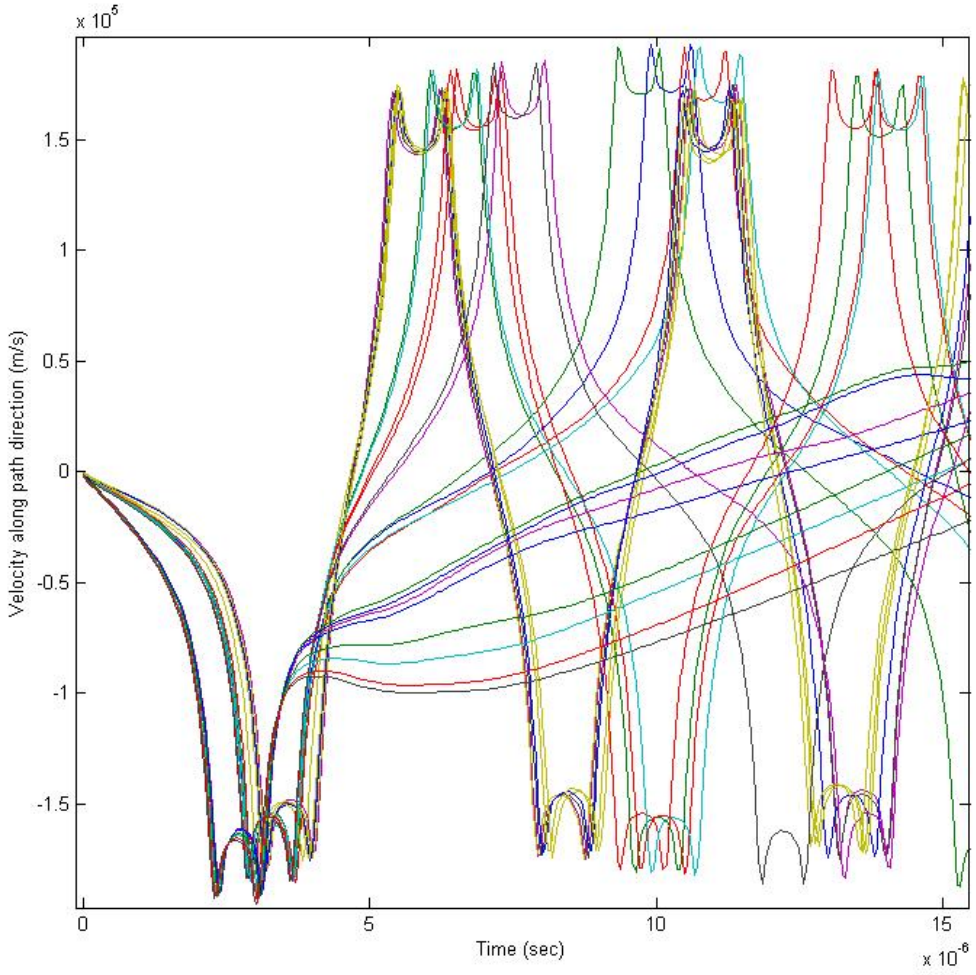

Figure 4.54 Desynchronization of high density bunches, velocity vs. time for peak bunch density of $1 \cdot 10^{13}$ m^{-3}, colors represent the 24 bunches

Low density de-synchronization occurs from the lack of appreciable space charge forces. Here the particles drift according to the initial spread of total mechanical energy acquired from small errors in assigning velocities to the initial positions. Further, numerical heating associated with the integration scheme will cause particles to drift

apart with time. For very low initial densities, the particles are observed to spread quickly despite a tight '1/1000' initial state, as shown in Figure 4.58.

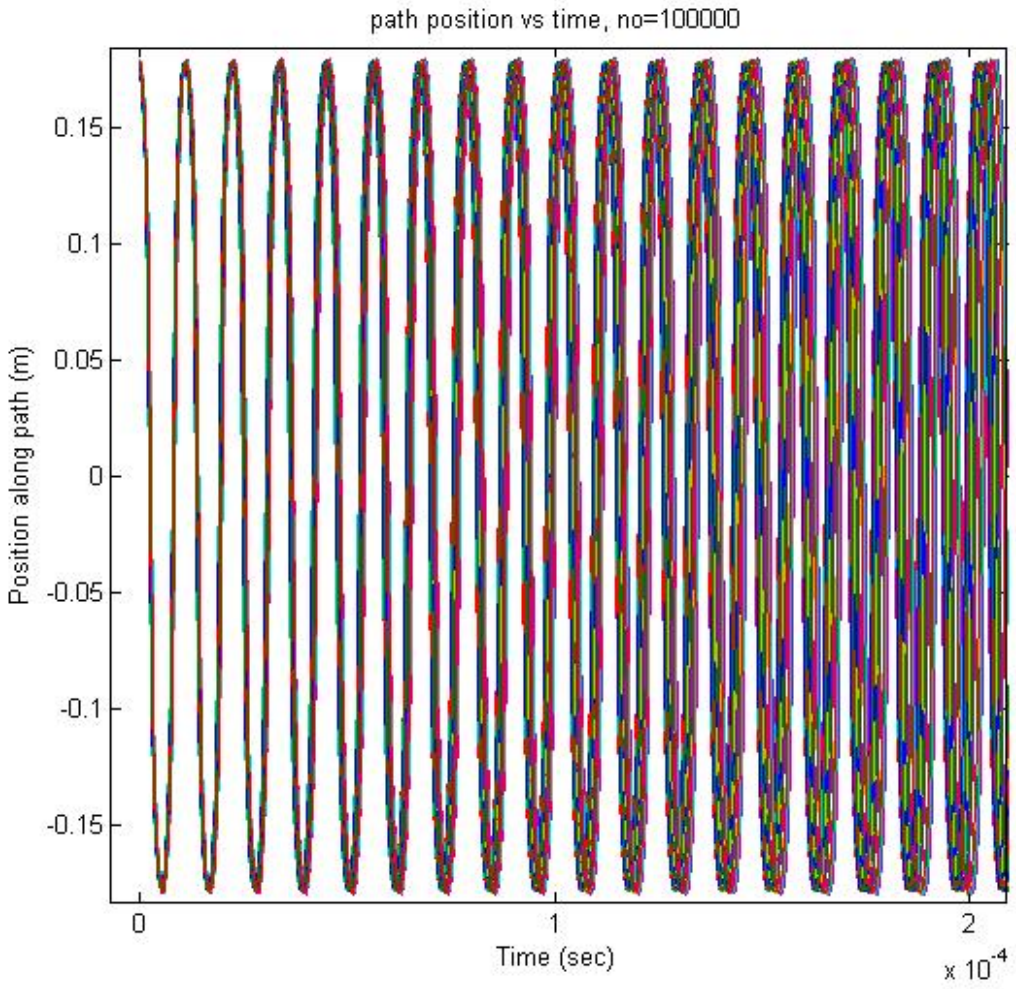

Figure 4.55 Desynchronization of low density bunches, position vs. time for peak bunch density of $n_o=1\cdot10^5$ m^{-3}, colors represent the 24 bunches

In the low density cases, no cycling is observed. Particle order tends to be preserved over the course of the simulation. For the above case, the bunches are effectively spread over the device over about 40 passes and the phase space is shown in Figure 4.56. The clumping of particles is thought to arise from the random initial conditions, and not due to collective behavior. This can be seen more clearly in Figure 4.57, where the relative velocity and positions are plotted. As opposed to previous

relative phase plots, the absolute values of the state variables are not taken to provide a clearer plot.

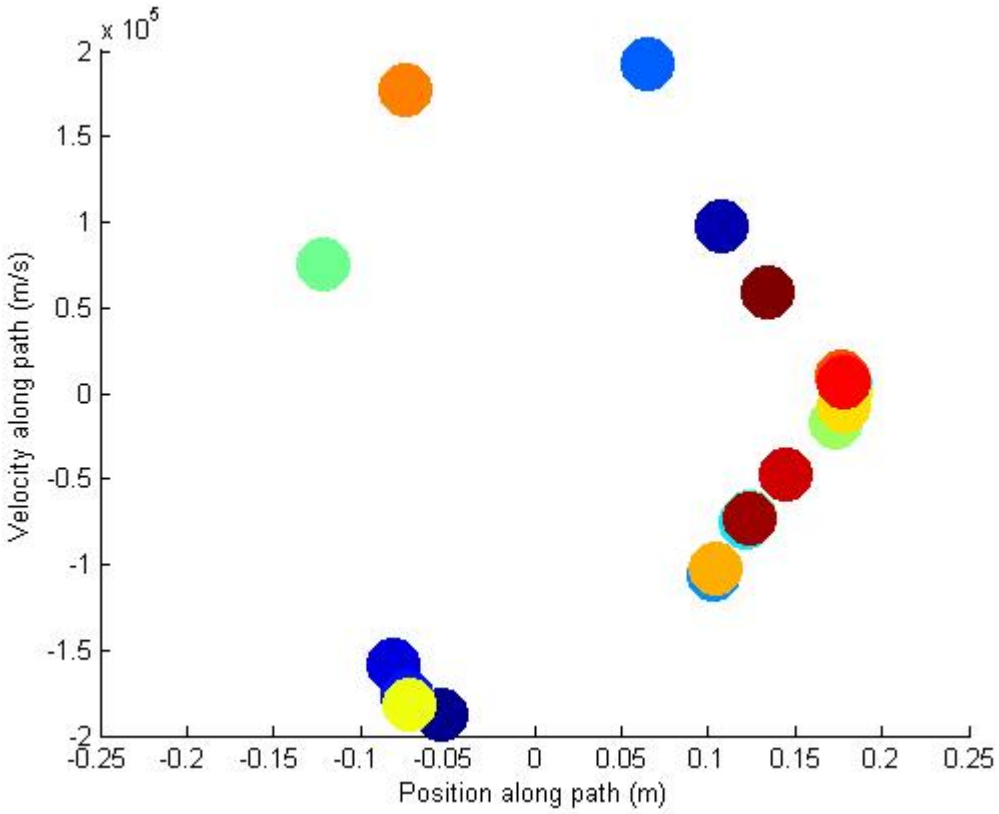

Figure 4.56 Velocity vs. position for low peak bunch density of $n_o=1\cdot10^5$ m^{-3}, colors represent the 24 bunches.

Note that Figure 4.57 is of relative velocity vs relative path position, plotted for every pass through the device center. This means that the plotted phase of a bunch will jump back and forth between opposing diagonal sectors on each consecutive pass. Bunches begin the simulation closely packed but spread out until they reach the extent of the relative phase space. The limits of the phase space are set by the physical dimensions and maximum velocities in the device, roughly 0.4 m for position and ~$4\cdot10^5$ m/s for 10 keV Argon ions. Some of the paths are more or less straight lines, while others are more curved.

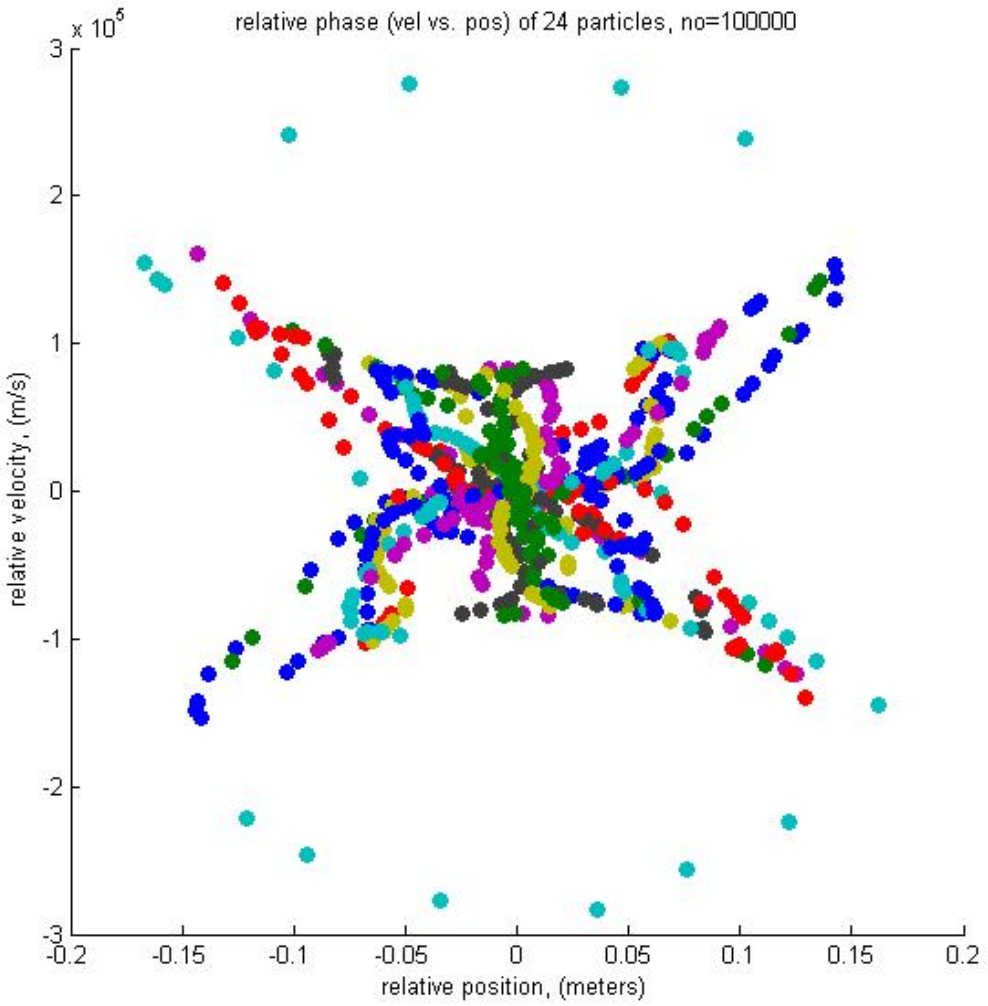

Figure 4.57 Relative phase space for low peak bunch density of $n_o=1\cdot10^5$ m^{-3}, colors represent the 24 bunches, 120 passes elapsed

A numerical experiment was conducted to find boundaries of the density bracket in which synchronization occurs. As before, 24 bunches were used with 2 bunches started opposed on each of 12 beam paths. The bunch size was 2 cm as before. The initial random separation was only 1/1000 of the path, 0.18 mm. For such a tight initial case, bunches were observed to expand for all density cases. The simulation was run for 50 passes, which was assumed to correspond to a stable steady-state. The assumption of steady-state behavior applies to well-synchronized cases, but non-synchronized cases are

by no means at steady-state after only 50 passes. This is acceptable, however, because the chosen metric of 'synchronicity' is insensitive to the non-synchronized cases. The 'size' of the collection of bunches in the relative phase space is used to measure how strongly the collection is synchronized. This metric is evaluated at two discrete locations for each bunch, at the anode turn-around point and the device center. The metric must be localized as such to account for the spreading in relative space caused by the accelerating fields. Whether or not the ensemble is bunched and undergoing cycling behavior is also recorded for each case. The results follow in Table 4-4, and the data are shown graphically in Figure 4.58 and Figure 4.59.

Table 4-4 Synchronization stability results for three dimensional model with Argon ions and $\sigma = 0.02$ m.

peak density (m^-3)	v-r, anode (m/s)	p-r, anode (m)	v-r, center (m/s)	p-r, center (m)	bunched	cycling
1.0E+12	1.30E+05	0.1200	1.6E+05	0.2000	No	No
5.0E+11	1.20E+05	0.1000	1.6E+05	0.1600	No	No
3.0E+11	3500	0.0090	2000	0.0325	Yes	Yes
2.5E+11	3500	0.0070	1200	0.0300	Yes	Yes
1.0E+11	3000	0.0025	400	0.0200	Yes	Yes
7.5E+10	2600	0.0023	325	0.0200	Yes	Yes
5.0E+10	2750	0.0016	250	0.0160	Yes	Yes
2.5E+10	3000	0.0010	160	0.0160	Yes	Yes
1.0E+10	5000	0.0012	350	0.0250	Yes	Yes
7.5E+09	5000	0.0009	300	0.0250	Yes	Yes
5.0E+09	6000	0.0011	900	0.0300	Yes	Yes
2.5E+09	7000	0.0012	1500	0.0400	Yes	Yes
1.0E+09	8000	0.0016	4500	0.0400	Yes	Yes
5.0E+08	3.00E+04	0.0012	1.0E+05	0.1200	Yes	Yes
1.0E+08	3.00E+04	0.0014	1.0E+05	0.1200	No	No
1.0E+07	6.00E+04	0.0400	1.5E+05	0.1600	No	No
1.0E+06	3.00E+04	0.0120	1.0E+05	0.1200	No	No

All cases that remained bunched after 50 passes were also observed to cycle bunches around the middle of the group. Also, enough time had elapsed so that even the lowest density case presented here spreads at the anode to 67 times its initial relative position spread.

The boundaries of the density bracket seem to be sharp, where the synchronization 'turns off' within an order of magnitude in density. There is some fuzziness at the lower density boundary between 1e8 and 5e8. Here the particles are still bunched and cycling, yet are widely separated in velocity. This shows that there are shades of gray in the behavior.

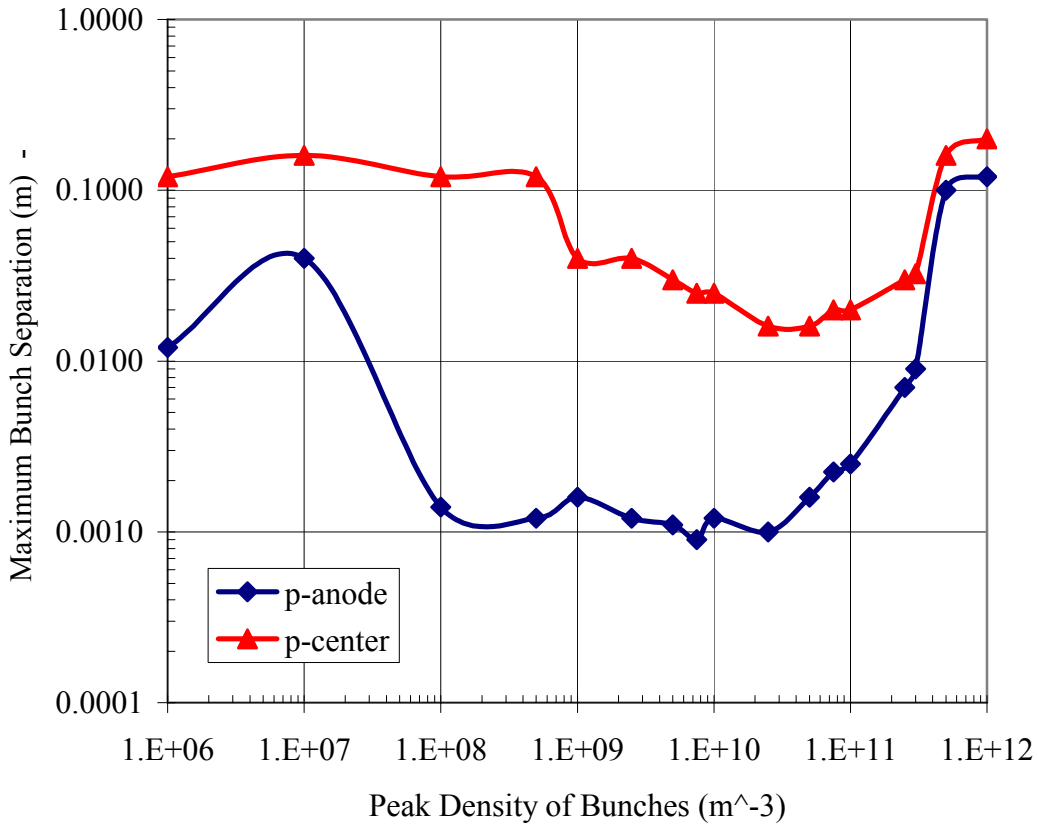

Figure 4.58 Maximum separation of bunches in meters along their respective paths at the 1) anode and 2) center of the device as a function of peak bunch density with $\sigma = 0.02$ m, Argon ions

Notice in Figure 4.58 that as density is increased, the spreading in position space is observed in the center before the anode. This is due to the limited time spent in the device center, which makes it more sensitive to small changes in position spread that are somewhat hidden at the anode. The anode behavior for both position and velocity spreads appear 'flatter' due to this insensitivity. The center position and velocity clearly shows a minimum behavior, and is more pronounced in the velocity plot of Figure 4.59. While this is possibly due to un-steady state conditions at 50 passes, the fixed time period shows a non-random variation in the time-averaged rate of ensemble expansion.

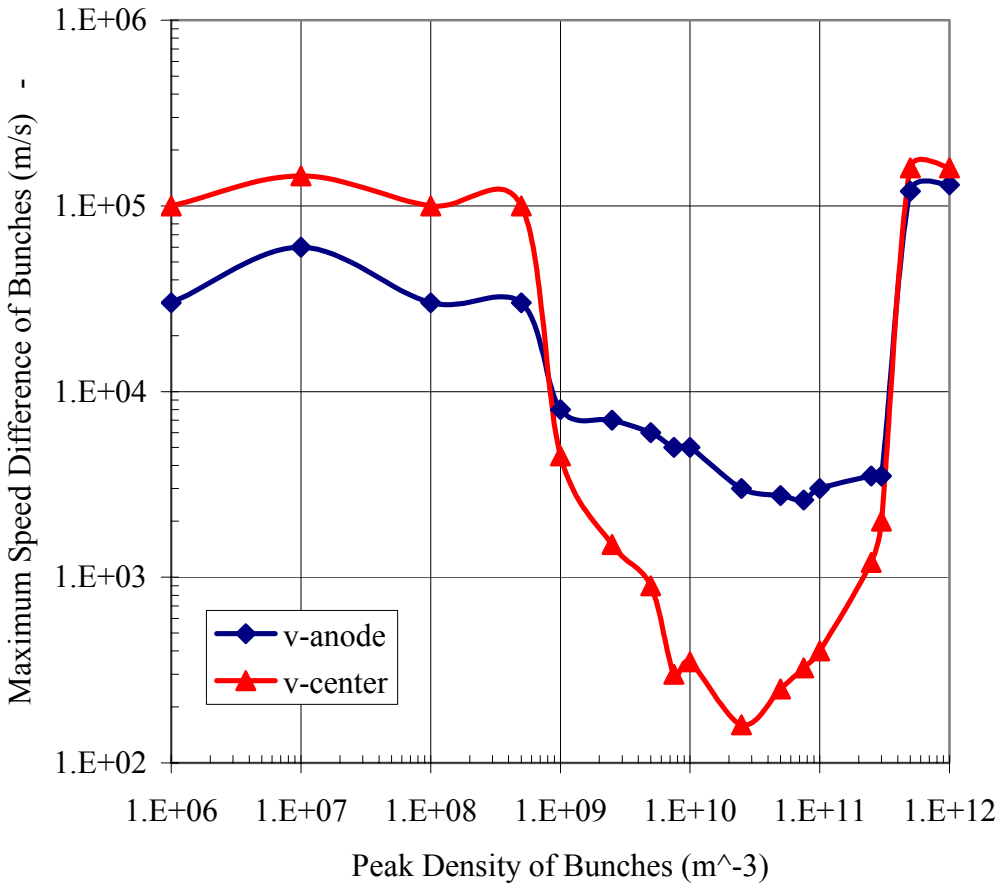

Figure 4.59 Maximum speed difference of bunches in meters per second along their respective paths at the 1) anode and 2) center of the device as a function of peak bunch density with $\sigma = 0.02$ m, Argon ions

The relative velocities in the device center for minimum cases are amazingly low, showing that the energy of bunches is almost equal. In fact, the relative spread in the velocities at the center are an order of magnitude smaller than at the anode, in spite of the high absolute velocities in the device center. The energy spread at the anode is most likely confused by the fact the ions spend most of the time there. The relative velocity at the anode is calculated when each bunch turns, so that it is unlikely that the mean position will be in the same place for each particle. Even the tight spread of only 1 mm at the anode for the best case is enough to cause this 'spread' in anode velocities.

The upper density limit is fairly low. Also, the observed ejection mechanism doesn't bode well for running the device at these higher densities. The collective behavior is unstable because too much energy is being exchanged, and this also means that the excess energy will carry particles out of the device, effectively upscattering them in energy. This occurs much faster than the classical collisions. Also, in this non-neutralized IEC, the long range effect of the Coulomb force is not limited by invoking Debye shielding of the potential. One would expect significant differences in the synchronization behavior in a IEC with significant electron populations. This complication is yet another avenue of possible future IEC research.

4.6 Summary

An interesting self-organizing collective behavior termed synchronization is observed in numerical particle-in-cell simulations. The initially uniform ion beams in a multiple grid IEC form bunches of particles and gradually evolves in to a system of bunches oscillating in the IEC, all reaching the device center at the same time. Fourier

transform analysis of the simulation data show that initially short wavelength bunches are important, later yielding a large wavelength bunch. The simulation exhibits particle lifetimes of tens of thousands of passes (tenths of a second) in the synchronized configuration.

Synchronization is a process common to other manmade and natural systems. Prior work from the Weizmann Institute of Science in Rehovot, Israel, on an electrostatic linear ion trap showed experimental evidence of synchronization. The group's theoretical work establishes criteria for stable synchronization of ion bunches. Poincare sections are introduced as an effective visualization of a mapping technique is used to explain the synchronization of two ions on a single beam path.

The Israeli work dealt with an initially bunched system, but the IEC synchronization evolves from initially uniform beams. A 2-stream instability analysis shows that the anode region is unstable and begins the process of bunching. The growth rates predicted by the 2-stream analysis agree with the numerical observations of the particle-in-cell model.

A 2-particle collision model is used to explain the mechanism of synchronization between the multiple ion beams in an IEC device. The collisions of bunches from different beams are found to occur over long distances and the same special kinematics responsible for synchronization on a single beam work for the multi-beam system. Further, the bunch collision model is used to calculate an estimate of the time constant for the development of the synchronized state as a function of density.

Lastly, a 3-D N-body bunch simulation reproduces the steady-state synchronization, allowing one to visualize the phenomenon through Poincare sections.

This simpler version of the full particle-in-cell model shows the mechanisms responsible for break-down of synchronization at high and low densities. At high density, the Coulomb interaction is so strong that some bunches gain significant amounts of energy from the other bunches and are ejected from the system. At low densities, the interaction is too weak to overcome the spreading caused by initial differences in bunch energies.

Chapter 5 Implications and Conclusions

5.1 Conclusions

The lightweight IEC fusion reactor concept must be improved if it is to produce more power than it consumes. Several techniques are proposed and analyzed in this work, including operating at lower pressures and with multiple grids. Reaction rate scaling arguments show that a high fraction of ions must fuse to reach breakeven, and this means that fusion reactions must occur on a similar time scale to other processes. Reducing the background pressure lengthens the loss time scale for background collisions. Multiple grids allow for the creation of focusing channels which shield out field asymmetries and create focusing channels for ions. These channels stabilize the ion trajectories so that in the absence of space charge, an ion can recirculate indefinitely within the device. Electron streaming losses are another important loss mechanism addressed by the multiple grids. An innermost decelerating grid creates a potential barrier to streaming electrons created in the core and as secondaries from grid impacts on the inner grid. Ion-ion collisions are addressed in two ways. High angle scattering events from the core are shown to be effectively slower than fusion since most of the deflected ions will be deflected centrally onto another ion beam path and not be lost. The small fraction that hits the inner grid also are lost at an energy much less than if they would have hit the cathode grid. Thermalizing collisions are the most interesting loss mechanism, and as such have the most interesting 'solution'.

The increased ion confinement of the multigrid approach allows collective behavior to develop in the ion beams. The kinematics of the trap and the ion-ion Coulomb interaction result in the initially uniform beams self-organizing into a synchronized system of pulsing bunches. The ions in a particular bunch orbit stably about the collective center of mass in relative phase space. Furthermore, bunches on separate beams interact via a similar mechanism so that bunches stay in synch with each other, orbiting about each other in their relative phase space. While it is usually thought to cause thermalization of plasma, in this situation the ion-ion interaction actually maintains a non-thermal distribution.

The self-organizing behavior appears after minimum density requirements are met. It is understood to begin as a two-stream instability, and the growth rate of the synchronization agrees well with unstable waves originating near the anode region of the beams. The saturated state of the instability is synchronized bunches, 2 per ion channel, each reaching the anode at the same time and collapsing as a group into the device center. While the ions are well-confined and most likely to fuse, the density is severely limited for the non-neutralized system. The collective behavior responsible for synchronization also acts as a natural mechanism to prevent excess charge. As ion density builds from recirculation or simply high input currents, the collective behavior violently expels particles from the system. The steady-state peak ion density is found to be only a weak function of the input current, so that for a given geometry and voltage setting, the collective behavior sets a space charge limit. The potential associated with this limiting density is about 10% of the background potential in the device core, for example a 50 kV will reach steady state when the ion core potential reaches about 5 kV. Thus, while a low

density device may theoretically operate at energy break-even or better, there are serious problems with scaling up the density to reach useful reaction rates and powers. As a near term application, gunned multigrid IECs operating at lower background pressures could be made to operate as more efficient neutron sources, improving the economics of running the devices at the price of increased complexity.

In order to increase the fusion power to useful levels, at least some level of neutralization will be required to counteract the strong space charge interaction. Miniaturizing the device would be beneficial, but raises serious complications due to the high electric fields and complex geometry. A hybrid design with magnetic lenses may allow high levels of space charge to be confined, and it is unclear how this would affect the synchronization mechanism. Other applications of this phenomenon could try to exploit the self-organizing behavior to produce long lived pulse trains, possibly useful for mass spectrometry and pulsed reactions at a set frequency. While the IEC clearly needs more work before we baseline it for a Mars mission, this study has discovered some interesting physics which may be applicable in other systems.

5.2 Contributions

This thesis makes two main contributions. First, a multi-grid IEC device is shown to be capable of confining a non-neutral ion population for lifetimes at least 3 orders of magnitude greater than state of the art IEC devices. Second, the increased lifetime allows the development of a self-organizing synchronization behavior which enables a low-power, breakeven non-neutral IEC fusion reactor.

More specifically, several significant contributions include:

- A detailed understanding of reaction rate scaling and confinement limitations in recirculating beam IEC devices is derived.
- Several improvements to the IEC concept are proposed and analyzed, including operation at lower pressure, multiple grids to provide ion channels, and electron trapping grids to prevent electron streaming.
- Ion confinement lifetimes are shown to improve from fewer than 10 passes in a standard single cathode IEC to over 30,000 passes in a multiple grid IEC, and no upper limit is expected for sufficiently low injection currents.
- A self-organizing, synchronized pulsing system of bunches is predicted to develop in well-confined IEC ion beams, based on observations of particle-in-cell simulations.
- The synchronization phenomenon on a single beam and between multiple beams is understood as a combination of the ion-ion Coulomb interaction and the kinematics of the IEC device.
- The collective behavior of the well-confined ion beams is found to effectively place a space charge limit on ion density in the system.
- While it would be a very low power device, a synchronized multigrid IEC should be able to approach fusion breakeven.

Not only would a high power, breakeven IEC have enormous potential as a terrestrial power source, it would be a very lightweight method to harness nuclear fusion for fast, intrasolar system travel. The synchronization mechanism provides a concrete example of how non-Maxwellian, non-neutral plasmas can be maintained by using the very forces that usually thermalize it. Perhaps the technique of using external fields to

tailor the ion distributions to control the thermalization of ion beams can be used in other fusion reactor concepts and plasma devices in general.

5.3 Concurrent experimental studies

Concurrent experimental work at the Massachusetts Institute of Technology by Carl Dietrich has shown both increased confinement with multiple grids and evidence of the synchronization effect [44]. These experimental studies were conducted in parallel to the research presented in this thesis. A figure showing both the increased confinement and synchronization effect is reproduced from Dietrich's Doctoral thesis below in Figure 5.1.

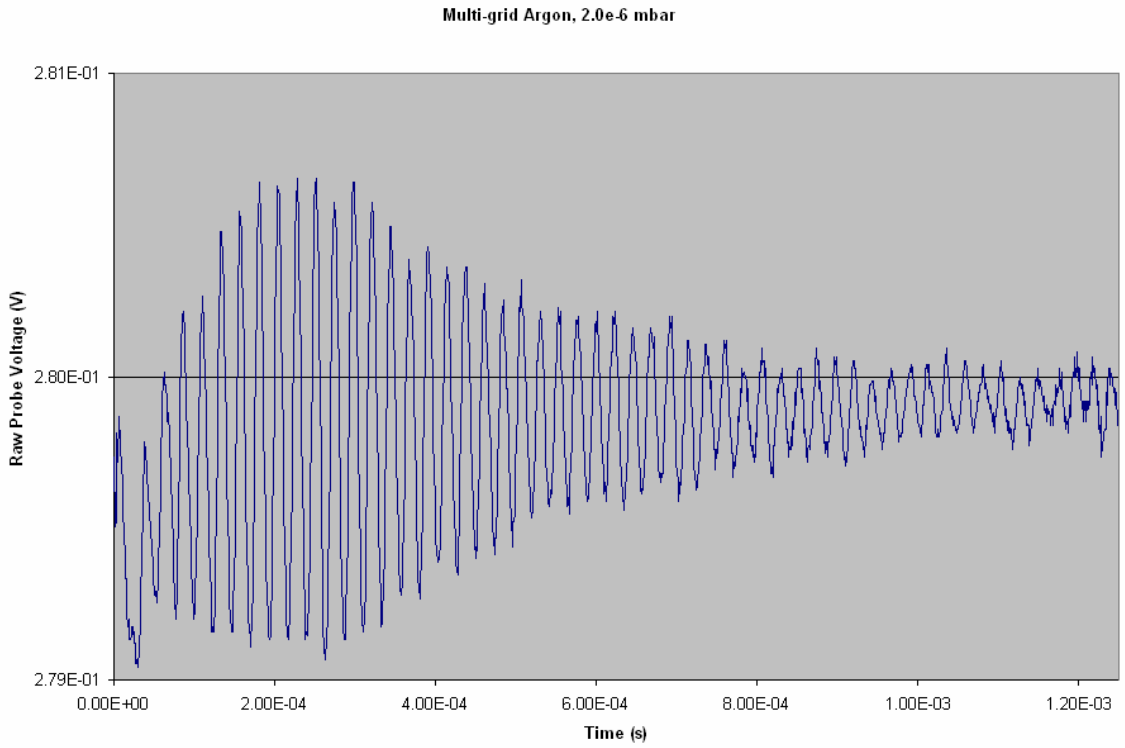

Figure 5.1 Evidence of two-stream instability at the bounce frequency, Argon $1.9 \cdot 10^{-6}$ mbar, reproduced from Dietrich, 2007, with permission [44].

Figure 5.1 shows a voltage trace over time, where the voltage is a capacitive measurement of the local potential near the anode of a multiple grid IEC system. Zero time is defined by the termination of input current. The oscillations in the Argon system are observed to grow and occur at the bounce frequency of 23 microseconds. Further, despite a background pressure of $1.9 \cdot 10^{-6}$ mbar, the oscillations and ion population persist for 104 passes in the above trace. Dietrich further shows that the characteristic decay time constant for this trace is significantly greater that what is possible for a standard single grid system, as predicted in this thesis. Dietrich's doctoral thesis is projected for completion in February 2007.

5.4 Recommended future endeavors

There are a few other areas ripe for follow-on work, some of which are under study by other students at MIT, including:

- Experimental verification of the increased confinement time of the multiple grid approach.
- Design of optimized multiple grid configurations.
- Experimental verification of the suppression of electron streaming losses.
- Experimental observation of synchronization phenomena in an IEC.
- Numerical and experimental study of focusing ability provided by multiple grids.
- Practical IEC issues such as lifetimes of grids, guns, and converter structures with regards to sputtering from energetic fuel ions and reaction products.
- Numerical studies of multi-species non-neutral plasmas such as deuterium-tritium mixes to determine the role of synchronization in the confinement of multiple species.

- Higher fidelity PIC modeling on more capable computers, allowing an increase in number of cells and more accurate modeling of the ion sources.
- Full three dimensional PIC modeling on more capable computers, which would be especially useful for looking at the intermediate pressure regime useful for neutron generators (low enough pressure to increase confinement times and efficiency, yet high enough background pressure to keep rates high).
- Numerical modeling of the IEC in a direct electric conversion scheme so as to explore the confinement properties of particles that are collectively scattered out of the current OOPIC model boundaries at high densities.
- Conceptual studies of hybrid IEC devices incorporating magnetic fields to enhance the ion beam density limits.
- Conceptual studies of localized neutralization of ion beams to increase the space charge limits and increase the core density and fusion rate.
- Application of the synchronization mechanism to other devices such as electrostatically plugged mirror and cusp machines.

As a last word, this cartoon I believe accurately describes the last 6 years of grad school research meetings and probably the careers of many a fusion scientist.

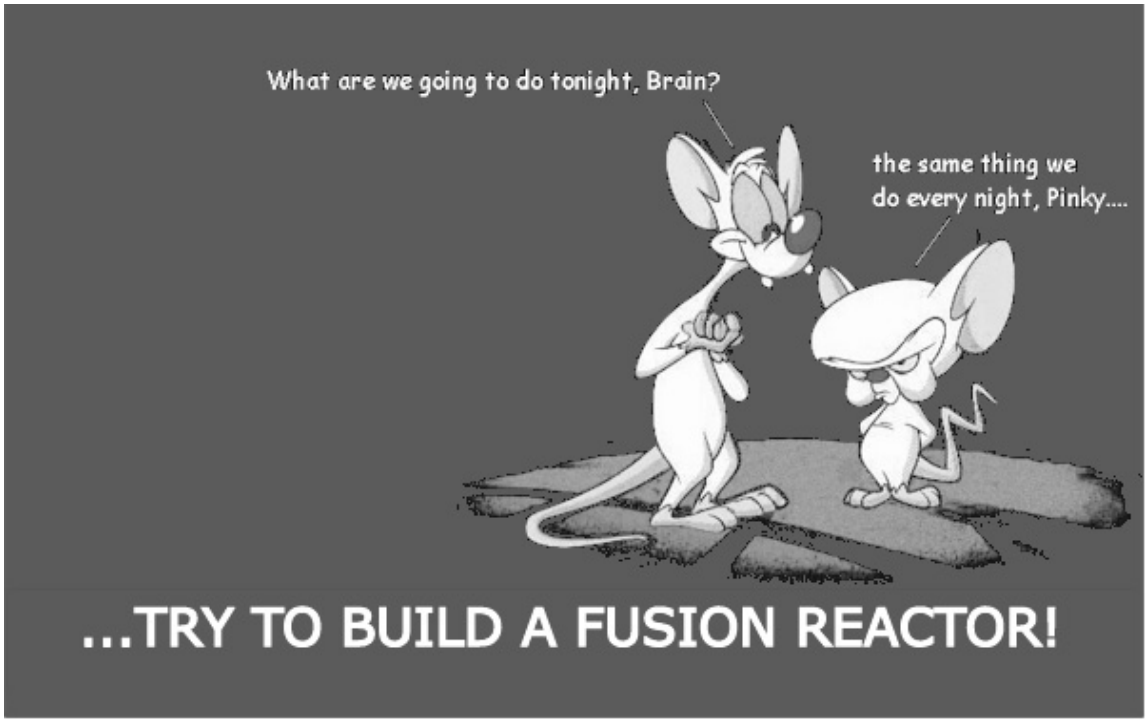

"Pinky and the Brain' characters and image from Warner Bros. Animation

"Narf."

Appendix A OOPIC Model Creation

The OOPIC input files for the thesis simulations are quite large. Each text file is in excess of fifty pages. While tedious to write, the format is simple and repetitive. Every line segment in the geometry model (Figure A.1) must be defined. The basic structure is a grid 'square', which consists of four segments surrounding a cell. The input file is written by copying and pasting this basic structure many times and changing the appropriate variables.

Care has been taken so that much of the model is scalable and movable within the space. For instance, variables at the top of the input file specify the spatial locations of the various grids, so that one doesn't have to change pages and pages of values in the actual grid definitions. These variables are the first thing defined in the code. Variables include the grid voltages, parameters governing the ion injection, and grid locations. The grid section sets the physical size of the model and the number of cells. The control block sets the time step and the field solver to be used. The MCC block sets parameters for background collisions with neutral particles. The species blocks define the properties of ions and electrons in the system, including charge, mass, collision model, and maximum particle number. When the maximum particle number is reached in the course of a simulation, the weighting is doubled and half the particles are eliminated. Next the particles are loaded into the system. A population can be initially loaded and this is sometimes used instead of emitters for diagnostic purposes. The main way ions are introduced is via beam emitters. These blocks define the ion beams and the local boundary conditions including whether or not they will re-emit ions which impact the surface.

The definition of the grids is by far the most tedious and substantial part of the code. First the anode segments are defined, then the various inner grids including the feed through stalks. A few dielectric regions are added to prevent ions from being accidentally trapped in the regions behind the emitters. This is really only a problem when running the code at higher background pressures as in the glow-discharge regime. Finally, a few user-defined diagnostics are added. These are added to help diagnose the pulsing behavior at the device center and to observe waves moving across the beam channels.

The figure below shows the major structures and the following code considerably shortened by deleting repeated sections. These areas are denoted by bold italics. Also to note, '//' precedes any comments present in the code.

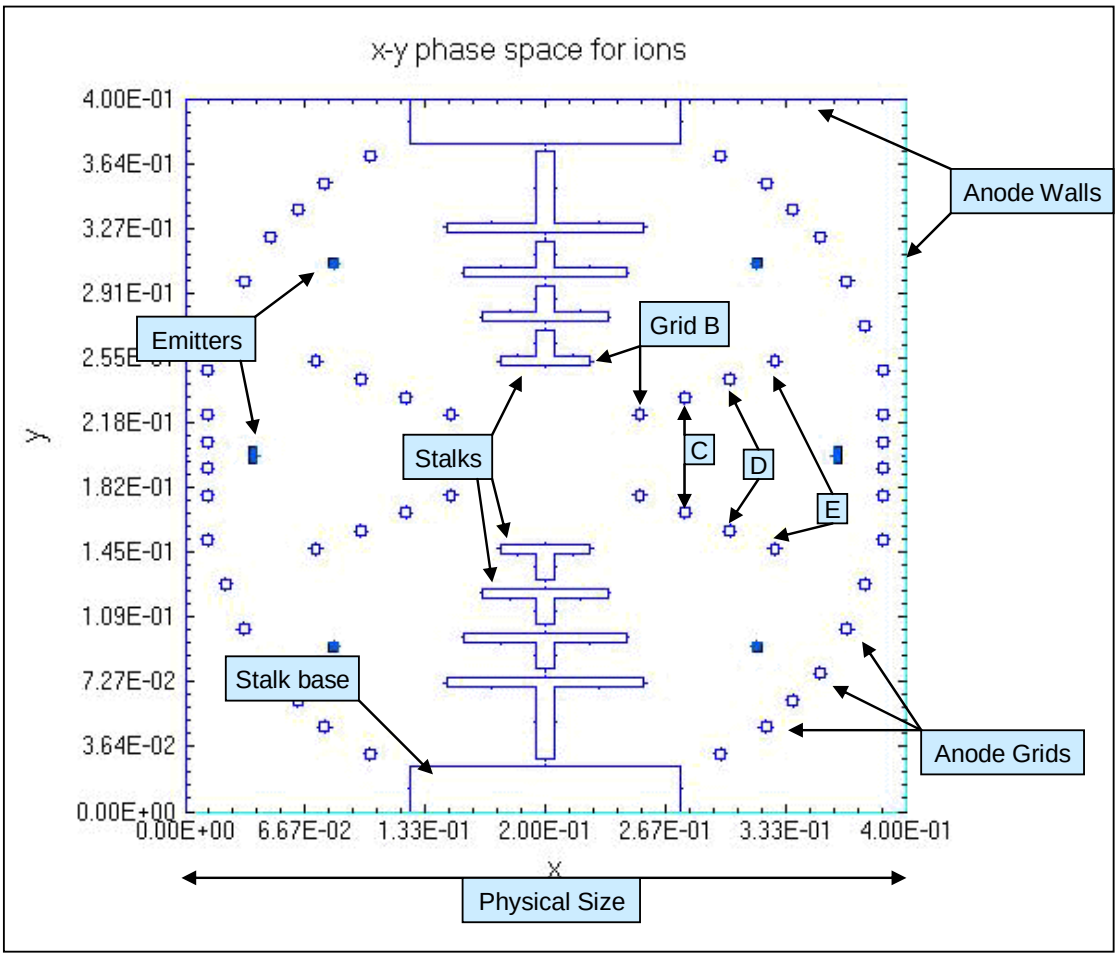

Figure A.1 OOPIC model geometry

```
thesis.inp

{
Thomas McGuire
Edited Oct. 30, 2006
}
Variables
{
 anode = 100      //anode wall potential in volts
 gridB = -200     //trapping grid potential in volts
 gridC = -2000    //cathode grid potential in volts
 gridD = -10000   //pinching grid near cathode
 gridE = -2000    //pinching grid near anode

 curr = 1e-6      //gun currents in Amps
 idrift = 100     //ion injection velocity, 100 eV
 wght = 1e5       //particle weighting
 gdm = 1          //emitter cell size
 dem = 27   //diagonal emitter location
 dFAC = 1   //turn diagonal injection on or off
 oFAC = 1   //turn orthogonal injection on or off
 dur = 1e-3 //duration of current injection in seconds
```

```
 emitsec = 1      //turn emitter re-emission of ions on or off
 BASE = 40
 XX = 1     //scaling factor
 R = BASE*XX    //device radius in cells

 ZX = XX* 17 //diagonal injector position
 ZY = XX* 19
 W = XX* 8  //orthogonal injector position
    // 8 is most in sync with diagonal position 17,19
 BX = XX* 29 //initial x-position of gridB
 BY = XX* 15 //initial y-position of gridB
 CX = XX* 31
 CY = XX* 20
 DX = XX* 33
 DY = XX* 25
 EX = XX* 35
 EY = XX* 30

 A1X = XX* 13 //anode grid positions
 A1Y = XX* 13
 A2X = XX* 10
 A2Y = XX* 16
 A3X = XX* 7
 A3Y = XX* 21
 A4X = XX* 5
 A4Y = XX* 26
 A5X = XX* 3
 A5Y = XX* 31
 A6X = XX* 3
 A6Y = XX* 36
 A7X = XX* 3
 A7Y = XX* 39
 A8X = XX* 25
 A8Y = XX* 5
 A9X = A3Y
 A9Y = A3X
 A10X= A2Y
 A10Y= A2X

}
Region    //this code has only one region
{

Grid
{
 J = R*2
 x1s = 0.0  //define physical domain size
 x1f = 0.4  //define physical domain size
 n1 = 1.0
 K = R*2
 x2s = 0.0  //define second physical deimension
 x2f = 0.4
 n2 = 1.0
 Geometry = 1  //planar geometry switch
}
```

```
Control
{
 dt = 1e-8 //ions move 1/2 - 1/4 cell per step
 ElectrostaticFlag = 1
 BoltzmannFlag = 0
}

MCC
{
 gas = Ar
 pressure = 1e-10    //pressure in torr
 eSpecies = electrons
 iSpecies = ions
 collisionFlag = 1
}

Species
{
        name = electrons
        m = 9.11E-31
        q = -1.6e-19
 particleLimit = 1e5
 collisionModel = 1
 supercycle = 50
}

Species
{
        name = ions
        m = 1.673e-27*40  //argon mass
        q = 1.6e-19
 particleLimit = 1e5
 collisionModel = 2
}

Load   //load ions in a uniform cloud, not always used
{
x1MinMKS = 0.00
x1MaxMKS = 0.4
x2MinMKS = 0.00
x2MaxMKS = 0.4
speciesName = ions
density = 1.0e1
temperature = 10
}

EmitPort  //right emitter , vertical
{
 speciesName = ions
 j1 = 2*R- W
 k1 = R - 1
 j2 = 2*R- W
 k2 = R + 1
 normal = -1
 I = curr*oFAC

  a1 = 1
```

```
 a0 = 0
 tdelay =0
 trise = 0
 tpulse = dur
 tfall = 0

 v1drift = -idrift
 v2drift = 0
 np2c = wght
 Secondary
 {
  secondary = emitsec
  secSpecies = ions
  iSpecies = ions
 }
}
```

Repeat for each emitter surface

```
Equipotential  //Anode Walls
{
      C = anode  //top wall
      Segment
      {
      j1 = 0
      k1 = 2*R
      j2 = 2*R
      k2 = 2*R
      normal = -1
      }
      Segment  //bottom wall
      {
      j1 = 0
      k1 = 0
      j2 = 2*R
      k2 = 0
      normal = 1
      }

      Segment  //left wall
      {
      j1 = 0
      k1 = 0
      j2 = 0
      k2 = 2*R
      normal = 1
      }

      Segment  //right wall
      {
      j1 = 2*R
      k1 = 0
      j2 = 2*R
      k2 = 2*R
      normal = -1
      }
```

```
   //Base Rectangle Bottom
      Segment // left wall
      {
      j1 = A8X
      k1 = A8Y
      j2 = A8X
      k2 = 0
      normal = -1
      }
      Segment // right wall
      {
      j1 = 2*R - A8X
      k1 = A8Y
      j2 = 2*R - A8X
      k2 = 0
      normal = 1
      }
      Segment // top wall
      {
      j1 = A8X
      k1 = A8Y
      j2 = 2*R - A8X
      k2 = A8Y
      normal = 1
      }

   //Base Rectangle Top
      Segment // left wall
      {
      j1 = A8X
      k1 = 2*R - A8Y
      j2 = A8X
      k2 = 2*R
      normal = -1
      }
      Segment // right wall
      {
      j1 = 2*R - A8X
      k1 = 2*R - A8Y
      j2 = 2*R - A8X
      k2 = 2*R
      normal = 1
      }
      Segment // top wall
      {
      j1 = A8X
      k1 = 2*R - A8Y
      j2 = 2*R - A8X
      k2 = 2*R - A8Y
      normal = -1
      }

//grid A1
    //grid  A1 LEFT-BOTTOM
      Segment  //top
      {
      j1 = A1X - 1
```

```
      k1 = A1Y
      j2 = A1X
      k2 = A1Y
      normal = 1
      }
      Segment  //bottom
      {
      j1 = A1X - 1
      k1 = A1Y - 1
      j2 = A1X
      k2 = A1Y - 1
      normal = -1
      }
      Segment //right
      {
      j1 = A1X
      k1 = A1Y - 1
      j2 = A1X
      k2 = A1Y
      normal = 1
      }
      Segment // left
      {
      j1 = A1X - 1
      k1 = A1Y - 1
      j2 = A1X - 1
      k2 = A1Y
      normal = -1
      }
```

repeat for every grid composing the anode

```
Equipotential  //gridB
{
      C = gridB
      Secondary
      {
            secondary = 1
            secSpecies = electrons
            iSpecies = ions
      }

    //grid  LEFT-BOTTOM
      Segment  //top
      {
      j1 = BY - 1
      k1 = BX + 1
      j2 = BY
      k2 = BX + 1
      normal = 1
      }
      Segment  //bottom
      {
      j1 = BY - 1
      k1 = BX
      j2 = BY
      k2 = BX
```

```
      normal = -1
      }
      Segment //right
      {
      j1 = BY
      k1 = BX
      j2 = BY
      k2 = BX + 1
      normal = 1
      }
      Segment // left
      {
      j1 = BY - 1
      k1 = BX
      j2 = BY - 1
      k2 = BX + 1
      normal = -1
      }
```

repeat for each quadrant

```
    //grid STALK-BOTTOM   Define high voltage stalks
      Segment  //top
      {
      j1 = BX
      k1 = BY
      j2 = 2*R - BX
      k2 = BY
      normal = 1
      }
      Segment  //bottom-left
      {
      j1 = BX
      k1 = BY - 1
      j2 = R - 1
      k2 = BY - 1
      normal = -1
      }
      Segment  //bottom-right
      {
      j1 = 2*R - BX
      k1 = BY - 1
      j2 = R + 1
      k2 = BY - 1
      normal = -1
      }
      Segment  //stalk-bottom
      {
      j1 = R - 1
      k1 = A8Y + 1
      j2 = R + 1
      k2 = A8Y + 1
      normal = -1
      }
      Segment  //left side
      {
      j1 = BX
```

```
  k1 = BY
  j2 = BX
  k2 = BY - 1
  normal = -1
  }
  Segment  //right side
  {
  j1 = 2*R-BX
  k1 = BY
  j2 = 2*R-BX

  k2 = BY - 1
  normal = 1
  }
  Segment  //stalk-left side
  {
  j1 = R-1
  k1 = BY-1
  j2 = R-1
  k2 = A8Y+1
  normal = -1
  }
  Segment  //stalk-right side
  {
  j1 = R+1
  k1 = BY-1
  j2 = R+1
  k2 = A8Y+1
  normal = 1
  }

//grid STALK-TOP
  Segment  //top
  {
  j1 = BX
  k1 = 2*R - BY
  j2 = 2*R - BX
  k2 = 2*R - BY
  normal = -1
  }
  Segment  //bottom-left
  {
  j1 = BX
  k1 = 2*R - BY + 1
  j2 = R - 1
  k2 = 2*R - BY + 1
  normal = 1
  }
  Segment  //bottom-right
  {
  j1 = 2*R - BX
  k1 = 2*R - BY + 1
  j2 = R + 1
  k2 = 2*R - BY + 1
  normal = 1
  }
  Segment  //stalk-bottom
```

```
	{
	j1 = R - 1
	k1 = 2*R - A8Y - 1
	j2 = R + 1
	k2 = 2*R - A8Y - 1
	normal = 1
	}
	Segment  //left side
	{
	j1 = BX
	k1 = 2*R - BY
	j2 = BX
	k2 = 2*R - BY + 1
	normal = -1
	}
	Segment  //right side
	{
	j1 = 2*R-BX
	k1 = 2*R - BY
	j2 = 2*R-BX
	k2 = 2*R - BY + 1
	normal = 1
	}
	Segment  //stalk-left side
	{
	j1 = R-1
	k1 = 2*R - BY + 1
	j2 = R-1
	k2 = 2*R - A8Y - 1
	normal = -1
	}
	Segment  //stalk-right side
	{
	j1 = R+1
	k1 = 2*R - BY + 1
	j2 = R+1
	k2 = 2*R - A8Y - 1
	normal = 1
	}
}
```

repeat for each grid, including grids and stalks

```
//Regions for Emitters

DielectricRegion  //left emitter
{
	QuseFlag = 0
	j1 = W
	k1 = R-1
	j2 = W-1
	k2 = R+1
	Secondary
	{
		secondary = emitsec  //switch
		secSpecies = ions
		iSpecies = ions
```

```
      }
}

*repeat for each dielectric area behind emitters

*define a few diagnostics that are not built-in to the code:

Diagnostic //trace the potential in the device center
{
       HistMax = 100000 //store the last 100000 time steps
       Comb = 0
       Ave = 0
       j1 = R
       k1 = R
       j2 = R
       k2 = R
       VarName = phi
       title = phi at center position
       x1_Label = time
       x2_Label = phi at center
}
Diagnostic //time history of equatorial beam space charge distribution
{
       HistMax = 400
       Comb = 0
       Ave = 1
       j1 = 0
       k1 = 40
       j2 = 80
       k2 = 40
       VarName = rho
       title = rho at equator
       x1_Label = equator position
       x2_Label = time (sec)
}
Diagnostic //trace the potential in the device center
{
       HistMax = 100000
       Comb = 0
       Ave = 0
       j1 = R
       k1 = R
       j2 = R
       k2 = R
       VarName = rho
       title = rho at center position
       x1_Label = time
       x2_Label = rho at center
}

}
```

Appendix B Matlab N-particle Collision Codes

The typical Matlab code for the N-body simulation of bunches is included here for reference. It consists of a main Matlab script and function file. Files which hold the indexed potential and gradient along the beam line shown in Figure 4.46 are also required, but are not included here.

```
%3D Synchronization Model, requires synchroindex.m, a.mat, gb.mat,
phi.mat

clear all
close all
drawnow
disp('Propagating.............');
warning off all;
      %declare global variables
load a.mat  %index vector of potential vs. radius
load gb.mat       %use indexed version of gradient function
dr = a(2)-a(1);
rmin = a(1);
rmaxindex = length(a);

load phi.mat      %load the polynomial fit for background potential for
      %initialization only
global P M ec m epzero no sigma pie ra rc phic phi rmin dr gb rmaxindex
      %initialize simulation parameters
sigma = 0.02;     %bunch variance in meters
no = 2e10;        %peak bunch density m^-3
epzero = 8.85e-12;
pie = 3.14159;
m = 40*1.6726e-27;      %mass in kg
ec = 1.602e-19;         %charge per particle
ra = 0.25;              %anode radius      %OBSOLETE
rs = 0.18;        %starting turnaround point
Period = 5.72e-6;       %expected period in seconds %4e-6 sec in OOPIC
NP = 10;          %expected number of passes
NDES = 5;         %number of passes desired for analysis
phis = polyval(phi,rs);
M = 24;     %number of particles, each particle has its own path
defined
P = zeros(M,3);   %initialize path vectors
P(1,:) = [1 0 0];
P(2,:) = [0 1 0];
P(3,:) = [-1 0 0];
P(4,:) = [0 -1 0];
```

```
P(5,:) = [1 1 0];
P(6,:) = [-1 -1 0];
P(7,:) = [1 -1 0];
P(8,:) = [-1 1 0];
P(9,:) = [0.7071 0 0.7071];
P(10,:) = [0 0.7071 0.7071];
P(11,:) = [0.5 0.5 0.7071];
P(12,:) = [-0.7071 0 0.7071];
P(13,:) = [0 -0.7071 0.7071];
P(14,:) = [-0.5 -0.5 0.7071];
P(15,:) = [0.5 -0.5 0.7071];
P(16,:) = [-0.5 0.5 0.7071];
P(17,:) = [0.7071 0 -0.7071];
P(18,:) = [0 0.7071 -0.7071];
P(19,:) = [0.5 0.5 -0.7071];
P(20,:) = [-0.7071 0 -0.7071];
P(21,:) = [0 -0.7071 -0.7071];
P(22,:) = [-0.5 -0.5 -0.7071];
P(23,:) = [0.5 -0.5 -0.7071];
P(24,:) = [-0.5 0.5 -0.7071];
      %initialize starting positions for each particle
xs(1:M) = rs-rs./1000.*rand(1,M);

for i = 1:M       %normalize path vectors
    ss = P(i,:).*P(i,:);
    st = ss(1) + ss(2) + ss(3);
    mag = st^0.5;
     P(i,:) = P(i,:)./mag;
            %determine starting velocities
    phir(i) = polyval(phi,xs(i));
    vs(i) = -1*(2*ec/m*(phis-phir(i)))^0.5;
            %calculate beginning pos and vel vectors

    xo(i,:) = xs(i) * P(i,:);
    vo(i,:) = vs(i) * P(i,:);       %particles start moving inwards
end

TSPAN = [0 NP*Period];        %timespan for integration
KO = [xs vs]';    %initial particle positions and velocities

      %call ODE45 to accomplish integrations in time
options = odeset('RelTol',1e-6,'AbsTol',1e-6);
tic
[t,k] = ode45(@synchroindex,TSPAN, KO, options);
toc

       %Determine the actual number of passes calculated
telapse = t(length(t));
NACT = telapse/Period  %actual number of passes calculated
newlength = length(t)*NDES/NACT;
NP = NACT;
if NACT > NDES
    t = t(1:newlength);
    k = k(1:newlength,:);
    NP = NDES;
end
NP
```

```
      %Trim output matrix to 100 points per pass, huge memory savings
L = length(t);
t = t(1:L/NP/100:L);
k = k(1:L/NP/100:L,:);

figure(1)
plot(t(:),k(:,1:M))
title(['path position vs time, no=' num2str(no)])

figure(2)
plot(t(:),k(:,M+1:2*M))
title(['path velocity vs time, no=' num2str(no)])

L = length(t);
    %RACETRACK PLOT
figure(3)
C = 1:1:M;

for i = 1:ceil(L/NP/10):L
scatter(k(i,1:M),k(i,M+1:2*M),400,C,'filled')
axis([-ra ra -2e5 2e5])
drawnow
end

clear XRL VRL
figure(4)
clf
      %plot relative phases
xmean = mean(k(:,1:M),2);
vmean = mean(k(:,M+1:2*M),2);
xrel = zeros(L,M);
vrel = xrel;
for i = 1:24
 xrel(:,i) = k(:,i) - xmean;
 vrel(:,i) = k(:,M+i) - vmean;
 LL = length(find(abs(k(:,i))<0.001));
 XRL(1:LL,i) = xrel(find(abs(k(:,i))<0.001),i);
 VRL(1:LL,i) = vrel(find(abs(k(:,i))<0.001),i);
      %only plot points as they cross axis, 0.001 plots about 3 points
per pass

scatter(xrel(find(abs(k(:,i))<0.001),i),vrel(find(abs(k(:,i))<0.001),i)
,50,'filled')
 hold on

end

title(['relative phase (vel vs. pos) of 24 particles, no='
num2str(no)])
xlabel('relative position, (meters)')
ylabel('relative velocity, (m/s)')
hold off

figure(6)
      %plot relative phases
      %find index of turning points
```

```
turn = sign(k(:,M+1:2*M));
turn = (turn + 1)./2;
turn = abs(diff(turn));
      %find index of center crossings
cen = sign(k(:,1:M));
cen = (cen + 1)./2;
cen = abs(diff(cen));

rabs = abs(k(:,1:M));
vabs = abs(k(:,M+1:2*M));
rmean = mean(rabs,2);
vmean = mean(vabs,2);
rrel = zeros(L,M);
vrel = rrel;

plot(rmean,vmean)
title(['Mean Radius, abs(r), vs. Mean Speed, no=' num2str(no)])
xlabel('mean radius, (meters)')
ylabel('mean speed, (m/s)')

for i = 1:M  %M
 rrel(:,i) = rabs(:,i) - rmean;
 vrel(:,i) = vabs(:,i) - vmean;
      %only plot points as they cross axis, 0.001 plots about 3 points
per pass
 figure(7)
 scatter( rrel( find(cen(:,i)),i ) ,
vrel( find(cen(:,i)),i ) ,50,'filled')
 hold on
 figure(8)
 scatter( rrel( find(turn(:,i)),i ) ,
vrel( find(turn(:,i)),i ) ,50,'filled')
 hold on
end

figure(7)
title(['At CENTER, relative phase (vel vs. pos) of 24 particles, no='
num2str(no)])
xlabel('relative position, (meters)')
ylabel('relative speed, (m/s)')
hold off

figure(8)
title(['At ANODE, relative phase (vel vs. pos) of 24 particles, no='
num2str(no)])
xlabel('relative position, (meters)')
ylabel('relative speed, (m/s)')
hold off

clear rrcen rrturn vvcen vvturn
for i = 1:24 %M
 rrel(:,i) = rabs(:,i) - rmean;
 vrel(:,i) = vabs(:,i) - vmean;
      %only plot points as they cross axis, 0.001 plots about 3 points
per pass
  LC = length( find(cen(:,i)) );
 LT = length( find(turn(:,i)) );
```

```
 rrcen(1:LC,i) = rrel( find(cen(:,i)),i );
 vvcen(1:LC,i) = vrel( find(cen(:,i)),i );
 rrturn(1:LT,i) = rrel( find(turn(:,i)),i );
 vvturn(1:LT,i) = vrel( find(turn(:,i)),i );
end

figure(9)
hold on
plot(rrcen,vvcen)
title(['At CENTER, relative phase (vel vs. pos) of 24 particles, no='
num2str(no)])
xlabel('relative position, (meters)')
ylabel('relative speed, (m/s)')
hold off

figure(10)
hold on
plot(rrturn,vvturn)
title(['At ANODE, relative phase (vel vs. pos) of 24 particles, no='
num2str(no)])
xlabel('relative position, (meters)')
ylabel('relative speed, (m/s)')
hold off

t(length(t))
disp('Simulation End..............');
disp(' ');
```

```
function dY = synchroindex(t,k)
global P M ec m epzero no sigma pie ra rc phic rmin dr gb rmaxindex

x = P(1:M,1) .* k(1:M);
y = P(1:M,2) .* k(1:M);
z = P(1:M,3) .* k(1:M);

dx = x*ones(1,M) - (x*ones(1,M))';
dy = y*ones(1,M) - (y*ones(1,M))';
dz = z*ones(1,M) - (z*ones(1,M))';

ax = ec*ec/m/epzero*no*sigma*sigma./dx./dx;
ax = ax.*( (pie/2)^0.5*sigma*erf(dx./sigma./2^0.5) - dx.*exp(-
1.*dx.*dx./2./sigma./sigma)) ;
ax(isnan(ax)) = [0];
AX = sum(ax,2);

ay = ec*ec/m/epzero*no*sigma*sigma./dy./dy;
ay = ay.*( (pie/2)^0.5*sigma*erf(dy./sigma./2^0.5) - dy.*exp(-
1.*dy.*dy./2./sigma./sigma)) ;
ay(isnan(ay)) = [0];
AY = sum(ay,2);

az = ec*ec/m/epzero*no*sigma*sigma./dz./dz;
az = az.*( (pie/2)^0.5*sigma*erf(dz./sigma./2^0.5) - dz.*exp(-
1.*dz.*dz./2./sigma./sigma)) ;
az(isnan(az)) = [0];
AZ = sum(az,2);

as = AX.*P(1:M,1) + AY.*P(1:M,2) + AZ.*P(1:M,3);

      %indexing algorithm
ii = ( abs(k(1:M)) - rmin )/dr + 1;
ii(find(ii(:) > rmaxindex)) = [rmaxindex];
iiL = floor(ii);
iiH = ceil(ii);
aback = (ii-iiL).*(gb(iiH)-gb(iiL)) + gb(iiL);
aback = -1*ec/m*aback;

aback = sign(k(1:M)) .* aback;
a = as + aback;
dY = [k(M+1:2*M) ; a];        %return derivatives
```

Appendix C Derivation of Central Ion Collision Energy Transfer

The energy transferred between two equal mass ions which collide at the center of an IEC is derived here in 2 major steps. The first step is to calculate the deflection angle of the relative velocity vector that occurs because of the collision. The second step is to construct velocity triangles to find the energy gained and lost by the 2 particles in the lab frame, using the deflection angle from step one. The derivation uses the general language and geometry of Mitchner and Kruger in their derivations of classical elastic scattering [26].

Assume that the two particles far apart at positions $\mathbf{r}_1$, $\mathbf{r}_2$ with velocities $\mathbf{v}_1$, $\mathbf{v}_2$ directed at the device center with an angle of φ between the two velocity vectors. Then define the relative 'lead' or 'lag' of the particles in terms of a nominal position and velocity as follows:

$$\left|\vec{v}_1\right| = v_o$$
$$\left|\vec{v}_2\right| = v_o + \Delta v$$
$$\left|\vec{r}_1\right| = r_o$$
$$\left|\vec{r}_2\right| = r_o + \Delta r$$

Then write the relative position and velocity vectors in a 2D coordinate system. The magnitude of the relative velocity vector is then used to calculate the 90 degree impact parameter, 'bo', as usual for Coulomb ion-ion collisions [26].

$$|\vec{g}| = v_o \sqrt{4\left(1+\frac{\Delta v}{v_o}\right)\sin^2\frac{\varphi}{2}+\left(\frac{\Delta v}{v_o}\right)^2}$$

$$|\vec{r}| = r_o \sqrt{4\left(1+\frac{\Delta r}{r_o}\right)\sin^2\frac{\varphi}{2}+\left(\frac{\Delta r}{r_o}\right)^2}$$

$$b_o = \frac{Z^2 e^2}{4\pi\varepsilon_o m_{12} g^2}$$

'm_{12}' is the reduced mass, here equal to m/2. Now calculate the angle 'η' between the relative position and velocity vectors. This angle is then used to find the impact parameter, 'b', for the collision.

$$\cos\eta = \frac{\vec{r}\bullet\vec{g}}{|\vec{r}||\vec{g}|}$$

$$b = \frac{|\vec{r}|}{2}\sin\eta$$

The deflection angle, 'θ_m', can now be calculated:

$$\theta_m = 2\tan^{-1}\left(\frac{b_o}{b}\right)$$

Now that we have calculated the deflection of the relative velocity vector after the collision, the velocity vectors of the 2 ions post-collision can be written in the lab frame. The post-collision relative velocity vector is given by multiplying the original vector by a rotation matrix.

$$\vec{g}' = \begin{pmatrix} \cos(2\theta_m) & -\sin(2\theta_m) \\ \sin(2\theta_m) & \cos(2\theta_m) \end{pmatrix}\vec{g}$$

Velocity triangles are then used to find the post-collision velocity vectors. These can then be normalized by the original velocity of particle 1, 'v_o'.

$$\left(\frac{v_1'}{v_o}\right)^2 = \left(1+\frac{\Delta v}{v_o}\right)\left(1-\sin\varphi\sin 2\theta_m - \frac{\Delta v}{v_o}\cos 2\theta_m\right) + \frac{1}{2}\left(\frac{\Delta v}{v_o}\right)^2\left(1+\cos 2\theta_m\right)$$

$$\left(\frac{v_2'}{v_o}\right)^2 = \left(1+\frac{\Delta v}{v_o}\right)\left(1+\sin\varphi\sin 2\theta_m + \frac{\Delta v}{v_o}\cos 2\theta_m\right) + \frac{1}{2}\left(\frac{\Delta v}{v_o}\right)^2\left(1-\cos 2\theta_m\right)$$

The above relations show that whether an ion gains or loses energy in the collision depends on the sign of deflection angle. The sign of the angle directly follows from the sign of the impact parameter. This means that shows that for an arbitrary lead or lag in both radius and velocity, what really matters is which particle effectively is 'in front' when the particles reach the vicinity of the device center. The amount of energy actually transferred additionally depends on the angle between the initial ion paths.

References

[1] Santarius, John F., "D-3He Magnetic Fusion Space Propulsion," 20th International Space Development Conference, Albuquerque, New Mexico (May 24-28, 2001).

[2] Walter E. Hammond, Matt Coventry, John Hanson, Ivana Hrbud, George H. Miley, Jon Nadler, "IEC Fusion: The Future Power and Propulsion System for Space," Space Technology and Applications Forum, STAIF (2000).

[3] R. W. Moir and W. L. Barr, " "Venetian-blind" Direct Energy Converter for Fusion Reactors," Nuclear Fusion Vol. **13**, pp. 35-44 (1973)

[4] W. L. Barr, R. W. Moir, and G. W. Hamilton, "Test Results on a High-Power, 100 keV Beam Direct Converter," J. Fusion Energy, Vol. **2**, No. 131 (1982).

[5] Philo T. Farnsworth, "Electric Discharge Device for Producing Interactions between Nuclei," U.S. Patent # 3,258,402 (issued June 28, 1966).

[6] Philo T. Farnsworth, "Method and Apparatus for Producing Nuclear Fusion Reactions," U.S. Patent # 3,386,883 (issued June 4, 1968).

[7] Philo T. Farnsworth, "Electrostatic Containment in Fusion Reactors," U.S. Patent # 3,664,920 (issued May 23, 1972).

[8] R. L. Hirsch, "Inertial Electrostatic Confinement of Ionized Fusion Gases," J. Appl. Phys. **38** (11), pp. 4522-34 (October, 1967).

[9] R. L. Hirsch, "Experimental Studies of a Deep, Negative, Electrostatic Potential Well in Spherical Geometry," Phys. Fluids **11** (11), pp. 2486-90 (November, 1968).

[10] D. C. Baxter and G. W. Stuart, "The Effect of Charge Exchange on Ion Guns and an Application to Inertial-Electrostatic Confinement Devices," Journal of Applied Physics, Vol. **53**, No. 7, pp. 4597-4601 (July 1982).

[11] John F. Santarius, Gerald L. Kulcinski, and Robert P. Ashley, "Progress in Inertial-Electrostatic Confinement Fusion," American Nuclear Society, Fusion Energy Division Newsletter (December 2002).

[12] R. A. Nebel and D. C. Barnes, "The Periodically Oscillating Plasma Sphere," Fusion Technology Vol. **34**, No. 28 (1998).

[13] G. H. Miley, Y. Gu, J. M. DeMora, R. A. Stubbers, T. A. Hochberg, J. H. Nadler and R. A. Anderl, "Discharge Chararcteristics of the Spherical Inertial Electrostatic Confinement (IEC) Device," IEEE Transactions on Plasma Science Vol. **25** (4), pp. 733-739 (August, 1997).

[14] Kulcinski, G.L., et al., "Demonstration of D^3He Fusion in an Inertial Electrostatic Confinement Device," Progress Report, Fusion Technology Institute, University of Wisconsin (Jan 29, 1998-Jan. 28, 1999).

[15] J. W. Weidner, G. L. Kulcinski, J. F. Santarius, R. P. Ashley, G. Piefer, B. Cipiti, R. Radel, and S. K. Murali, "Production of 13N via Inertial Electrostatic Confinement Fusion," Fusion Science and Technology, Vol. **44**, pp. 539 (2003).

[16] Robert W. Bussard, "Some physics considerations of magnetic inertial-electrostatic confinement: a new concept for spherical converging-flow fusion," Fusion Technology Vol. **19**, pp. 273-293 (Mar. 1991).

[17] Nicholas A. Krall, "The Polywell: a spherically convergent ion focus concept," Fusion Technology, Vol. **22**, pp. 42-49 (Aug. 1992).

[18] Gu, Yibin, "Experimental Study of Proton Rate Density in a Spherical Inertial Electrostatic Confinement Fusion Device", Doctoral Thesis, University of Illinois at Urbana Champaign (1998).

[19] R. Moses, "Enhancing IEC performance with Focusing Grids," presented at the Phys. Spherical Continuous Inertial Fusion Workshop, LANL, Santa Fe, NM (Jan. 1995).

[20] International Atomic Energy Agency, Atomic cross-sections physics database, IAEA AMDIS ALLADIN, Collisional Database, http://www-amdis.iaea.org/aladdin.html Dataset: ORNL-CFADC, 1990-01-06.

[21] Huba, J.D., NRL Plasma Formulary, Naval Research Laboratory (1998).

[22] Ashley, et al. "Steady-State D-^{3}He Proton Production in an IEC Fusion Device" 14th Topical meeting on the Technology of Fusion Energy (October 15-19, 2000), Park City, UT.

[23] T. A. Thorson, R. D. Durst, R. J. Fonck, A. C. Sontag, "Fusion reactivity characterization of a spherically-convergent ion focus," Nuclear Fusion Vol. **38** (4), pp. 495-507 (1998).

[24] Chen, Francis F. , Introduction to Plasma Physics and Controlled Fusion, Volume 1: Plasma Physics, (1984).

[25] J. H. Nadler and G. H. Miley, "A Breakeven Fusion Power Unit for Space Applications," Final Report NASA SBIR Contract #NAS8-99044, NPL Associates, Champaign, IL (June, 1999).

[26] M. Mitchner, Charles H. Kruger, Jr., Partially Ionized Gases, John Wiley and Sons, Inc., USA, (1973).

[27] Todd H. Rider, Fundamental Limitations on Plasma Fusion Systems not in Thermodynamic Equilibrium, MIT Ph.D. Thesis, Department of Electrical Engineering and Computer Science (June 1995).

[28] W. M. Nevins, "Can Inertial Electrostatic Confinement Work Beyond the Ion-Ion Collisional Time Scale?" Phys. Plasmas Vol. **2**, No. 10 (October 1995).

[29] C. K. Birdsall, A. B. Langdon, Plasma Physics via Computer Simulation, McGraw-Hill, New York (1985).

[30] C. K. Birdsall, "Particle-in-Cell Charged-Particle Simulations, Plus Monte Carlo Collisions with Neutral Atoms, PIC-MCC," IEEE Transactions on Plasma Science, Vol. **19**, No. 2, pp. 65-85 (April 1991).

[31] J. P. Verboncouer, A. B. Langdon, and N. T. Gladd, "An Object-Oriented Electromagnetic PIC Code," Computer Physics Communications, Vol. **87**, pp.199-211 (May 11, 1995).

[32] OOPIC Pro Software Data Sheet, Tech-X Corporation website, "www.txcorp.com/products/OOPIC_Pro/" Boulder, Colorado (2006).

[33] Robert C. Elson, Allen I. Selverston, Ramon Huerta, Nikolai F. Rulkov, Mikhail I. Rabinovich, and Henry D. I. Abarbanel, "Synchronous Behavior of Two Coupled Biological Neurons," Phys. Rev. Lett. Vol. **81**, pp. 5692–5695 (1998).

[34] D. Zajfman, O. Heber, L. Vejby-Christensen, I. Ben-Itzhak, M. Rappaport, R. Fishman, and M. Dahan, "Electrostatic Bottle for Long-term Storage of Fast Ion Beams," Phys. Rev. A Vol. **55**, No. 3, pp. R1577-R1580 (March 1997).

[35] M. Dahan, R. Fishman, O. Heber, M. Rappaport, N. Altstein, D. Zajfman, and W.J. van der Zande, "A New Type of Electrostatic Ion Trap for Storage of Fast Ion Beams," Rev. Sci. Instrum. Vol. **69**, No. 1, pp 76-83 (January 1998).

[36] H. B. Pedersen, D. Strasser, S. Ring, O. Heber, M. L. Rappaport, Y. Rudich, I. Sagi, and D. Zajfman, "Ion Motion Synchronization in an Ion-Trap Resonator," Phys. Rev. Letters, Vol. **87**, No. 5 (30 July 2001).

[37] H. B. Pedersen, D. Strasser, O. Heber, M.L. Rappaport, and D. Zajfman, "Stability and Loss in an Ion-trap Resonator," Phys. Rev. A, Vol. **65**, 042703 (2002).

[38] H. B. Pedersen, D. Strasser, B. Amarant, O. Heber, M.L. Rappaport, and D. Zajfman, "Diffusion and Synchronization in an Ion-trap Resonator," Phys. Rev. A, Vol. **65**, 042704 (2002).

[39] D. Strasser, T. Geyer, H.B. Pedersen, O. Heber, S. Goldberg, B. Amarant, A. Diner, Y. Rudich, I. Sagi, M. Rappaport, D.J. Tannor, and D. Zajfman, "Negative Mass Instability for Interacting Particles in a 1D Box: Theory and Application," Phys. Rev. Letters, Vol. **89**, No. 28 (31 December 2002).

[40] T. Geyer and D. Tannor, "A Mapping Approach to Synchronization in the 'Zajfman Trap': Stability Conditions and Synchronization Mechanism," J. Phys. B: At. Mol. Opt. Phys., Vol. **37**, pp. 73-92 (2003).

[41] D. Zajfman, O. Heber, M.L. Rappaport, H.B. Pedersen, D. Strasser, and S. Goldberg, "Self-bunching Effect in an Ion-trap Resonator," J. Opt. Soc. Am. B, Vol. **20**, No. 5, pp. 1028-1032 (May 2005).

[42] L. H. Andersen, O. Heber, and D. Zajfman, "Physics with Electrostatic Rings and Traps," J. Phys. B: At. Mol. Opt. Phys. Vol. **37**, pp. R57-R88 (2004).

[43] J.L. Delcroix and A. Bers, English Translation of Physique des Plasmas, Vol. 1, InterEditions, Paris, France Chapter 8, pp 50-52 (1994).

[44] C. Dietrich, Doctoral Thesis, Massachusetts Institute of Technology, Department of Aeronautics and Astronautics, projected graduation, February 2007.